

報告番号 甲第 3128 巻

AN EXPERIMENTAL STUDY OF QCD  
AND JETS IN  $e^+e^-$  ANNIHILATION \*

陽電子電子対消滅反応における QCD とジェットの  
実験による研究

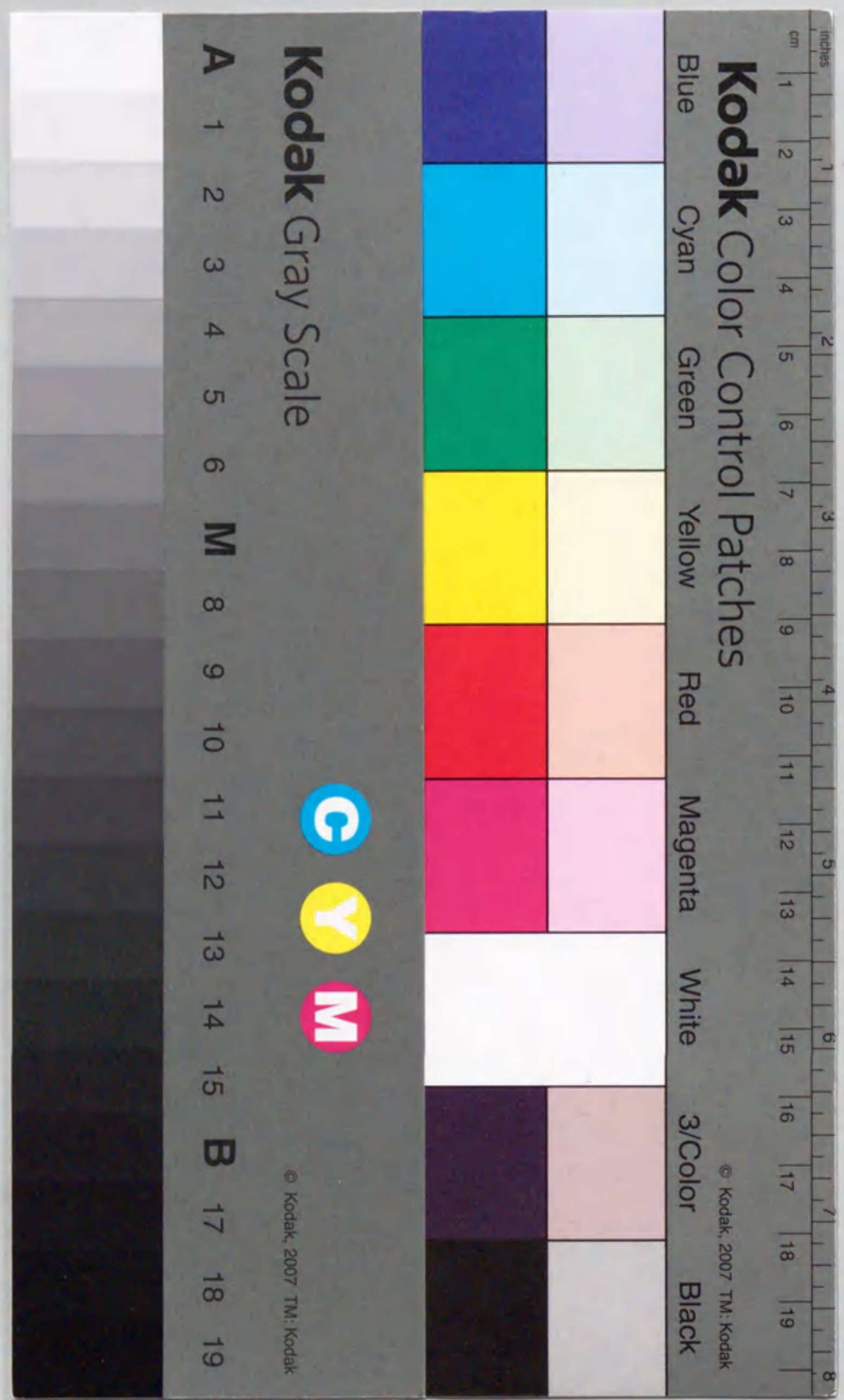
大西 幸喜

名古屋大学 理学研究科 物理学専攻

1994年12月

博士論文

\*この研究はアメリカ合州国エネルギー省 (DE-AC03-76SF00515) と高エネルギー物理学における日米協力実験プロジェクトによって支えられています。



①

AN EXPERIMENTAL STUDY OF QCD  
AND JETS IN  $e^+e^-$  ANNIHILATION\*

YUKIYOSHI OHNISHI

*Department of Physics, Nagoya University  
Nagoya 464, Japan*

December 1994

Ph.D Dissertation

---

\*This work was supported by Department of Energy contracts: DE-AC03-76SF00515; and the Japan-US Cooperative Research Project on High Energy Physics.

## Abstract

This thesis is concerned with an experimental study of QCD and JETS using hadronic decays of  $Z^0$  bosons by the SLD experiment at the SLAC Linear Collider.

The strong coupling  $\alpha_s(M_Z^2)$  has been measured, which is an important test of perturbative QCD theory. This comprehensive study comprised fifteen observables that describe hadronic final states; six event shapes, differential 2-jet rates defined by six different jet resolution/recombination schemes, energy-energy correlations and their asymmetry, and the jet cone energy fraction. The data were compared with QCD predictions both at fixed order,  $\mathcal{O}(\alpha_s^2)$ , and including resummed analytic formulae based on the leading and next-to-leading logarithmic approximation.

The consistency was checked between  $\alpha_s(M_Z^2)$  values extracted from these different measures. A final average of  $\alpha_s(M_Z^2) = 0.1200 \pm 0.0025(\text{exp.}) \pm 0.0078(\text{theor.})$ , corresponding to  $\Lambda_{\overline{MS}} = 253_{-96}^{+130}$  MeV, was obtained by combining all results. The dominant uncertainty is from uncalculated higher order contributions.

## Acknowledgements

My experiences in collider physics as an experimentalist has begun in 1991. I have joined the TOPAZ experiment for the first two years and spent rest years at the SLD experiment. I am very happy to be able to participate in those two experiments at different energy scales; 58 GeV for the TOPAZ and 91.2 GeV for the SLD. This thesis is concerned with the SLD experiment, and its purpose is a comprehensive analysis through measurements of  $\alpha_s$ .

I met many people who supported me a lot. I would like to thank I. Adachi and J. Fujimoto for their kind advice and we discussed many items concerned with both theoretical and experimental techniques. I also thank R. Itoh who gave me knowledge about the physics analysis utilities. I am quite thankful to K. Hagiwara, K. Kato, T. Munehisa, and K. Teshima for a lot of suggestions about the QCD theory. I would like to express my gratitude to G. Cowan, M. Ronan, and M. Yamauchi who invited me to the PEP-TOPAZ-ALEPH (PTA) collaboration and we discussed the significance of the analysis at the different energy scales.

I am extremely thankful to P.N. Burrows, D. Muller, and H. Masuda for their brilliant suggestions. We had a luncheon meeting of  $\alpha_s$  measurement on every Wednesday at SLAC. I can never forget such a valuable experience. I thank S.J. Brodsky, S.D. Ellis, C.J. Maxwell, P. Nason and D. Ward for helpful comments and suggestions related to this analysis.

I also thank the personnel of the SLAC accelerator department and the technical staffs of our collaborating institutions for their efforts which resulted in the successful operation of the SLC and the SLD.

I would like to thank Prof. H. Yuta, K. Abe, T. Akagi, and F. Suekane. Especially I am indebted to T. Nagamine who helped me in making our own computing environment at SLAC and made hadronic event analysis enjoyable for me. Without his support, I could not carry out many many calculations

for this thesis. I also thank Y. Hasegawa, M.D. Hildreth, and Y. Iwasaki with whom I enjoyed working and SLAC life.

I would like to appreciate Prof. R. Kajikawa, S. Suzuki, and A. Sugiyama for their continuous encouragement and warm guidance.

Finally I thank my family for their patience and support.

Contents

1	Introduction	1
2	Theory of Parabolic QED	2
3	3.1. Quantum Chromodynamics	3
4	3.2. The Non-Abelian Gauge Theory	4
5	3.3. The Renormalization Group Equation	5
6	3.4. The Parabolic Coupling Constant	6
7	3.5. The Parabolic Equation of QED	7
8	3.6. The Parabolic Equation	8
9	3.7. Experimental Apparatus	9
10	4. The SLAC Linear Collider	10
11	4.1. The SLAC Linear Collider	11
12	4.2. The SLAC Linear Collider	12
13	4.3. The SLAC Linear Collider	13
14	4.4. The SLAC Linear Collider	14
15	4.5. The SLAC Linear Collider	15
16	4.6. The SLAC Linear Collider	16
17	4.7. The SLAC Linear Collider	17
18	4.8. The SLAC Linear Collider	18
19	4.9. The SLAC Linear Collider	19
20	4.10. The SLAC Linear Collider	20
21	4.11. The SLAC Linear Collider	21
22	4.12. The SLAC Linear Collider	22
23	4.13. The SLAC Linear Collider	23
24	4.14. The SLAC Linear Collider	24
25	4.15. The SLAC Linear Collider	25
26	4.16. The SLAC Linear Collider	26
27	4.17. The SLAC Linear Collider	27
28	4.18. The SLAC Linear Collider	28
29	4.19. The SLAC Linear Collider	29
30	4.20. The SLAC Linear Collider	30
31	4.21. The SLAC Linear Collider	31
32	4.22. The SLAC Linear Collider	32
33	4.23. The SLAC Linear Collider	33
34	4.24. The SLAC Linear Collider	34
35	4.25. The SLAC Linear Collider	35
36	4.26. The SLAC Linear Collider	36
37	4.27. The SLAC Linear Collider	37
38	4.28. The SLAC Linear Collider	38
39	4.29. The SLAC Linear Collider	39
40	4.30. The SLAC Linear Collider	40
41	4.31. The SLAC Linear Collider	41
42	4.32. The SLAC Linear Collider	42
43	4.33. The SLAC Linear Collider	43
44	4.34. The SLAC Linear Collider	44
45	4.35. The SLAC Linear Collider	45
46	4.36. The SLAC Linear Collider	46
47	4.37. The SLAC Linear Collider	47
48	4.38. The SLAC Linear Collider	48
49	4.39. The SLAC Linear Collider	49
50	4.40. The SLAC Linear Collider	50
51	4.41. The SLAC Linear Collider	51
52	4.42. The SLAC Linear Collider	52
53	4.43. The SLAC Linear Collider	53
54	4.44. The SLAC Linear Collider	54
55	4.45. The SLAC Linear Collider	55
56	4.46. The SLAC Linear Collider	56
57	4.47. The SLAC Linear Collider	57
58	4.48. The SLAC Linear Collider	58
59	4.49. The SLAC Linear Collider	59
60	4.50. The SLAC Linear Collider	60
61	4.51. The SLAC Linear Collider	61
62	4.52. The SLAC Linear Collider	62
63	4.53. The SLAC Linear Collider	63
64	4.54. The SLAC Linear Collider	64
65	4.55. The SLAC Linear Collider	65
66	4.56. The SLAC Linear Collider	66
67	4.57. The SLAC Linear Collider	67
68	4.58. The SLAC Linear Collider	68
69	4.59. The SLAC Linear Collider	69
70	4.60. The SLAC Linear Collider	70
71	4.61. The SLAC Linear Collider	71
72	4.62. The SLAC Linear Collider	72
73	4.63. The SLAC Linear Collider	73
74	4.64. The SLAC Linear Collider	74
75	4.65. The SLAC Linear Collider	75
76	4.66. The SLAC Linear Collider	76
77	4.67. The SLAC Linear Collider	77
78	4.68. The SLAC Linear Collider	78
79	4.69. The SLAC Linear Collider	79
80	4.70. The SLAC Linear Collider	80
81	4.71. The SLAC Linear Collider	81
82	4.72. The SLAC Linear Collider	82
83	4.73. The SLAC Linear Collider	83
84	4.74. The SLAC Linear Collider	84
85	4.75. The SLAC Linear Collider	85
86	4.76. The SLAC Linear Collider	86
87	4.77. The SLAC Linear Collider	87
88	4.78. The SLAC Linear Collider	88
89	4.79. The SLAC Linear Collider	89
90	4.80. The SLAC Linear Collider	90
91	4.81. The SLAC Linear Collider	91
92	4.82. The SLAC Linear Collider	92
93	4.83. The SLAC Linear Collider	93
94	4.84. The SLAC Linear Collider	94
95	4.85. The SLAC Linear Collider	95
96	4.86. The SLAC Linear Collider	96
97	4.87. The SLAC Linear Collider	97
98	4.88. The SLAC Linear Collider	98
99	4.89. The SLAC Linear Collider	99
100	4.90. The SLAC Linear Collider	100

# Contents

<b>1</b>	<b>Introduction</b>	<b>1</b>
<b>2</b>	<b>Theory of Perturbative QCD</b>	<b>5</b>
2.1	Quantum Chromodynamics	5
2.2	The Renormalization Group Equation	6
2.3	The Running Coupling $\alpha_s$	8
2.4	Theoretical Predictions of QCD	10
<b>3</b>	<b>Experimental Apparatus</b>	<b>17</b>
3.1	The SLAC Linear Collider	17
3.2	The SLC Large Detector	21
3.2.1	Vertex Detector	21
3.2.2	Drift Chambers	24
3.2.3	Čerenkov Ring Imaging Detector	25
3.2.4	Liquid Argon Calorimeter	26
3.2.5	Warm Iron Calorimeter	28
3.2.6	Luminosity Monitor	29
3.3	Trigger System	29
3.4	Data Taking History	29
<b>4</b>	<b>Hadronic Event Selection and Simulations</b>	<b>31</b>
4.1	Hadronic Event Selection	31

4.2	Monte Carlo Simulations	32
4.2.1	Event Generators	33
4.2.2	Detector Simulation	39
4.3	Comparison of Data and Monte Carlo Simulations	40
<b>5</b>	<b>Hadronic Event Observables</b>	<b>43</b>
5.1	Event Shapes	43
5.1.1	Thrust	43
5.1.2	Oblateness	45
5.1.3	The C-parameter	48
5.1.4	Heavy jet mass	51
5.1.5	Jet broadening	56
5.2	Jet Rates	62
5.2.1	Jet Clustering Algorithms	62
5.3	Particle Correlations	78
5.4	Angular Energy Flow	80
<b>6</b>	<b>Measurement of <math>\alpha_s(M_Z^2)</math></b>	<b>87</b>
6.1	Data Analysis	87
6.2	Measurement of $\alpha_s(M_Z^2)$ from $\mathcal{O}(\alpha_s^2)$ Calculation	98
6.3	Measurement of $\alpha_s(M_Z^2)$ from Resummed+ $\mathcal{O}(\alpha_s^2)$ Calculation	109
<b>7</b>	<b>Discussions</b>	<b>119</b>
7.1	Running Coupling of $\alpha_s$	119
7.2	Optimization of Renormalization Scale	122
<b>8</b>	<b>Conclusions</b>	<b>127</b>

## List of Tables

2.1	Schematic representation of the expansion in the resummation of the LL, NLL, and subleading parts. . . . .	15
3.1	The parameters of the SLC. . . . .	20
3.2	The parameters of the Vertex Detector (VXD). . . . .	23
3.3	The parameters of the barrel Čerenkov Imaging Ring Detector (CRID). . . . .	27
4.1	The main parameters of JETSET and HERWIG. . . . .	39
5.1	Coefficients of the $\tilde{\alpha}_s$ and $\tilde{\alpha}_s^2$ terms for $\tau$ and $O$ . . . . .	47
5.2	Coefficients of the $\tilde{\alpha}_s$ and $\tilde{\alpha}_s^2$ terms for $C$ and $\rho$ . . . . .	53
5.3	Coefficients of the $\tilde{\alpha}_s$ and $\tilde{\alpha}_s^2$ terms for $B_T$ and $B_W$ . . . . .	61
5.4	Jet finging algorithm . . . . .	63
5.5	Coefficients of the $\tilde{\alpha}_s$ and $\tilde{\alpha}_s^2$ terms for E-, E0-, P-, and P0-scheme. . . . .	66
5.6	Coefficients of the $\tilde{\alpha}_s$ and $\tilde{\alpha}_s^2$ terms for D- and G-scheme. . . . .	67
5.7	Coefficients of the $\tilde{\alpha}_s$ and $\tilde{\alpha}_s^2$ terms for <i>EEC</i> . . . . .	79
5.8	Coefficients of the $\tilde{\alpha}_s$ and $\tilde{\alpha}_s^2$ terms for <i>JCEF</i> . . . . .	85
6.1	Distributions of $\tau$ and $\rho$ . . . . .	93
6.2	Distributions of $B_T$ and $B_W$ . . . . .	93
6.3	Distributions of $O$ and $C$ . . . . .	94
6.4	$D_2(y_{cut})$ calculated in the E-scheme, the E0-scheme, and the P-scheme. . . . .	95

6.5	$D_2(y_{cut})$ calculated in the P0-scheme, the D-scheme, and the G-scheme. . . . .	95
6.6	The <i>EEC</i> . . . . .	96
6.7	The <i>AEEC</i> and <i>JCEF</i> . . . . .	97
6.8	Observables used in $\mathcal{O}(\alpha_s^2)$ QCD fits. . . . .	99
6.9	The $\alpha_s(M_Z^2)$ values derived from $\mathcal{O}(\alpha_s^2)$ QCD fits. . . . .	100
6.10	Observables used in resummed+ $\mathcal{O}(\alpha_s^2)$ fits. . . . .	111
6.11	The $\alpha_s(M_Z^2)$ values derived from resummed+ $\mathcal{O}(\alpha_s^2)$ QCD fits. . . . .	113
6.12	Observables used in resummed+ $\mathcal{O}(\alpha_s^2)$ fits with the fit ranges extended into the two-jet region. . . . .	114
6.13	The $\alpha_s(M_Z^2)$ values derived from resummed+ $\mathcal{O}(\alpha_s^2)$ QCD fits with the fit ranges extended into the two-jet region. . . . .	116
7.1	Summary of some of the $\alpha_s$ measurement at the $Z^0$ resonance. . . . .	121

## List of Figures

2.1	Triple-gluon and four-gluon couplings. . . . .	6
2.2	The running of $\alpha_s$ . . . . .	9
2.3	Feynman diagrams in $\mathcal{O}(\alpha_s)$ for 3-parton. . . . .	10
2.4	Dalitz plot for 3-parton final state. . . . .	11
2.5	Feynman diagrams up to $\mathcal{O}(\alpha_s^2)$ for 2-, 3-, and 4-parton. . . . .	12
3.1	The layout of the SLAC Linear Collider. . . . .	18
3.2	North (electron) damping ring beam transport. . . . .	19
3.3	The cutaway and quadrant view of the SLC Large Detector. . . . .	22
3.4	The SLD Vertex Detector (VXD). . . . .	23
3.5	Operation of the barrel Čerenkov Ring Imaging Detector (CRID). . . . .	26
3.6	A module of the barrel Liquid Argon Calorimeter (LAC). . . . .	28
3.7	SLC luminosity performance for 1991-1993. . . . .	30
4.1	Schematic picture of parton shower evolution. . . . .	33
4.2	A picture of cluster fragmentation . . . . .	37
4.3	The polar angle $\cos\theta_{track}$ and transverse momentum of charged particles. . . . .	40
4.4	A comparison of experimental hadronic events and Monte Carlo predictions. . . . .	42
5.1	Histograms for the function (a) $\tau A(\tau)$ and (b) $\tau B(\tau)$ . . . . .	45
5.2	Dependences of $\Lambda_{\overline{MS}}$ and $f$ for thrust. . . . .	46

5.3	Histograms for the function (a) $OA(O)$ and (b) $OB(O)$ . . . . .	49
5.4	Dependences of $\Lambda_{\overline{MS}}$ and $f$ for oblateness . . . . .	50
5.5	Histograms for the function (a) $CA(C)$ and (b) $CB(C)$ . . . . .	51
5.6	Dependences of $\Lambda_{\overline{MS}}$ and $f$ for C-parameter . . . . .	52
5.7	Histograms for the function (a) $\rho A(\rho)$ and (b) $\rho B(\rho)$ . . . . .	54
5.8	Dependences of $\Lambda_{\overline{MS}}$ and $f$ for heavy jet mass. . . . .	55
5.9	Histograms for the function (a) $B_T A(B_T)$ and (b) $B_T B(B_T)$ . . . . .	58
5.10	Histograms for the function (a) $B_W A(B_W)$ and (b) $B_W B(B_W)$ . . . . .	58
5.11	Dependences of $\Lambda_{\overline{MS}}$ and $f$ for total jet broadening. . . . .	59
5.12	Dependences of $\Lambda_{\overline{MS}}$ and $f$ for wide jet broadening. . . . .	60
5.13	Plots for the function (a) $A_3(y_{cut})$ and (b) $B_4(y_{cut})$ for E-, E0-, P-, and P0-scheme. . . . .	68
5.14	Plots for the function $B_3(y_{cut})$ for (a) E-, (b) E0-, (c) P-, and (d) P0-scheme. . . . .	69
5.15	Plots for the function (a) $A_3(y_{cut})$ , (b) $B_3(y_{cut})$ , and (c) $B_4(y_{cut})$ for D-scheme. . . . .	70
5.16	Plots for the function (a) $A_3(y_{cut})$ , (b) $B_3(y_{cut})$ , and (c) $B_4(y_{cut})$ for G-scheme. . . . .	71
5.17	Dependences of $\Lambda_{\overline{MS}}$ and $f$ for E-scheme. . . . .	72
5.18	Dependences of $\Lambda_{\overline{MS}}$ and $f$ for E0-scheme. . . . .	73
5.19	Dependences of $\Lambda_{\overline{MS}}$ and $f$ for P-scheme. . . . .	74
5.20	Dependences of $\Lambda_{\overline{MS}}$ and $f$ for P0-scheme. . . . .	75
5.21	Dependences of $\Lambda_{\overline{MS}}$ and $f$ for D-scheme. . . . .	76
5.22	Dependences of $\Lambda_{\overline{MS}}$ and $f$ for G-scheme. . . . .	77
5.23	Histograms for the function (a) $\sin\chi A(\chi)$ and (b) $\sin\chi B(\chi)$ of the $EEC$ . . . . .	80
5.24	Dependences of $\Lambda_{\overline{MS}}$ and $f$ for $EEC$ . . . . .	81
5.25	Dependences of $\Lambda_{\overline{MS}}$ and $f$ for $AEEC$ . . . . .	82
5.26	Schematic view of hadronic event. . . . .	83

5.27	Histograms for the function (a) $\sin \chi A(\chi)$ and (b) $\sin \chi B(\chi)$ of the <i>JCEF</i> . . . . .	84
5.28	Dependences of $\Lambda_{\overline{MS}}$ and $f$ for <i>JCEF</i> . . . . .	86
6.1	The measured event shapes corrected to the hadron level. . . . .	90
6.2	The measured differential 2-jet rate corrected to the hadron level. . . . .	91
6.3	The measured <i>EEC</i> , <i>AEEC</i> , and <i>JCEF</i> corrected to the hadron level. . . . .	92
6.4	The measured $\tau$ , $\rho$ , $B_T$ , and $B_W$ corrected to the parton level. . . . .	104
6.5	The measured $O$ , $C$ , $D_2(E)$ , and $D_2(E0)$ corrected to the parton level. . . . .	105
6.6	The measured $D_2(P)$ , $D_2(P0)$ , $D_2(D)$ , and $D_2(G)$ corrected to the parton level. . . . .	106
6.7	The measured <i>EEC</i> , <i>AEEC</i> , and <i>JCEF</i> corrected to the parton level. . . . .	107
6.8	(a) $\alpha_s(M_Z^2)$ and (b) $\chi_{dof}^2$ from the $\mathcal{O}(\alpha_s^2)$ fits to the event shapes and jet rates as a function of $f$ . . . . .	108
6.9	(a) $\alpha_s(M_Z^2)$ and (b) $\chi_{dof}^2$ from the $\mathcal{O}(\alpha_s^2)$ fits to the <i>EEC</i> , <i>AEEC</i> , and <i>JCEF</i> as a function of $f$ . . . . .	109
6.10	(a) $\alpha_s(M_Z^2)$ and (b) $\chi_{dof}^2$ from the resummed+ $\mathcal{O}(\alpha_s^2)$ fits with <i>lnR</i> - and <i>modified lnR</i> -matching as a function of $f$ . . . . .	117
6.11	(a) $\alpha_s(M_Z^2)$ and (b) $\chi_{dof}^2$ from the resummed+ $\mathcal{O}(\alpha_s^2)$ fits with <i>R</i> - and <i>modified R</i> -matching as a function of $f$ . . . . .	118
7.1	The energy scale dependence of $\alpha_s$ . . . . .	120
7.2	Optimized scale $f$ as a function of variable for event shapes. . . . .	125
7.3	The results of $\alpha_s$ using various scale optimizing methods. . . . .	126
8.1	Compilation of final values of $\alpha_s(M_Z^2)$ . . . . .	130

## Chapter 1

### Introduction

Achieving precision tests of the Standard Model of elementary particle interactions is one of the key aims of high energy physics experiments. Some measurements in the electroweak sector have reached a precision of better than 1 %.<sup>1</sup> However, measurements of strong interactions, and hence tests of the theory of Quantum Chromodynamics (QCD),<sup>2</sup> have not yet achieved the same level of precision. This is largely due to the difficulty of performing QCD calculations, both at higher order in perturbation theory and in the non-perturbative regime, where effects due to the hadronization process are important. Perturbative QCD is a theory with one free parameter, the strong coupling  $\alpha_s$ , which can also be written in terms of a scale parameter  $\Lambda$ . Tests of the perturbative QCD can therefore be reduced to a comparison of measurements of  $\alpha_s$ , either in different *hard processes* which is QCD processes involving sufficiently large exchanges of momenta where  $\alpha_s$  is small enough for the perturbative approach to be valid, such as hadron-hadron collisions or  $e^+e^-$  annihilations, or at different energy scales  $Q$ . This thesis presents an experimental study of QCD and JETS\*, by means of measurement of  $\alpha_s$ , in hadronic decays of  $Z^0$  bosons produced by  $e^+e^-$  annihilations at the SLAC

\*The term of JETS is defined by the group which contains particles fly toward the almost same direction.



Linear Collider (SLC) and recorded in the SLC Large Detector (SLD).

Complications arise in making accurate QCD predictions. In practice, because of the large number of Feynman diagrams involved, QCD calculations are only possible with present techniques to low order in perturbation theory. Perturbative calculations are performed within a particular *renormalization scheme*,<sup>3</sup> which also defines the strong coupling. Translation between different schemes is possible, without changing the final predictions, by appropriate redefinition of  $\alpha_s$  and of the *renormalization scale*.<sup>4</sup> This leads to a *scheme-dependence* of  $\alpha_s$ , which can be alleviated in practice by choosing one particular scheme as a standard and translating all  $\alpha_s$  measurements to it. The modified minimal subtraction scheme ( $\overline{\text{MS}}$  scheme)<sup>3</sup> is presently used widely as this standard.

An additional complication is the truncation of the perturbative series at finite order which yields a residual dependence on the renormalization scale, often denoted by  $\mu$  or equivalently by  $f = \mu^2/Q^2$ , which then becomes an arbitrary unphysical parameter. It has been shown that the dominant uncertainty in  $\alpha_s(M_Z^2)$  measurements arises from this *renormalization scale ambiguity*.<sup>5,6</sup> Given that infinite order perturbative QCD calculations would be independent of  $\mu$ , the scale uncertainty inherent in  $\alpha_s$  measurements is a reflection of the neglected higher order terms.

Distributions of observables in the process  $e^+e^- \rightarrow \text{hadrons}$  have been calculated exactly up to  $\mathcal{O}(\alpha_s^2)$  in QCD perturbation theory.<sup>7</sup> One expects *a priori* that the size of the uncalculated  $\mathcal{O}(\alpha_s^3)$  and higher order terms will in general be different for each observable, and hence that the scale dependence of the  $\alpha_s$  values measured using different observables will also be different. In order to make a realistic determination of  $\alpha_s$  and its associated theoretical uncertainty using  $\mathcal{O}(\alpha_s^2)$  calculations it is therefore advantageous to employ as many different observables as possible. In this analysis the data sample collected by the SLD in 1992 and 1993, comprising approximately 60,000 events,

have been used to make measurement of  $\alpha_s(M_Z^2)$  using fifteen observables presently calculated up to  $\mathcal{O}(\alpha_s^2)$  in perturbative QCD.

In addition, for six of these fifteen observables, improved calculations can be formulated incorporating the resummation<sup>8-13</sup> of leading and next-to-leading logarithms matched to the  $\mathcal{O}(\alpha_s^2)$  results; these matched calculations, i.e. resummed+ $\mathcal{O}(\alpha_s^2)$  calculations are expected *a priori* both to describe the data in a larger region of phase space than the fixed order results, and to yield a reduced dependence of  $\alpha_s(M_Z^2)$  on the renormalization scale. The resummed+ $\mathcal{O}(\alpha_s^2)$  calculations have been employed for six observables to determine  $\alpha_s(M_Z^2)$ , and the uncertainties involved in the matching procedure have been studied.

Organization of this thesis is as follows; chapter 2 reviews the perturbative QCD predictions. Chapter 3 is devoted to a brief review of the SLC and the SLD. The hadronic event trigger and selection criteria are described in chapter 4. Monte Carlo event simulations are also treated there. The definitions of hadronic event observables and investigations of sensitivity for measurement of  $\alpha_s(M_Z^2)$  using  $\mathcal{O}(\alpha_s^2)$  calculations are described in chapter 5. The analysis of the data and derivation of  $\alpha_s(M_Z^2)$  using both  $\mathcal{O}(\alpha_s^2)$  and resummed+ $\mathcal{O}(\alpha_s^2)$  calculations are presented in chapter 6. In chapter 7 the running of  $\alpha_s$  compared with other experimental results and the optimization of the renormalization scale are discussed. Chapter 8 summarizes the results and concludes this thesis.

## Chapter 2

# Theory of Perturbative QCD

### 2.1 Quantum Chromodynamics

Quantum chromodynamics (QCD),<sup>2</sup> which is a non-Abelian gauge theory, describes the strong interactions of quarks and gluons by means of a color force. The color charge, which has three kinds, namely *red*, *green*, and *blue*, is the source of the strong force. Each quark, belonging to a  $SU(3)_c$  triplet, has one of the three colors, while the gluon, belonging to a  $SU(3)_c$  octet, carries two labels, one is color and the other is anti-color. As a remarkable nature of non-Abelian theories, QCD has a triple gluon coupling as well as a four-gluon coupling as shown in Fig. 2.1. The gluon self-couplings have no analog in QED and are responsible for the asymptotic freedom, a remarkable property of QCD. This implies the strong coupling of QCD,  $\alpha_s$ , decreases as energy scale (momentum transfer) increases. In high energy  $e^+e^-$  annihilation processes, therefore,  $\alpha_s$  is small enough to allow perturbative calculations. In contrast with the high energy processes,  $\alpha_s$  becomes so large when the energy decreases that the theory enters a strongly coupled regime (the infra-red slavery) thereby making perturbative treatments invalid. The color confinement is believed to be a direct consequence of this infra-red slavery.

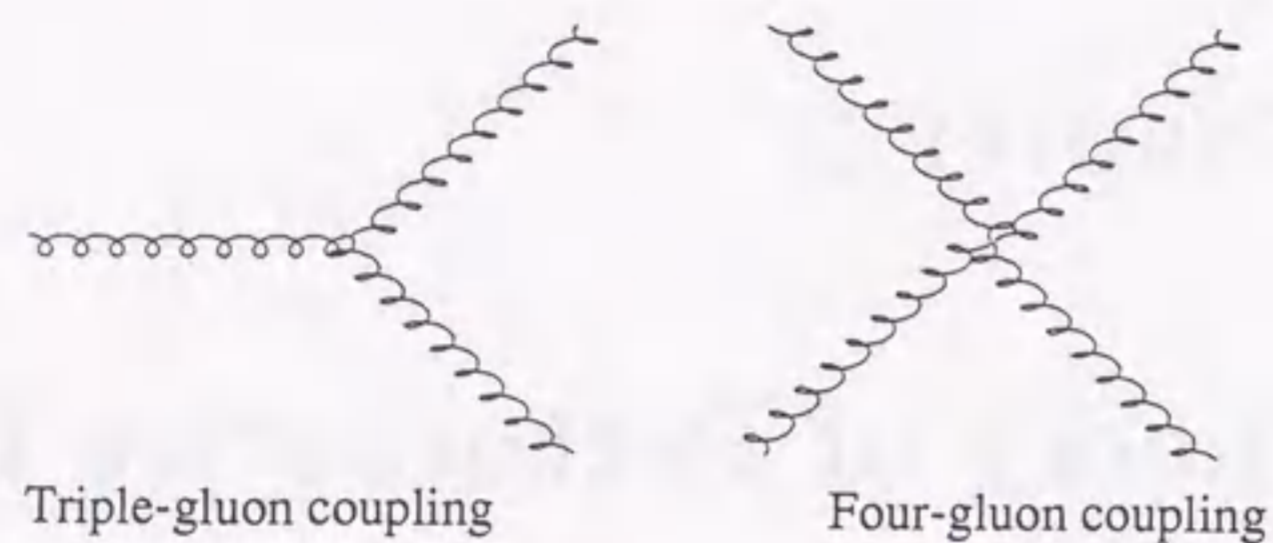


Fig. 2.1. Triple-gluon and four-gluon couplings.

## 2.2 The Renormalization Group Equation

When one calculates Feynman diagrams that contain loops, divergent integrals over loop momenta occur. In order to avoid this divergence, first the divergent expressions are made *finite* temporarily using some *regularization* procedure.<sup>14</sup> This introduces additional parameters, for example, a gluon mass  $m_g$ , an ultraviolet momentum cut-off  $\kappa$ , or a fractional space-time dimension  $D = 4 - \epsilon$ . Then these regularized divergences of perturbation theory are removed by absorbing them into the definitions of physical quantities through a *renormalization* procedure.<sup>15</sup> This is done by some specified treatment but arbitrary, which introduces a new dimensional scale  $\mu$ . Different renormalization treatments with different scale  $\mu$  must lead to the same amplitudes for a physical observable. The equations that express the invariance of the physics under changes of the parameter  $\mu$  are known as the *Renormalization Group Equation* (RGE).<sup>16</sup>

Renormalization is performed on the sum of connected Feynman dia-

grams with the external propagators removed. One way to control divergences in a quantity  $\Gamma$  is to introduce an ultraviolet cut-off  $\kappa$  in the loop momentum integrals. Thus unrenormalized quantity  $\Gamma_U(p_i, g_0, \kappa)$  is considered, where  $p_i$  is momenta of external particle and  $g_0$  is the basic vertex coupling. For a renormalizable theory such as QCD, it is possible to define renormalized quantity  $\Gamma_R$  by

$$\Gamma_R(p_i, g, \mu) = Z_\Gamma(g_0, \kappa/\mu) \Gamma_U(p_i, g_0, \kappa), \quad (2.1)$$

which are finite in the  $\kappa \rightarrow \infty$  limit but depends on the scale parameter  $\mu$  and a renormalized coupling  $g$ . Because  $\Gamma_U$  does not depend on  $\mu$ , one obtains

$$\frac{d\Gamma_U}{d\mu} = \frac{\partial Z_\Gamma^{-1}}{\partial \mu} + Z_\Gamma^{-1} \left( \frac{\partial}{\partial \mu} + \frac{\partial g}{\partial \mu} \frac{\partial}{\partial g} \right) \Gamma_R = 0 \quad (2.2)$$

This expression can be usually written as

$$\left( \mu \frac{\partial}{\partial \mu} + \beta \frac{\partial}{\partial g} + \gamma_\Gamma \right) \Gamma_R(p_i, g, \mu) = 0, \quad (2.3)$$

where the  $\beta$  function  $\beta(g)$  and the *anomalous dimension*  $\gamma(g)$  are defined by:

$$\beta = \mu \frac{\partial g}{\partial \mu} \quad (2.4)$$

$$\gamma_\Gamma = -\frac{\mu}{Z_\Gamma} \frac{\partial Z_\Gamma}{\partial \mu}. \quad (2.5)$$

The  $\beta$  function is universal, while the  $\gamma$  function depends on the quantity  $\Gamma$ . If  $Z_\Gamma$  is expressed as a product of renormalization factors,  $\gamma$  may be expressed as a sum of the corresponding contributions.

In the method described above, the infinities from the divergent integral that has a form like  $\int \frac{d^4 k}{k^2}$  has been made finite by taking a fixed cut-off parameter,  $\kappa$ , on the momentum. Hence the infinity appears in the form  $\lim_{\kappa \rightarrow \infty} \ln \kappa^2$ , and this term is cancelled with the bare coupling  $g_0$  to give a finite result at scale  $\mu$ . This is called the *Momentum Scheme* of renormalization (*MOM*). In an alternative approach, the most often used is *dimensional regularization*.<sup>14</sup>

This considers the integral  $\int \frac{d^D k}{k^2}$  as a function of the space-time dimension  $D = 4 - \epsilon$ . This diverges like

$$\Gamma\left(1 - \frac{D}{2}\right) \approx -\frac{2}{\epsilon} - \frac{3}{2} + \gamma_E, \quad (2.6)$$

where  $\gamma_E$  is Euler's constant, i.e. 0.5772... The  $2/\epsilon$  term is infinite in the  $D \rightarrow 4$  limit, however it can be cancelled in the same way as the  $\ln \kappa^2$  in the *MOM* scheme. This is the *Minimal Subtraction scheme (MS)*. Alternatively, one can put  $-3/2 + \gamma_E$  into this infinity and those terms are also cancelled. This is essentially equivalent to the *Modified Minimal Subtraction scheme ( $\overline{MS}$ )*<sup>3</sup> which is commonly used. A scale  $\mu$  also appears in such a scheme as a necessary quantity to keep the dimensions correct.

### 2.3 The Running Coupling $\alpha_s$

The renormalization scale dependence of the effective QCD coupling  $\alpha_s \equiv g_s^2/4\pi$  is controlled by the  $\beta$  function (Eq. (2.4)):

$$\begin{aligned} \mu \frac{\partial \alpha_s}{\partial \mu} &= -\frac{\beta_0}{2\pi} \alpha_s^2 - \frac{\beta_1}{4\pi^2} \alpha_s^3 - \dots, \\ \beta_0 &= 11 - \frac{2}{3} n_f, \\ \beta_1 &= 51 - \frac{19}{3} n_f, \end{aligned} \quad (2.7)$$

where  $n_f$  is the number of massless quarks than the energy scale  $\mu$ .

In the Next-to-Leading Order (NLO),  $\alpha_s$  can be written by a solution to Eq. (2.7) as

$$\alpha_s(\mu^2) = \frac{4\pi}{\beta_0 \ln(\mu^2/\Lambda^2)} \left( 1 - \frac{2\beta_1}{\beta_0^2} \frac{\ln(\ln(\mu^2/\Lambda^2))}{\ln(\mu^2/\Lambda^2)} \right). \quad (2.8)$$

Figure 2.2 shows the running coupling  $\alpha_s$  as a function of energy scale  $\mu$  from Eq. (2.8).

If one only considers Leading Order (LO), the solution of Eq. (2.7) is

$$\alpha_s(\mu^2) = \frac{4\pi}{\beta_0 \ln(\mu^2/\Lambda^2)}, \quad (2.9)$$

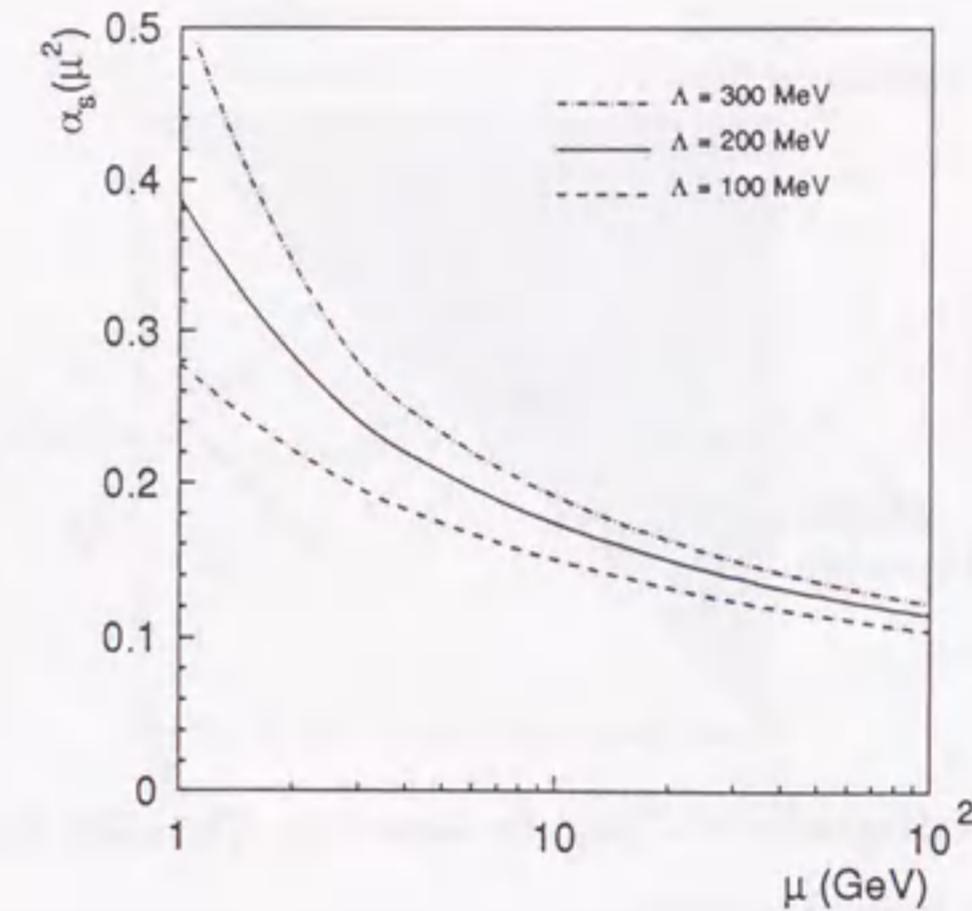


Fig. 2.2. The running of  $\alpha_s$ .

then it can be found that a change of the scale  $\mu$  by a factor of order 1, say  $\mu' = 2\mu$  yields

$$\begin{aligned} \alpha_s(\mu'^2)_{LO} &= \frac{4\pi}{\beta_0 \ln(\mu'^2/\Lambda^2)} \\ &\simeq \frac{4\pi}{\beta_0 \ln(\mu^2/\Lambda^2)} \left( 1 - \mathcal{O}\left(\frac{1}{\ln(\mu^2/\Lambda^2)}\right) \right) \\ &= \alpha_s(\mu^2)_{LO} + \text{NLO correction}, \end{aligned} \quad (2.10)$$

and includes a change in  $\alpha_s$  which is of the NLO. Therefore in the leading order of perturbation theory one can not specify the scale at which  $\alpha_s$  is evaluated, and it is necessary to go beyond the leading order. The form of Eq. (2.8) is scheme independent since the coefficients  $\beta_0$ ,  $\beta_1$  are independent of the renormalization scheme. However, the expressions of physical cross sections are scheme dependent, and therefore the fitted value of  $\Lambda$  depends on the renormalization scheme.

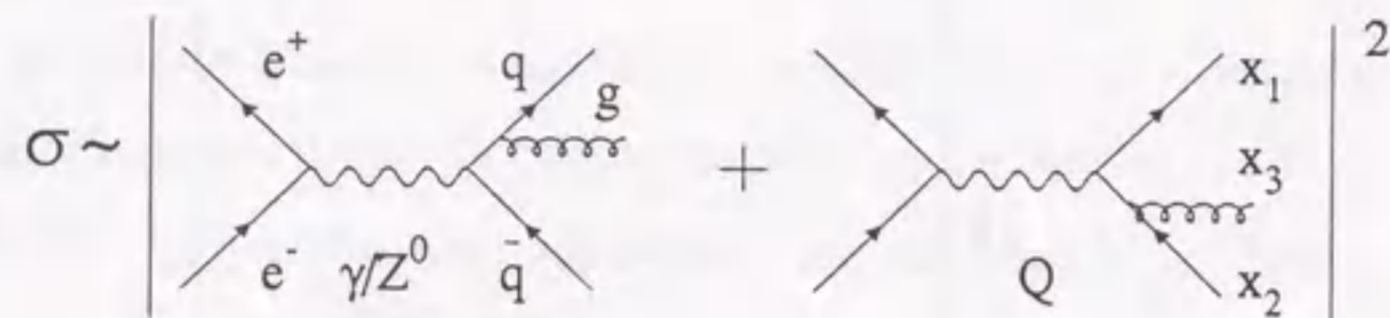


Fig. 2.3. Feynman diagrams in  $\mathcal{O}(\alpha_s)$  for 3-parton. The solid line stands for fermion and the curly line indicates gluon.

## 2.4 Theoretical Predictions of QCD

In the  $e^+e^-$  annihilation, the perturbative QCD calculation of the hadronic cross sections in  $\mathcal{O}(\alpha_s)$  for 3-parton final states gives

$$\frac{1}{\sigma_0} \frac{d\sigma}{dx_1 dx_2} = \frac{2\alpha_s}{3\pi} \frac{x_1^2 + x_2^2}{(1-x_1)(1-x_2)}, \quad (2.11)$$

where  $\sigma_0$  is Born cross section. Here the dimensionless energy fractions are defined as

$$x_i \equiv \frac{2E_i}{Q}, \quad (2.12)$$

where  $E_i$  is the energy of three decay particles ( $i = 1$ :quark,  $2$ :anti-quark,  $3$ :gluon) and  $Q$  is the center-of-mass energy. Figure 2.3 shows the Feynman diagrams considered.

The differential cross section in Eq. (2.11) diverges as  $x_1$  or  $x_2$  goes to 1 and  $\sigma$  is infinite. In other words, the differential cross section diverges when the energy of the gluon goes to zero or when the outgoing quark (or anti-quark) and gluon become parallel. The first type of divergence is referred to as an infra-red divergence (soft singularity), while the second is referred to as

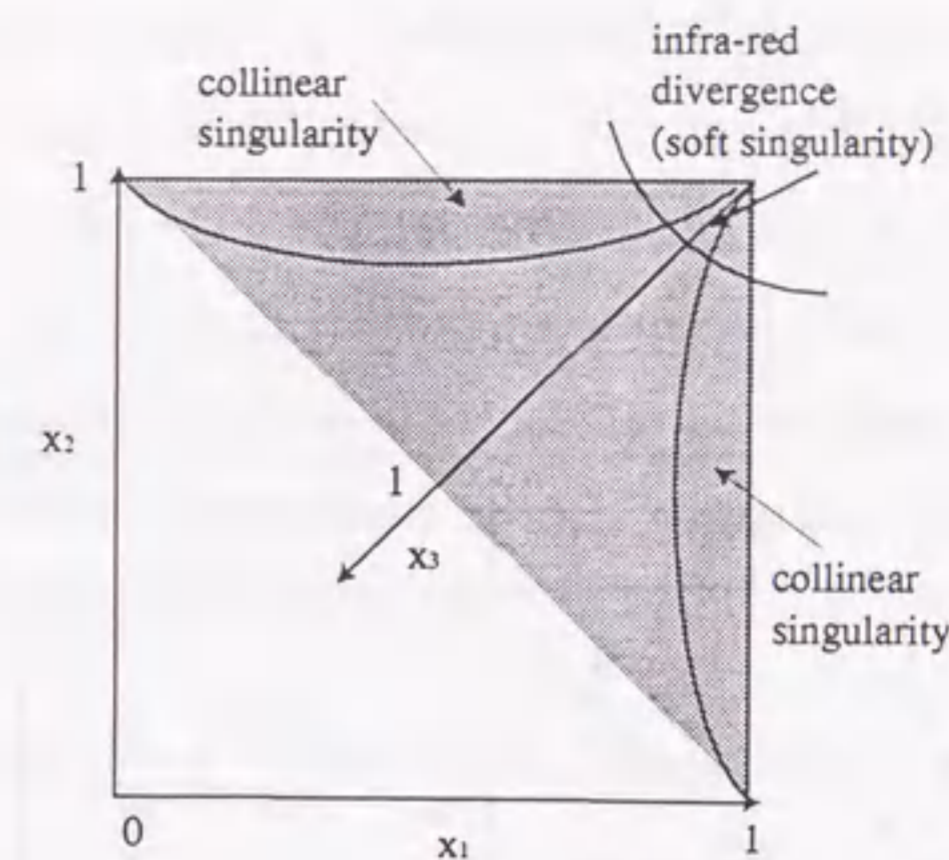


Fig. 2.4. Dalitz plot for 3-parton final state. Each quark, anti-quark, and gluon is carrying fractional energy  $x_i = 2E_i/Q$ . The shaded area is the allowed kinematic region in the massless case.

a collinear singularity. In order to make the origin of these divergences clear, Fig. 2.4 shows the Dalitz plot for the decay of a virtual photon (or  $Z^0$  boson) with invariant mass  $Q$  into a massless quark, anti-quark, and gluon. These singularities can be avoided by taking some regularization procedure.

The QCD predictions up to  $\mathcal{O}(\alpha_s^2)$ <sup>7,17</sup> for all observables defined in chapter 5 have the general form

$$\frac{1}{\sigma_t} \cdot \frac{d\sigma(y)}{dy} = A(y)\tilde{\alpha}_s + [B(y) + A(y)2\pi b_0 \ln f] \tilde{\alpha}_s^2, \quad (2.13)$$

where  $y$  is the variable in question;  $\sigma_t$  is the total hadronic cross section;  $\tilde{\alpha}_s = \alpha_s/2\pi$ ;  $f = \mu^2/s$ ;  $b_0 = (33 - 2n_f)/(12\pi)$ ; and  $n_f$  is the number of active quark flavors;  $n_f = 5$  at  $\sqrt{s} = M_Z$ . Feynman diagrams up to  $\mathcal{O}(\alpha_s^2)$  for 2-, 3-, and 4-parton is shown in Fig. 2.5. We have computed the coefficients  $A(y)$  and  $B(y)$  using the EVENT program, which was developed by Kunszt and Nason.<sup>7</sup> It should be noted that a dependence on the QCD renormalization scale  $\mu$  enters explicitly in the second order term in Eq. (2.13).

It has been found recently<sup>8-13</sup> that several observables, namely thrust

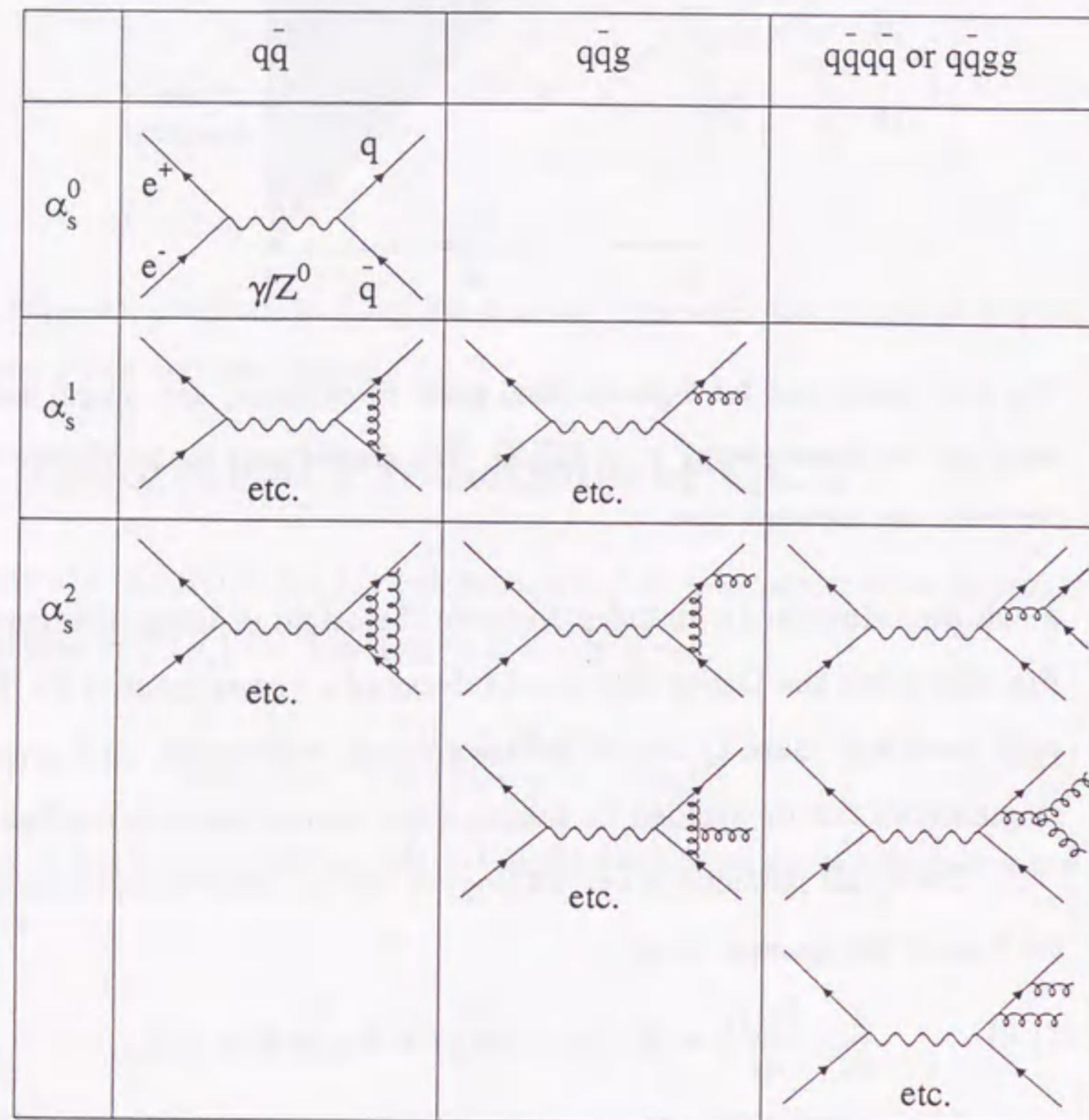


Fig. 2.5. Feynman diagrams up to  $\mathcal{O}(\alpha_s^2)$  for 2-, 3-, and 4-parton. The solid line stands for fermion and the curly line indicates gluon.

( $\tau$ ),<sup>18</sup> heavy jet mass ( $\rho$ ),<sup>19</sup> jet broadenings ( $B_T$ ,  $B_W$ ),<sup>20</sup> differential 2-jet rate with Durham scheme ( $D_2(D$ -scheme)),<sup>21</sup> and energy-energy correlations ( $EEC$ ),<sup>22</sup> can be resummed, that is, leading and next-to-leading logarithmic terms can be calculated to all orders in  $\alpha_s$  using an exponentiation technique. This procedure is expected *a priori* to yield formulae which are less dependent on the renormalization scale. Using  $L \equiv \ln(1/y)$ , the fraction  $R(y, \alpha_s)$  can then be written in the general form

$$R(y, \alpha_s) \equiv \frac{1}{\sigma_t} \int_0^y \frac{d\sigma}{dy} dy = C(\alpha_s) \exp\{\Sigma(\alpha_s, L)\} + F(y, \alpha_s), \quad (2.14)$$

where

$$C(\alpha_s) = 1 + \sum_{n=1}^{\infty} C_n \tilde{\alpha}_s^n, \quad (2.15)$$

$$\Sigma(\alpha_s, L) = \sum_{n=1}^{\infty} \tilde{\alpha}_s^n \sum_{m=1}^{n+1} G_{nm} L^m, \quad (2.16)$$

$$F(y, \alpha_s) = \sum_{n=1}^{\infty} F_n(y) \tilde{\alpha}_s^n. \quad (2.17)$$

The factor  $\Sigma$  to be exponentiated can be written

$$\Sigma(\alpha_s, L) = L \cdot f_{LL}(\alpha_s L) + f_{NLL}(\alpha_s L) + \mathcal{O}\left(\frac{1}{L} \cdot (\alpha_s L)^n\right), \quad (2.18)$$

where  $f_{LL}(\alpha_s L)$  and  $f_{NLL}(\alpha_s L)$  are the Leading Logarithms (LL) and Next-to-Leading Logarithms (NLL). The functions  $f_{LL}$  and  $f_{NLL}$  depend only on the product  $\alpha_s L$  and are given in Refs.<sup>8-13</sup> The resummed calculations are thus given by an approximate expression for  $R(y, \alpha_s)$  in the form

$$R^{resum}(y, \alpha_s) = (1 + C_1 \tilde{\alpha}_s + C_2 \tilde{\alpha}_s^2) \exp\{\Sigma^{resum}(\alpha_s, L)\}, \quad (2.19)$$

where

$$\Sigma^{resum}(\alpha_s, L) = L \cdot f_{LL}(\alpha_s L) + f_{NLL}(\alpha_s L). \quad (2.20)$$

Whereas the leading logarithmic ( $L \cdot f_{LL}$ ) and next-to-leading logarithmic ( $f_{NLL}$ ) terms in  $\Sigma$  have been calculated, the subleading terms in Eq. (2.18)

have not been completely computed. However, some subleading terms included in  $\Sigma$  (Eq. (2.17)), as well as  $C$  and  $F$ , are included in the  $\mathcal{O}(\alpha_s^2)$  calculation. In order to make reliable predictions, including hard gluon emission, with the resummed calculations it is necessary to combine them with the second order calculations, taking overlapping terms into account. This procedure is called *matching*. Four matching schemes have been proposed in the literature.

The  $\mathcal{O}(\alpha_s^2)$  QCD formula (Eq. (2.13)) can also be cast into the integrated form

$$R^{\mathcal{O}(\alpha_s^2)}(y, \alpha_s) = 1 + \mathcal{A}(y)\tilde{\alpha}_s + \mathcal{B}(y)\tilde{\alpha}_s^2, \quad (2.21)$$

where

$$\mathcal{A}(y) = \int_0^y A(y')dy' \quad \text{and} \quad \mathcal{B}(y) = \int_0^y B(y')dy', \quad (2.22)$$

$\mathcal{A}(y)$  and  $\mathcal{B}(y)$  are the cumulative forms of  $A(y)$  and  $B(y)$  in Eq. (2.13). Taking the logarithm of the resummed formula (Eq. (2.19)) and the  $\mathcal{O}(\alpha_s^2)$  formula (Eq. (2.21)),

$$\begin{aligned} \ln R^{\text{resum}}(y, \alpha_s) &= \Sigma^{\text{resum}}(\alpha_s, L) \\ &+ C_1\tilde{\alpha}_s + \left(C_2 - \frac{C_1^2}{2}\right)\tilde{\alpha}_s^2 + \mathcal{O}(\alpha_s^3), \end{aligned} \quad (2.23)$$

and

$$\ln R^{\mathcal{O}(\alpha_s^2)}(y, \alpha_s) = \mathcal{A}(y)\tilde{\alpha}_s + \left(\mathcal{B}(y) - \frac{\mathcal{A}^2(y)}{2}\right)\tilde{\alpha}_s^2 + \mathcal{O}(\alpha_s^3). \quad (2.24)$$

Adding Eq. (2.23) and Eq. (2.24), and subtracting the overlapping first and second order terms from Eq. (2.23), yields<sup>8,9</sup>

$$\begin{aligned} \ln R^{\text{resum}+\mathcal{O}(\alpha_s^2)}(y, \alpha_s) &= \Sigma^{\text{resum}}(\alpha_s, L) \\ &- \Sigma^{\text{resum}(1)}(\alpha_s, L) - \Sigma^{\text{resum}(2)}(\alpha_s, L) \\ &+ \mathcal{A}(y)\tilde{\alpha}_s + \left(\mathcal{B}(y) - \frac{\mathcal{A}^2(y)}{2}\right)\tilde{\alpha}_s^2, \end{aligned} \quad (2.25)$$

	Resummed formula				$\mathcal{O}(\alpha_s^2)$ QCD	
	LL	NLL	Subleading			
1st	$\tilde{\alpha}_s L^2$	$+\tilde{\alpha}_s L$	$+\tilde{\alpha}_s$	$+\tilde{\alpha}_s \mathcal{O}(L^{-1})$	$A(y)\tilde{\alpha}_s$	
2nd	$+\tilde{\alpha}_s^2 L^3$	$+\tilde{\alpha}_s^2 L^2$	$+\tilde{\alpha}_s^2 L$	$+\tilde{\alpha}_s^2$	$+\tilde{\alpha}_s^2 \mathcal{O}(L^{-1})$	$(B(y) - A^2(y)/2)\tilde{\alpha}_s^2$
3rd	$+\tilde{\alpha}_s^3 L^4$	$+\tilde{\alpha}_s^3 L^3$	$+\tilde{\alpha}_s^3 L^2$	$+\tilde{\alpha}_s^3 L$	$+\tilde{\alpha}_s^3$	$+\tilde{\alpha}_s^3 \mathcal{O}(L^{-1})$
4th	$+\tilde{\alpha}_s^4 L^5$	$+\tilde{\alpha}_s^4 L^4$	...	...	...	...
⋮	⋮	⋮	⋮	⋮	⋮	⋮

Table 2.1. Schematic representation of the expansion in the resummation of the LL, NLL, and subleading parts for  $\ln R(y, \alpha_s)$ . An expansion for the  $\mathcal{O}(\alpha_s^2)$  QCD calculation is also shown.

where

$$\Sigma^{\text{resum}(1)}(\alpha_s, L) = G_{12}\tilde{\alpha}_s L^2 + G_{11}\tilde{\alpha}_s L \quad (2.26)$$

$$\Sigma^{\text{resum}(2)}(\alpha_s, L) = G_{23}\tilde{\alpha}_s^2 L^3 + G_{22}\tilde{\alpha}_s^2 L^2. \quad (2.27)$$

Finally, one can derive  $R^{\text{resum}+\mathcal{O}(\alpha_s^2)}(y, \alpha_s)$  by taking the exponential of Eq. (2.25). This procedure is called *lnR-matching*. The expression of  $\ln R(y, \alpha_s)$  is shown schematically in Table 2.1.

In an alternative approach, the overlapping terms  $\Sigma^{\text{resum}(1)}(\alpha_s, L)$  and  $\Sigma^{\text{resum}(2)}(\alpha_s, L)$  are subtracted from  $\Sigma^{\text{resum}}(\alpha_s, L)$  in the form of an exponential. The exact formula up to  $\mathcal{O}(\alpha_s^2)$  is then to obtain as follows<sup>12,13</sup>:

$$\begin{aligned} R^{\text{resum}+\mathcal{O}(\alpha_s^2)}(y, \alpha_s) &= (1 + C_1\tilde{\alpha}_s + C_2\tilde{\alpha}_s^2) [\exp \{ \Sigma^{\text{resum}}(\alpha_s, L) \} \\ &- \exp \{ \Sigma^{\text{resum}(1)}(\alpha_s, L) + \Sigma^{\text{resum}(2)}(\alpha_s, L) \}] \\ &+ 1 + \mathcal{A}(y)\tilde{\alpha}_s + \mathcal{B}(y)\tilde{\alpha}_s^2 \\ &= (1 + C_1\tilde{\alpha}_s + C_2\tilde{\alpha}_s^2) \exp \{ \Sigma^{\text{resum}}(\alpha_s, L) \} \\ &- (C_1\tilde{\alpha}_s + \Sigma^{\text{resum}(1)}(\alpha_s, L)) \\ &- [C_2\tilde{\alpha}_s^2 + C_1\tilde{\alpha}_s \Sigma^{\text{resum}(1)}(\alpha_s, L) \\ &+ \frac{1}{2} \{ \Sigma^{\text{resum}(1)}(\alpha_s, L) \}^2 + \Sigma^{\text{resum}(2)}(\alpha_s, L)] \end{aligned}$$

$$+ \mathcal{A}(y)\tilde{\alpha}_s + \mathcal{B}(y)\tilde{\alpha}_s^2. \quad (2.28)$$

This is called *R-matching*, and differs from *lnR-matching* in that the subleading term  $G_{21}\tilde{\alpha}_s^2 L$  is not exponentiated. In order to raise this procedure to the same level as the *lnR-matching* scheme, Eq. (2.28) may be modified by replacing  $\Sigma^{\text{resum}}(\alpha_s, L)$  and  $\Sigma^{\text{resum}(2)}(\alpha_s, L)$  with  $\Sigma(\alpha_s, L)$  and  $\Sigma^{(2)}(\alpha_s, L) = G_{23}\tilde{\alpha}_s^2 L^3 + G_{22}\tilde{\alpha}_s^2 L^2 + G_{21}\tilde{\alpha}_s^2 L$ , respectively. This procedure is called *modified R-matching*\*.<sup>12</sup>

The predictions of these matching schemes have some troublesome features near the upper kinematic limit  $y_{\text{max}}$  because terms of third and higher order generated by the resummed calculations do not vanish at this limit. This situation can be corrected by invoking a replacement of  $L = \ln(1/y)$  in Eq. (2.25) with  $L' = \ln(1/y - 1/y_{\text{max}} + 1)$ . This procedure is called *modified lnR-matching*.<sup>25</sup> *lnR-* and *modified lnR-matching* are not applicable to *EEC*. We took the value of  $y_{\text{max}}$  to be 0.5 for  $\tau$ , 0.42 for  $\rho$ , 0.41 for  $B_T$ , 0.325 for  $B_W$ , and 0.33 for  $D_2(D)$ .

Finally, in order to account for the renormalization scale dependence,  $f_{NLL}(\alpha_s L)$  should be modified to  $f_{NLL}(\alpha_s L) + (\alpha_s L)^2 \frac{df_{LL}(\alpha_s L)}{d(\alpha_s L)} b_0 \ln f$ , and  $\mathcal{B}(y)$  and  $G_{22}$  should be modified to  $\mathcal{B}(y) + \mathcal{A}(y)2\pi b_0 \ln f$  and  $G_{22} + G_{12}2\pi b_0 \ln f$ , respectively.<sup>7,13</sup> Thus,  $\alpha_s$  is observed in terms of the perturbative prediction of any observable in the form

$$R(Q) = r_0 + r_1 \alpha_s(\mu^2) + r_2(f) \alpha_s^2(\mu^2) + \dots \quad (2.29)$$

If all orders can be calculated, the dependence on the *arbitrary* renormalization scale factor  $f \equiv \mu^2/Q^2$  would cancel completely between  $\alpha_s$  and the coefficient  $r_i$ . However, if one choose  $\mu$  much different from the natural scale  $Q$  then large logarithms of  $f$  remain uncanceled in any finite order, making prediction unreliable, which is discussed in chapter 6 in detail.

\*It has also been called *R-G<sub>21</sub>-matching*,<sup>23</sup> or *intermediate matching*.<sup>24</sup>

## Chapter 3

# Experimental Apparatus

### 3.1 The SLAC Linear Collider

The SLAC Linear Collider (SLC) is the linear collider, which accelerates both electron and positrons to an energy of up to 50 GeV, built at Stanford Linear Accelerator Center (SLAC). As shown in Fig. 3.1, the SLC consists of mainly five systems; a polarized electron gun, damping rings, a linear accelerator (LINAC), arcs, and a final focus system.

A longitudinally polarized electron beam can be created by irradiating a GaAs semiconductor cathode with a circularly polarized laser.<sup>26</sup> In 1993 a new type of strained lattice cathode was introduced to produce electrons with up to 80% polarization.<sup>27</sup> The laser strikes the cathode two times per 120 Hz machine cycle. The photo-emitted electrons are accumulated into a *bunch*. While one bunch of electrons eventually comes into collision with positrons at the interaction point (IP), the other electron bunch is used to create positrons. The electrons are accelerated through a high-gradient field to an energy of 50 MeV and then enter the first section of the LINAC. The electrons reach an energy of 50 MeV and positrons come from the positron target are accelerated to an energy of 1.2 GeV.



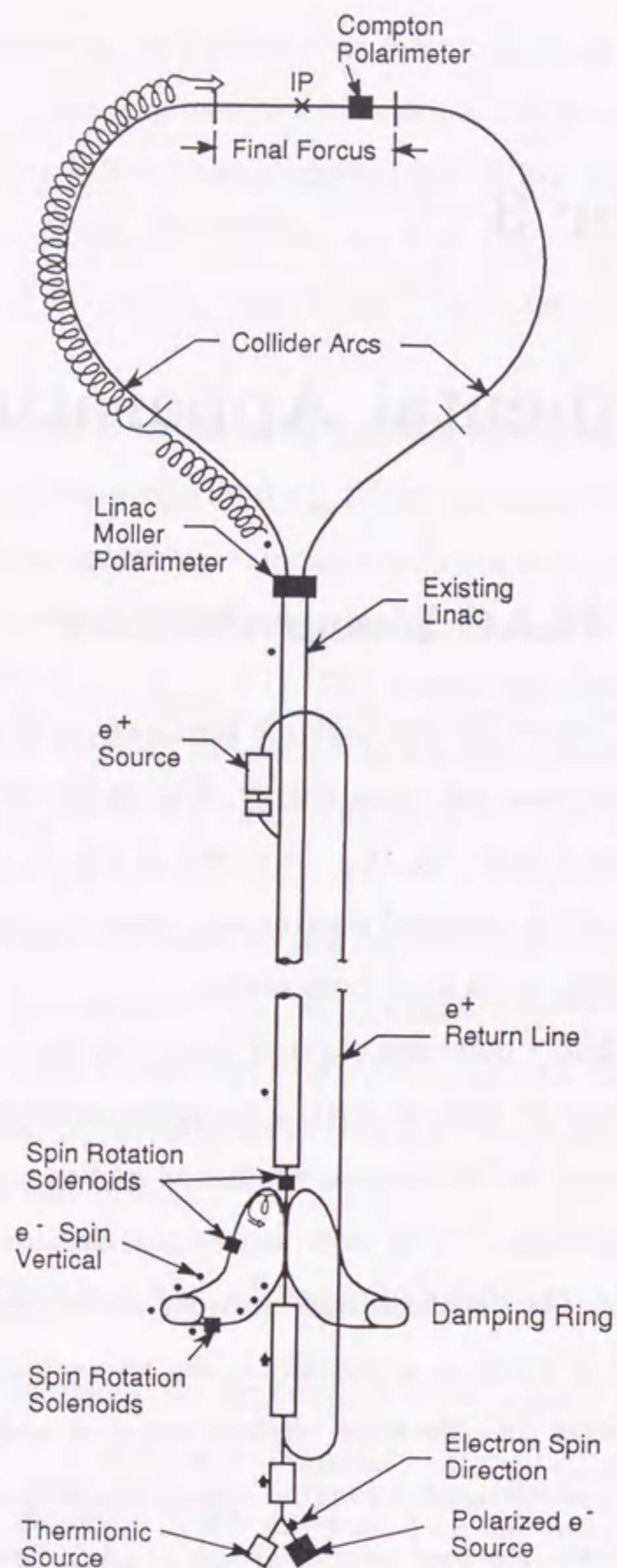


Fig. 3.1. The layout of the SLAC Linear Collider.

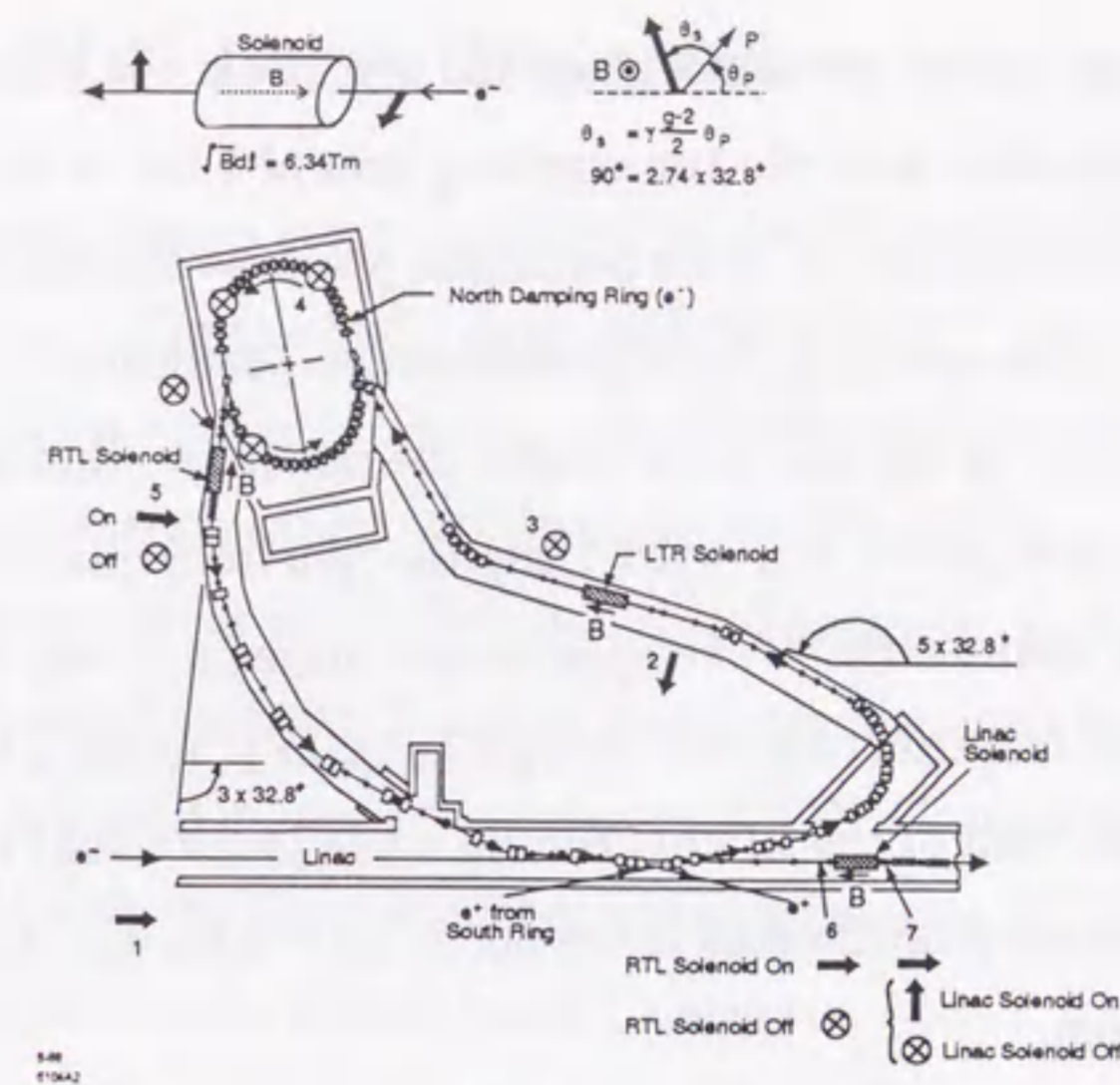


Fig. 3.2. North (electron) damping ring beam transport.

The electrons and positrons are diverted from the first section of the LINAC into two different damping rings. The damping rings<sup>28</sup> which are 35 m in circumference are used to compress the bunches and remove any energy fluctuations (see Fig. 3.2). The electron spin is rotated from the horizontal plane to the vertical plane in order to preserve polarization in the damping ring. During the 1992 polarized run, the electron beam exiting the damping ring was made to pass through a pair of solenoids in the Ring-to-Linac (RTL) line, thus rotating the electron spin back to near longitudinal in order to finally achieve longitudinal polarization at the IP. For the 1993 run the IP spot size could be reduced by producing flat beam (i.e. *elliptical*) in the damping rings. In that case the RTL solenoids were off since a solenoidal field will introduce  $x$ - $y$  coupling of the beam phase space due to the beam betatron motion. The electron spin is still transverse to the motion when the electron bunch comes into the LINAC.

After traveling around the damping rings, the electron and positron

bunches are guided out of the rings and sent down the main two-mile 50 GeV linear accelerator and into two opposing arcs of 1 km in length.

The arcs do not lie in the horizontal plane, so the beam transport is complicated by the motion in both dimensions perpendicular to the momentum of the electrons. In the flat beam mode, the north arc, through which the electrons are transported, is utilized to flip the spin from transverse to longitudinal by way of *spin bumps*.<sup>29</sup> The spin bumps utilize a strong resonance between the vertical betatron tune and the spin tune. In practice, a vertically polarized beam at the end of the LINAC can be made longitudinal at the IP by a pair of large betatron oscillations in the north arc.<sup>30</sup> This was standard practice for the 1993 run.

Three superconducting quadrupole magnets in the final focus compress both  $e^+$  and  $e^-$  beams to 2.6 by 0.8  $\mu\text{m}$  widths just before the collision. One electron and positron in each bunch occasionally interact with producing a Z boson. The parameters of the SLC are listed in Table 3.1.

parameters	1992	1993
Horizontal Emittance	$3.5-4.0 \times 10^{-5} \text{ m}$	$4.0 \times 10^{-5} \text{ m}$
Vertical Emittance	$3.5-4.0 \times 10^{-5} \text{ m}$	$0.8 \times 10^{-5} \text{ m}$
$e^+$ Intensity	$2.9 \times 10^{10}$	$3.2 \times 10^{10}$
$e^-$ Intensity	$2.9 \times 10^{10}$	$3.1 \times 10^{10}$
Horizontal Beam Size	2.2 $\mu\text{m}$	2.6 $\mu\text{m}$
Vertical Beam Size	1.7 $\mu\text{m}$	0.8 $\mu\text{m}$
Repetition Rate	120 Hz	120 Hz
Up time	60%	70%
Luminosity	23 Zs/hour	40 Zs/hour
Total Zs, Unpolarized	1,000	—
Total Zs, Polarized	10,000	50,000
Polarization	22%	62%

Table 3.1. The parameters of the SLC.

## 3.2 The SLC Large Detector

The  $e^+e^-$  annihilation events produced at the  $Z^0$  resonance by the SLC have been recorded using the SLC Large Detector (SLD).<sup>31</sup> The SLD, shown in Fig. 3.3, combines excellent tracking, calorimetry, and particle identification into a state-of-the-art experimental apparatus. The SLD is a cylindrically symmetric detector within a 0.6 Tesla solenoidal magnetic field to measure momentum of charged particles. Charged tracks are measured in the central drift chamber (CDC) and in the vertex detector (VXD). Charged particle identification is made with the Čerenkov Ring Imaging Detector (CRID). Particle energies are measured in the Liquid Argon Calorimeter (LAC), which contains both electromagnetic and hadronic sections, and in the Warm Iron Calorimeter (WIC) which is also used for muon tracking and identification.

The coordinate system used by the SLD is defined that its origin is at the center of the detector,  $z$ -axis points to the positron direction,  $y$ -axis vertically up, and  $x$ -axis makes the overall frame right-handed.

Major components of the SLD are described in the following.

### 3.2.1 Vertex Detector

The innermost detector, the vertex detector (VXD),<sup>32</sup> surrounds the small beam pipe as shown in Fig. 3.4. The feasibility of the VXD lies in getting 3 dimensional information on charged tracks. The VXD uses silicon chips called *charged coupled devices* (CCDs)\*, to make high resolution space point measurements of charged particle tracks. One major disadvantage of CCDs is that they require a long time to read out signals as shown in Table 3.2. Because of this reason, CCDs can not be used for much higher beam crossing rate, for example at LEP, than at the SLC.

\*The same type of solid state devices are also utilized in modern video cameras.

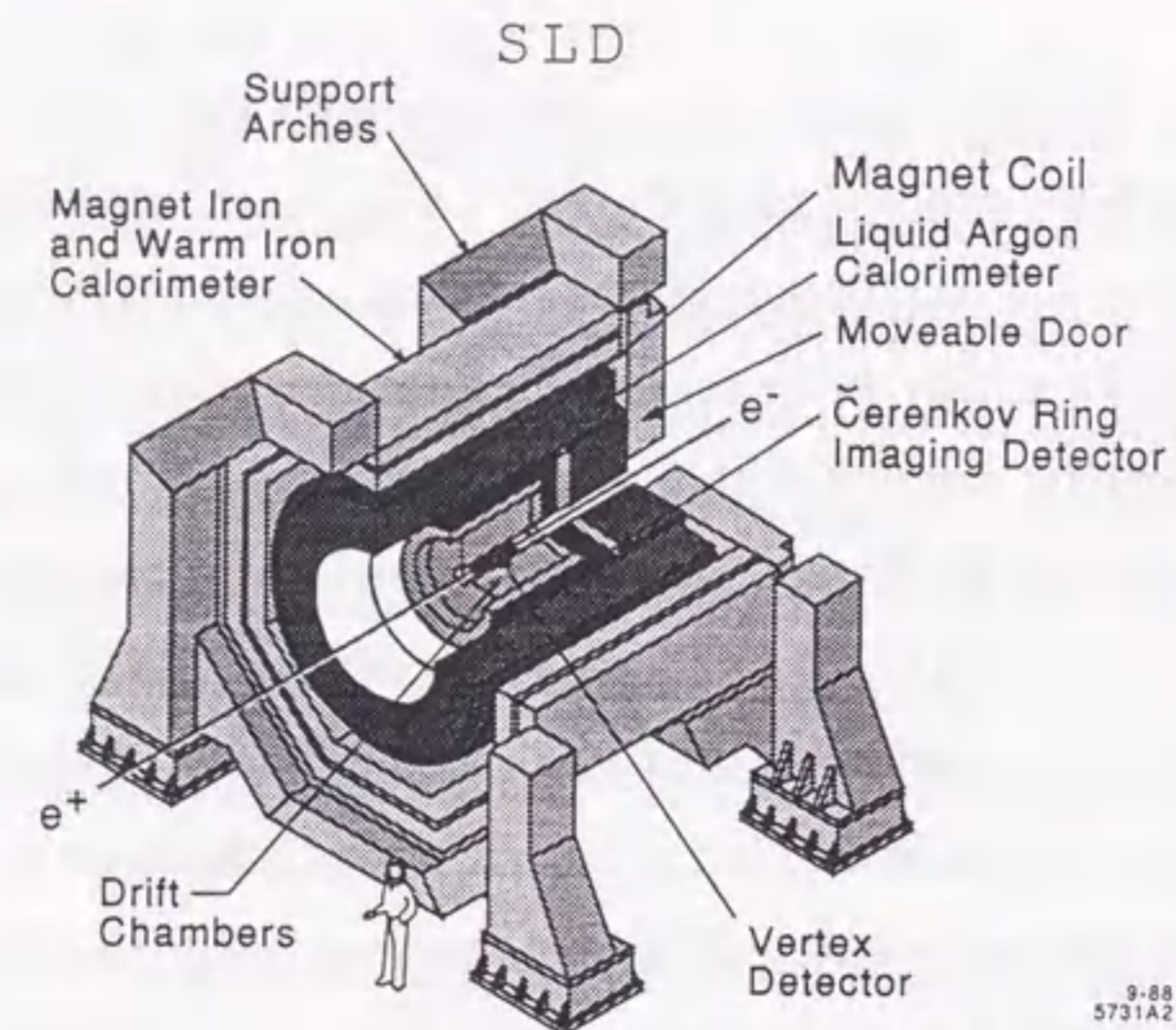
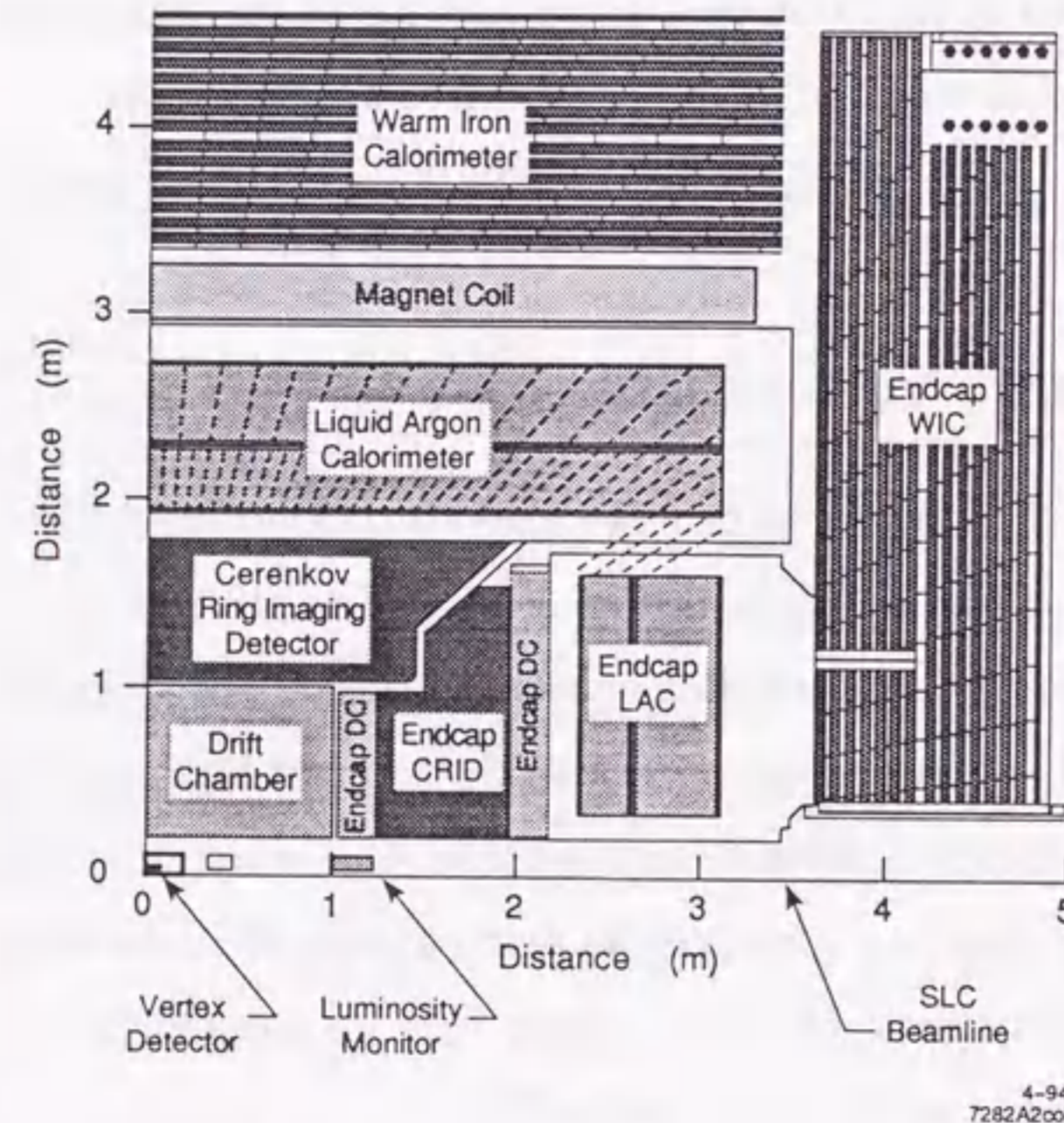
9-88  
5731A24-94  
7282A2001

Fig. 3.3. The cutaway and quadrant view of the SLC Large Detector.

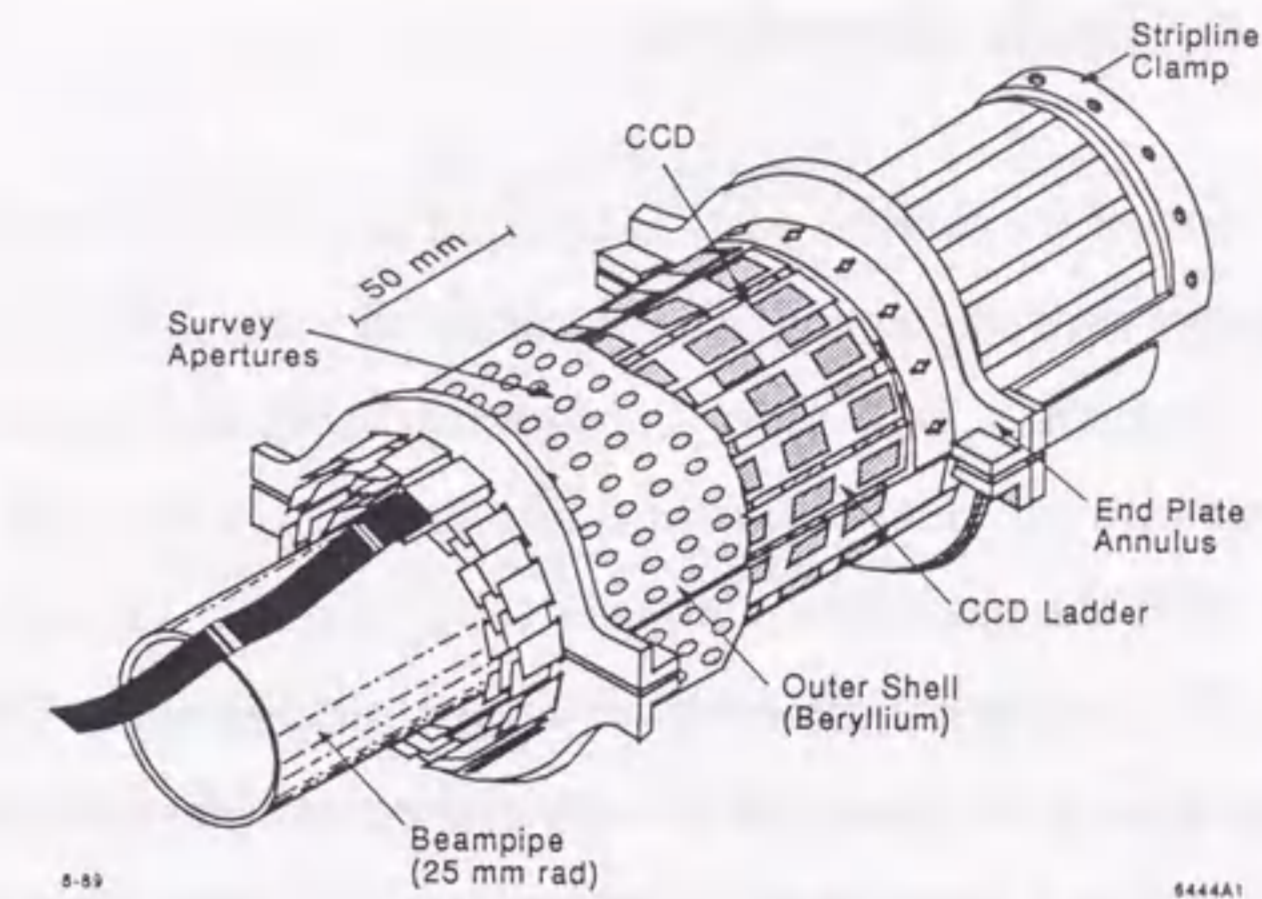


Fig. 3.4. The SLD Vertex Detector (VXD).

The VXD is comprised of 480 CCDs, mounted on 60 thin aluminum-ceramic boards (ladders) arranged in four cylindrical layers. The various parameters of the CCDs and the VXD are listed in Table 3.2.

CCD parameters	
Pixel cell size	$22 \mu\text{m} \times 22 \mu\text{m}$
Area of CCD	$385 \text{ pixels} \times 578 \text{ pixels} (8.5 \times 12.7 \text{ mm}^2)$
Number of pixels/CCD	222,530
Track cluster size	80% of charged deposited in 1 to 2 pixels
VXD parameters	
Active area of ladder	$8.5 \times 100 \text{ mm}^2$
Number of ladders	60
Total number of pixels	107 Mpixels
Readout time	152 ms (19 beam crossings)
Spatial resolution ( $xy$ )	$10 \mu\text{m}$
Spatial resolution ( $rz$ )	$8 \mu\text{m}$

Table 3.2. The parameters of the Vertex Detector (VXD).

### 3.2.2 Drift Chambers

Most of the charged particle tracking is carried out by the drift chambers. A central drift chamber (CDC)<sup>31</sup> covers the barrel region and four endcap drift chambers (EDC) cover the forward/backward regions. The CDC is 2 m long with an inner radius of 0.2 m and an outer radius of 1.0 m, and is filled with the gas mixture of 75%  $CO_2$ , 21%  $Ar$ , 4% isobutane, and 0.3%  $H_2O$ . The primary component of the gas mixture chose  $CO_2$  because of its character both of a low drift velocity and of low diffusion constant. Isobutane was added as a quencher at a level low enough to keep the mix nonflammable. Argon was added to increase the gain to the desired level as wire stability was marginal despite large tension in the high field electrostatic design of the basic cell. Finally water was added and its presence could ameliorate the effects of wire aging in the radiation environment of SLC. The CDC contains 640 cells arranged in 10 concentric superlayers. There are eight sense wires per cell. The layers alternate between giving axial and stereo information. The stereo layers are angled at  $\pm 41$  mrad with respect to the beam axis.

Charged particles passing through the CDC sensitive region ionize gas molecules and liberate electrons along their trajectories. Since high voltages are applied to the guard and field-shaping wires, the liberated electrons drift towards a sense wires at a mostly uniform velocity of  $9 \mu\text{m}/\text{ns}$ . Near the surface of the sense wires, the electric field becomes strong enough that when electrons reach its vicinity they produce a cascade, amplifying the charge. It is possible to determine how long it took the electrons to drift from the charged track to the sense wire by means of measuring the time information when the cascade is produced. This measured time combined with the drift velocity makes spatial information. Each wires of the CDC has an intrinsic resolution of  $82 \mu\text{m}$ , however, slight alignment errors in the wires and uncertainties in the drift velocity reduce the effective resolution of the CDC to  $92 \mu\text{m}$ . An inverse momentum

resolution of the CDC with 0.6 Tesla magnetic field is obtained to be:

$$\sigma (\text{GeV}/c)^{-1} = \sqrt{0.0049^2 + (0.0095/p)^2}. \quad (3.1)$$

The combined the CDC with the VXD momentum resolution is estimated to be:

$$\sigma (\text{GeV}/c)^{-1} = \sqrt{0.0026^2 + (0.0095/p)^2}. \quad (3.2)$$

A resolution for two-track separation is 1 mm at 50% efficiency. Although the CDC is not designed for optimal energy-loss measurement, a  $dE/dx$  resolution of 6.5% is achieved for electrons in wide-angle Bhabha events, after correcting for geometry effects, diffusion, transport loss, and gain variations.

### 3.2.3 Čerenkov Ring Imaging Detector

When a velocity of a particle exceeds the speed of light in a medium, the particle emits Čerenkov radiation. The Čerenkov angle which is an opening angle  $\theta$  of a cone of Čerenkov light is related to the velocity of the particle as:

$$\cos \theta = \frac{1}{\beta n}, \quad (3.3)$$

where  $n$  is the index of refraction of the material and  $\beta$  is the velocity of the particle in the material. From the measurement of the Čerenkov angle, combined with momentum information from the drift chambers, the mass of the particle and hence the identity of the particle species can be ascertained. The Čerenkov Ring Imaging Detector (CRID),<sup>33</sup> as shown in Fig. 3.5, is designed to measure the Čerenkov angle of the tracks and therefore perform particle identification. The barrel CRID uses liquid and gas radiators (see Table 3.3). The liquid radiator can differentiate between low momentum particles, while the gas radiator was chosen to be sensitive to the higher momentum particles. The CRID measures circles of light by using a *time proportional chamber* which is basically a long drift chamber. The photons are converted by photo-ionization

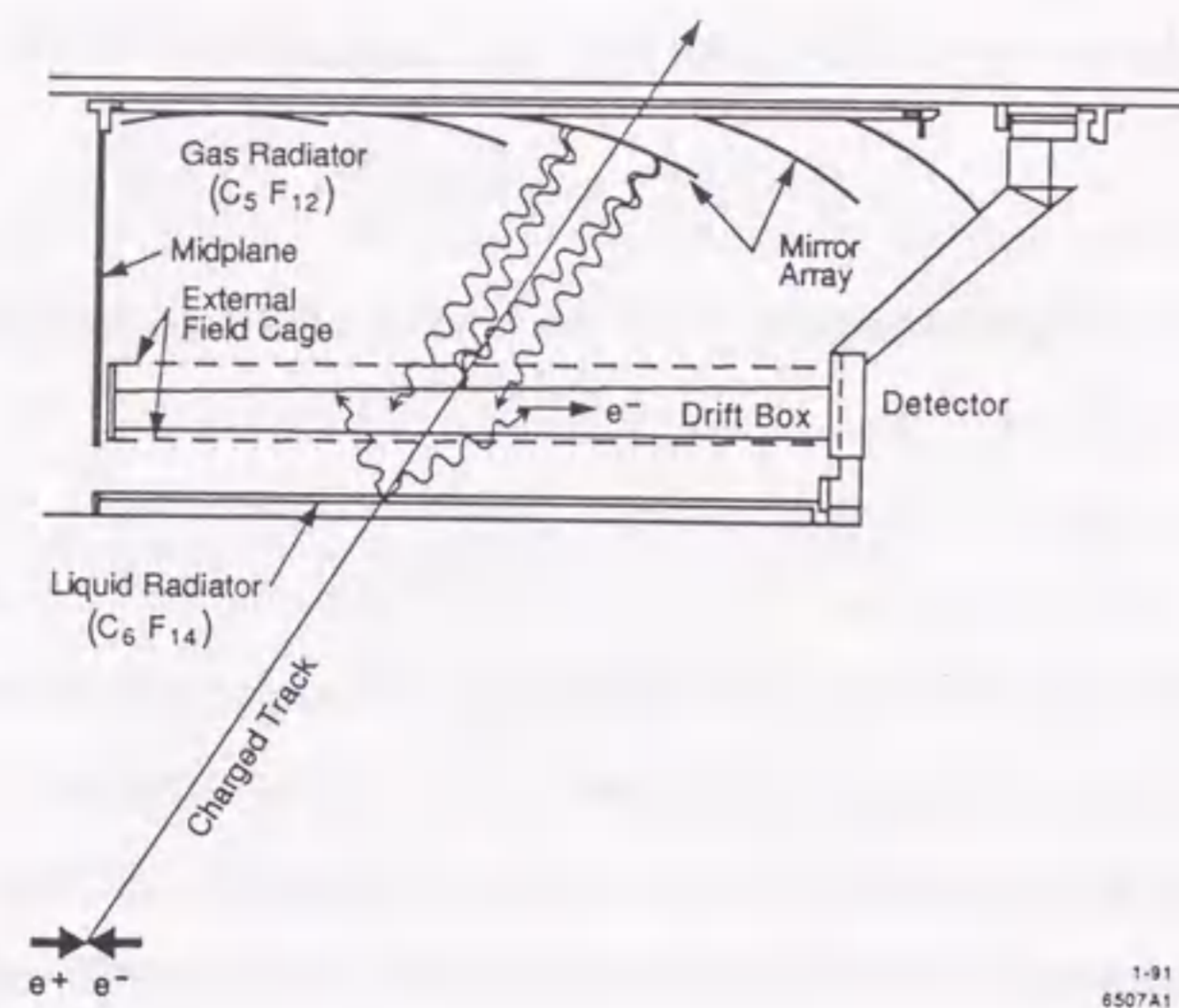


Fig. 3.5. Operation of the barrel Čerenkov Ring Imaging Detector (CRID).

in the mixed ethane gas with 0.1% tetrakis (dimethylamino) ethylene (TMAE). When the molecule is hit by a single photon from Čerenkov light, it releases a single electron. The photo-electrons then drift to the end of the detector where they are measured by proportional wires. The drift time yields information regarding the conversion depth, photon rings then may be reconstructed and the Čerenkov angle measured.

### 3.2.4 Liquid Argon Calorimeter

The main calorimeter of the SLD is the Liquid Argon Calorimeter (LAC)<sup>34</sup> covering both barrel and endcap region. The LAC consists of projective towers, longitudinally segmented into two electromagnetic (EM) sections of 21 radiation lengths in total depth, and two hadronic (HAD) sections, which combine with the EM sections to give 2.8 interaction lengths. The LAC covers 98% of the total solid angle, with about 80% of this in the barrel section. The remainder is covered by silicon-tungsten calorimetry at small scattering angles

	Liquid	Gas
Radiator material	$C_6F_{14}$	70% $C_2F_{12}$ and 30% $N_2$
Index of refraction (for $\lambda = 190.7$ nm)	1.277	1.001725
Thickness of radiator	1 cm	$\sim 45$ cm
Čerenkov angle (for $\beta = 1$ )	672 mrad	59 mrad
Radius of Čerenkov ring (for $\beta = 1$ )	17 cm	2.9 cm
Local angle resolution	$\sim 12$ mrad	$\sim 4$ mrad
Cumulative misalignment resolution	$\sim 10$ mrad	$\sim 10$ mrad
Number of photoelectrons (for $\beta = 1$ )	$\sim (13 - 16)$	$\sim (7 - 9)$
Momentum threshold:		
e	$\sim 1$ MeV/c	$\sim 9.5$ MeV/c
$\pi$	0.23 GeV/c	2.6 GeV/c
K	0.80 GeV/c	9.1 GeV/c
p	1.5 GeV/c	17.3 GeV/c
Particle separation at $90^\circ$ ( $3\sigma$ level)		
e/ $\pi$	0.2 - 6.2 GeV/c	
$\mu/\pi$	0.2 - 1.1 GeV/c	2.1 - 3.8 GeV/c
$\pi/K$	0.23 - 23 GeV/c	
K/p	0.80 - 37 GeV/c	

Table 3.3. The parameters of the barrel Čerenkov Imaging Ring Detector (CRID).

used to measure luminosity with Bhabha scattering. Figure 3.6 shows the structure of a barrel LAC module. The barrel consists of 48 such modules in azimuth and 3 along the barrel in  $z$ . There are a total of 32448 towers in the barrel and 8640 in the endcap, providing a high degree of transverse segmentation.

The performance of the LAC is studied by using Bhabha events. The energy resolution of the EM section is estimated to be  $\sigma(E)/E = 15\%/\sqrt{E}$ . The resolution of the HAD section is estimated by comparing the momentum measurement in the drift chamber of isolated tracks with the energy response of the LAC. The resolution of the HAD section is obtained  $\sigma(E)/E = 55\%/\sqrt{E}$  (preliminary).

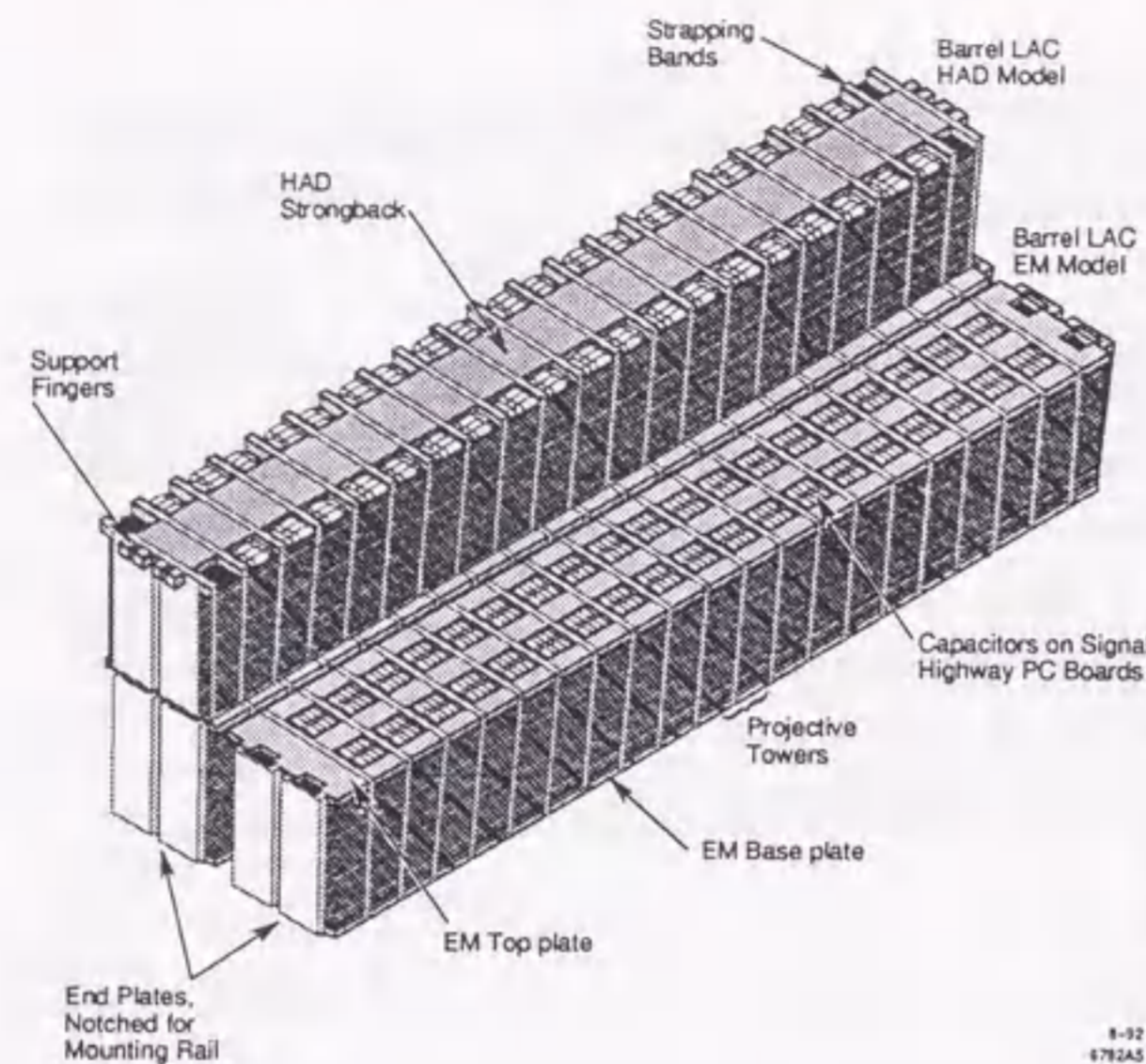


Fig. 3.6. A module of the barrel Liquid Argon Calorimeter (LAC).

### 3.2.5 Warm Iron Calorimeter

The outermost detector of the SLD is the Warm Iron Calorimeter (WIC),<sup>35</sup> which is sampling calorimeter with limited streamer tube and muon tracker. The total thickness of the WIC is 4.2 nuclear interaction lengths, comprised of 14 steel plates 5 cm thick. Wire planes between the steel layers are plastic streamer tubes bundled together to form planar chambers. The tower segmentation of the WIC follows that of the LAC. Muon tracking is also performed with the WIC. The chambers contain copper strips which are 1 cm wide and run the length of the chamber. Muon tracks are identified by matching extrapolated CDC tracks with hits in the WIC strips. The expected energy resolution of the WIC is  $\sigma(E)/E = 80\%/\sqrt{E}$ , which will give a hadronic energy resolution by combining with the LAC of  $\sigma(E)/E = 60\%/\sqrt{E}$ .

### 3.2.6 Luminosity Monitor

The integrated luminosity of the SLC is determined by the rate of the Bhabha events occur. This rate is proportional to how well the accelerator is colliding the electron and positron bunches. The cross section of the Bhabha events at small polar angles with respect to the beam axis is dominated by the photon t-channel process. This cross section has been calculated to high precision. The luminosity monitor<sup>36</sup> was designed to measure these small angle electrons and positrons and thus measure the beam luminosity. The luminosity monitor is useful for measuring the total Z boson cross section which is an important part of testing the Standard Model.

The luminosity monitor employs silicon sampling detector with a pseudoprojective pad readout. The energy resolution of this detector for measuring the energy of electrons is  $\sigma(E)/E = 20\%/\sqrt{E}$ .

## 3.3 Trigger System

Three triggers were used for hadronic events. In the 1993 (1992) runs the first required a total LAC electromagnetic energy greater than 12 GeV (8 GeV); the second required at least two well-separated tracks in the CDC; and the third required at least 4 GeV (8 GeV) in the LAC and one track in the CDC. A selection of hadronic events was then made by two independent methods, one based on the topology of energy depositions in the calorimeters, the other on the number and topology of charged tracks measured in the CDC.

## 3.4 Data Taking History

Figure 3.7 shows how the SLC luminosity has evolved since 1991. It gives integrated luminosity in terms of numbers of the Z events delivered by the SLC (one Z is defined as  $30 \text{ nb}^{-1}$ ), whereas the actual number of events recorded

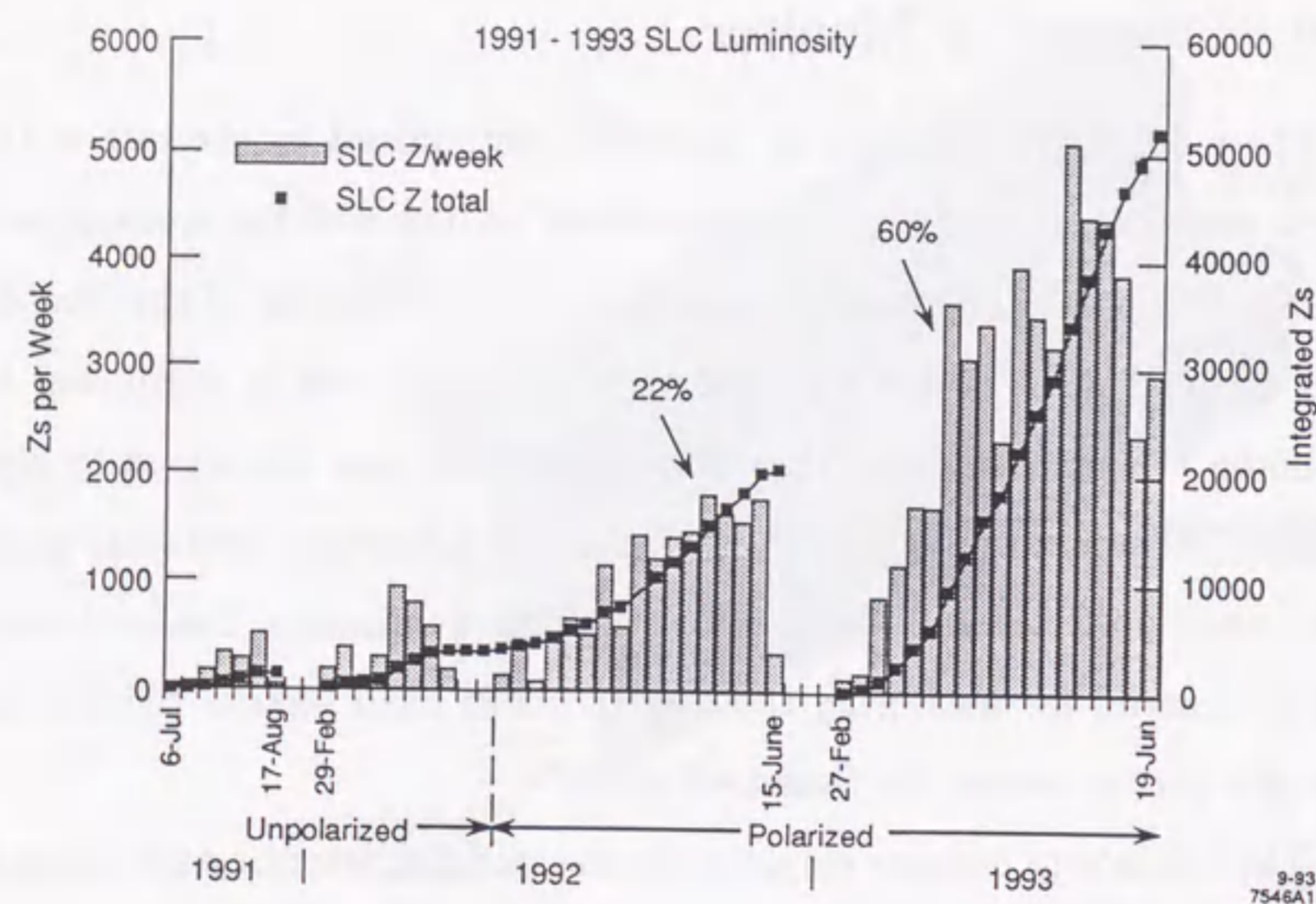


Fig. 3.7. SLC luminosity performance for 1991-1993. The last two months of the 1993 run are not indicated.

by the SLD detector is reduced by data taking efficiency (typically  $\sim 90\%$ ). The maximum luminosity in 1993 was about  $5 \times 10^{29} \text{ cm}^{-2} \text{ s}^{-1}$  using the flat beams. By the end of the 1993 run the number of  $Z$  events recorded by the SLD was about 60,000.

## Chapter 4

# Hadronic Event Selection and Simulations

This chapter deals with criteria for hadronic event selection, Monte Carlo event generation and detector simulation which perform a center role in data corrections. The comparisons of the experimental data and Monte Carlo predictions on various quantities follow this in order to demonstrate validity of the Monte Carlo simulations and the data corrections based on them.

### 4.1 Hadronic Event Selection

The quark and anti-quark pair produced in an  $e^+e^-$  annihilation manifests itself as jets of hadrons in the detector. Each of the pair has energy almost equal to the beam energy. The signature of hadronic events is therefore large number of charged particles in the tracking devices, and a large fraction of the center-of-mass energy in the tracking devices and the calorimeters.

A selection of hadronic events was then made by two independent methods, one based on the topology of energy depositions in the calorimeters, the other on the number and topology of charged tracks measured in the CDC.

The analysis presented here used the charged tracks measured in the CDC

and VXD. A set of cuts was applied to the data to select well-measured tracks and events well-contained within the detector acceptance. The charged tracks were required to have: (i) a distance from the measured interaction point, at the point of closest approach, within 5 cm in the direction transverse to the beam axis and 10 cm along the beam axis; (ii) a polar angle  $\theta$  with respect to the beam axis within  $|\cos\theta| < 0.80$ ; and (iii) a momentum transverse to the beam axis  $p_{\perp} > 0.15$  GeV/c. Events were required to have: (i) a minimum of five such tracks; (ii) a thrust axis<sup>18</sup> direction within  $|\cos\theta_T| < 0.71$ ; (iii) a total visible energy  $E_{vis}$  of at least 20 GeV, which was calculated from the selected tracks assigned the charged pion mass. From our 1992 and 1993 data samples 37,226 events passed these cuts. The efficiency for selecting hadronic events satisfying the  $|\cos\theta_T|$  cut was estimated to be above 96 %. The background in the selected event sample was estimated to be  $0.3 \pm 0.1$  %, dominated by  $Z^0 \rightarrow \tau^+\tau^-$  events. Distributions of single particle and event topology observables in the selected events were found to be well described by Monte Carlo models of hadronic  $Z^0$  decays<sup>37,38</sup> combined with a simulation of the SLD.

## 4.2 Monte Carlo Simulations

Monte Carlo simulations are essential to estimate detection efficiencies, radiative corrections, and hadronization effects. The production of Monte Carlo simulated data consists of three steps. The first step is the event generation, which generates hadronic events include jets of particles according to the differential cross sections predicted by the standard model. Once a pair of quark and anti-quark is produced, the probabilities of quark and gluon emissions obey the perturbative QCD. However, the momentum transfer becomes enough small, typically  $\sim 1$  GeV/ $c^2$  where hadrons (mesons and baryons) should be produced, that the limitation of the perturbative QCD is appeared. To produce

the hadrons some pragmatical models have to be assumed. We call this fragmentation model which are described in the next subsection in more detail. After fragmentation process the decay modes and branching ratio should also be taken into account. The second step is the detector simulation, which simulates the propagation of the particles and the signals induced by them in the detector, thus producing Monte Carlo raw data. In the third step, the Monte Carlo raw data are then fed the same event reconstruction and the same selection programs as used for the real data. This procedure allows us to reliably estimate a performance of the detector and the event reconstruction software as well as the acceptance edges introduced by the selection cuts.

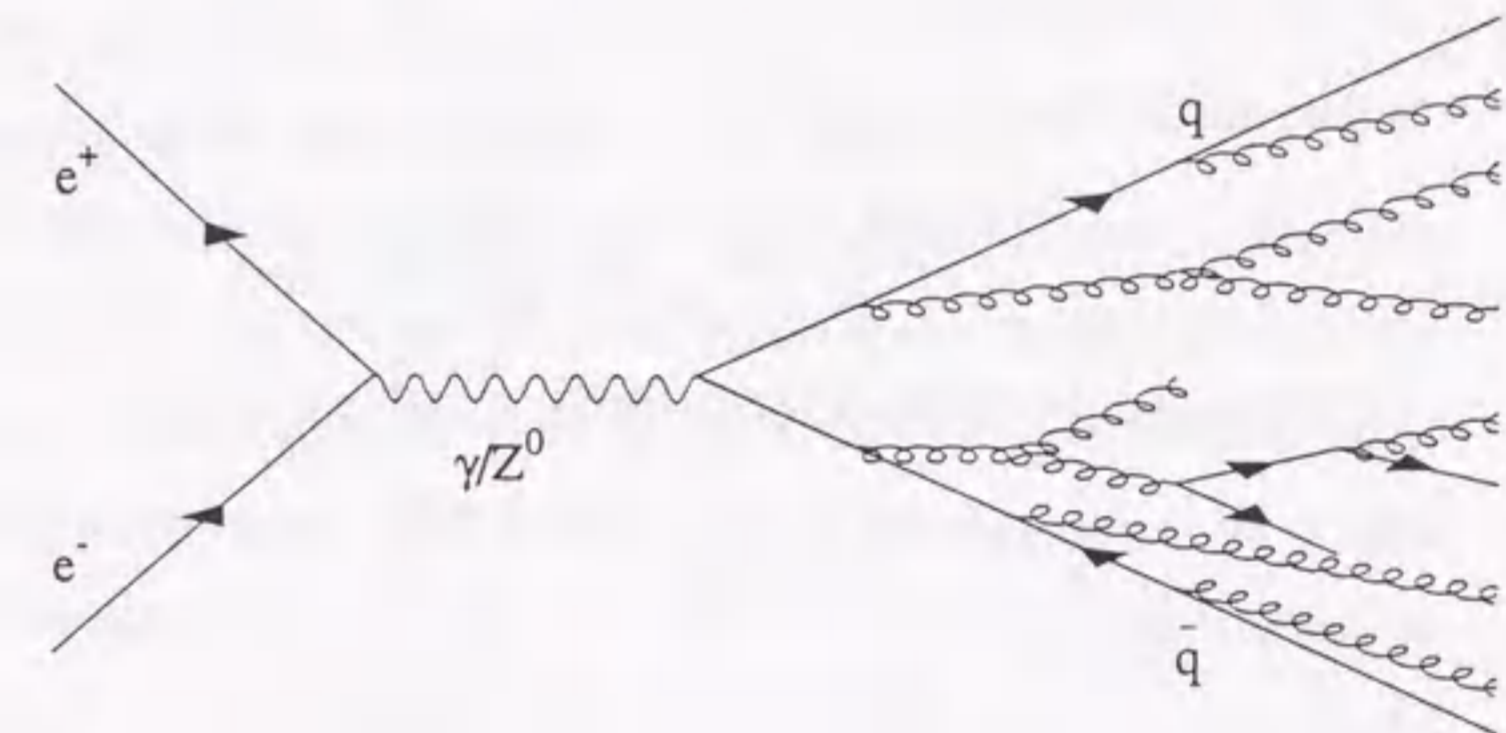


Fig. 4.1. Schematic picture of parton shower evolution in  $e^+e^-$  annihilation.

### 4.2.1 Event Generators

In this section, parton shower model and hadronization models with string fragmentation and cluster fragmentation are discussed.

#### Parton Showers



The Monte Carlo event generator produces quark and anti-quark pairs at a given center-of-mass energy. Their flavors are assigned according to their total cross section. The initial state photon radiation as well as initial virtual corrections based on the work by Berends, Kleiss and Jadach are included.<sup>39</sup> The parton shower method is widely used in the QCD generators<sup>40,41</sup> such as JETSET<sup>37,42</sup> and HERWIG.<sup>38</sup> The parton shower picture is derived within the framework of the leading logarithm approximation (LLA).<sup>43-45</sup> Most parton shower algorithms are based on an iterative use of the basic branchings, i.e.  $q \rightarrow qg$ ,  $g \rightarrow gg$ , and  $g \rightarrow q\bar{q}$ . Figure 4.1 shows schematic picture of parton shower evolution. The parton shower develops until the virtual mass of each parton reaches a cut-off mass ( $\sim 1 \text{ GeV}/c^2$ ). The probability  $P$  that a parton branching  $a \rightarrow bc$  will take place during a small change  $dt = dQ_{evol}^2/Q_{evol}^2$  of the evolution parameter  $t = \ln(Q_{evol}^2/\Lambda^2)$  is given by the Altarelli-Parisi equations.<sup>43</sup> The Altarelli-Parisi equation is given by

$$\frac{dP_{a \rightarrow bc}}{dt} = \int dz \frac{\alpha_s(Q^2)}{2\pi} P_{a \rightarrow bc}(z), \quad (4.1)$$

where  $P_{a \rightarrow bc}(z)$  are the Altarelli-Parisi splitting functions

$$P_{q \rightarrow qg}(z) = C_F \frac{1+z^2}{1-z}, \quad (4.2)$$

$$P_{g \rightarrow gg}(z) = N_C \frac{(1-z(1-z^2))^2}{z(1-z)}, \quad (4.3)$$

$$P_{g \rightarrow q\bar{q}}(z) = T_R(z^2 + (1-z)^2), \quad (4.4)$$

where  $C_F = 4/3$ ,  $N_C = 3$ , and  $T_R = n_f/2$ . The  $z$  variable specifies the sharing of four momentum between the daughters, with daughter  $b$  taking fraction  $z$  and  $c$  taking  $1-z$ .

The probability that no branching occurs during a small range of  $t$  values,  $\delta t$ , is given by  $(1 - \delta t dP/dt)$ . When summed over many small intervals, the no-emission probability exponentiates

$$P_{no-emission}(t_{max}, t) = \exp\left(-\int_t^{t_{max}} dt' \frac{dP_{a \rightarrow bc}}{dt'}\right). \quad (4.5)$$

Thus the probability for a branching at a given  $t$  is the naive probability for a branching, Eq. (4.1), multiplied by the probability Eq. (4.5) that a branching has not already taken place. Generally the Sudakov form factor<sup>46</sup> is introduced as

$$S_a(t) = \exp\left(-\int_{t_{min}}^t dt' \int_{z_{min}(t')}^{z_{max}(t')} dz \frac{\alpha_s(Q^2)}{2\pi} P_{a \rightarrow bc}(z)\right), \quad (4.6)$$

which is the probability that a parton starting from a maximum virtuality  $t$  will reach the fixed order cut-off  $t_{min}$ , which is related to the effective gluon mass  $Q_0$ , without branching. The no-emission probability  $P_{no-emission}(t_{max}, t)$  is then  $S_a(t_{max})/S_a(t)$ . It is easy to pretabulate, for a each flavor  $a$ , at the beginning of a Monte Carlo run since the Sudakov form factor only depends on the parameter  $t$ . This is used for many programs as a part of the generation strategy.

#### String Fragmentation

The generated partons fragment into hadrons (hadronization). This process can not be treated by the perturbative QCD because it takes place in the low momentum transfer region in which  $\alpha_s$  become large. This process should be treated with phenomenological models. One of the fragmentation models is the string fragmentation.<sup>47</sup> A *string* is stretched between a quark  $q$  and an anti-quark  $\bar{q}$ , and a gluon is modeled as a kink on the string. As the  $q$  and  $\bar{q}$  move apart, the potential energy stored in the string increases, and the string may break by the production of a new  $q'\bar{q}'$  pair, so that the system splits into two color singlet systems  $q\bar{q}'$  and  $q'\bar{q}$ . If the invariant mass of either of these string pieces is large enough, further breaks may occur.

In the Lund string model,<sup>48</sup> the string breakup process is assumed to proceed until only on-mass-shell hadrons remain, each hadron corresponding to a small piece of string. The Lund model invokes the idea of quantum mechanical tunneling to produce the quark and anti-quark pairs which lead to string breakups. The tunneling probability, where  $q\bar{q}$  will appear, in terms of

the transverse mass  $m_{\perp}$  of the  $q'$  is given by

$$\exp\left(-\frac{\pi m_{\perp}^2}{\kappa}\right) = \exp\left(-\frac{\pi m^2}{\kappa}\right) \exp\left(-\frac{\pi p_{\perp}^2}{\kappa}\right), \quad (4.7)$$

where  $\kappa$  is a string constant, i.e. the amount of energy per unit length, deduced to be  $\sim 1$  GeV/fm from hadron mass spectroscopy. This formula implies a suppression of heavy quark production from the sea (vacuum),  $u : d : s : c \sim 1 : 1 : 0.3 : 10^{-11}$ . Hence,  $c$ - and  $b$ -quark productions are negligible in the soft fragmentation in practice. The suppression of  $s$ -quark production, which would strongly affect the charge identification of the primary quark, is left as a free parameter. At least qualitatively, the experimental value agrees with theoretical prediction. The partons are formed into colorless hadrons with repetition of the string breakings. After this fragmentation process is completed, the unstable hadrons are decayed leaving stable hadrons.

A fragmentation process described in terms of string at the  $q$  end of the system and fragmenting towards the  $\bar{q}$  end should be equivalent. This asymmetry constrains the allowed shape of fragmentation functions  $f(z)$ , where  $z$  is the fraction of available energy taken by a hadron, especially for two-jet  $z$  is the fraction of  $E + p_{\parallel}$  along the jet axis. With some simplifying assumptions, the symmetric fragmentation function takes the form

$$f(z) \propto z^{-1}(1-z)^a \exp(-bm_{\perp}^2/z), \quad (4.8)$$

with the two free parameters  $a$  and  $b$ , which should be optimized to reproduce experimental data.

The width of the jets is given by

$$\frac{d\sigma}{dp_{\perp}^2} = \exp(-p_{\perp}^2/\sigma_q^2), \quad (4.9)$$

with  $\sigma_q$  is also a free parameter controls the width of quark transverse momentum.

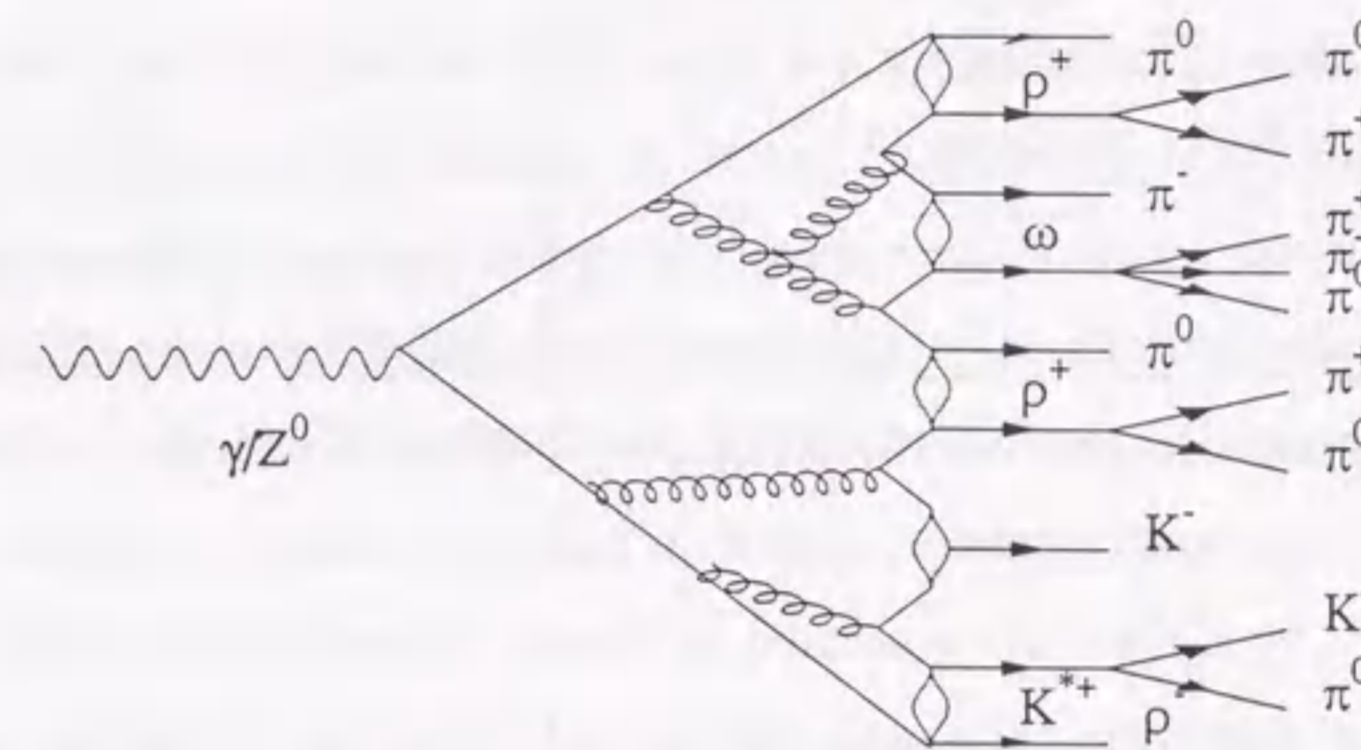


Fig. 4.2. One cluster fragmentation scenario; shower evolution, forced  $g \rightarrow q\bar{q}$  branchings, cluster formation, and cluster decays.

#### Cluster Fragmentation

Cluster models are found in HERWIG. A parton shower picture is used to produce a partonic configuration. At the end of the shower evolution, remaining gluons are forcibly split into  $q\bar{q}$  pairs. Figure 4.2 shows the picture of the cluster fragmentation. The quark of one splitting may be combined with the antiquark from an adjacent one to form a colorless cluster. These clusters subsequently decay into the final hadrons in HERWIG.

The concept of cluster fragmentation offers a simple, local and universal description of hadronization. The long ordered fragmentation chains, present both in the string fragmentation and in the independent fragmentation,<sup>41</sup> are disappeared in the cluster fragmentation. Simple clusters are appeared in their place and they are assumed to be the basic units from which the hadrons are produced. A cluster is ideally only characterized by its total mass and total flavor content. It does not possess an internal structure as the string

fragmentation.

Parton shower evolution should give a cluster mass spectrum strongly damped at masses above a few GeV, so that two body decays would give a sufficient description. This is the concept of the *preconfinement*.<sup>49</sup> In order to avoid a rather large spread of cluster masses, which can not be treated by the preconfinement, it is necessary to introduce the possibility for a high-mass cluster to produce more than two hadrons. This is typically done by allowing branchings  $\text{cluster} \rightarrow \text{cluster} + \text{hadron}$  or  $\text{cluster} \rightarrow \text{cluster} + \text{cluster}$ .

Flavors are generated at several different stages. First, at the branching  $g \rightarrow q\bar{q}$  when the clusters are formed, the relative probabilities are given by the parton mass assignments in HERWIG. The second stage of flavor production occurs when larger clusters decay into smaller ones. A cluster  $q_1\bar{q}_2$  breaks, by the production of an intermediate  $q_3\bar{q}_3$  pair, into clusters  $q_1\bar{q}_3$  and  $q_3\bar{q}_2$ . The third stage of flavor production is when a cluster decays into two hadrons. The flavor flow is above, i.e. a new  $q_3\bar{q}_3$  pair splits the old cluster in the middle. Here quark, diquark, even charm production is allowed in HERWIG, with relative probability dictated by the phase space alone.

#### Parameters in the Event Generators

The parameters for the parton shower and phenomenological fragmentation processes in JETSET and HERWIG were optimized to reproduce various quantities. Both in the JETSET and HERWIG program, the parton production step is controlled by the scale parameter,  $\Lambda_{QCD}$ , and the invariant mass cut-off,  $Q_0$  in JETSET, which corresponds to the gluon mass,  $m_g$ , in HERWIG. The controlled parameters for parton shower and fragmentation parameters to describe the hadronization process are listed in Table 4.1.

JETSET version 7.3			HERWIG version 5.5		
Parameter	Name	Value	Parameter	Name	Value
$\Lambda_{QCD}$	PARJ(81)	0.26 GeV	$\Lambda_{QCD}$	QC DLAM	0.18 GeV
$Q_0$	PARJ(82)	1.0 GeV	$m_g$	RMASS(13)	0.75 GeV
$a$	PARJ(41)	0.18	$M_{max}$	CLMAX	3.35 GeV
$b$	PARJ(42)	0.34 GeV <sup>-2</sup>			
$\sigma_q$	PARJ(21)	0.39 GeV			

Table 4.1. The main parameters of JETSET and HERWIG. The values are used for this analysis.

#### 4.2.2 Detector Simulation

The particles generated by event generators are traced through the detector by the SLD detector simulator based on the GEANT program.<sup>50</sup> This detector simulator was designed to take into account all the conceivable interactions which the particles might experience in the detector and to mimic the detector response to the particles as closely as possible. The structures and materials of the detectors are precisely coded in the program and each particle is propagated by a small step from the interaction point. At each step, interactions such as decays, multiple scattering, and the bremsstrahlungs take place according to probabilities associated with them. Electromagnetic and hadronic showers are simulated via the GFLASH algorithm.<sup>51</sup>

After the events are passed through the GEANT simulation, they are superimposed on a set of luminosity-weighted random triggers to simulate the backgrounds produced by the SLC accurately. The events are processed identically to the real data after they have been simulated and overlaid onto a random event.

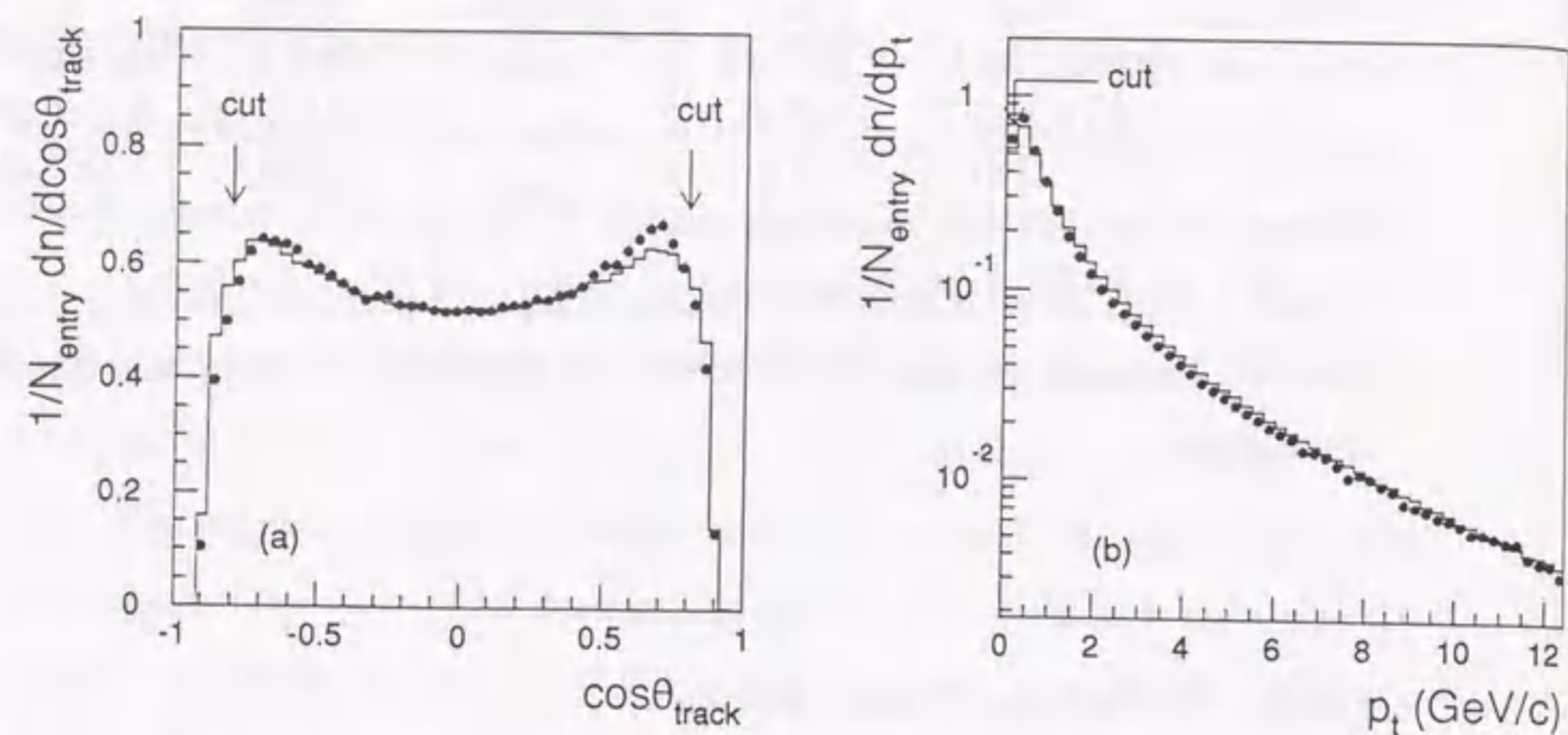


Fig. 4.3. The polar angle  $\cos\theta_{track}$  and transverse momentum of charged particles. Plots with error bars show experimental data and histograms indicate the Monte Carlo predictions (JETSET).

### 4.3 Comparison of Data and Monte Carlo Simulations

The detector simulator outputs the Monte Carlo event data in the format which is used for the real data collected with our data acquisition system. The Monte Carlo data are therefore fed to the same reconstruction program as used for the real data to take into account effects of reconstruction inefficiencies and fake tracks.

In order to reliably estimate the detector acceptance and efficiency, it is essential for the Monte Carlo events to reproduce the real data. We compare, in this section, the real data with the Monte Carlo (JETSET) data. Figure 4.3 shows (a) the polar angle of the charged tracks with respect to the beam axis and (b) the transverse momentum of the charged tracks. In order to extract

good quality tracks, the selection cuts described in section 4.1 were applied. Figures 4.4 (a)-(c) show the observables for which the location of the hadronic event selection cuts may affect the detection efficiency significantly. The points with error bars are experimental data and histograms indicate the Monte Carlo predictions. Unless stated explicitly, the data plotted in these figures are those which passed all the cuts of the standard hadronic event selection except for the cut on the observable in question.

As seen from the  $\cos\theta_T$  distribution, where  $\theta_T$  is the polar angle of the thrust axis with respect to the beam axis, in Fig. 4.4 (a), the direction of the thrust axis is well reproduced by the Monte Carlo simulation. The visible energy, defined by the total energy of charged tracks with assuming that the charged pion mass in an event, is shown in Fig. 4.4 (b). The distinct peak around 5 GeV is the contribution from the beam-wall background and two-photon events. Slightly off-energy particles in the SLC accelerator tend to strike the surface of the SLD's beam pipe and produce several low-energy tracks. The signature of the two-photon event is low multiplicity and low visible energy because the most of the available energy is carried away by the electron and positron into the beam pipe. Another peak around 50 GeV is from hadronic events. This figure tells us that the visible energy cut effectively removes the background events with a small loss of hadronic events. Figure 4.4 (c) shows the raw charged multiplicity distribution after all the cuts of the standard hadronic event selection.

The good agreement between the real data and the Monte Carlo predictions demonstrates that the acceptance corrections, discussed in chapter 6, to be applied to the experimental data can be reliably calculated by our Monte Carlo program.

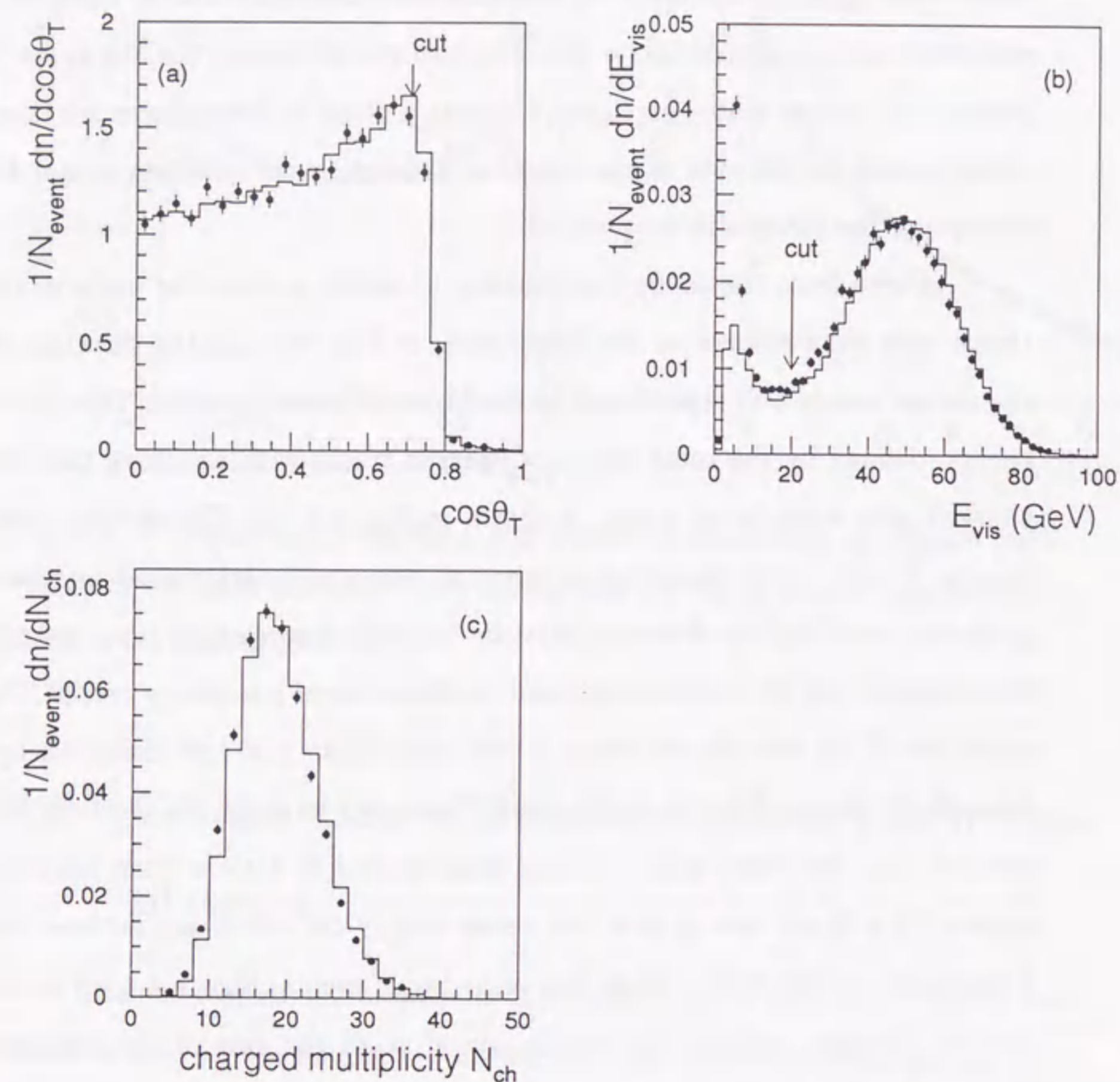


Fig. 4.4. A comparison of experimental hadronic events and Monte Carlo predictions at  $\sqrt{s} = 91.2$  GeV. Plots with error bars show experimental data and histograms indicate the Monte Carlo predictions (JETSET). The distributions are (a) the polar angle of the thrust axis before thrust axis cut, (b) visible energy which is the sum of charged track energies assumed charged pion mass before visible energy cut, and (c) charged track multiplicity after hadronic event selection.

## Chapter 5

### Hadronic Event Observables

In this chapter the observables used in measurement of  $\alpha_s(M_Z^2)$  are defined and discussed their features. The  $\mathcal{O}(\alpha_s^2)$  perturbative QCD calculations exist for the observables, which include six event shapes, differential 2-jet rate calculated in six schemes, two particle correlations, and an angular energy flow.

#### 5.1 Event Shapes

##### 5.1.1 Thrust

Hadronic event observables based on linear sums of particle momenta are stable against collinear splittings and therefore have a feasibility to be both free of singularities at the quark-gluon level and to be insensitive to fragmentation effects. One such a variable is thrust  $T$  defined by<sup>18</sup>:

$$T = \max \frac{\sum_i |\vec{p}_i \cdot \vec{n}_T|}{\sum_i |\vec{p}_i|}, \quad (5.1)$$

where  $\vec{p}_i$  is the momentum vector of particle  $i$  and  $\vec{n}_T$  is the thrust axis to be determined. Thrust is expressed as sum of the length of the longitudinal momenta of the final state particles relative to the thrust axis  $\vec{n}_T$  chosen to maximize  $T$ . We define  $\tau \equiv 1 - T$ . For back-to-back two-parton final states

$\tau$  has a value of zero, while  $0 \leq \tau \leq \frac{1}{3}$  for planar three-parton final states. Spherical events have  $\tau = \frac{1}{2}$ .

The cross section for the thrust at the renormalization scale  $\mu$  using the  $\mathcal{O}(\alpha_s^2)$  formula is given by<sup>7</sup>

$$\frac{1}{\sigma_0} \cdot \frac{d\sigma(\tau)}{d\tau} = A_0(\tau)\tilde{\alpha}_s + [B_0(\tau) + A_0(\tau)2\pi b_0 \ln f] \tilde{\alpha}_s^2, \quad (5.2)$$

and

$$\tilde{\alpha}_s \equiv \frac{\alpha_s(\mu^2, \Lambda_{\overline{MS}})}{2\pi}, \quad (5.3)$$

where  $\sigma_0$  is the cross section of  $e^+e^- \rightarrow q\bar{q}$ , the renormalization scale factor  $f \equiv \mu^2/s$ ,  $b_0 = \frac{33-2n_f}{12\pi}$ , and  $n_f$  is the number of active quark flavors;  $n_f = 5$  at  $\sqrt{s} = M_Z$ . In order to compare with the measured cross section, Eq. (5.2) has to be translated as follows:

$$\begin{aligned} \frac{1}{\sigma_t} \cdot \frac{d\sigma}{d\tau} &= \frac{1}{\sigma_0(1 + \frac{\alpha_s}{\pi} + \mathcal{O}(\alpha_s^2))} \frac{d\sigma}{d\tau} \\ &\simeq \left(1 - \frac{\alpha_s}{\pi}\right) \frac{1}{\sigma_0} \cdot \frac{d\sigma}{d\tau} \\ &= A_0(\tau)\tilde{\alpha}_s + [B_0(\tau) - 2A_0(\tau) + A_0(\tau)2\pi b_0 \ln f] \tilde{\alpha}_s^2 \\ &= A(\tau)\tilde{\alpha}_s + [B(\tau) + A(\tau)2\pi b_0 \ln f] \tilde{\alpha}_s^2, \end{aligned} \quad (5.4)$$

where  $\sigma_t$  is the total hadronic cross section,  $A(\tau) \equiv A_0(\tau)$  and  $B(\tau) \equiv B_0(\tau) - 2A_0(\tau)$ . The coefficients  $A_0(\tau)$  and  $B_0(\tau)$  can be computed by the EVENT program,<sup>7</sup> hence  $A(\tau)$  and  $B(\tau)$  are shown in Table 5.1. The errors of the coefficients are given by the standard deviation. The histogram for  $\tau A(\tau)$  and  $\tau B(\tau)$  are shown in Fig. 5.1. The EVENT program generates three and four-parton events with an appropriate weight which is not necessary positive. From Fig. 5.1(a) and 5.1(b) one can see the different kinematic boundary for the three and four-parton productions. It can be also found that  $B(\tau)$  has a singularity at  $\tau = 1/3$ , the boundary of the three-parton region.

From formula (5.4) and Table 5.1 one can easily calculate the thrust distribution at any given value of  $\tau$ , the energy scale  $\sqrt{s}$ ,  $\Lambda_{\overline{MS}}$ , and the renormalization scale  $\mu$ . In Fig. 5.2 (a) the predictions of QCD for the thrust are plotted

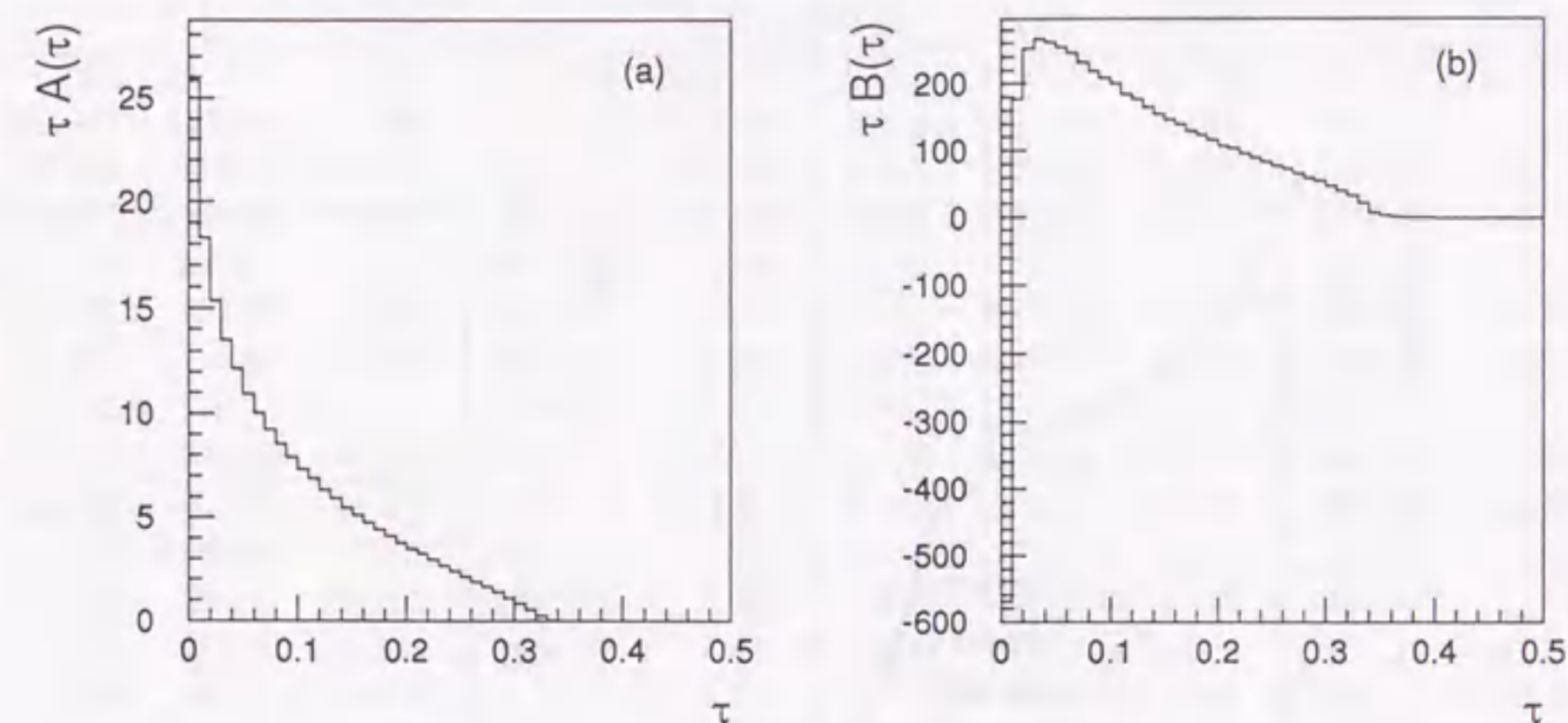


Fig. 5.1. Histograms for the function (a)  $\tau A(\tau)$  and (b)  $\tau B(\tau)$  of the thrust.

for energy scale  $\sqrt{s} = M_Z = 91.2$  GeV at four different values of  $\Lambda_{\overline{MS}} = 100, 200, 300,$  and  $400$  MeV at  $f = 1.0$ , and (b) deviations for  $\Lambda_{\overline{MS}} = 100, 300,$  and  $400$  MeV from  $\Lambda_{\overline{MS}} = 200$  MeV at  $f = 1$ . Fig. 5.2 also shows (c) the predictions for energy scale  $\sqrt{s} = M_Z = 91.2$  GeV at four different values of  $f = 0.01, 0.1, 1.0,$  and  $10.0$  at  $\Lambda_{\overline{MS}} = 200$  MeV \*, and (d) deviations for  $f = 0.01, 0.1, 10.0$  from  $f = 1.0$ . The four curves for different values of  $f$  give an estimation of a part of the uncalculated higher order effect.

### 5.1.2 Oblateness

Oblateness is defined in terms of the energy flow of the event. The distribution of the energy flow is described using three orthogonal axes. First axis has been defined as  $\vec{n}_T$  in previous section. The other two axes are denoted as  $\vec{n}_{maj}$  and  $\vec{n}_{min}$ . The axis  $\vec{n}_{maj}$  can be found to maximize the momentum sum transverse to  $\vec{n}_T$ . Finally, the axis  $\vec{n}_{min}$  is defined to be perpendicular to the

\*This value is used for the discussions throughout this chapter.

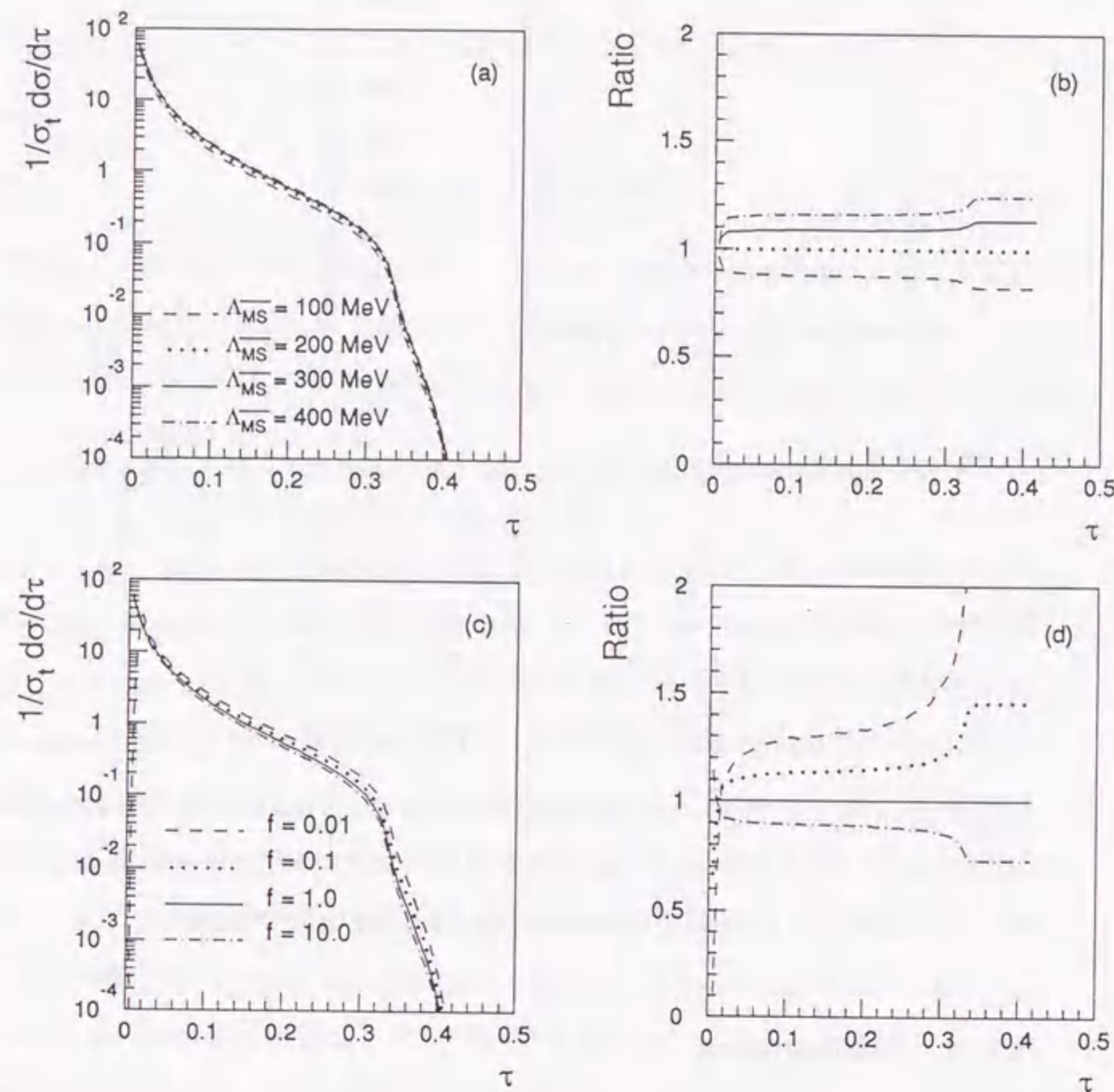


Fig. 5.2. Physical prediction up to  $\mathcal{O}(\alpha_s^2)$  for the thrust distribution at  $\sqrt{s} = 91.2$  GeV. (a) Dependence of  $\Lambda_{\overline{MS}}$  and (b) deviation from the case of  $\Lambda_{\overline{MS}} = 200$  MeV at  $f = 1$ . (c) Dependence of  $f$  and (d) deviation from the case of  $f = 1$ .

$\tau$	$\frac{1}{\sigma_t} \frac{d\sigma}{d\tau}$				$\frac{1}{\sigma_t} \frac{d\sigma}{dO}$				
	$A(\tau)$	$\Delta A(\tau)$	$B(\tau)$	$\Delta B(\tau)$	$O$	$A(O)$	$\Delta A(O)$	$B(O)$	$\Delta B(O)$
0.005	5166.00	7.282	-114032.	3562.03	0.010	5199.00	28.570	-461498.	81580.0
0.015	1218.67	1.993	11755.96	180.24	0.030	1227.00	3.075	-42220.7	618.03
0.025	614.00	1.076	10092.00	82.71	0.050	620.80	1.396	-13419.6	197.84
0.035	386.29	0.708	7598.86	50.08	0.070	390.14	0.824	-5568.86	105.80
0.045	269.33	0.504	5814.66	34.64	0.090	272.56	0.560	-2852.89	67.01
0.055	199.09	0.392	4605.46	26.08	0.110	201.82	0.405	-1654.55	48.03
0.065	154.31	0.306	3774.46	20.53	0.130	156.54	0.304	-1008.61	36.29
0.075	122.93	0.251	3096.80	16.75	0.150	125.00	0.238	-704.93	28.10
0.085	100.19	0.208	2573.74	14.02	0.170	102.06	0.195	-482.47	22.95
0.095	82.83	0.172	2191.18	11.94	0.190	83.89	0.157	-398.26	19.24
0.105	69.42	0.150	1908.78	10.30	0.210	70.43	0.130	-357.52	16.09
0.115	59.52	0.128	1600.96	9.00	0.230	59.48	0.110	-333.04	13.55
0.125	50.45	0.111	1414.30	7.91	0.250	50.80	0.094	-299.20	11.84
0.135	43.79	0.097	1217.62	6.99	0.270	43.59	0.080	-293.63	10.22
0.145	37.81	0.086	1067.13	6.27	0.290	37.52	0.070	-292.10	8.87
0.155	33.07	0.077	944.18	5.67	0.310	32.42	0.060	-276.16	7.86
0.165	28.87	0.068	847.71	5.09	0.330	28.17	0.052	-299.83	6.98
0.175	25.28	0.060	738.58	4.56	0.350	24.48	0.045	-298.22	6.21
0.185	22.14	0.054	663.29	4.14	0.370	21.21	0.040	-299.93	5.62
0.195	19.44	0.049	594.96	3.76	0.390	18.37	0.035	-309.31	5.02
0.205	17.07	0.043	519.51	3.43	0.410	15.90	0.030	-308.39	4.45
0.215	15.00	0.039	480.23	3.15	0.430	13.61	0.027	-321.17	4.00
0.225	13.12	0.035	424.88	2.89	0.450	11.56	0.023	-321.79	3.60
0.235	11.37	0.032	381.73	2.62	0.470	9.74	0.021	-329.06	3.19
0.245	9.88	0.029	341.42	2.39	0.490	7.97	0.018	-334.10	2.79
0.255	8.45	0.026	304.27	2.17	0.510	6.28	0.015	-331.77	2.41
0.265	7.14	0.023	274.96	1.95	0.530	4.64	0.013	-321.72	2.02
0.275	5.96	0.021	239.64	1.75	0.550	2.87	0.010	-283.75	1.52
0.285	4.87	0.018	209.23	1.59	0.570	0.87	0.005	-116.05	0.85
0.295	3.76	0.016	188.11	1.39	0.590			33.90	0.17
0.305	2.77	0.014	158.98	1.17	0.610			17.20	0.10
0.315	1.76	0.011	127.05	0.94	0.630			8.95	0.07
0.325	0.80	0.007	104.62	0.66	0.650			4.11	0.04
0.335	0.05	0.002	64.94	0.34	0.670			1.34	0.02
0.345			25.32	0.14	0.690			0.20	0.01
0.355			12.76	0.09					
0.365			6.80	0.06					
0.375			3.47	0.04					
0.385			1.82	0.03					
0.395			0.80	0.02					
0.405			0.29	0.01					
0.415			0.056	0.005					

Table 5.1. Coefficients of the  $\alpha_s$  and  $\alpha_s^2$  terms for  $\tau$  and  $O$ .

two axes  $\vec{n}_T$  and  $\vec{n}_{maj}$ . The variables thrust-major,  $T_{maj}$ , and thrust-minor,  $T_{min}$ , are obtained by

$$T_{maj} = \frac{\sum_i |\vec{p}_i \cdot \vec{n}_{maj}|}{\sum_i |\vec{p}_i|}, \quad (5.5)$$

$$T_{min} = \frac{\sum_i |\vec{p}_i \cdot \vec{n}_{min}|}{\sum_i |\vec{p}_i|}. \quad (5.6)$$

The oblateness  $O$  is then defined by<sup>52</sup>:

$$O = T_{maj} - T_{min}. \quad (5.7)$$

The value of  $O$  is zero for collinear or cylindrically symmetric final states, and extends from zero to  $\frac{1}{\sqrt{3}}$  for three-parton final states.

The oblateness can be given in the general form similar to the thrust case (Eq. (5.4)):

$$\frac{1}{\sigma_t} \cdot \frac{d\sigma(O)}{dO} = A(O)\tilde{\alpha}_s + [B(O) + A(O)2\pi b_0 \ln f] \tilde{\alpha}_s^2. \quad (5.8)$$

The coefficients  $A(O)$  and  $B(O)$  are tabulated in Table 5.1. Figure 5.3 shows the histograms of (a)  $OA(O)$  and (b)  $OB(O)$ .

It should be noted that the second order corrections are negative in sign for the most of region. In Fig. 5.4 (a) the predictions of QCD for the oblateness are plotted for energy scale  $\sqrt{s} = M_Z = 91.2$  GeV at four different values of  $\Lambda_{\overline{MS}} = 100, 200, 300,$  and  $400$  MeV at  $f = 1.0$ , and (b) deviations for  $\Lambda_{\overline{MS}} = 100, 300,$  and  $400$  MeV from  $\Lambda_{\overline{MS}} = 200$  MeV at  $f = 1$ . Fig. 5.4 also shows (c) the predictions for energy scale  $\sqrt{s} = M_Z = 91.2$  GeV at four different values of  $f = 0.01, 0.1, 1.0,$  and  $10.0$  at  $\Lambda_{\overline{MS}} = 200$  MeV, and (d) deviations for  $f = 0.01, 0.1, 10.0$  from  $f = 1.0$ .

### 5.1.3 The C-parameter

The C-parameter is derived from the eigenvalues of the infrared-safe momentum tensor<sup>53</sup>:

$$\theta_{\rho\sigma} = \frac{\sum_i p_i^\rho p_i^\sigma / |\vec{p}_i|}{\sum_i |\vec{p}_i|}, \quad (5.9)$$

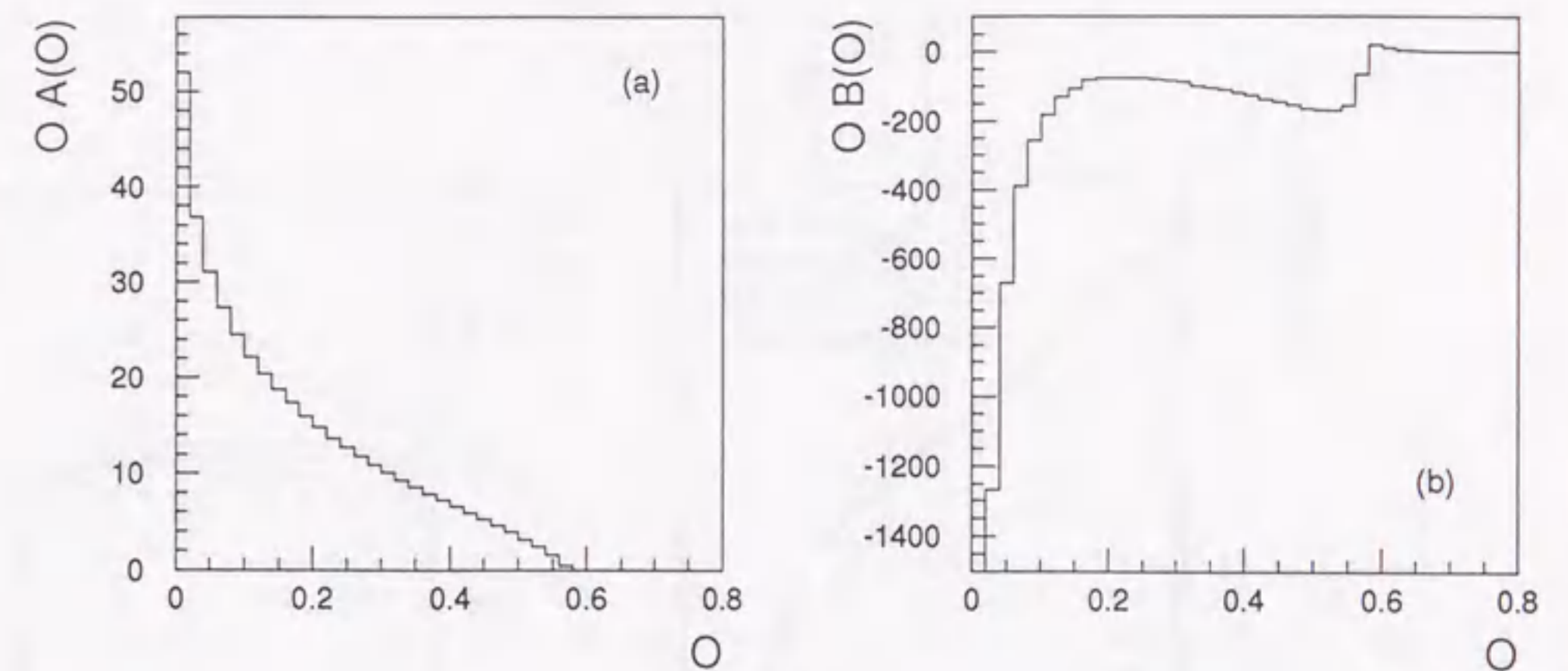


Fig. 5.3. Histograms for the function (a)  $OA(O)$  and (b)  $OB(O)$  of the oblateness

where  $p_i^\rho$  is the  $\rho$ -th component of the three momentum of particle  $i$ , and  $i$  runs over all the final state particles. The tensor  $\theta_{\rho\sigma}$  is normalized to have unit trace, and the C-parameter is defined by:

$$C = 3(\lambda_1\lambda_2 + \lambda_2\lambda_3 + \lambda_3\lambda_1), \quad (5.10)$$

where  $\lambda_i$  ( $i = 1, 2, 3$ ) are the eigenvalues of the tensor  $\theta_{\rho\sigma}$ . For back-to-back two-parton final states  $C$  is zero, while for planar three-parton final states  $0 \leq C \leq \frac{2}{3}$ . For spherical events  $C = 1$ .

The C-parameter can be parametrized by the form:

$$\frac{1}{\sigma_t} \cdot \frac{d\sigma(C)}{dC} = A(C)\tilde{\alpha}_s + [B(C) + A(C)2\pi b_0 \ln f] \tilde{\alpha}_s^2. \quad (5.11)$$

The coefficients  $A(C)$  and  $B(C)$  are tabulated in Table 5.2. Figure 5.5 shows the histograms of (a)  $CA(C)$  and (b)  $CB(C)$ .

In Fig. 5.6 (a) the predictions of QCD for the C-parameter are plotted for energy scale  $\sqrt{s} = M_Z = 91.2$  GeV at four different values of  $\Lambda_{\overline{MS}} = 100, 200, 300,$  and  $400$  MeV at  $f = 1.0$ , and (b) deviations for  $\Lambda_{\overline{MS}} = 100, 300,$  and  $400$



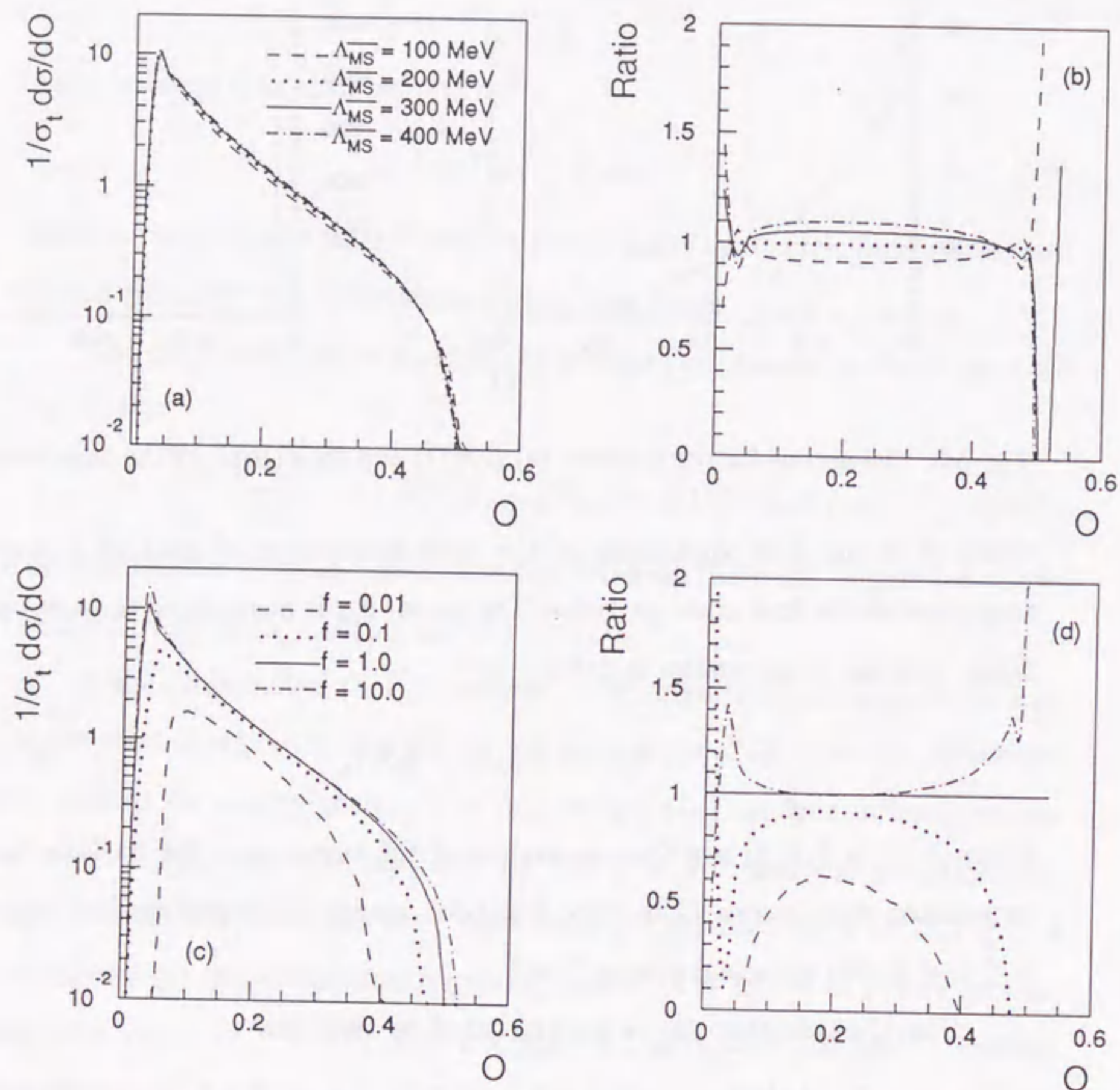


Fig. 5.4. Physical prediction up to  $\mathcal{O}(\alpha_s^2)$  for the oblateness distribution at  $\sqrt{s} = 91.2$  GeV. (a) Dependence of  $\Lambda_{\overline{MS}}$  and (b) deviation from the case of  $\Lambda_{\overline{MS}} = 200$  MeV at  $f = 1$ . (c) Dependence of  $f$  and (d) deviation from the case of  $f = 1$ .

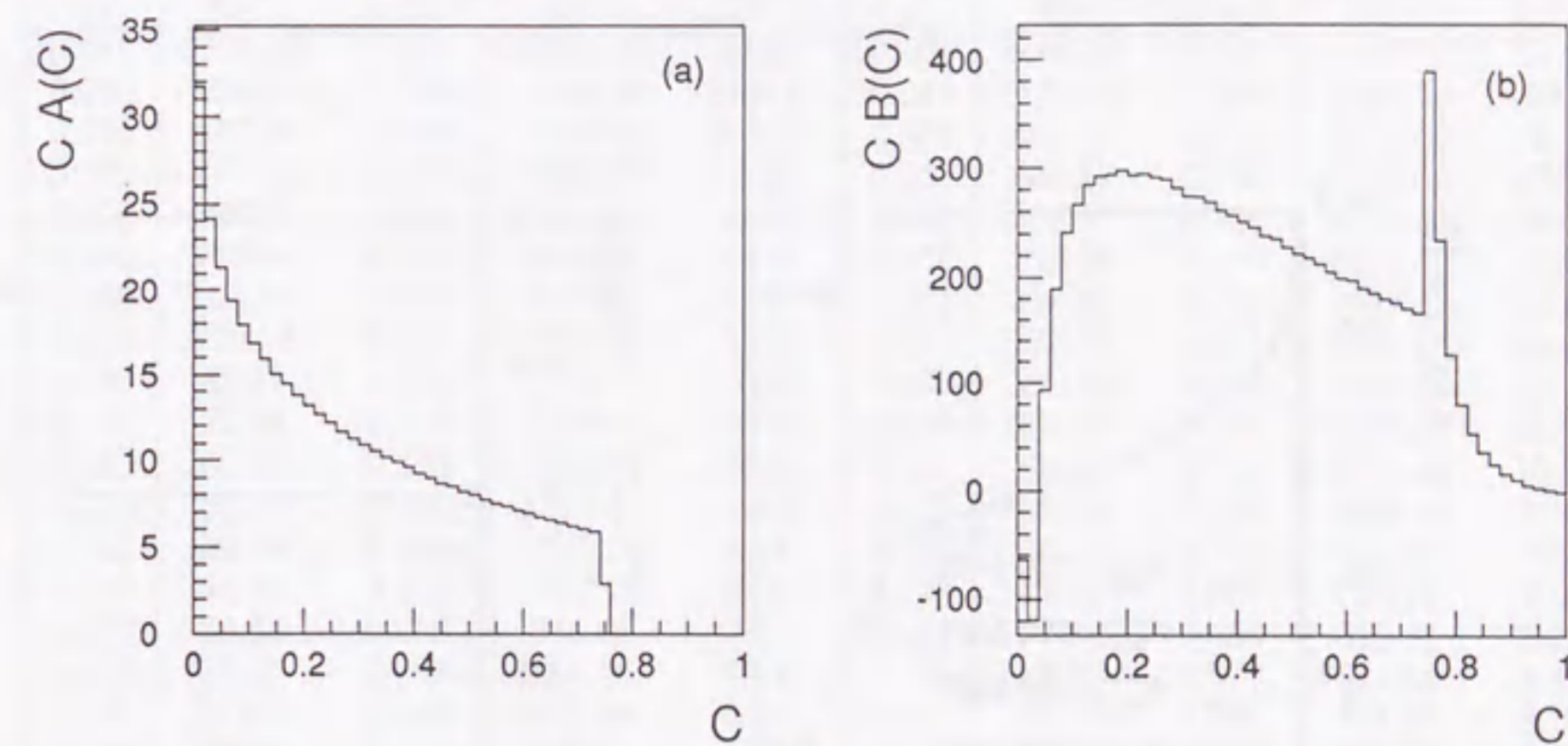


Fig. 5.5. Histograms for the function (a)  $CA(C)$  and (b)  $CB(C)$  of the  $C$ -parameter.

MeV from  $\Lambda_{\overline{MS}} = 200$  MeV at  $f = 1$ . Fig. 5.6 also shows (c) the predictions for energy scale  $\sqrt{s} = M_Z = 91.2$  GeV at four different values of  $f = 0.01, 0.1, 1.0,$  and  $10.0$  at  $\Lambda_{\overline{MS}} = 200$  MeV, and (d) deviations for  $f = 0.01, 0.1, 10.0$  from  $f = 1.0$ .

#### 5.1.4 Heavy jet mass

Events can be divided into two hemispheres  $a$ , and  $b$  by a plane perpendicular to the thrust axis  $\vec{n}_T$ . The heavy jet mass  $M_H$  is then defined as<sup>19</sup>:

$$M_H = \max(M_a, M_b), \quad (5.12)$$

where  $M_a$  and  $M_b$  are the invariant masses of the two hemispheres calculated by using four-momentum  $p_i$  of the particles:

$$M_a = \sum_{i \in a} \sqrt{p_i^2} \quad \text{and} \quad M_b = \sum_{i \in b} \sqrt{p_i^2}. \quad (5.13)$$

Here we define the normalized quantity:

$$\rho \equiv \frac{M_H^2}{E_{vis}^2}, \quad (5.14)$$

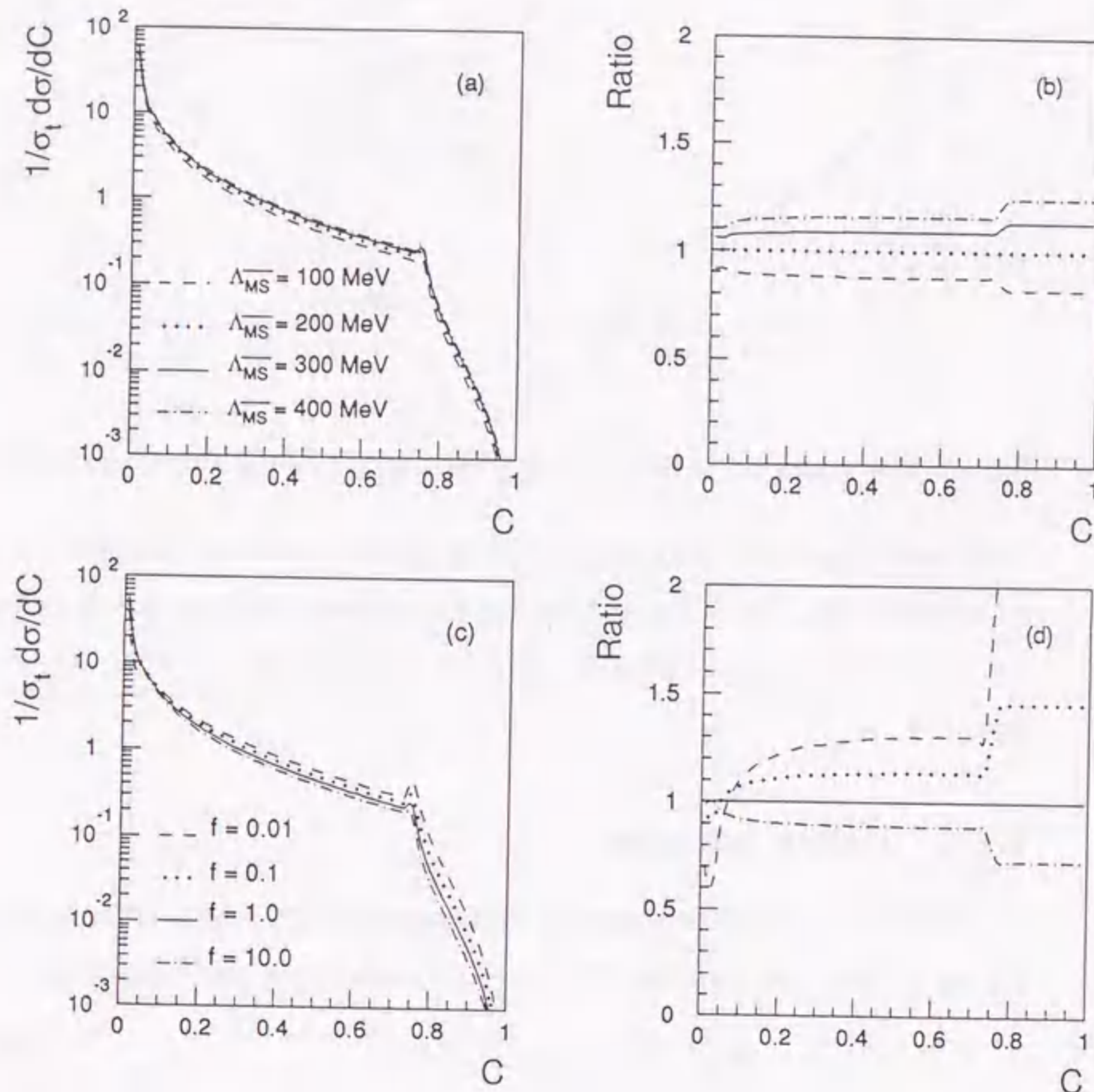


Fig. 5.6. Physical prediction up to  $\mathcal{O}(\alpha_s^2)$  for the C-parameter distribution at  $\sqrt{s} = 91.2$  GeV. (a) Dependence of  $\Lambda_{\overline{MS}}$  and (b) deviation from the case of  $\Lambda_{\overline{MS}} = 200$  MeV at  $f = 1$ . (c) Dependence of  $f$  and (d) deviation from the case of  $f = 1$ .

$C$	$\frac{1}{\sigma_1} \frac{d\sigma}{dC}$				$\rho$	$\frac{1}{\sigma_1} \frac{d\sigma}{d\rho}$			
	$A(C)$	$\Delta A(C)$	$B(C)$	$\Delta B(C)$		$A(\rho)$	$\Delta A(\rho)$	$B(\rho)$	$\Delta B(\rho)$
0.010	3172.00	6.446	-6344.00	12.89	0.005	5166.00	7.282	-10332.0	14.56
0.030	805.00	1.799	-3983.33	239.06	0.015	1218.67	1.993	5149.33	165.71
0.050	427.20	0.986	1867.60	105.70	0.025	614.00	1.076	6416.00	76.15
0.070	277.00	0.663	2690.29	63.23	0.035	386.29	0.708	5176.00	47.08
0.090	199.67	0.483	2676.23	43.33	0.045	269.33	0.504	4061.33	33.13
0.110	153.18	0.373	2424.55	32.34	0.055	199.09	0.392	3221.82	25.14
0.130	122.69	0.307	2186.93	25.38	0.065	154.31	0.306	2652.92	20.01
0.150	100.13	0.251	1949.06	20.59	0.075	122.93	0.251	2166.13	16.42
0.170	85.12	0.214	1729.76	17.15	0.085	100.19	0.208	1793.74	13.72
0.190	72.68	0.186	1566.21	14.56	0.095	82.83	0.172	1505.92	11.75
0.210	62.76	0.159	1395.91	12.51	0.105	69.42	0.150	1291.64	10.20
0.230	55.13	0.140	1280.61	11.03	0.115	59.52	0.128	1068.79	8.94
0.250	48.68	0.124	1163.04	9.69	0.125	50.45	0.111	921.50	7.87
0.270	43.26	0.110	1072.00	8.65	0.135	43.79	0.097	756.13	6.99
0.290	38.83	0.099	971.65	7.72	0.145	37.81	0.086	655.41	6.23
0.310	35.23	0.090	884.06	6.94	0.155	33.07	0.077	545.28	5.61
0.330	31.97	0.080	827.58	6.34	0.165	28.87	0.068	473.65	5.09
0.350	29.09	0.073	767.54	5.76	0.175	25.28	0.060	394.87	4.58
0.370	26.77	0.066	704.83	5.27	0.185	22.14	0.054	328.10	4.13
0.390	24.64	0.062	658.42	4.81	0.195	19.44	0.049	285.58	3.78
0.410	22.57	0.056	612.91	4.44	0.205	17.07	0.043	226.83	3.47
0.430	20.93	0.052	570.94	4.09	0.215	15.00	0.039	199.16	3.15
0.450	19.32	0.048	529.80	3.78	0.225	13.12	0.035	157.32	2.89
0.470	18.06	0.044	500.91	3.51	0.235	11.37	0.032	130.28	2.64
0.490	16.76	0.040	463.84	3.25	0.245	9.88	0.029	99.09	2.41
0.510	15.73	0.038	435.00	3.01	0.255	8.45	0.026	76.78	2.19
0.530	14.62	0.035	412.64	2.84	0.265	7.14	0.023	57.75	2.00
0.550	13.69	0.033	386.62	2.66	0.275	5.96	0.021	38.55	1.79
0.570	12.88	0.030	360.20	2.43	0.285	4.87	0.018	22.34	1.59
0.590	12.09	0.028	338.69	2.27	0.295	3.76	0.016	14.32	1.39
0.610	11.40	0.026	324.58	2.13	0.305	2.77	0.014	7.32	1.19
0.630	10.70	0.024	301.13	1.98	0.315	1.76	0.011	0.76	0.95
0.650	10.10	0.022	285.96	1.84	0.325	0.80	0.007	12.04	0.64
0.670	9.48	0.021	269.24	1.72	0.335	0.05	0.002	24.08	0.29
0.690	9.01	0.019	255.88	1.60	0.345			9.69	0.09
0.710	8.49	0.018	241.05	1.49	0.355			4.37	0.06
0.730	8.04	0.017	229.26	1.37	0.365			2.10	0.04
0.750	3.85	0.011	518.30	0.99	0.375			0.94	0.02
0.770			305.20	0.48	0.385			0.43	0.01
0.790			161.77	0.30	0.395			0.15	0.01
0.810			99.81	0.22	0.405			0.024	0.003
0.830			65.25	0.16	0.415			0.003	0.001
0.850			43.82	0.13					
0.870			29.10	0.10					
0.890			18.99	0.08					
0.910			12.14	0.06					
0.930			7.13	0.04					
0.950			3.80	0.03					
0.970			1.55	0.02					
0.990			0.31	0.01					

Table 5.2. Coefficients of the  $\bar{\alpha}_s$  and  $\bar{\alpha}_s^2$  terms for  $C$  and  $\rho$ .

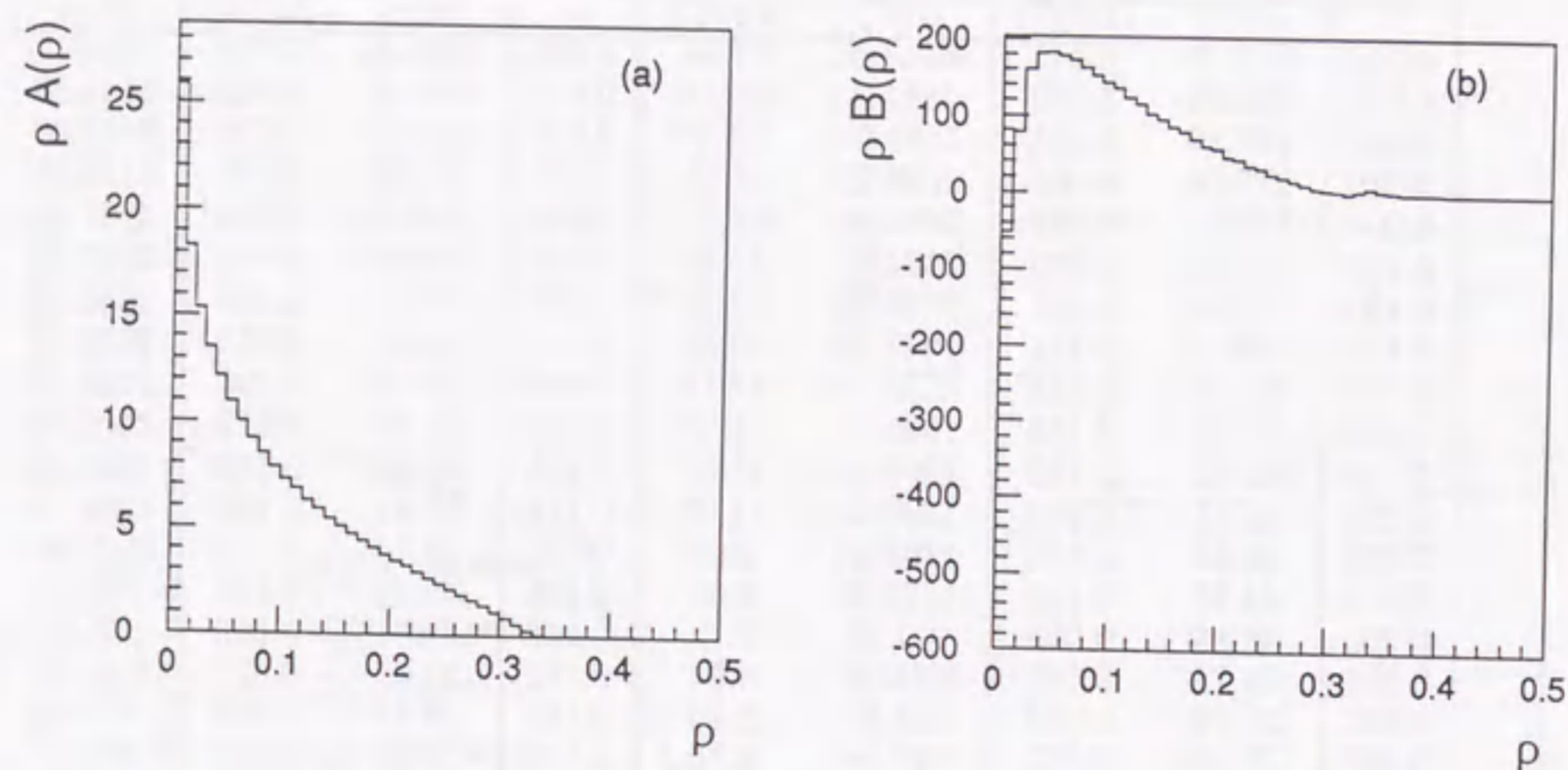


Fig. 5.7. Histograms for the function (a)  $\rho A(\rho)$  and (b)  $\rho B(\rho)$  of the heavy jet mass.

where  $E_{vis}$  is the total energy measured in a hadronic event. To first order in perturbative QCD, and for massless partons, the heavy jet mass and thrust are related by  $\tau = \rho$ .

The heavy jet mass can be parametrized by the form:

$$\frac{1}{\sigma_t} \cdot \frac{d\sigma(\rho)}{d\rho} = A(\rho)\tilde{\alpha}_s + [B(\rho) + A(\rho)2\pi b_0 \ln f] \tilde{\alpha}_s^2. \quad (5.15)$$

The coefficients  $A(\rho)$  and  $B(\rho)$  are tabulated in Table 5.2. Figure 5.7 shows the histograms of (a)  $\rho A(\rho)$  and (b)  $\rho B(\rho)$ .

In Fig. 5.8 (a) the predictions of QCD for the heavy jet mass are plotted for energy scale  $\sqrt{s} = M_Z = 91.2$  GeV at four different values of  $\Lambda_{\overline{MS}} = 100, 200, 300,$  and  $400$  MeV at  $f = 1.0$ , and (b) deviations for  $\Lambda_{\overline{MS}} = 100, 300,$  and  $400$  MeV from  $\Lambda_{\overline{MS}} = 200$  MeV at  $f = 1$ . Fig. 5.8 also shows (c) the predictions for energy scale  $\sqrt{s} = M_Z = 91.2$  GeV at four different values of  $f = 0.01, 0.1, 1.0,$  and  $10.0$  at  $\Lambda_{\overline{MS}} = 200$  MeV, and (d) deviations for  $f = 0.01, 0.1, 10.0$  from  $f = 1.0$ .

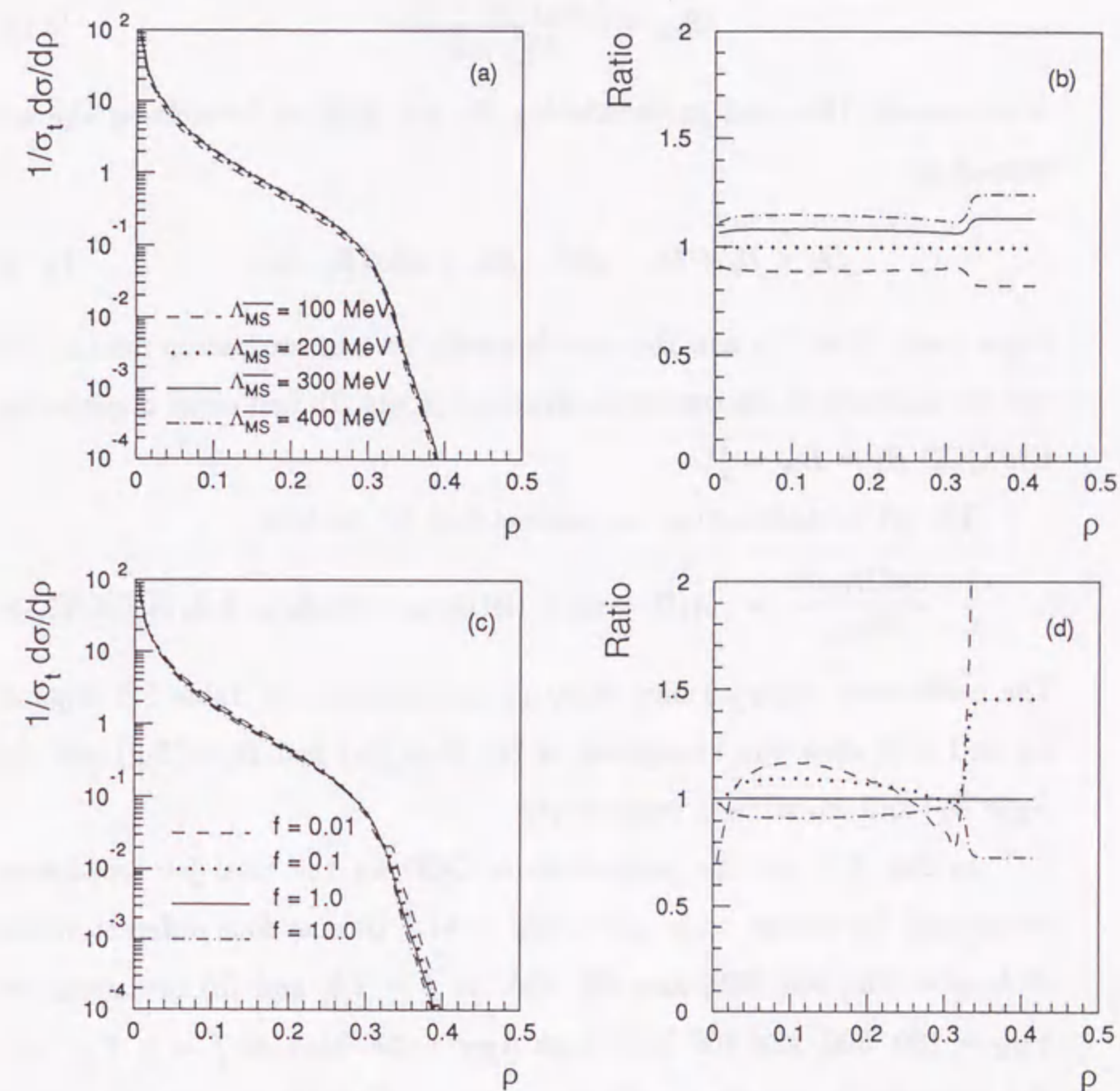


Fig. 5.8. Physical prediction up to  $\mathcal{O}(\alpha_s^2)$  for the heavy jet mass distribution at  $\sqrt{s} = 91.2$  GeV. (a) Dependence of  $\Lambda_{\overline{MS}}$  and (b) deviation from the case of  $\Lambda_{\overline{MS}} = 200$  MeV at  $f = 1$ . (c) Dependence of  $f$  and (d) deviation from the case of  $f = 1$ .

### 5.1.5 Jet broadening

Jet broadening has been used mainly for the study of hadron collisions<sup>54</sup> but also proposed for  $e^+e^-$  physics.<sup>20</sup> In each hemisphere  $a, b$ :

$$B_{a,b} = \frac{\sum_{i \in a,b} |\vec{p}_i \times \vec{n}_T|}{2 \sum_i |\vec{p}_i|} \quad (5.16)$$

is calculated. The total jet broadening  $B_T$  and wide jet broadening  $B_W$  are defined by

$$B_T = B_a + B_b \quad \text{and} \quad B_W = \max(B_a, B_b), \quad (5.17)$$

respectively. Both  $B_T$  and  $B_W$  are identically zero in two-parton final states, and are sensitive to the transverse structure of jets. To first order in perturbative QCD  $B_T = B_W = \frac{1}{2}O$ .

The jet broadening can be parametrized by the form:

$$\frac{1}{\sigma_t} \frac{d\sigma(B_{T,W})}{dB_{T,W}} = A(B_{T,W})\tilde{\alpha}_s + [B(B_{T,W}) + A(B_{T,W})2\pi b_0 \ln f] \tilde{\alpha}_s^2 \quad (5.18)$$

The coefficients  $A(B_{T,W})$  and  $B(B_{T,W})$  are tabulated in Table 5.3. Figures 5.9 and 5.10 show the histograms of (a)  $B_T A(B_T)$  and  $B_W A(B_W)$  and (b)  $B_T B(B_T)$  and  $B_W B(B_W)$ , respectively.

In Fig. 5.11 (a) the predictions of QCD for the total jet broadening are plotted for energy scale  $\sqrt{s} = M_Z = 91.2$  GeV at four different values of  $\Lambda_{\overline{MS}} = 100, 200, 300,$  and  $400$  MeV at  $f = 1.0$ , and (b) deviations for  $\Lambda_{\overline{MS}} = 100, 300,$  and  $400$  MeV from  $\Lambda_{\overline{MS}} = 200$  MeV at  $f = 1$ . Fig. 5.11 also shows (c) the predictions for energy scale  $\sqrt{s} = M_Z = 91.2$  GeV at four different values of  $f = 0.01, 0.1, 1.0,$  and  $10.0$  at  $\Lambda_{\overline{MS}} = 200$  MeV, and (d) deviations for  $f = 0.01, 0.1, 10.0$  from  $f = 1.0$ .

In Fig. 5.12 (a) the predictions of QCD for the wide jet broadening are plotted for energy scale  $\sqrt{s} = M_Z = 91.2$  GeV at four different values of  $\Lambda_{\overline{MS}} = 100, 200, 300,$  and  $400$  MeV at  $f = 1.0$ , and (b) deviations for  $\Lambda_{\overline{MS}} = 100, 300,$  and  $400$  MeV from  $\Lambda_{\overline{MS}} = 200$  MeV at  $f = 1$ . Fig. 5.11

also shows (c) the predictions for energy scale  $\sqrt{s} = M_Z = 91.2$  GeV at four different values of  $f = 0.01, 0.1, 1.0,$  and  $10.0$  at  $\Lambda_{\overline{MS}} = 200$  MeV, and (d) deviations for  $f = 0.01, 0.1, 10.0$  from  $f = 1.0$ .

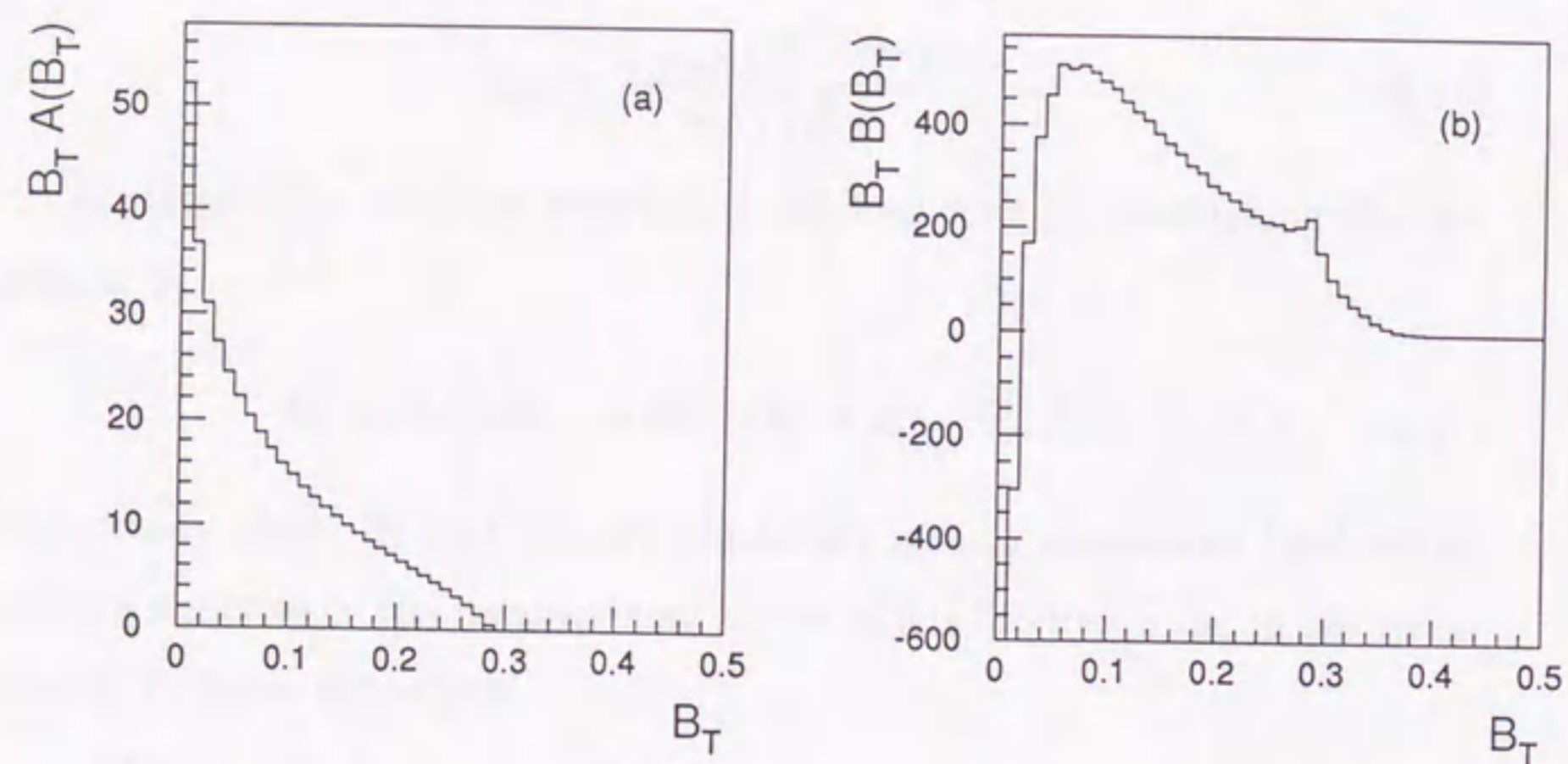


Fig. 5.9. Histograms for the function (a)  $B_T A(B_T)$  and (b)  $B_T B(B_T)$  of the total jet broadening.

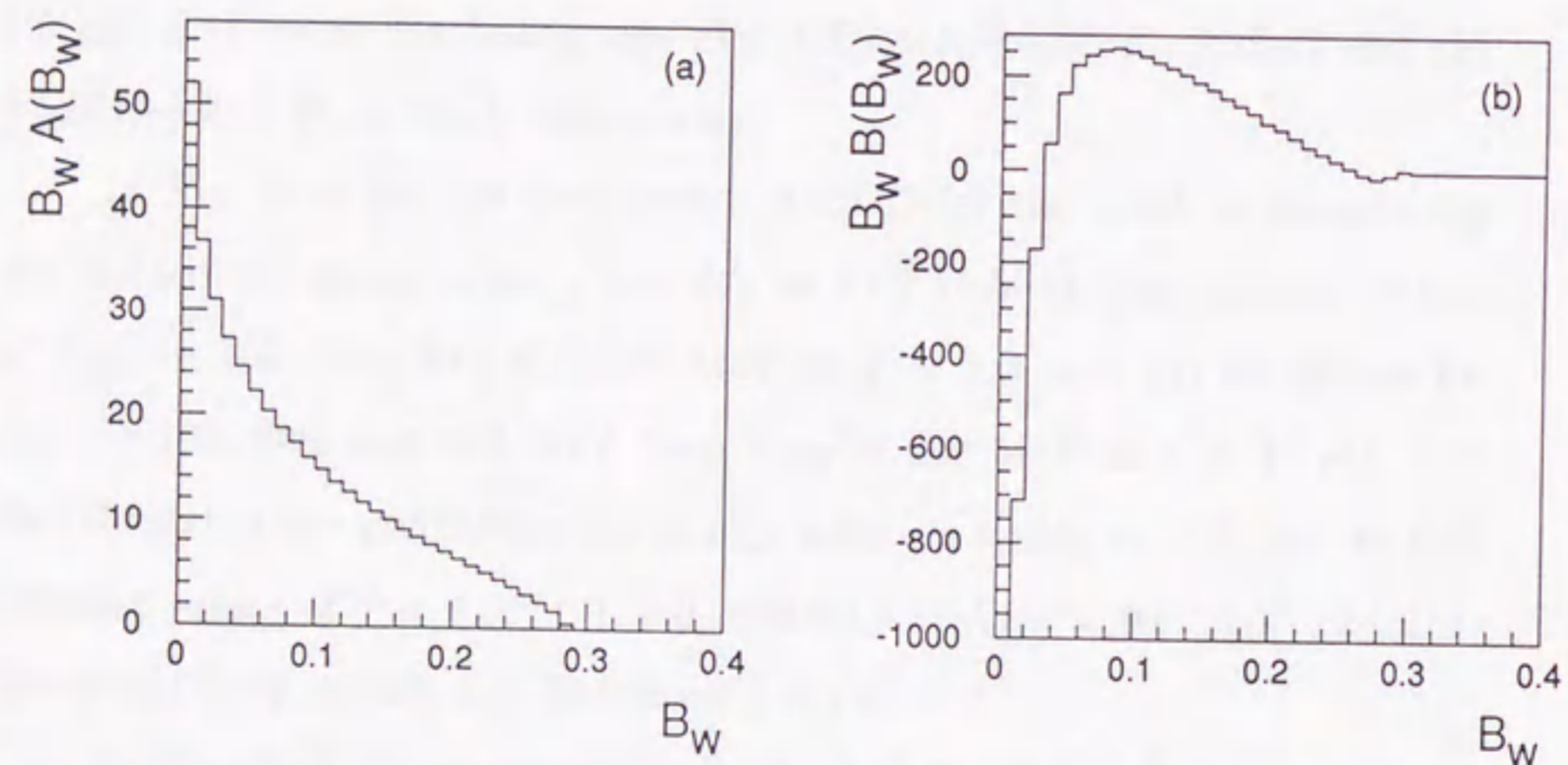


Fig. 5.10. Histograms for the function (a)  $B_W A(B_W)$  and (b)  $B_W B(B_W)$  of the wide jet broadening.

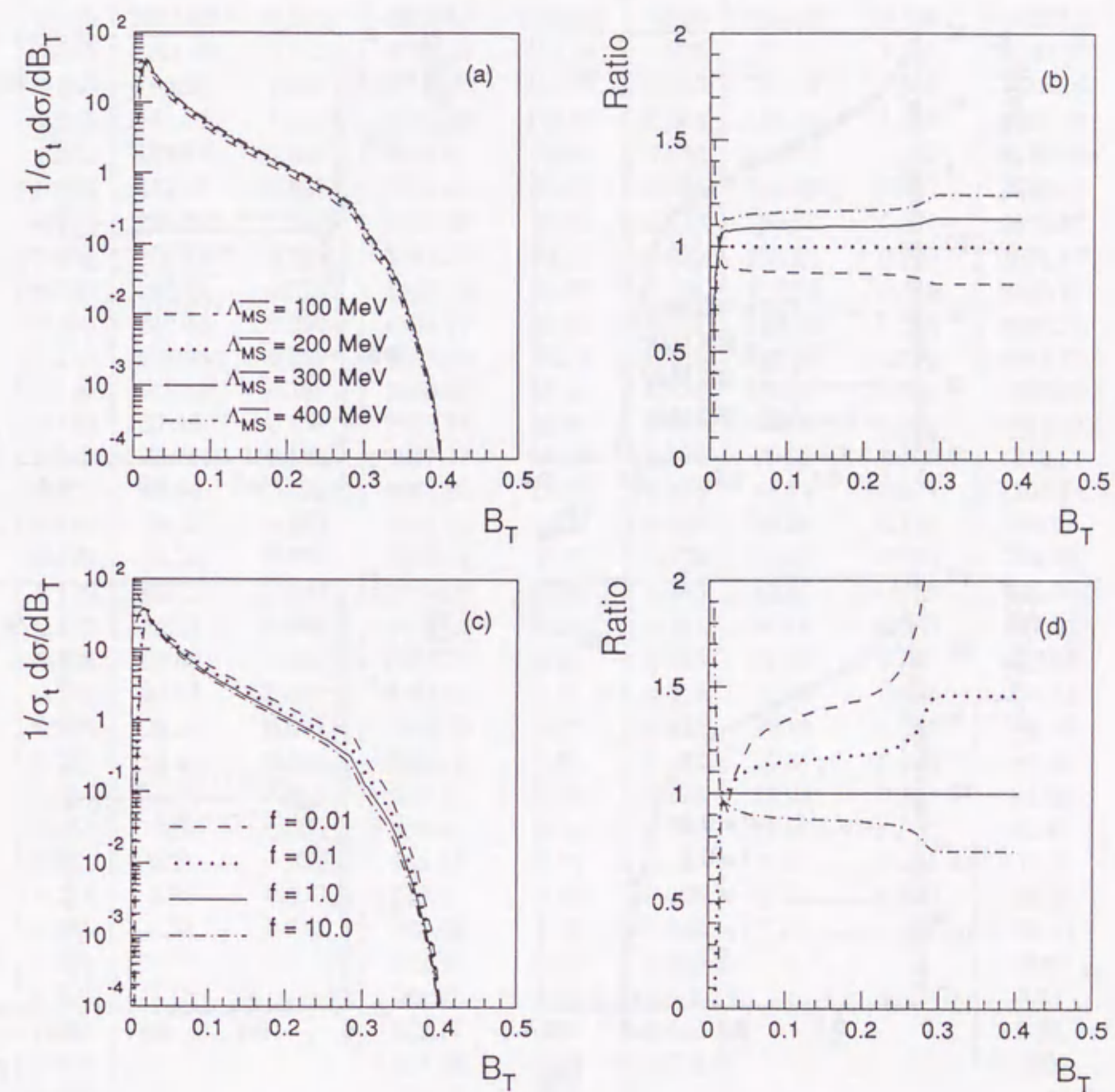


Fig. 5.11. Physical prediction up to  $\mathcal{O}(\alpha_s^2)$  for the total jet broadening distribution at  $\sqrt{s} = 91.2$  GeV. (a) Dependence of  $\Lambda_{\overline{MS}}$  and (b) deviation from the case of  $\Lambda_{\overline{MS}} = 200$  MeV at  $f = 1$ . (c) Dependence of  $f$  and (d) deviation from the case of  $f = 1$ .

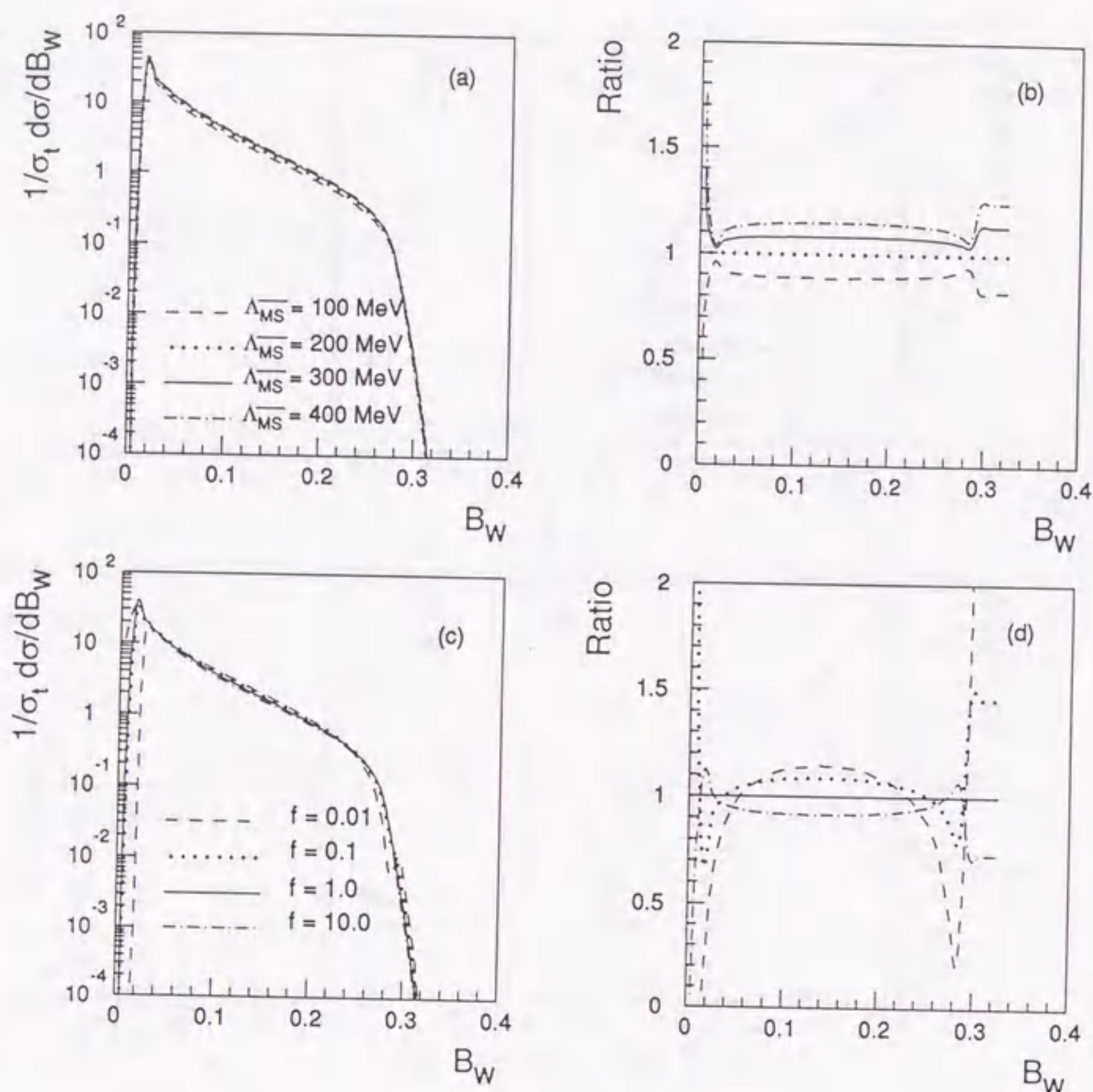


Fig. 5.12. Physical prediction up to  $\mathcal{O}(\alpha_s^2)$  for the wide jet broadening distribution at  $\sqrt{s} = 91.2$  GeV. (a) Dependence of  $\Lambda_{\overline{MS}}$  and (b) deviation from the case of  $\Lambda_{\overline{MS}} = 200$  MeV at  $f = 1$ . (c) Dependence of  $f$  and (d) deviation from the case of  $f = 1$ .

$B_T$	$\frac{1}{\sigma_t} \frac{d\sigma}{dB_T}$				$B_W$	$\frac{1}{\sigma_t} \frac{d\sigma}{dB_W}$			
	$A(B_T)$	$\Delta A(B_T)$	$B(B_T)$	$\Delta B(B_T)$		$A(B_W)$	$\Delta A(B_W)$	$B(B_W)$	$\Delta B(B_W)$
0.005	10398.0	57.140	-494196.	247800.	0.005	10396.0	57.140	-706792.	207000.
0.015	2454.00	6.151	-20274.7	1474.72	0.015	2454.00	6.151	-47228.0	1155.40
0.025	1241.60	2.792	6792.80	443.64	0.025	1241.60	2.792	-6843.20	288.21
0.035	780.29	1.648	10722.33	221.02	0.035	780.29	1.648	1585.14	127.67
0.045	545.11	1.119	10185.38	136.00	0.045	545.11	1.119	3620.89	73.12
0.055	403.64	0.810	9383.63	91.92	0.055	403.64	0.810	4029.09	48.45
0.065	313.08	0.607	7824.62	65.63	0.065	313.08	0.607	3738.47	34.33
0.075	250.00	0.477	6852.00	50.16	0.075	250.00	0.477	3370.67	25.95
0.085	204.12	0.389	5895.29	39.22	0.085	204.12	0.389	3021.17	20.63
0.095	167.79	0.314	5101.26	31.67	0.095	167.79	0.314	2640.21	16.66
0.105	140.86	0.259	4468.77	26.26	0.105	140.86	0.259	2297.34	13.70
0.115	118.96	0.220	3883.83	21.72	0.115	118.96	0.220	1984.70	11.44
0.125	101.60	0.189	3396.80	18.40	0.125	101.60	0.189	1720.00	9.76
0.135	87.19	0.159	3027.11	15.81	0.135	87.19	0.159	1502.67	8.42
0.145	75.03	0.139	2647.17	13.53	0.145	75.03	0.139	1279.59	7.34
0.155	64.84	0.121	2361.93	11.77	0.155	64.84	0.121	1107.74	6.39
0.165	56.35	0.103	2091.55	10.34	0.165	56.35	0.103	939.43	5.63
0.175	48.96	0.090	1848.94	9.13	0.175	48.96	0.090	799.79	4.94
0.185	42.42	0.080	1669.22	8.14	0.185	42.42	0.080	665.98	4.36
0.195	36.74	0.069	1462.41	7.25	0.195	36.74	0.069	527.03	3.88
0.205	31.80	0.061	1321.76	6.50	0.205	31.80	0.061	432.00	3.45
0.215	27.21	0.053	1193.01	5.81	0.215	27.21	0.053	334.78	3.06
0.225	23.12	0.047	1063.53	5.23	0.225	23.12	0.047	240.86	2.72
0.235	19.49	0.042	969.12	4.73	0.235	19.49	0.042	167.97	2.42
0.245	15.94	0.036	879.14	4.28	0.245	15.94	0.036	96.08	2.12
0.255	12.55	0.030	825.87	3.74	0.255	12.55	0.030	36.42	1.82
0.265	9.27	0.025	765.23	3.18	0.265	9.27	0.025	-18.51	1.51
0.275	5.75	0.020	748.51	2.59	0.275	5.75	0.020	-51.24	1.16
0.285	1.73	0.011	774.08	1.76	0.285	1.73	0.011	-23.22	0.67
0.295			532.20	0.97	0.295			13.87	0.11
0.305			344.92	0.67	0.305			2.37	0.04
0.315			239.11	0.51	0.315			0.25	0.01
0.325			166.92	0.39	0.325			0.002	0.001
0.335			111.31	0.30					
0.345			64.23	0.21					
0.355			31.89	0.14					
0.365			15.50	0.09					
0.375			7.02	0.06					
0.385			2.72	0.03					
0.395			0.73	0.02					
0.405			0.05	0.004					

Table 5.3. Coefficients of the  $\bar{\alpha}_s$  and  $\bar{\alpha}_s^2$  terms for  $B_T$  and  $B_W$ .

## 5.2 Jet Rates

### 5.2.1 Jet Clustering Algorithms

Another useful method of classifying the structure of hadronic final states is in terms of jets. Jets may be reconstructed using iterative clustering algorithms<sup>21</sup> in which a measure  $y_{ij}$ , such as scaled invariant mass, is calculated for all pairs of particles  $i$  and  $j$ , and the pair with the smallest  $y_{ij}$  is combined into a single particle. This procedure is repeated until all pairs have  $y_{ij}$  exceeding a value  $y_{cut}$ , and the jet multiplicity of the event is defined as the number of particles remaining. The  $n$ -jet rate  $R_n(y_{cut})$  is the fraction of events classified as  $n$ -jet, and the differential 2-jet rate is defined as<sup>55</sup>:

$$D_2(y_{cut}) \equiv \frac{R_2(y_{cut}) - R_2(y_{cut} - \Delta y_{cut})}{\Delta y_{cut}}. \quad (5.19)$$

In contrast to  $R_n$ , each event contributes to  $D_2$  at only one  $y_{cut}$ .

Several algorithms have been proposed featuring different  $y_{ij}$  definitions and recombination methods. We have applied the E, E0, P, and P0 variations of the JADE algorithm<sup>56</sup> as well as the Durham (D) and Geneva (G) schemes.<sup>21</sup> The six definitions of the jet resolution parameter  $y_{ij}$  and recombination procedure are given below.

In the E-scheme,  $y_{ij}$  is defined as the square of the invariant mass of the pair of particles  $i$  and  $j$  scaled by the visible energy in the event,

$$y_{ij} = \frac{(p_i + p_j)^2}{E_{vis}^2}, \quad (5.20)$$

with the recombination performed as

$$p_k = p_i + p_j, \quad (5.21)$$

where  $p_i$  and  $p_j$  are four-momenta of the particles and pion masses are assumed in calculating particle energies. Energy and momentum are explicitly conserved in this scheme.

scheme	resolution parameter	recombination
E	$(p_i + p_j)^2 / Q^2$	$p_k = p_i + p_j$ $Q = E_{vis}$
E0		$E_k = E_i + E_j$ $\vec{p}_k = \frac{E_k}{ \vec{p}_i + \vec{p}_j } (\vec{p}_i + \vec{p}_j)$ $Q = E_{vis}$
P		$\vec{p}_k = \vec{p}_i + \vec{p}_j$ $E_k =  \vec{p}_k $ $Q = E_{vis}$
P0		$\vec{p}_k = \vec{p}_i + \vec{p}_j$ $E_k =  \vec{p}_k $ $Q = \sum_k E_k$
D	$\frac{2 \min(E_i^2, E_j^2) (1 - \cos \theta_{ij})}{E_{vis}^2}$	$p_k = p_i + p_j$
G	$\frac{8 E_i E_j (1 - \cos \theta_{ij})}{9 (E_i + E_j)^2}$	$p_k = p_i + p_j$

Table 5.4. Definition of the jet resolution parameter  $y_{ij}$  and of recombination schemes for the jet clustering algorithm.

The E0-, P-, and P0-schemes are variations of the E-scheme. In the E0-scheme  $y_{ij}$  is defined by Eq. (5.20), while the recombination procedure is defined by

$$E_k = E_i + E_j \quad (5.22)$$

$$\vec{p}_k = \frac{E_k}{|\vec{p}_i + \vec{p}_j|} (\vec{p}_i + \vec{p}_j), \quad (5.23)$$

where  $E_i$  and  $E_j$  are the energies, and  $\vec{p}_i$  and  $\vec{p}_j$  are the three-momenta of the particles. The three-momentum  $\vec{p}_k$  is rescaled so that particle  $k$  has zero invariant mass. This scheme does not conserve the total momentum sum of an

event.

In the P-scheme  $y_{ij}$  is defined by Eq. (5.21) and the recombination procedure is defined by

$$\vec{p}_k = \vec{p}_i + \vec{p}_j \quad (5.24)$$

$$E_k = |\vec{p}_k|. \quad (5.25)$$

This scheme conserves the total momentum of an event, but does not conserve the total energy.

The P0-scheme is similar to the P-scheme, but the total energy  $E_{vis}$  in Eq. (5.20) is recalculated at each iteration according to

$$E_{vis} = \sum_k E_k. \quad (5.26)$$

In the D-scheme,

$$y_{ij} = \frac{2\min(E_i^2, E_j^2)(1 - \cos \theta_{ij})}{E_{vis}^2}, \quad (5.27)$$

where  $\theta_{ij}$  is the angle between the pair of particles  $i$  and  $j$ . The recombination is defined by Eq. (5.21). With the D-scheme, a soft particle will only be combined with another soft particle, instead of being combined with a high-energy particle, if the angle it makes with the other soft particle is smaller than the angle that it makes with the high-energy particle.

The definition of  $y_{ij}$  for the G-scheme is

$$y_{ij} = \frac{8E_i E_j (1 - \cos \theta_{ij})}{9(E_i + E_j)^2}, \quad (5.28)$$

and the recombination is defined by Eq. (5.21). In this scheme soft particles are combined as in the D-scheme. In addition,  $y_{ij}$  depends only on the energy of the particles to be combined, and not on the  $E_{vis}$  of the event.

The ratio of tree-jet events with jet resolution  $y_{cut}$  for the total hadronic events can be parametrized in the form

$$R_3^s(y_{cut}) = A_3^s(y_{cut})\tilde{\alpha}_s + [B_3^s(y_{cut}) + A_3^s(y_{cut})2\pi b_0 \ln f] \tilde{\alpha}_s^2, \quad (5.29)$$

while the ratio of four-jet events can be given as

$$R_4^s(y_{cut}) = B_4^s(y_{cut})\tilde{\alpha}_s^2, \quad (5.30)$$

where  $s$  denotes E-, E0-, P-, P0-, D-, and G-scheme. Then the 2-jet rate can be defined by  $R_2(y_{cut}) \equiv 1 - R_3(y_{cut}) - R_4(y_{cut})$ . The values of the function  $A_3(y_{cut})$  and  $B_4(y_{cut})$  are the same for the E-, E0-, P-, and P0-scheme. There is no dependence on these schemes in the leading order. The values of  $A_3(y_{cut})$  and  $B_4(y_{cut})$  for E-, E0-, P-, and P0-scheme are given in Table 5.5. The next-to-leading order corrections for tree-partons  $B_3(y_{cut})$  for these schemes are also given in Table 5.5. The histograms corresponding with the values in Table 5.5 are shown in Figs. 5.13 and 5.14, respectively. The values of  $A_3(y_{cut})$ ,  $B_3(y_{cut})$ , and  $B_4(y_{cut})$  for D- and G-scheme are shown in Table 5.6. Figures 5.15 and 5.16 show the functions of  $A_3(y_{cut})$ ,  $B_3(y_{cut})$ , and  $B_4(y_{cut})$  for D- and G-scheme.

The G-scheme has the wide negative region rather than the other schemes for the next-to-leading corrections of 3-parton. In Fig. 5.17-5.22 (a) the differential 2-jet rate predicted by the second order QCD for the six jet clustering schemes changing  $\Lambda_{\overline{MS}}$  and (b) its deviations from  $\Lambda_{\overline{MS}} = 200$  MeV. The dependences of the renormalization scale are also plotted in Fig. 5.17-5.22(c)(d).



$y_{cut}$	E, E0, P, P0		E	E0	P	P0	E, E0, P, P0	
	$A_3(y_{cut})$	$B_3(y_{cut})$	$B_3(y_{cut})$	$B_3(y_{cut})$	$B_3(y_{cut})$	$B_3(y_{cut})$	$B_4(y_{cut})$	
0.01	37.238	593.948	9.932	-219.994	-204.669	334.784		
0.02	24.353	566.729	237.043	72.939	100.815	116.578		
0.03	18.095	479.362	253.045	124.764	152.370	52.412		
0.04	14.215	402.483	233.249	128.126	154.346	25.991		
0.05	11.521	339.652	206.784	118.089	143.046	13.418		
0.06	9.526	288.465	180.804	104.470	128.402	6.985		
0.07	7.983	246.383	157.206	90.562	113.654	3.581		
0.08	6.753	211.411	136.344	77.534	99.907	1.769		
0.09	5.751	182.050	118.089	65.765	87.489	0.820		
0.10	4.920	157.181	102.171	55.322	76.428	0.343		
0.11	4.222	135.954	88.299	46.147	66.642	0.118		
0.12	3.629	117.719	76.203	38.135	58.008	0.019		
0.13	3.122	101.969	65.645	31.170	50.398			
0.14	2.684	88.301	56.420	25.139	43.690			
0.15	2.305	76.395	48.353	19.938	37.775			
0.16	1.975	65.992	41.294	15.471	32.556			
0.17	1.687	56.880	35.118	11.656	27.947			
0.18	1.435	48.882	29.715	8.419	23.875			
0.19	1.214	41.853	24.993	5.696	20.274			
0.20	1.019	35.670	20.872	3.431	17.090			
0.21	0.849	30.229	17.283	1.573	14.273			
0.22	0.699	25.443	14.167	0.079	11.781			
0.23	0.568	21.235	11.473	-1.088	9.577			
0.24	0.453	17.540	9.154	-1.963	7.628			
0.25	0.354	14.302	7.171	-2.576	5.906			
0.26	0.267	11.471	5.490	-2.954	4.386			
0.27	0.192	9.006	4.079	-3.118	3.046			
0.28	0.128	6.869	2.912	-3.092	1.866			
0.29	0.074	5.026	1.965	-2.892	0.828			
0.30	0.028	3.448	1.215	-2.537	-0.082			
0.31		2.109	0.644	-2.040	-0.878			
0.32		0.987	0.235	-1.416	-1.573			
0.33		0.061	-0.027	-0.677	-2.177			

Table 5.5. Coefficients of the  $\bar{\alpha}_s$  and  $\bar{\alpha}_s^2$  terms for 3-jet rate ( $R_3$ ) and 4-jet rate ( $R_4$ ) calculated in E-, E0-, P-, and P0-scheme.

$y_{cut}$	D-scheme			G-scheme		
	$A_3(y_{cut})$	$B_3(y_{cut})$	$B_4(y_{cut})$	$A_3(y_{cut})$	$B_3(y_{cut})$	$B_4(y_{cut})$
0.01	15.709	122.921	83.984			
0.02	10.209	116.725	28.021	34.511	-664.349	750.938
0.03	7.606	97.983	12.102	26.760	-297.560	435.257
0.04	6.001	81.631	5.765	21.791	-130.236	277.089
0.05	4.887	68.351	2.860	18.235	-43.312	185.741
0.06	4.059	57.591	1.434	15.525	4.664	128.483
0.07	3.415	48.791	0.714	13.372	31.627	90.657
0.08	2.900	41.513	0.349	11.612	46.449	64.760
0.09	2.478	35.433	0.165	10.141	53.934	46.584
0.10	2.127	30.309	0.071	8.893	56.857	33.602
0.11	1.830	25.957		7.820	56.907	24.222
0.12	1.576	22.239		6.887	55.143	17.394
0.13	1.359	19.044		6.069	52.255	12.408
0.14	1.170	16.287		5.348	48.697	8.768
0.15	1.006	13.899		4.707	44.778	6.121
0.16	0.863	11.826		4.136	40.704	4.210
0.17	0.737	10.022		3.624	36.619	2.845
0.18	0.627	8.450		3.164	32.619	1.887
0.19	0.530	7.079		2.749	28.771	1.228
0.20	0.444	5.883		2.374	25.120	0.787
0.21	0.369	4.840		2.035	21.692	0.502
0.22	0.303	3.932		1.727	18.507	0.325
0.23	0.246	3.142		1.448	15.573	0.217
0.24	0.195	2.457		1.194	12.894	
0.25	0.151	1.865		0.964	10.470	
0.26	0.113	1.357		0.754	8.298	
0.27	0.081	0.922		0.563	6.374	
0.28	0.053	0.553		0.390	4.689	
0.29	0.029	0.243		0.233	3.239	
0.30	0.010	-0.014		0.090	2.013	
0.31	-0.006	-0.223		-0.039	1.005	
0.32	-0.018	-0.389		-0.156	0.205	
0.33	-0.027	-0.516		-0.261	-0.394	

Table 5.6. Coefficients of the  $\bar{\alpha}_s$  and  $\bar{\alpha}_s^2$  terms for 3-jet rate ( $R_3$ ) and 4-jet rate ( $R_4$ ) calculated in D- and G-scheme.

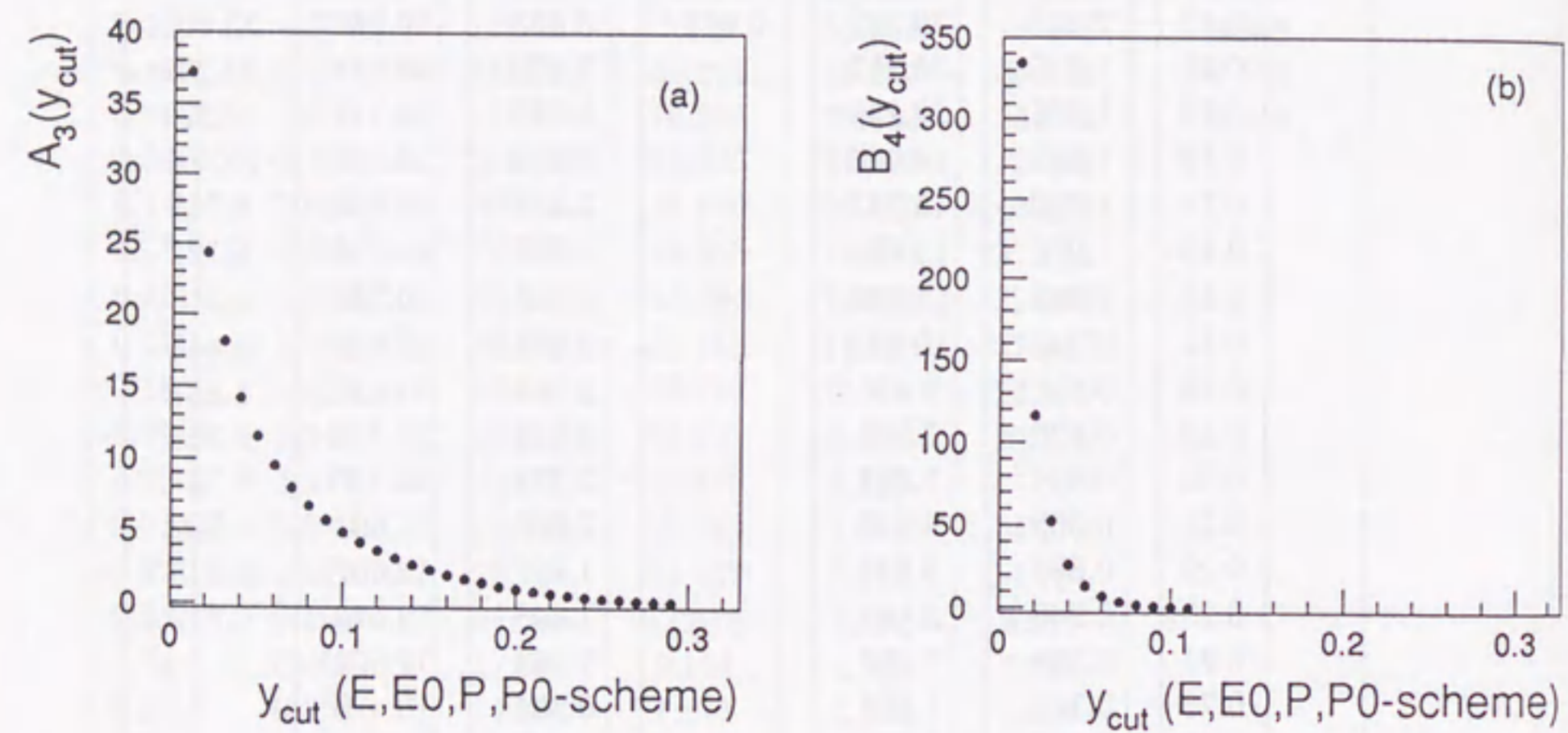


Fig. 5.13. Plots for the function (a)  $A_3(y_{cut})$  and (b)  $B_4(y_{cut})$  for E-, E0-, P-, and P0-scheme.

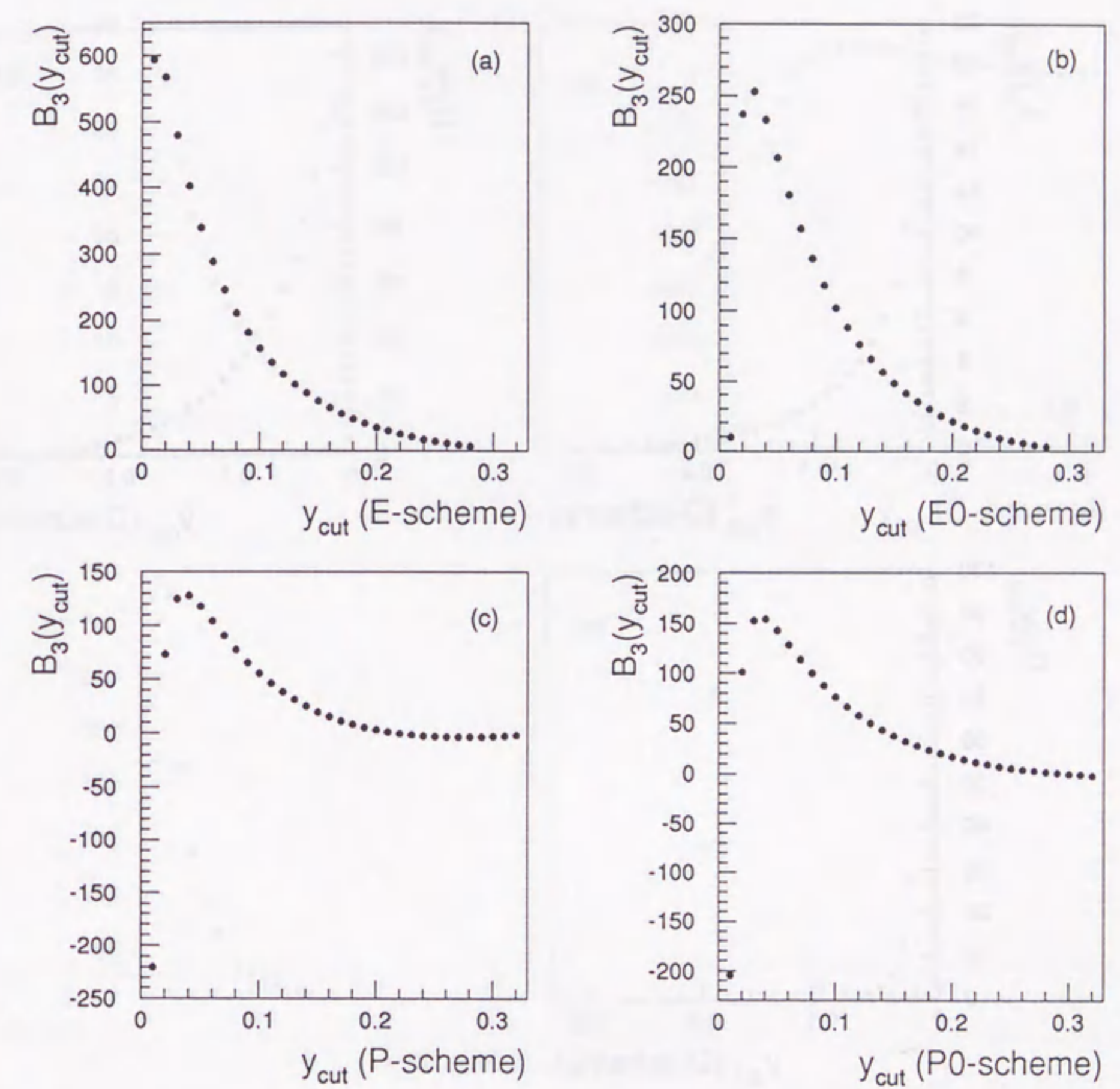


Fig. 5.14. Plots for the function  $B_3(y_{cut})$  for (a) E-, (b) E0-, (c) P-, and (d) P0-scheme.

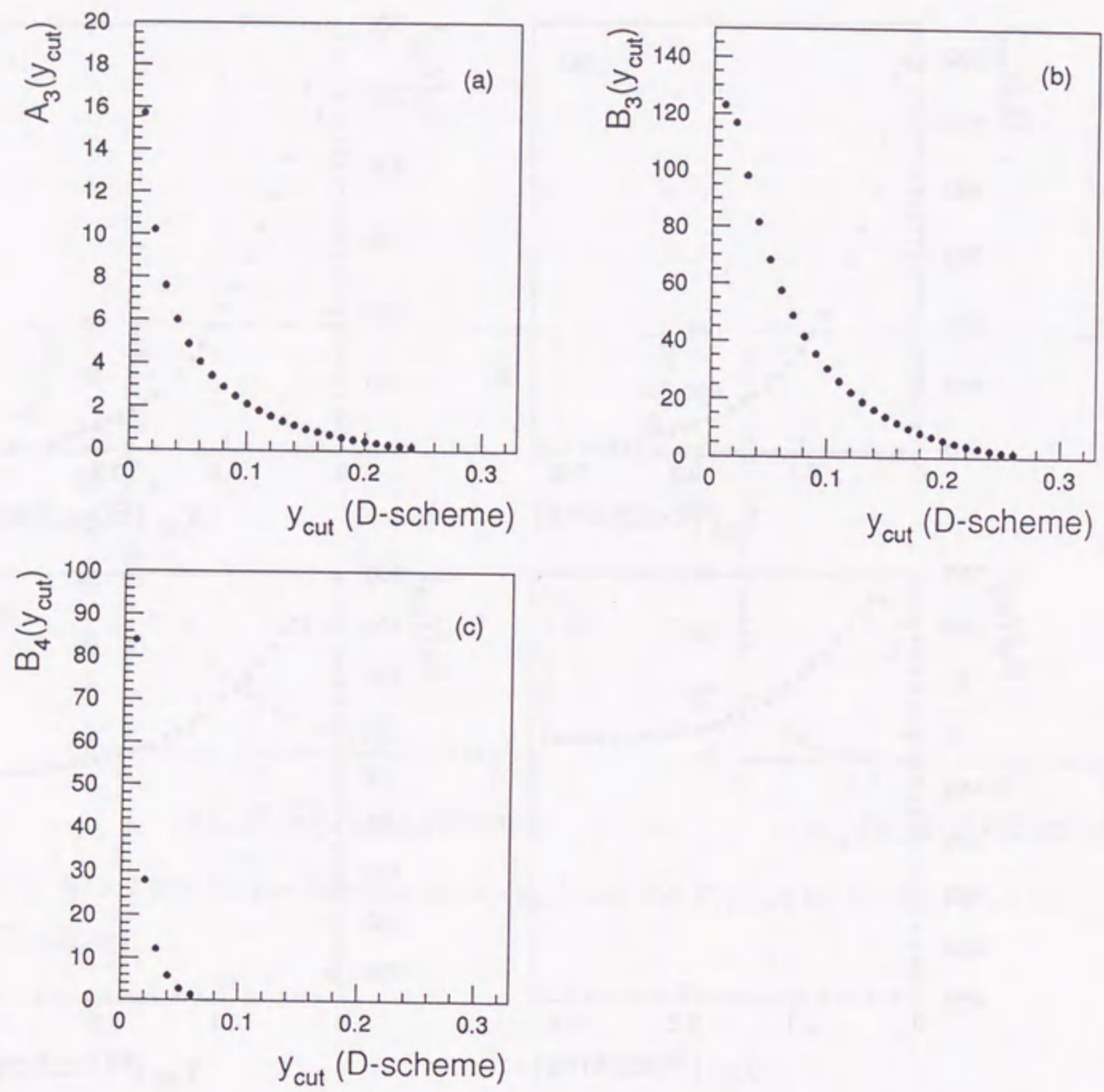


Fig. 5.15. Plots for the function (a)  $A_3(y_{cut})$ , (b)  $B_3(y_{cut})$ , and (c)  $B_4(y_{cut})$  for D-scheme.

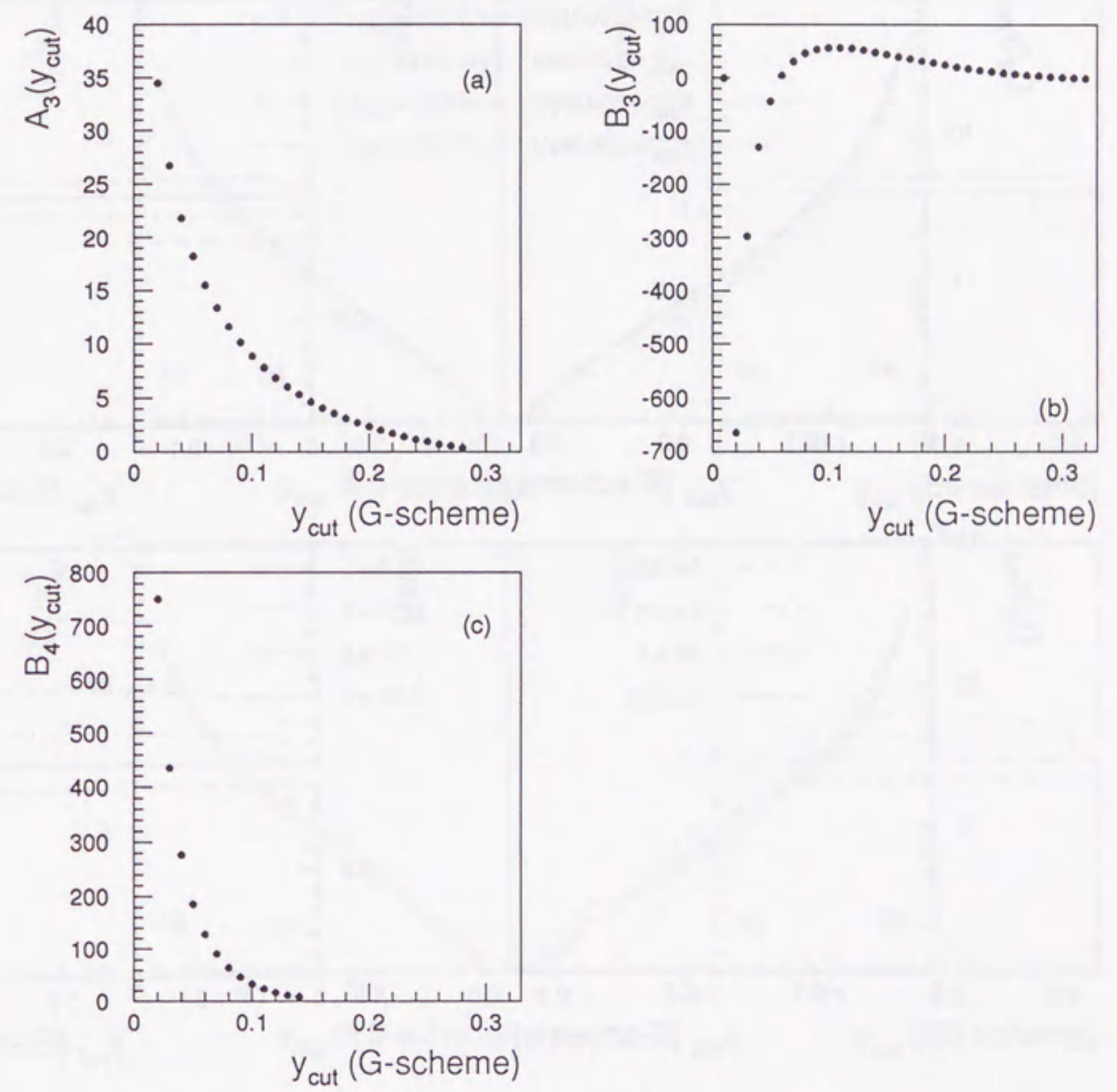


Fig. 5.16. Plots for the function (a)  $A_3(y_{cut})$ , (b)  $B_3(y_{cut})$ , and (c)  $B_4(y_{cut})$  for G-scheme.

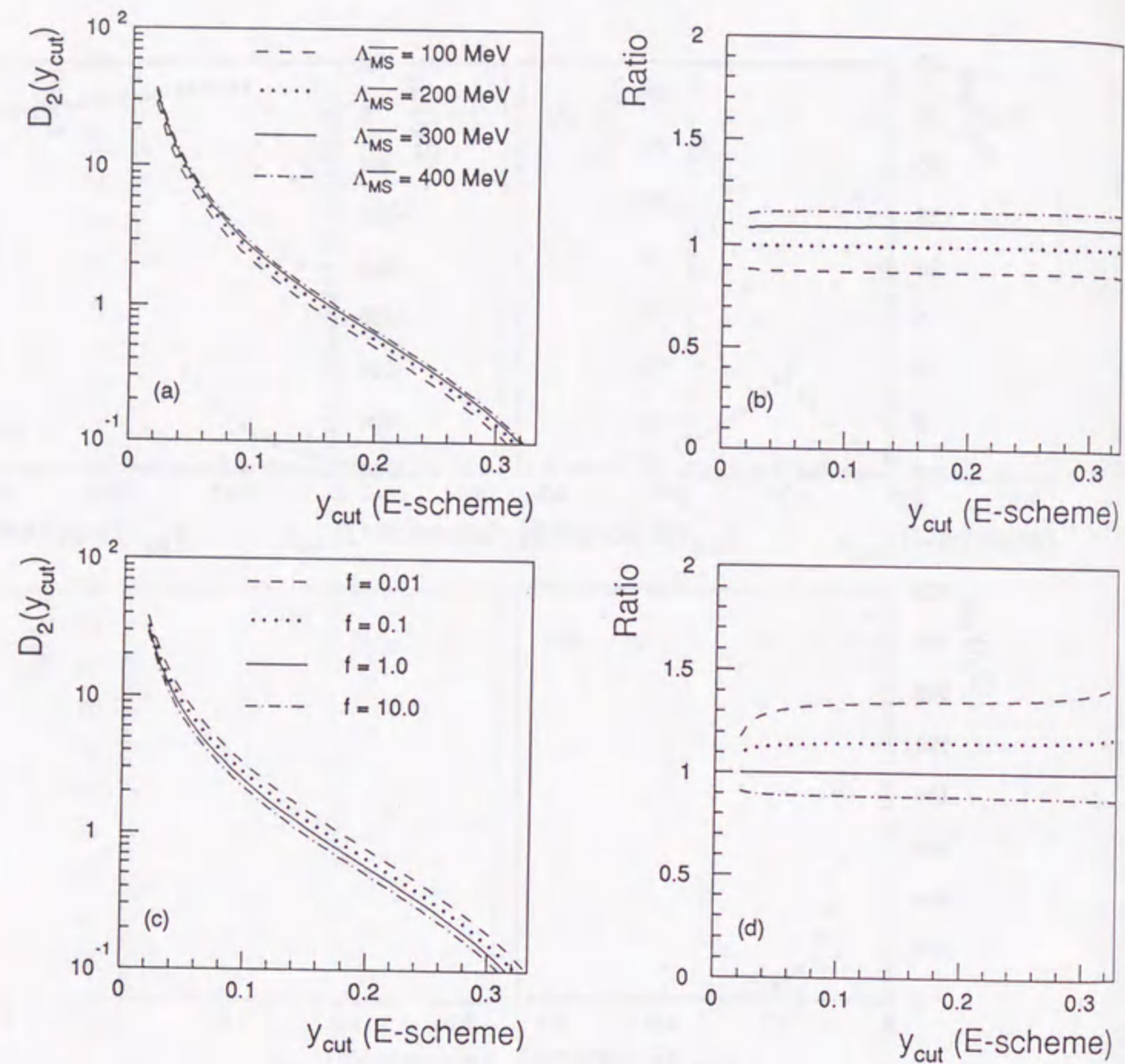


Fig. 5.17. Differential 2-jet rate with the E-scheme using up to  $\mathcal{O}(\alpha_s^2)$  QCD at  $\sqrt{s} = 91.2$  GeV. (a) Dependence of  $\Lambda_{\overline{MS}}$  and (b) deviation from the case of  $\Lambda_{\overline{MS}} = 200$  MeV at  $f = 1$ . (c) Dependence of  $f$  and (d) deviation from the case of  $f = 1$ .

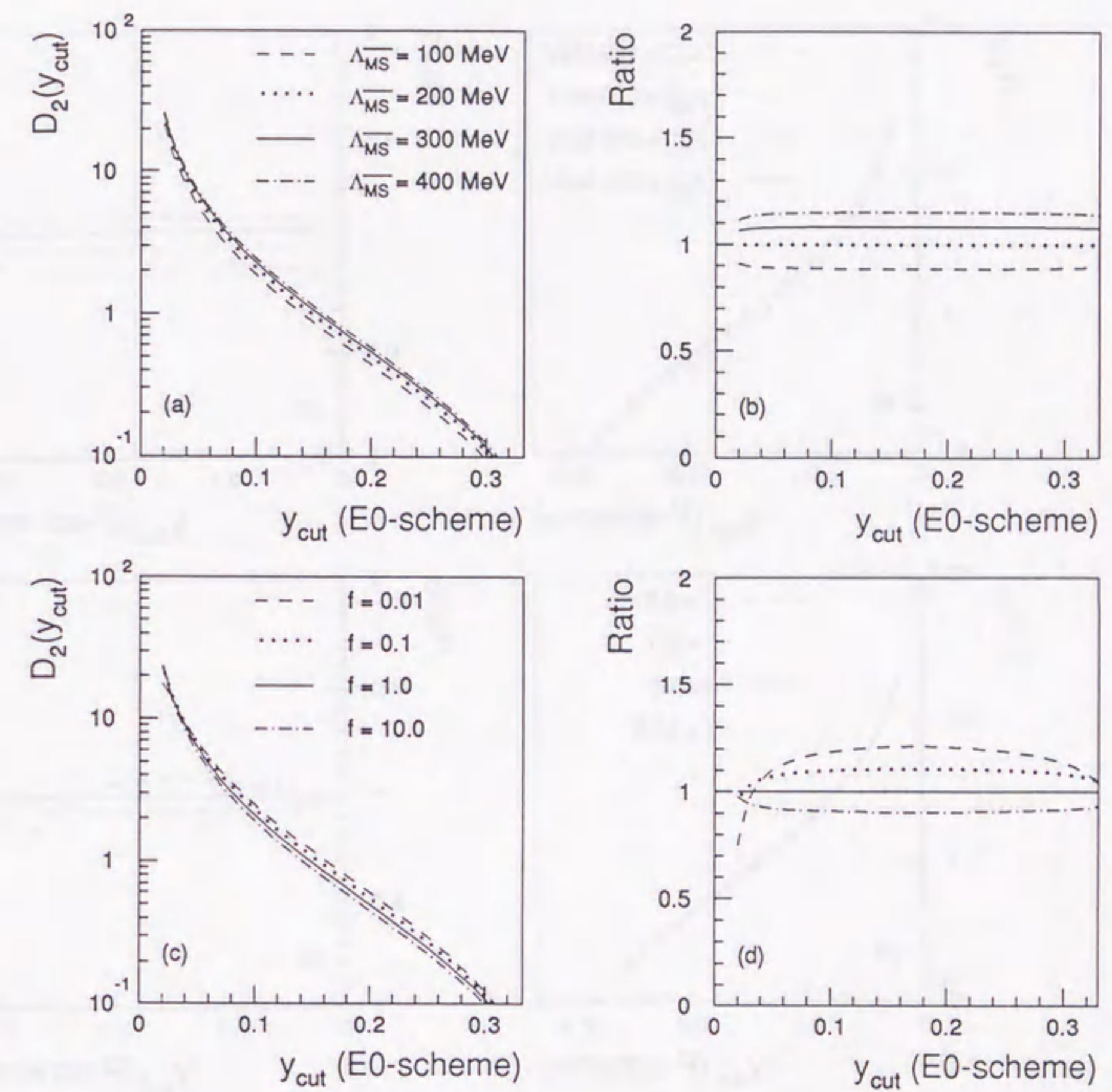


Fig. 5.18. Differential 2-jet rate with the E0-scheme using up to  $\mathcal{O}(\alpha_s^2)$  QCD at  $\sqrt{s} = 91.2$  GeV. (a) Dependence of  $\Lambda_{\overline{MS}}$  and (b) deviation from the case of  $\Lambda_{\overline{MS}} = 200$  MeV at  $f = 1$ . (c) Dependence of  $f$  and (d) deviation from the case of  $f = 1$ .

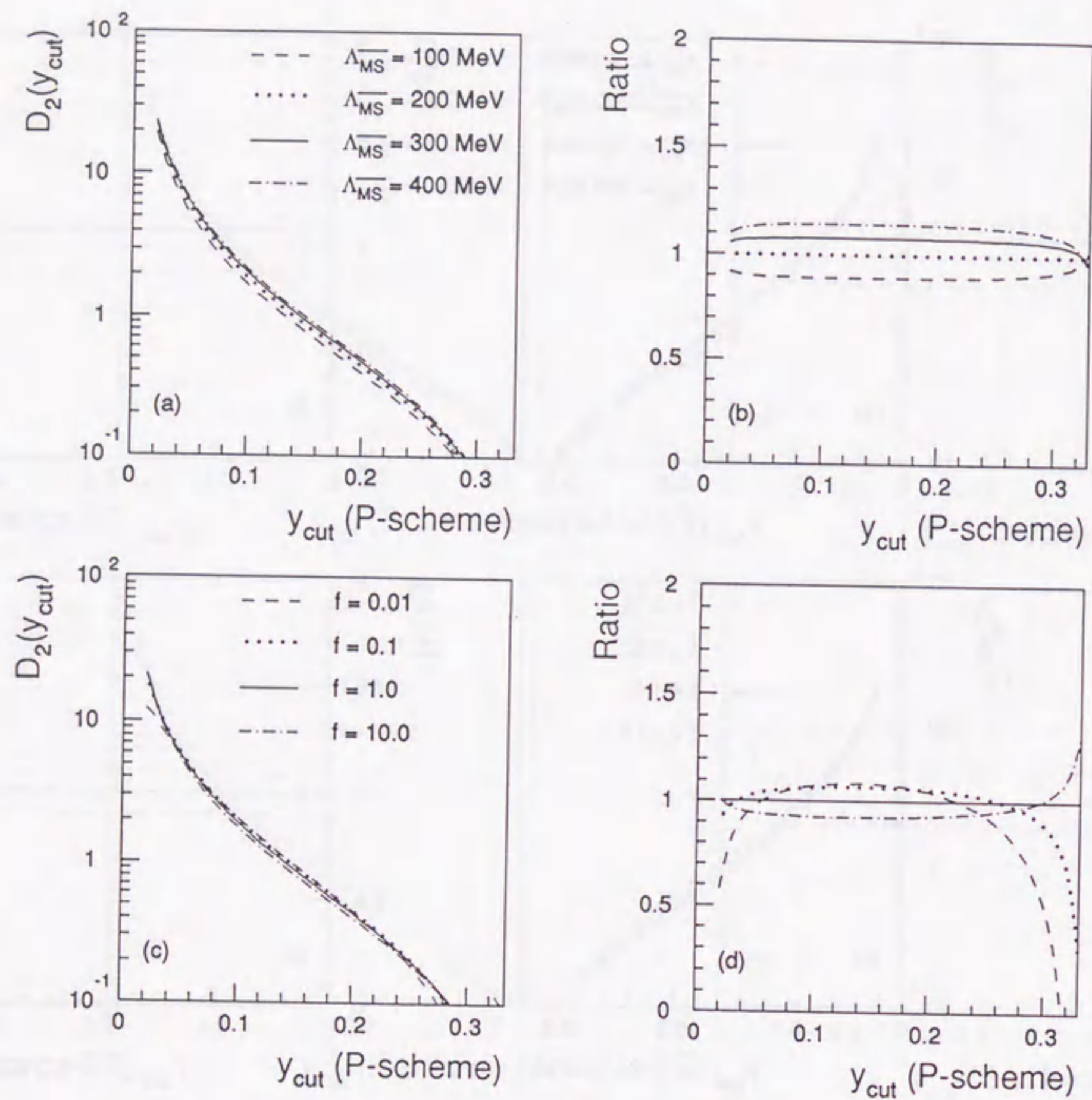


Fig. 5.19. Differential 2-jet rate with the P-scheme using up to  $\mathcal{O}(\alpha_s^2)$  QCD at  $\sqrt{s} = 91.2$  GeV. (a) Dependence of  $\Lambda_{\overline{MS}}$  and (b) deviation from the case of  $\Lambda_{\overline{MS}} = 200$  MeV at  $f = 1$ . (c) Dependence of  $f$  and (d) deviation from the case of  $f = 1$ .

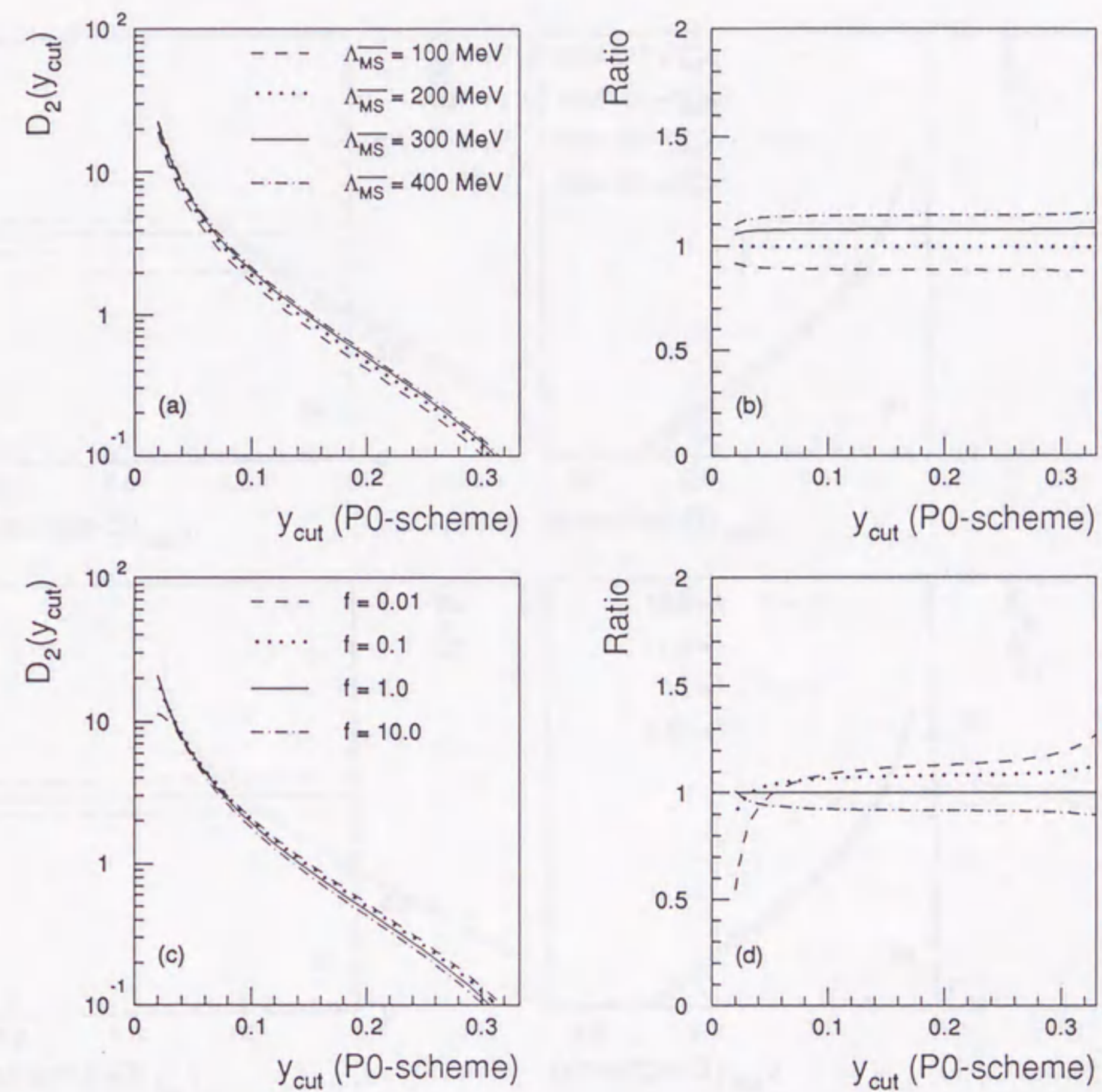


Fig. 5.20. Differential 2-jet rate with the P0-scheme using up to  $\mathcal{O}(\alpha_s^2)$  QCD at  $\sqrt{s} = 91.2$  GeV. (a) Dependence of  $\Lambda_{\overline{MS}}$  and (b) deviation from the case of  $\Lambda_{\overline{MS}} = 200$  MeV at  $f = 1$ . (c) Dependence of  $f$  and (d) deviation from the case of  $f = 1$ .

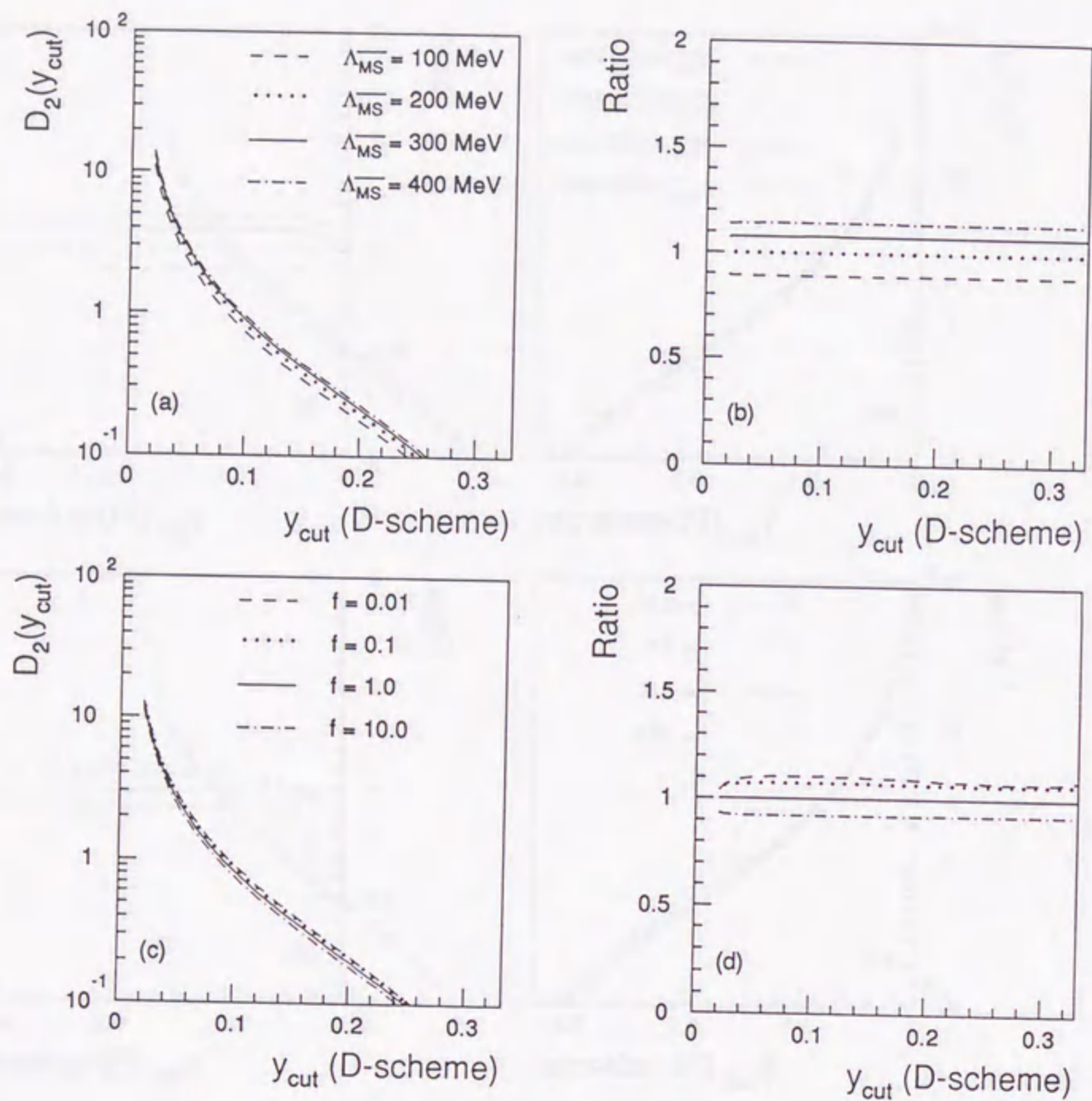


Fig. 5.21. Differential 2-jet rate with the D-scheme using up to  $\mathcal{O}(\alpha_s^2)$  QCD at  $\sqrt{s} = 91.2$  GeV. (a) Dependence of  $\Lambda_{\overline{MS}}$  and (b) deviation from the case of  $\Lambda_{\overline{MS}} = 200$  MeV at  $f = 1$ . (c) Dependence of  $f$  and (d) deviation from the case of  $f = 1$ .

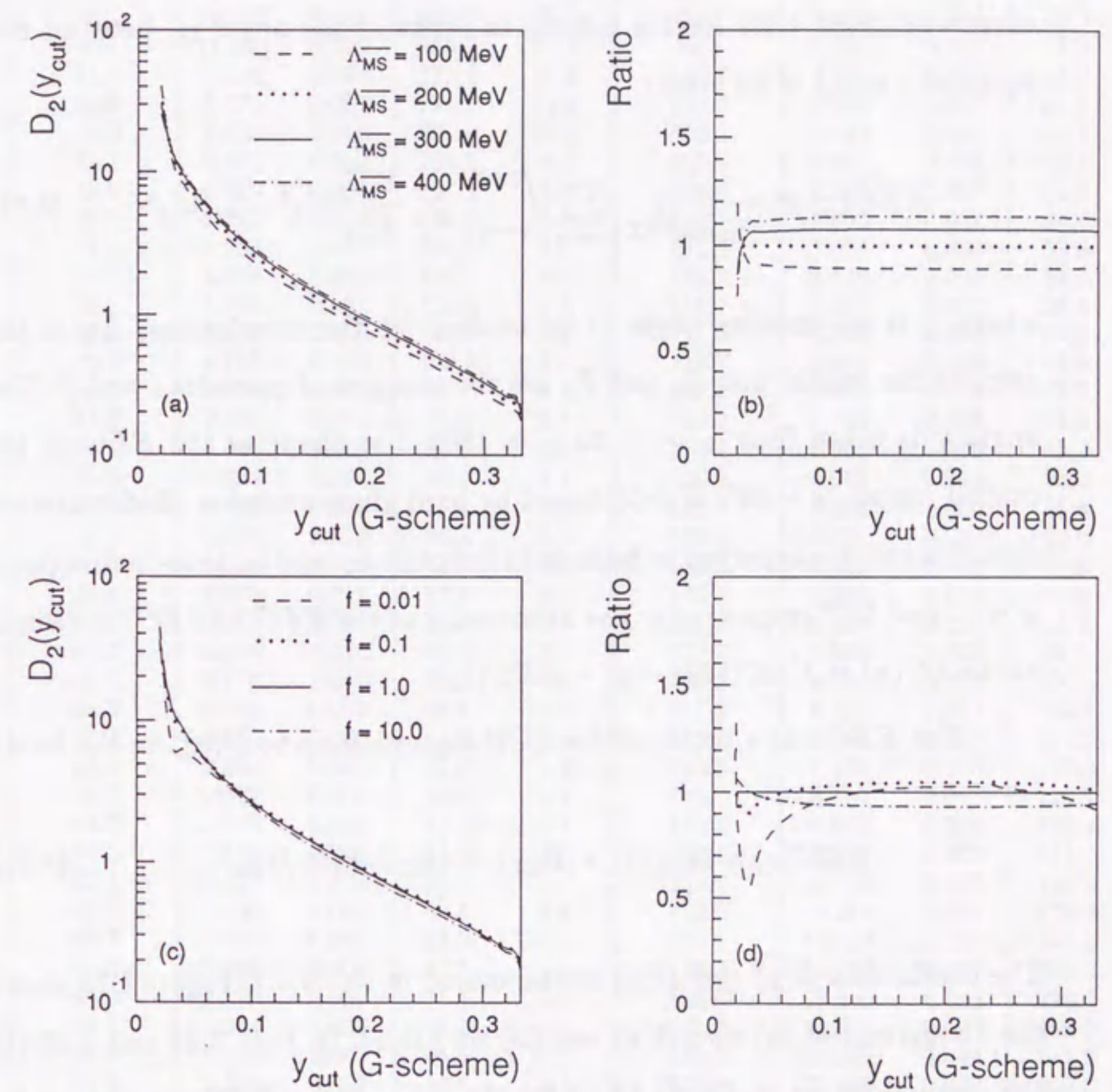


Fig. 5.22. Differential 2-jet rate with the G-scheme using up to  $\mathcal{O}(\alpha_s^2)$  QCD at  $\sqrt{s} = 91.2$  GeV. (a) Dependence of  $\Lambda_{\overline{MS}}$  and (b) deviation from the case of  $\Lambda_{\overline{MS}} = 200$  MeV at  $f = 1$ . (c) Dependence of  $f$  and (d) deviation from the case of  $f = 1$ .

### 5.3 Particle Correlations

Hadronic event observables can also be classified in terms of inclusive two-particle correlations. The energy-energy correlation ( $EEC$ )<sup>22</sup> is the normalized energy-weighted cross section defined in terms of the angle  $\chi_{ij}$  between two particles  $i$  and  $j$  in an event:

$$EEC(\chi) \equiv \frac{1}{N_{events} \Delta\chi} \sum_{events} \int_{\chi-\frac{\Delta\chi}{2}}^{\chi+\frac{\Delta\chi}{2}} \sum_{ij} \frac{E_i E_j}{E_{vis}^2} \delta(\chi' - \chi_{ij}) d\chi' \quad (5.31)$$

where  $\chi$  is an opening angle to be studied for the correlations,  $\Delta\chi$  is the angular bin width, and  $E_i$  and  $E_j$  are the energies of particles  $i$  and  $j$ . The angle  $\chi$  is taken from  $\chi = 0^\circ$  to  $\chi = 180^\circ$ . The shape of the  $EEC$  in the central region,  $\chi \sim 90^\circ$ , is determined by hard gluon emission. Hadronization contributions are expected to be large in the collinear and back-to-back regions,  $\chi \sim 0^\circ$  and  $180^\circ$  respectively. The asymmetry of the  $EEC$  ( $AEEC$ ) is defined as  $AEEC(\chi) = EEC(180^\circ - \chi) - EEC(\chi)$ .

The  $EEC$  has a perturbative QCD expansion up to  $\mathcal{O}(\alpha_s^2)$  in the form:

$$EEC(\chi) = A(\chi)\bar{\alpha}_s + [B(\chi) + A(\chi)2\pi b_0 \ln f] \bar{\alpha}_s^2. \quad (5.32)$$

The coefficients  $A(\chi)$  and  $B(\chi)$  are tabulated in Table 5.7. Figure 5.23 shows the histograms of (a)  $\sin \chi A(\chi)$  and (b)  $\sin \chi B(\chi)$ . In Figs. 5.24 and 5.25 (a) the predictions up to  $\mathcal{O}(\alpha_s^2)$  QCD for the  $EEC$  and  $AEEC$  are plotted for energy scale  $\sqrt{s} = M_Z = 91.2$  GeV at four different values of  $\Lambda_{\overline{MS}} = 100, 200, 300,$  and  $400$  MeV at  $f = 1$ , and (b) deviations for  $\Lambda_{\overline{MS}} = 100, 300,$  and  $400$  MeV from  $\Lambda_{\overline{MS}} = 200$  MeV at  $f = 1$ . Figures 5.24 and 5.25 also show (c) the predictions for energy scale  $\sqrt{s} = M_Z = 91.2$  GeV at four different values of  $f = 0.01, 0.1, 1.0,$  and  $10.0$  at  $\Lambda_{\overline{MS}} = 200$  MeV, and (d) deviations for  $f = 0.01, 0.1,$  and  $10.0$  from  $f = 1.0$ .

$\chi$ (deg.)	$A(\chi)$	$\Delta A(\chi)$	$B(\chi)$	$\Delta B(\chi)$	$\chi$ (deg.)	$A(\chi)$	$\Delta A(\chi)$	$B(\chi)$	$\Delta B(\chi)$
0.9	—	—	—	—	90.9	2.444	0.007	44.5	1.3
2.7	44.754	0.712	1984.0	901.3	92.7	2.476	0.007	44.0	1.5
4.5	26.121	0.305	1026.0	174.1	94.5	2.508	0.007	46.6	1.5
6.3	18.380	0.180	609.5	59.5	96.3	2.530	0.006	46.9	1.4
8.1	14.312	0.122	485.6	36.0	98.1	2.569	0.006	45.3	1.3
9.9	11.694	0.090	388.5	26.1	99.9	2.610	0.007	47.8	1.3
11.7	9.924	0.070	313.4	19.5	101.7	2.655	0.007	45.9	2.4
13.5	8.571	0.057	274.1	12.8	103.5	2.699	0.007	50.5	2.3
15.3	7.523	0.046	221.8	10.9	105.3	2.754	0.007	52.6	2.7
17.1	6.807	0.040	206.5	9.2	107.1	2.820	0.007	50.7	1.4
18.9	6.262	0.034	168.2	7.8	108.9	2.893	0.007	51.9	1.3
20.7	5.720	0.031	149.0	5.8	110.7	2.962	0.007	54.4	1.6
22.5	5.264	0.027	155.2	8.6	112.5	3.038	0.007	53.6	1.6
24.3	4.905	0.024	130.0	5.0	114.3	3.146	0.007	54.7	1.4
26.1	4.588	0.022	121.8	4.3	116.1	3.237	0.007	58.5	2.8
27.9	4.316	0.020	114.8	5.4	117.9	3.328	0.008	57.4	1.9
29.7	4.123	0.018	105.3	4.5	119.7	3.453	0.008	61.5	1.7
31.5	3.916	0.017	94.7	3.1	121.5	3.602	0.008	63.6	1.7
33.3	3.721	0.015	91.0	3.1	123.3	3.735	0.008	64.0	1.7
35.1	3.564	0.014	92.8	4.8	125.1	3.906	0.009	65.2	1.9
36.9	3.402	0.014	91.3	5.7	126.9	4.069	0.009	73.0	4.8
38.7	3.299	0.013	74.5	2.5	128.7	4.265	0.009	78.4	1.9
40.5	3.180	0.012	76.4	3.5	130.5	4.500	0.010	79.6	5.0
42.3	3.086	0.011	70.7	2.4	132.3	4.710	0.010	77.3	2.0
44.1	3.002	0.011	67.3	2.2	134.1	4.976	0.011	85.8	2.8
45.9	2.918	0.011	70.0	2.8	135.9	5.289	0.011	88.9	2.2
47.7	2.841	0.010	62.6	2.0	137.7	5.626	0.012	92.1	2.4
49.5	2.778	0.010	63.9	4.9	139.5	6.005	0.013	100.5	3.5
51.3	2.704	0.009	61.6	1.7	141.3	6.423	0.014	103.1	2.6
53.1	2.651	0.009	64.0	4.8	143.1	6.881	0.014	117.5	5.7
54.9	2.608	0.008	55.9	1.9	144.9	7.448	0.015	129.0	5.0
56.7	2.558	0.008	56.0	1.7	146.7	8.119	0.017	126.1	3.3
58.5	2.530	0.008	52.2	1.7	148.5	8.869	0.018	139.9	3.3
60.3	2.486	0.008	54.0	1.5	150.3	9.689	0.020	151.0	4.6
62.1	2.457	0.008	51.2	1.8	152.1	10.760	0.022	156.9	5.4
63.9	2.436	0.007	50.4	2.8	153.9	11.986	0.025	179.0	4.5
65.7	2.413	0.007	48.3	1.4	155.7	13.424	0.027	196.1	5.2
67.5	2.396	0.007	47.7	1.5	157.5	15.206	0.031	216.9	8.8
69.3	2.370	0.007	51.4	1.6	159.3	17.349	0.035	226.2	6.4
71.1	2.354	0.007	49.2	1.3	161.1	20.025	0.041	256.2	8.3
72.9	2.351	0.007	46.5	1.2	162.9	23.560	0.049	275.2	9.8
74.7	2.348	0.007	49.6	2.5	164.7	28.069	0.058	300.0	11.2
76.5	2.354	0.007	44.7	1.3	166.5	34.062	0.071	345.9	13.3
78.3	2.356	0.007	45.8	1.5	168.3	42.582	0.090	337.1	19.7
80.1	2.355	0.006	46.4	1.3	170.1	54.952	0.119	251.1	23.9
81.9	2.357	0.006	45.3	1.3	171.9	73.969	0.166	274.1	38.4
83.7	2.359	0.006	46.5	1.4	173.7	106.799	0.244	-235.4	54.6
85.5	2.381	0.006	44.9	1.4	175.5	174.695	0.427	-1449.5	178.8
87.3	2.401	0.006	43.5	1.4	177.3	361.594	1.029	-7999.8	403.1
89.1	2.424	0.006	46.4	1.3	179.1	—	—	—	—

Table 5.7. Coefficients of the  $\bar{\alpha}_s$  and  $\bar{\alpha}_s^2$  terms for  $EEC$ .

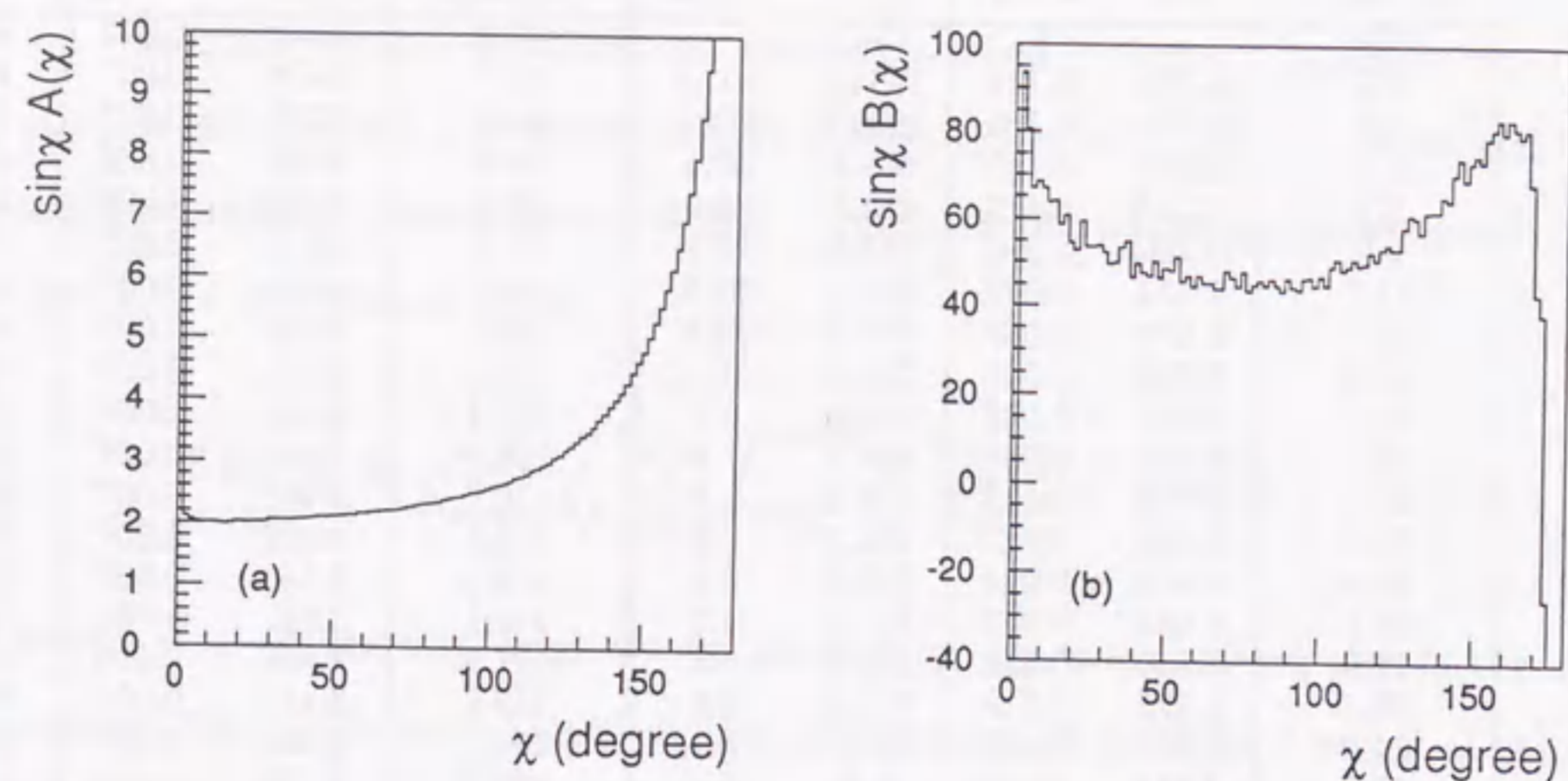


Fig. 5.23. Histograms for the function (a)  $\sin \chi A(\chi)$  and (b)  $\sin \chi B(\chi)$  of the  $EEC$ .

#### 5.4 Angular Energy Flow

Another procedure, related to the angle of particle emission, is to integrate the energy within a conical shell of opening angle  $\chi$  about the thrust axis. Here we define the *Jet Cone Energy Fraction* ( $JCEF$ )<sup>57</sup>:

$$JCEF(\chi) = \frac{1}{N_{events} \Delta \chi} \sum_{events} \int_{\chi - \frac{\Delta \chi}{2}}^{\chi + \frac{\Delta \chi}{2}} \sum_i \frac{E_i}{E_{vis}} \delta(\chi' - \chi_i) d\chi', \quad (5.33)$$

where

$$\chi_i = \arccos \left( \frac{\vec{p}_i \cdot \vec{n}_T}{|\vec{p}_i|} \right), \quad (5.34)$$

is the opening angle between a particle and the thrust axis vector,  $\vec{n}_T$ , whose direction is defined to point from the heavy jet mass hemisphere to the light jet mass hemisphere, and  $0^\circ \leq \chi \leq 180^\circ$ . Hard gluon emissions contribute to the region corresponding to the heavy jet mass hemisphere,  $90^\circ \leq \chi \leq 180^\circ$ . Schematic view of hadronic event is shown in Fig. 5.26.

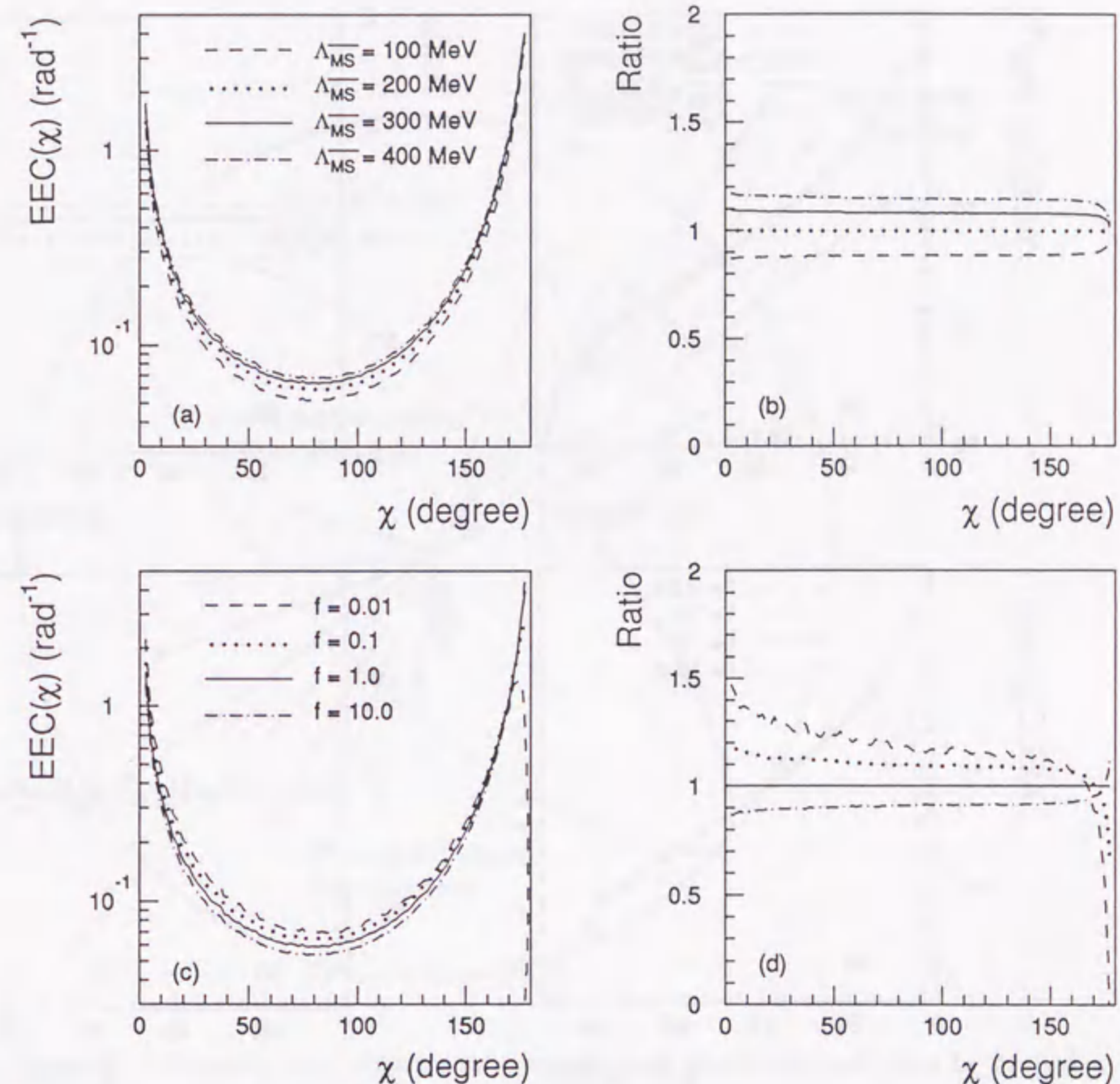


Fig. 5.24. Physical prediction up to  $\mathcal{O}(\alpha_s^2)$  for the  $EEC$  distribution at  $\sqrt{s} = 91.2$  GeV. (a) Dependence of  $\Lambda_{\overline{MS}}$  and (b) deviation from the case of  $\Lambda_{\overline{MS}} = 200$  MeV at  $f = 1$ . (c) Dependence of  $f$  and (d) deviation from the case of  $f = 1$ .



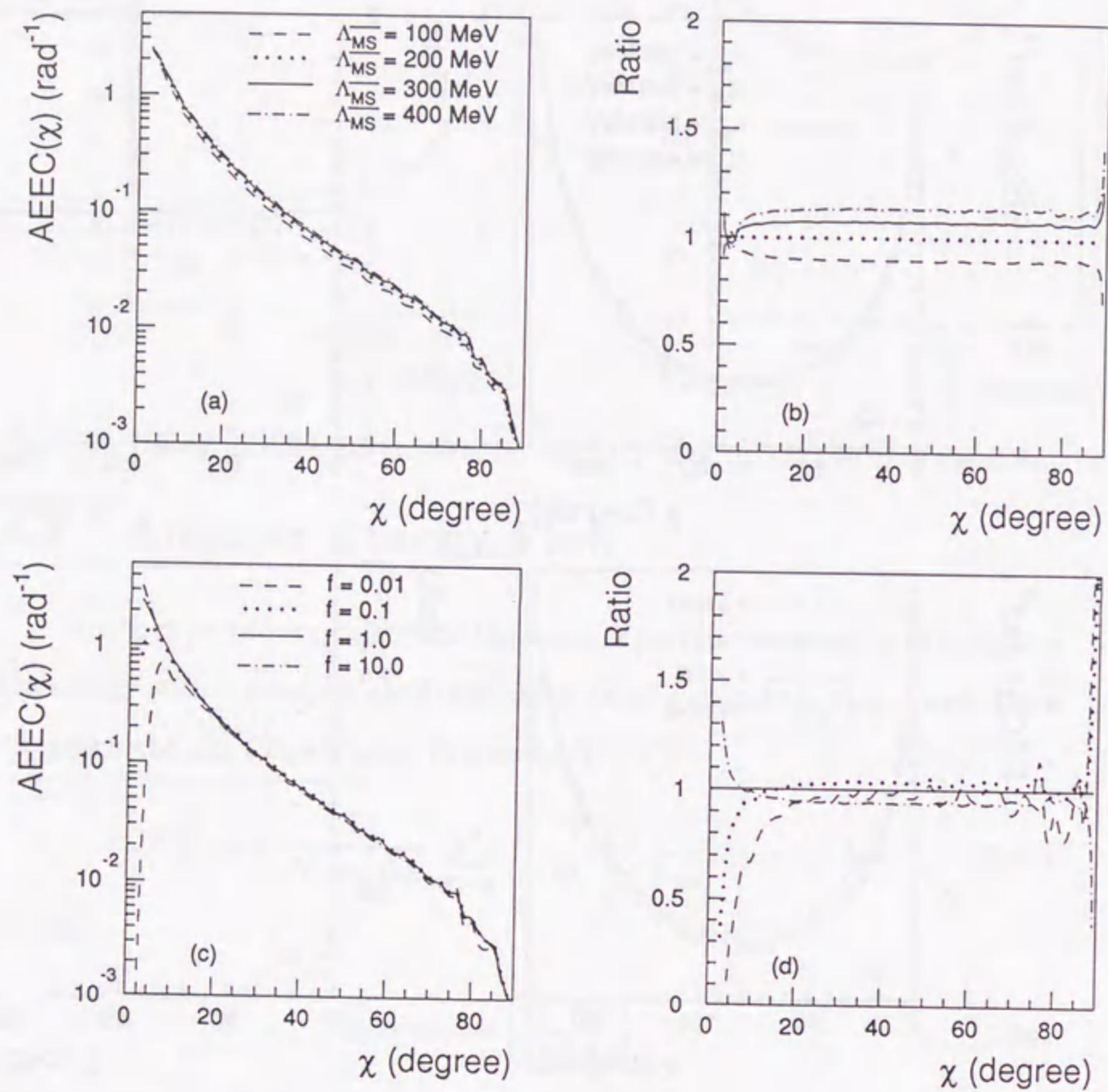


Fig. 5.25. Physical prediction up to  $\mathcal{O}(\alpha_s^2)$  for the  $AEEC$  distribution at  $\sqrt{s} = 91.2$  GeV. (a) Dependence of  $\Lambda_{\overline{MS}}$  and (b) deviation from the case of  $\Lambda_{\overline{MS}} = 200$  MeV at  $f = 1$ . (c) Dependence of  $f$  and (d) deviation from the case of  $f = 1$ .

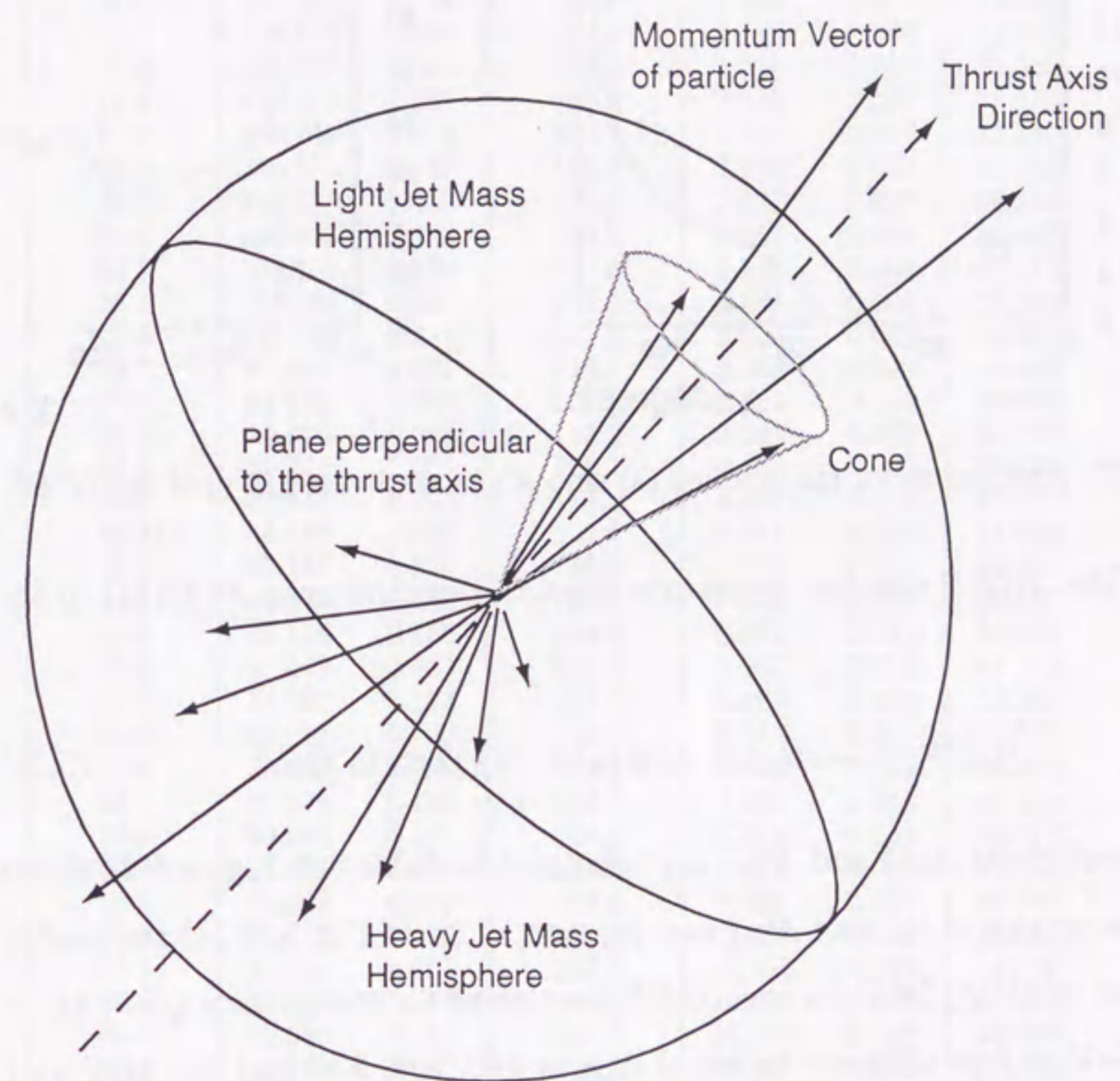


Fig. 5.26. Schematic view of hadronic event. Thrust axis is also indicated by dashed line. Direction of the thrust axis vector is defined to point from the heavy jet mass hemisphere to the light jet mass hemisphere in this thesis.

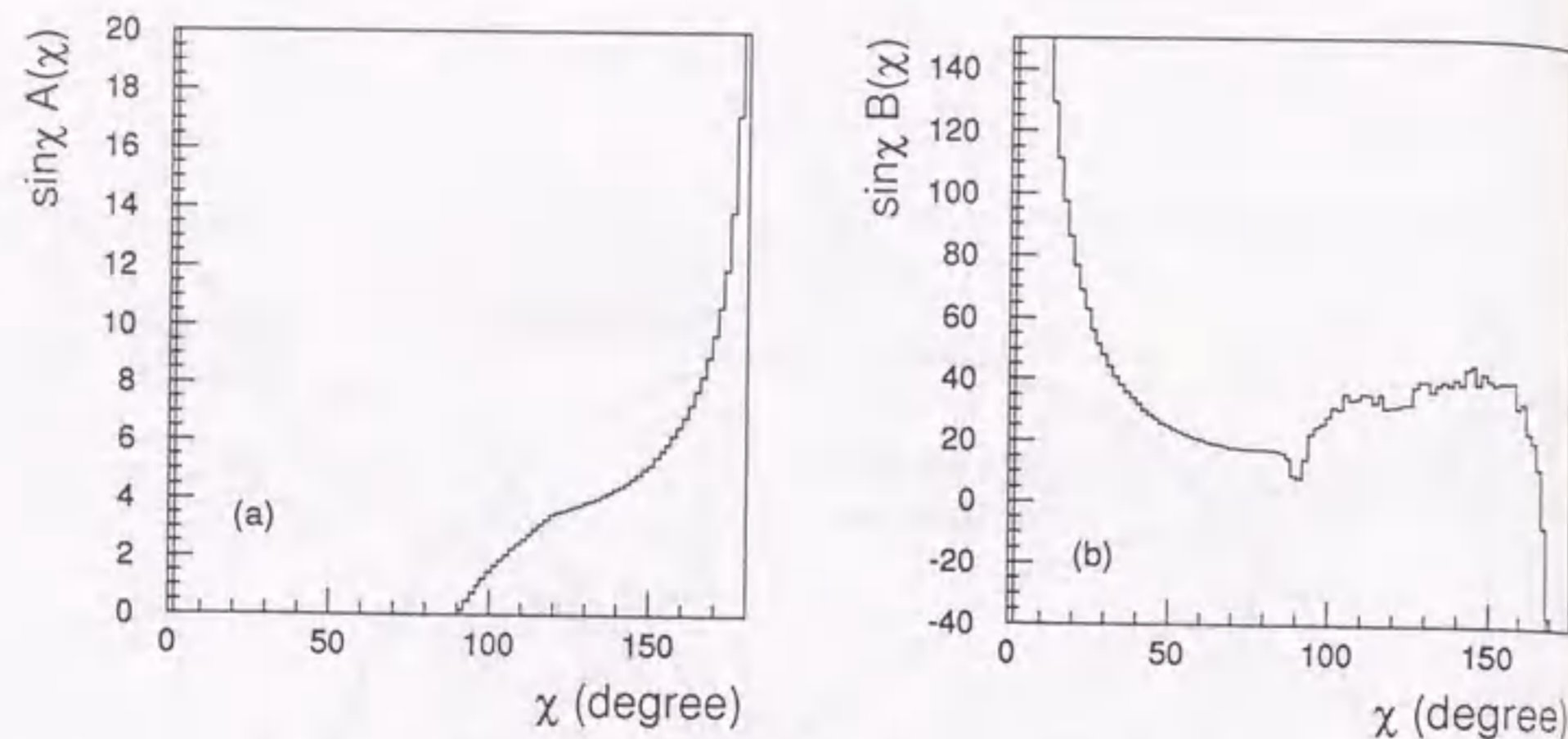


Fig. 5.27. Histograms for the function (a)  $\sin \chi A(\chi)$  and (b)  $\sin \chi B(\chi)$  of the *JCEF*.

The *JCEF* also has a perturbative QCD expansion up to  $\mathcal{O}(\alpha_s^2)$  in the form:

$$JCEF(\chi) = A(\chi)\bar{\alpha}_s + [B(\chi) + A(\chi)2\pi b_0 \ln f] \bar{\alpha}_s^2. \quad (5.35)$$

The coefficients  $A(\chi)$  and  $B(\chi)$  are tabulated in Table 5.8. Figure 5.27 shows the histograms of (a)  $\sin \chi A(\chi)$  and (b)  $\sin \chi B(\chi)$ . In Fig. 5.28 (a) the predictions up to  $\mathcal{O}(\alpha_s^2)$  QCD for the *JCEF* are plotted for energy scale  $\sqrt{s} = M_Z = 91.2$  GeV at four different values of  $\Lambda_{\overline{MS}} = 100, 200, 300,$  and  $400$  MeV at  $f = 1$ , and (b) deviations for  $\Lambda_{\overline{MS}} = 100, 300,$  and  $400$  MeV from  $\Lambda_{\overline{MS}} = 200$  MeV at  $f = 1$ . Figure 5.28 also shows (c) the predictions for energy scale  $\sqrt{s} = M_Z = 91.2$  GeV at four different values of  $f = 0.01, 0.1, 1.0,$  and  $10.0$  at  $\Lambda_{\overline{MS}} = 200$  MeV, and (d) deviations for  $f = 0.01, 0.1,$  and  $10.0$  from  $f = 1.0$ .

$\chi$ (deg.)	$B(\chi)$	$\Delta B(\chi)$	$\chi$ (deg.)	$A(\chi)$	$\Delta A(\chi)$	$B(\chi)$	$\Delta B(\chi)$
0.9	—	—	90.9	0.164	0.002	7.928	0.898
2.7	14968.3	217.0	92.7	0.475	0.004	14.308	1.174
4.5	5338.25	53.06	94.5	0.752	0.005	22.446	1.281
6.3	2720.98	18.85	96.3	1.016	0.005	24.989	1.275
8.1	1633.50	11.97	98.1	1.263	0.006	26.111	1.137
9.9	1062.26	5.741	99.9	1.495	0.006	28.895	1.227
11.7	765.472	10.58	101.7	1.717	0.006	32.016	1.457
13.5	553.248	3.003	103.5	1.926	0.007	31.562	1.262
15.3	420.379	2.057	105.3	2.137	0.007	36.979	2.602
17.1	330.769	1.812	107.1	2.353	0.007	35.150	1.229
18.9	265.279	1.412	108.9	2.570	0.007	36.021	1.245
20.7	216.693	1.089	110.7	2.777	0.007	38.124	1.546
22.5	180.596	1.383	112.5	2.987	0.008	38.481	1.497
24.3	152.407	2.359	114.3	3.235	0.008	36.174	1.313
26.1	127.483	0.487	116.1	3.466	0.008	39.769	2.723
27.9	110.180	0.511	117.9	3.698	0.008	35.049	1.799
29.7	97.231	1.637	119.7	3.963	0.008	36.283	1.530
31.5	84.454	0.366	121.5	4.152	0.009	36.953	1.595
33.3	74.370	0.281	123.3	4.289	0.009	38.737	1.579
35.1	66.520	0.251	125.1	4.468	0.009	39.760	1.839
36.9	59.645	0.253	126.9	4.637	0.009	47.781	4.800
38.7	54.145	0.239	128.7	4.841	0.010	51.052	1.767
40.5	49.166	0.340	130.5	5.087	0.010	52.278	4.969
42.3	44.674	0.158	132.3	5.304	0.011	49.667	1.924
44.1	41.138	0.166	134.1	5.582	0.011	54.039	2.668
45.9	37.672	0.133	135.9	5.907	0.012	57.342	2.062
47.7	34.922	0.112	137.7	6.257	0.013	57.960	2.315
49.5	32.681	0.127	139.5	6.652	0.013	62.727	3.372
51.3	30.562	0.129	141.3	7.093	0.014	62.590	2.439
53.1	28.671	0.133	143.1	7.569	0.015	73.442	5.608
54.9	26.946	0.101	144.9	8.159	0.016	79.252	4.874
56.7	25.491	0.091	146.7	8.852	0.018	71.620	3.078
58.5	24.213	0.099	148.5	9.631	0.019	82.093	3.069
60.3	23.222	0.109	150.3	10.479	0.021	81.658	3.543
62.1	22.070	0.065	152.1	11.585	0.023	84.317	5.200
63.9	21.297	0.112	153.9	12.846	0.026	90.906	4.230
65.7	20.626	0.112	155.7	14.324	0.028	96.887	4.399
67.5	19.761	0.065	157.5	16.152	0.032	105.264	8.497
69.3	19.142	0.071	159.3	18.352	0.037	90.321	5.787
71.1	18.753	0.068	161.1	21.079	0.042	103.774	7.758
72.9	18.352	0.051	162.9	24.683	0.050	81.440	9.254
74.7	18.105	0.051	164.7	29.267	0.060	79.09	10.62
76.5	17.888	0.048	166.5	35.340	0.073	52.85	12.58
78.3	17.785	0.062	168.3	43.957	0.091	-32.65	15.98
80.1	17.601	0.064	170.1	56.431	0.120	-210.72	23.28
81.9	17.223	0.045	171.9	75.573	0.168	-411.78	36.07
83.7	16.885	0.065	173.7	108.518	0.246	-1215.70	49.64
85.5	16.238	0.054	175.5	176.643	0.429	-3160.2	170.6
87.3	14.410	0.054	177.3	363.771	1.031	-12186.7	338.5
89.1	9.024	0.042	179.1	—	—	—	—

Table 5.8. Coefficients of the  $\bar{\alpha}_s$  and  $\bar{\alpha}_s^2$  terms for *JCEF*.

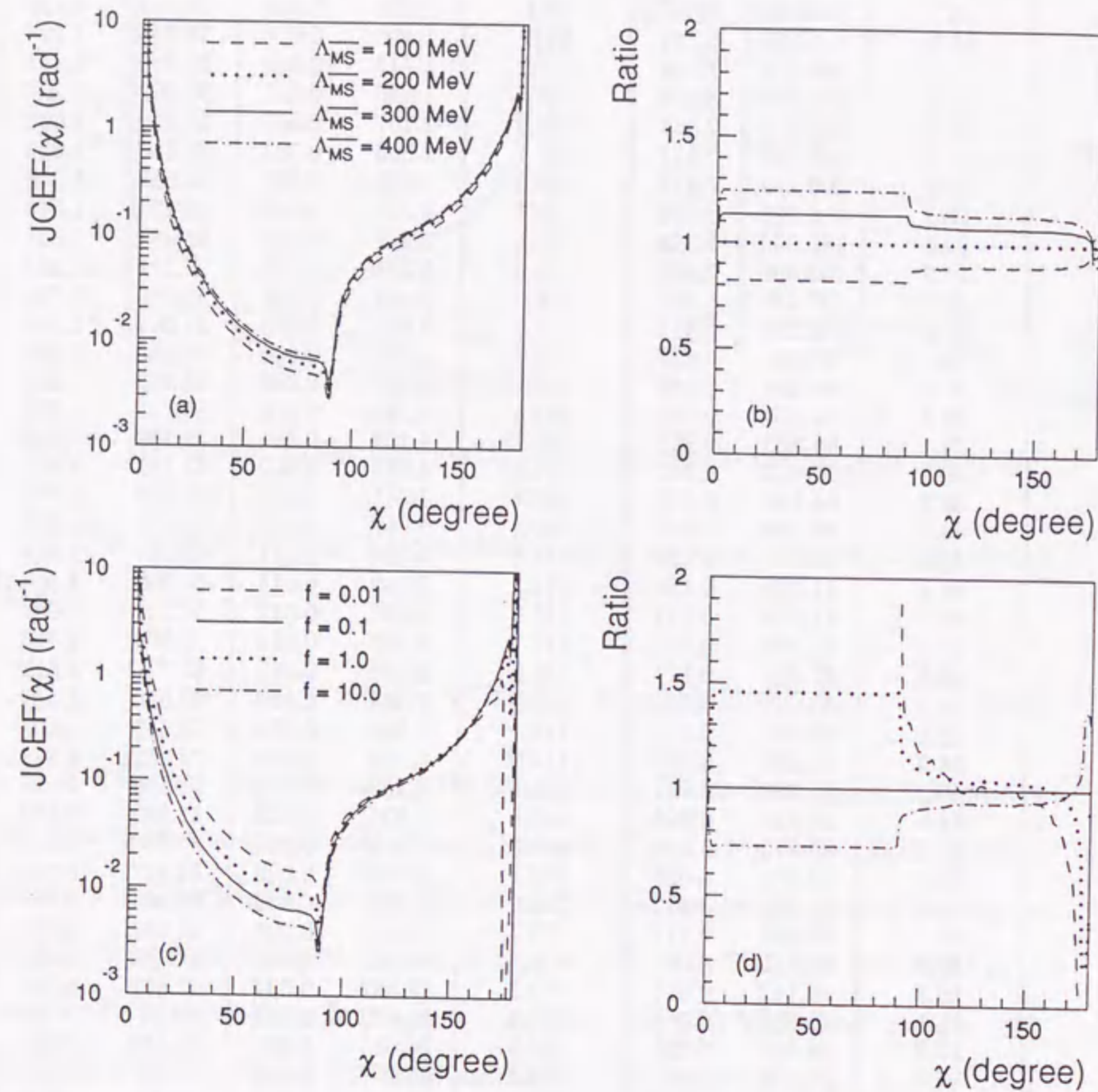


Fig. 5.28. Physical prediction up to  $\mathcal{O}(\alpha_s^2)$  for the  $JCEF$  distribution at  $\sqrt{s} = 91.2$  GeV. (a) Dependence of  $\Lambda_{\overline{MS}}$  and (b) deviation from the case of  $\Lambda_{\overline{MS}} = 200$  MeV at  $f = 1$ . (c) Dependence of  $f$  and (d) deviation from the case of  $f = 1$ .

## Chapter 6

# Measurement of $\alpha_s(M_Z^2)$

### 6.1 Data Analysis

The fifteen observables defined in chapter 5 were calculated from the experimental data using charged tracks in hadronic events selected according to the criteria defined in chapter 4. The experimental distributions  $D_{SLD}^{data}(y)$  were then corrected for the effects of selection cuts, detector acceptance, efficiency, and resolution, for neutral particles, particle decays and interactions within the detector, and for initial state photon radiation, using bin-by-bin correction factors  $C_D(y)$ :

$$C_D(y)_i = \frac{D_{hadron}^{MC}(y)_i}{D_{SLD}^{MC}(y)_i}, \quad (6.1)$$

where  $y$  is the observable;  $i$  is the bin index;  $D_{SLD}^{MC}(y)_i$  is the content of bin  $i$  of the distribution obtained from reconstructed charged particles in Monte Carlo events after simulation of the detector; and  $D_{hadron}^{MC}(y)_i$  is that from all generated particles with lifetimes greater than  $3 \times 10^{-10}$  s in Monte Carlo events with no SLD simulation and no initial state photon radiation. The bin widths were chosen from the estimated experimental resolution so as to minimize bin-to-bin migration effects. The  $C_D(y)$  were calculated using events generated with JETSET 6.3<sup>37</sup> using parameter values tuned to hadronic  $e^+e^-$

annihilation data.<sup>58</sup> In addition, the multiplicity and momentum spectra of  $B$  hadron decay products were tuned to  $\Upsilon_{4S}$  data.<sup>59</sup> The *hadron level* distributions are then given by

$$D_{hadron}^{data}(y)_i = C_D(y)_i \cdot D_{SLD}^{data}(y)_i. \quad (6.2)$$

Systematic effects were investigated using a variety of techniques. The experimental systematic errors arising from uncertainties in modeling the detector were estimated by varying the charged track and event selection criteria over wide ranges, and by varying the tracking efficiency and resolution in the detector simulation. In each case the correction factors  $C_D(y)$ , and hence the corrected data distributions  $D_{hadron}^{data}(y)$ , were rederived. The data correction procedure was repeated by recalculating the correction factors  $C_D(y)$  using events generated with HERWIG 5.5.<sup>38</sup> In addition, a matrix correction procedure<sup>60</sup> was employed, in which migrations between all pairs of bins are accounted for individually. The differences between the data distributions corrected by the bin-by-bin and matrix methods were found to be much smaller than the statistical errors.

The hadron level data are shown in Figs. 6.1-6.3 and listed in Tables 6.1-6.7, together with statistical and systematic errors; they may be compared with data from other experiments that have applied corrections for detector effects. The central values represent the data corrected by the central values of the correction factors  $C_D(y)$ , which are shown in Figs. 6.4 (c)-6.7(c). For the *EEC*, *AEEC*, and *JCEF*, where there are bin-to-bin correlations and multiple entries per event per bin, the statistical error in each bin was estimated by taking the *rms* deviation of the contents of that bin over 50 Monte Carlo samples, each comprising the same number of events as the data sample. The systematic errors derive from the uncertainties on the correction factors shown in Figs. 6.4 (c)-6.7 (c). Also shown in Figs. 6.1-6.3 are the predictions of the JETSET 7.3<sup>42</sup> and HERWIG 5.5<sup>38</sup> QCD + fragmentation event generators.

Good agreement between the data and model predictions is apparent in all cases.

Before they can be compared with the QCD predictions, the data must be corrected for the effects of hadronization. The correction procedure is similar to that described above for the detector effects. Bin-by-bin correction factors

$$C_H(y)_i = \frac{D_{parton}^{MC}(y)_i}{D_{hadron}^{MC}(y)_i}, \quad (6.3)$$

where  $D_{parton}^{MC}(y)_i$  is the content of bin  $i$  of the distribution obtained from Monte Carlo events generated at the parton level, were calculated and applied to the hadron level data distributions  $D_{hadron}^{data}(y)_i$  to obtain the *parton level* corrected data:

$$D_{parton}^{data}(y)_i = C_H(y)_i \cdot D_{hadron}^{data}(y)_i. \quad (6.4)$$

The phenomenological hadronization models implemented in JETSET 7.3 and HERWIG 5.5 were used to calculate the  $C_H(y)$ . In the case of JETSET the  $C_H(y)$  were also recalculated for values of the parton virtuality cutoff  $Q_0$ <sup>37,42</sup> in the range 0.5 to 2.0 GeV, and for reasonable variations of the parameters  $\Lambda_{QCD}$ ,  $a$ , and  $\sigma_q$ . The correction factors  $C_H(y)$  are shown in Figs. 6.4 (b)-6.7 (b), where the bands show the uncertainties due to model differences and parameter variations. The parton level data are shown in Figs. 6.4 (a)-6.7 (a). The data points correspond to the central values of the hadronization correction factors, and the errors shown are statistical and experimental systematic only; the hadronization uncertainty will be considered in the next sections which describe the fits to determine  $\alpha_s(M_Z^2)$ .

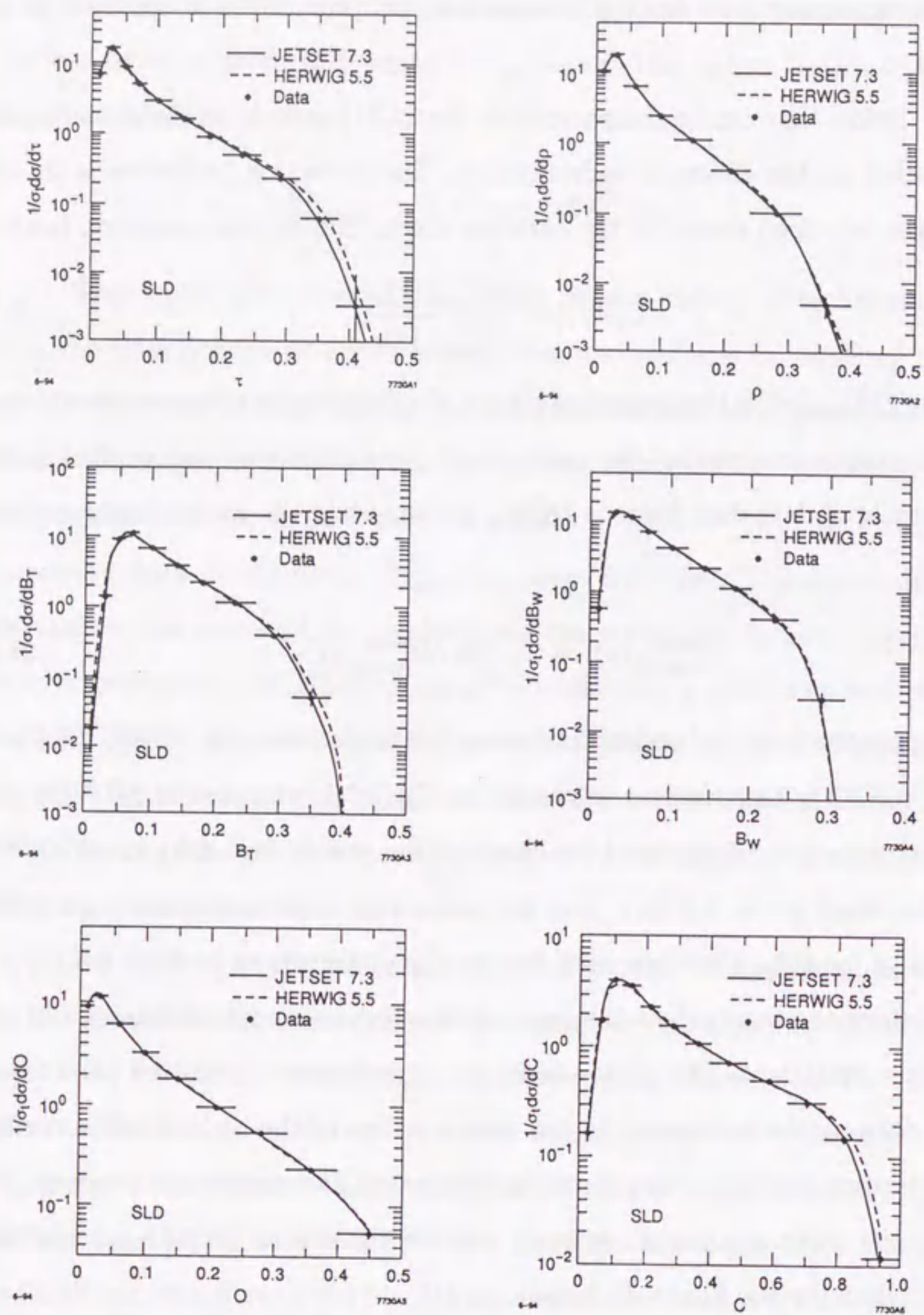


Fig. 6.1. The measured event shapes corrected to the hadron level. The error bars include the statistical and experimental systematic errors added in quadrature. The curves show the predictions of the QCD event generators JETSET 7.3 (solid) and HERWIG 5.5 (dashed line).

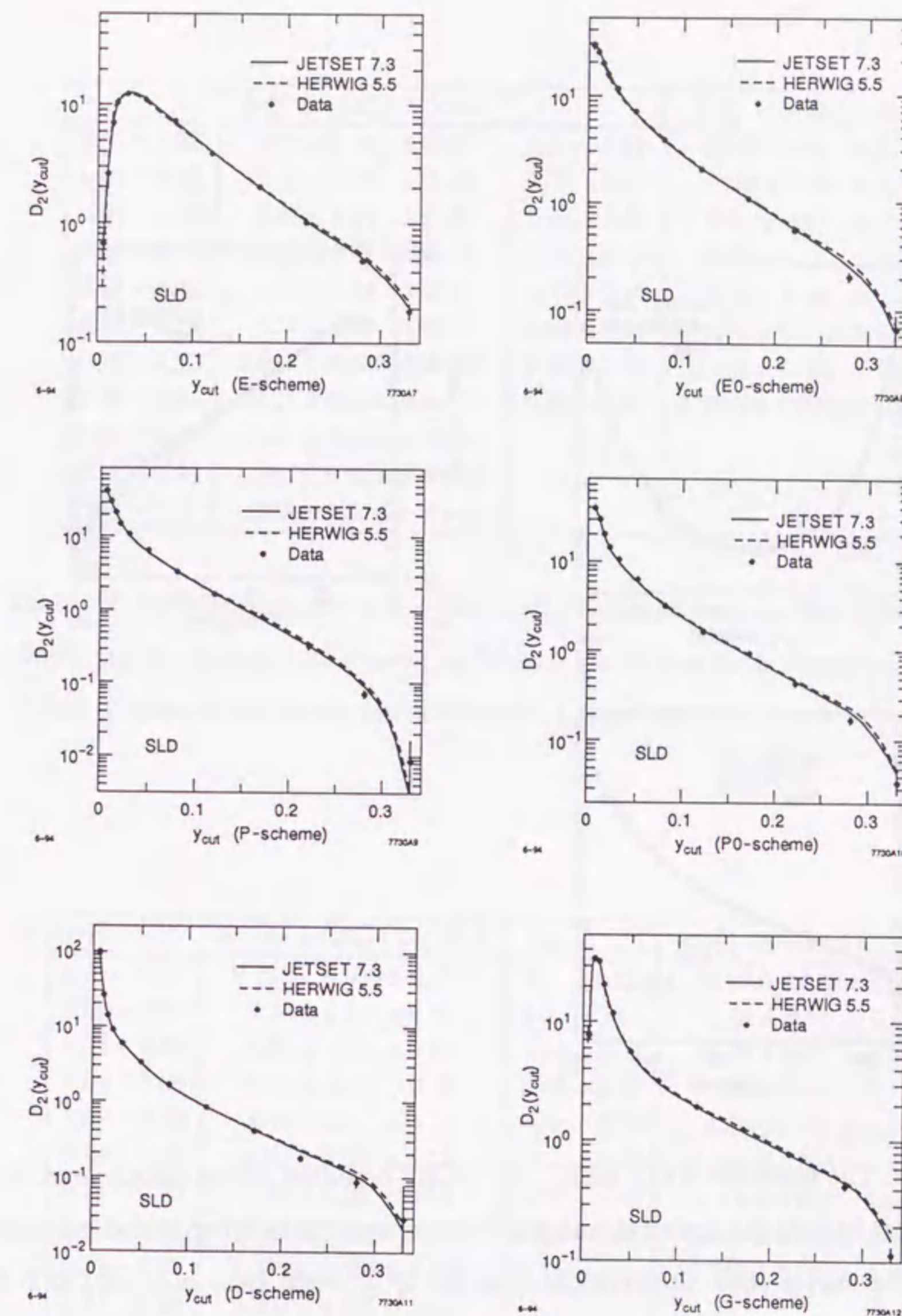


Fig. 6.2. The measured differential 2-jet rate corrected to the hadron level. The error bars include the statistical and experimental systematic errors added in quadrature. The curves show the predictions of the QCD event generators JETSET 7.3 (solid) and HERWIG 5.5 (dashed line).

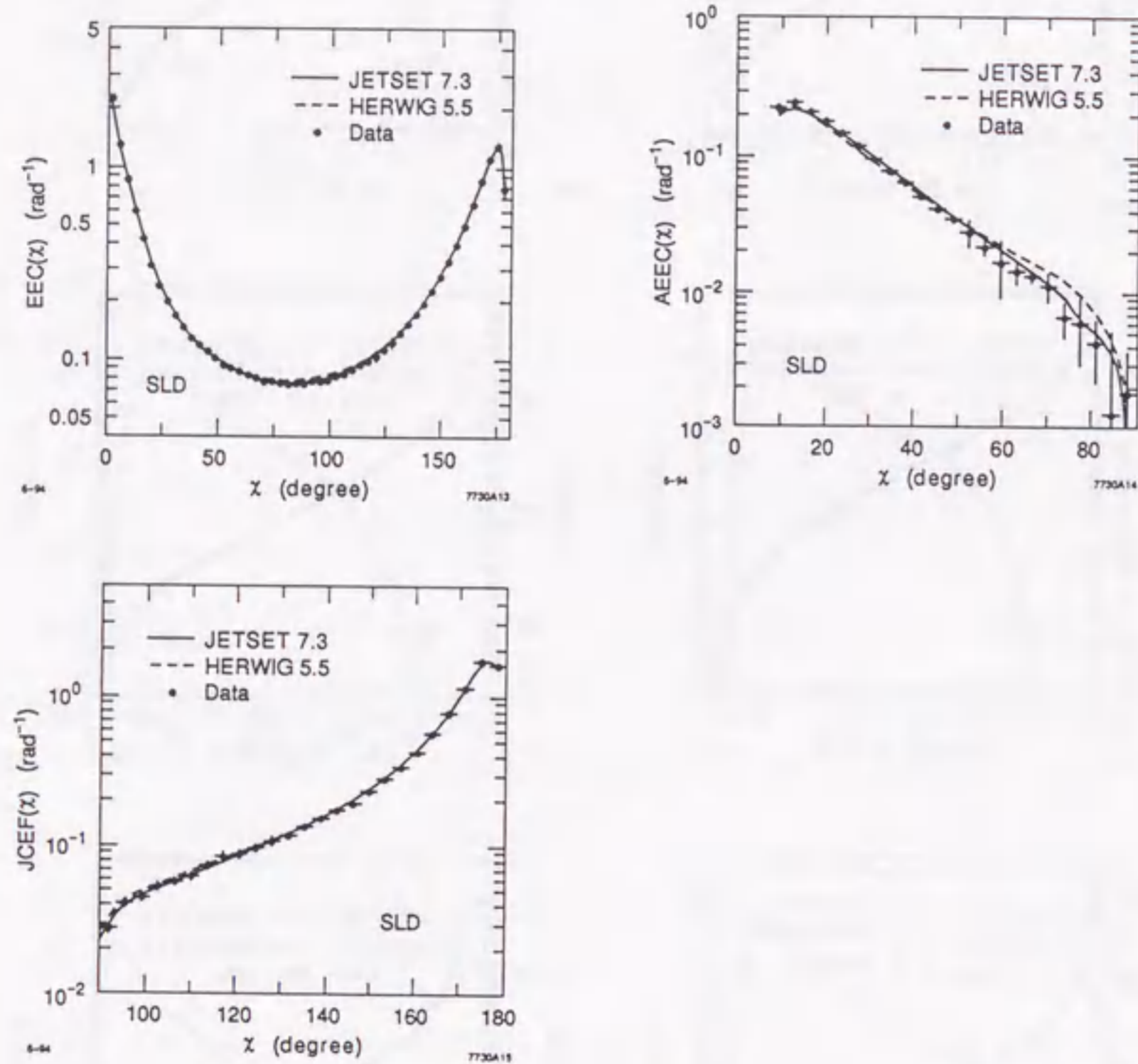


Fig. 6.3. The measured EEC, AEEC, and JCEF corrected to the hadron level. The error bars include the statistical and experimental systematic errors added in quadrature. The curves show the predictions of the QCD event generators JETSET 7.3 (solid) and HERWIG 5.5 (dashed line).

$\tau$	$\frac{1}{\sigma_t} \frac{d\sigma}{d\tau} \pm (stat.) \pm (exp.)$	$\rho$	$\frac{1}{\sigma_t} \frac{d\sigma}{d\rho} \pm (stat.) \pm (exp.)$
0.0 - 0.02	$7.01 \pm 0.10 \pm 0.50$	0.0 - 0.02	$10.53 \pm 0.12 \pm 0.41$
0.02 - 0.04	$16.10 \pm 0.15 \pm 0.15$	0.02 - 0.04	$17.38 \pm 0.15 \pm 0.14$
0.04 - 0.06	$8.67 \pm 0.11 \pm 0.05$	0.04 - 0.08	$6.21 \pm 0.07 \pm 0.16$
0.06 - 0.08	$5.08 \pm 0.08 \pm 0.16$	0.08 - 0.12	$2.39 \pm 0.04 \pm 0.09$
0.08 - 0.12	$2.91 \pm 0.04 \pm 0.06$	0.12 - 0.18	$1.08 \pm 0.02 \pm 0.04$
0.12 - 0.16	$1.57 \pm 0.03 \pm 0.05$	0.18 - 0.24	$0.404 \pm 0.014 \pm 0.021$
0.16 - 0.20	$0.917 \pm 0.025 \pm 0.028$	0.24 - 0.32	$0.102 \pm 0.006 \pm 0.010$
0.20 - 0.26	$0.495 \pm 0.015 \pm 0.025$	0.32 - 0.40	$0.0047 \pm 0.0013 \pm 0.0008$
0.26 - 0.32	$0.227 \pm 0.010 \pm 0.016$		
0.32 - 0.38	$0.061 \pm 0.005 \pm 0.006$		
0.38 - 0.44	$0.003 \pm 0.001 \pm 0.003$		

Table 6.1. Distributions of  $\tau$  and  $\rho$  (see text). The data were corrected for detector effects and for initial state photon radiation. The first error is statistical, and the second represents the experimental systematic uncertainty.

$B_T$	$\frac{1}{\sigma_t} \frac{d\sigma}{dB_T} \pm (stat.) \pm (exp.)$	$B_W$	$\frac{1}{\sigma_t} \frac{d\sigma}{dB_W} \pm (stat.) \pm (exp.)$
0.0 - 0.02	$0.018 \pm 0.005 \pm 0.007$	0.0 - 0.02	$0.570 \pm 0.028 \pm 0.213$
0.02 - 0.04	$1.36 \pm 0.04 \pm 0.18$	0.02 - 0.04	$13.86 \pm 0.14 \pm 0.45$
0.04 - 0.06	$8.81 \pm 0.11 \pm 0.32$	0.04 - 0.06	$11.71 \pm 0.13 \pm 0.20$
0.06 - 0.08	$10.64 \pm 0.12 \pm 0.16$	0.06 - 0.08	$7.38 \pm 0.10 \pm 0.11$
0.08 - 0.12	$6.52 \pm 0.07 \pm 0.10$	0.08 - 0.12	$4.29 \pm 0.05 \pm 0.08$
0.12 - 0.16	$3.65 \pm 0.05 \pm 0.04$	0.12 - 0.16	$2.185 \pm 0.038 \pm 0.128$
0.16 - 0.20	$2.10 \pm 0.04 \pm 0.06$	0.16 - 0.20	$1.12 \pm 0.028 \pm 0.061$
0.20 - 0.26	$1.12 \pm 0.02 \pm 0.03$	0.20 - 0.26	$0.403 \pm 0.014 \pm 0.025$
0.26 - 0.32	$0.384 \pm 0.013 \pm 0.023$	0.26 - 0.32	$0.030 \pm 0.004 \pm 0.005$
0.32 - 0.38	$0.050 \pm 0.005 \pm 0.011$		

Table 6.2. Distributions of  $B_T$  and  $B_W$  (see text). The data were corrected for detector effects and for initial state photon radiation. The first error is statistical, and the second represents the experimental systematic uncertainty.

$O$	$\frac{1}{\sigma_t} \frac{d\sigma}{dO} \pm (stat.) \pm (exp.)$	$C$	$\frac{1}{\sigma_t} \frac{d\sigma}{dC} \pm (stat.) \pm (exp.)$
0.0 - 0.02	$9.07 \pm 0.11 \pm 0.19$	0.0 - 0.04	$0.166 \pm 0.011 \pm 0.015$
0.02 - 0.04	$11.28 \pm 0.12 \pm 0.20$	0.04 - 0.08	$1.76 \pm 0.03 \pm 0.04$
0.04 - 0.08	$5.98 \pm 0.06 \pm 0.07$	0.08 - 0.12	$4.01 \pm 0.05 \pm 0.09$
0.08 - 0.12	$3.16 \pm 0.05 \pm 0.06$	0.12 - 0.18	$3.57 \pm 0.04 \pm 0.10$
0.12 - 0.18	$1.77 \pm 0.03 \pm 0.03$	0.18 - 0.24	$2.30 \pm 0.03 \pm 0.02$
0.18 - 0.24	$0.935 \pm 0.021 \pm 0.028$	0.24 - 0.32	$1.54 \pm 0.02 \pm 0.016$
0.24 - 0.32	$0.523 \pm 0.013 \pm 0.013$	0.32 - 0.40	$1.07 \pm 0.02 \pm 0.03$
0.32 - 0.40	$0.223 \pm 0.009 \pm 0.010$	0.40 - 0.52	$0.718 \pm 0.013 \pm 0.024$
0.40 - 0.50	$0.052 \pm 0.004 \pm 0.003$	0.52 - 0.64	$0.491 \pm 0.011 \pm 0.013$
		0.64 - 0.76	$0.311 \pm 0.008 \pm 0.022$
		0.76 - 0.88	$0.146 \pm 0.006 \pm 0.012$
		0.88 - 1.0	$0.012 \pm 0.002 \pm 0.001$

Table 6.3. Distributions of  $O$  and  $C$  (see text). The data were corrected for detector effects and for initial state photon radiation. The first error is statistical, and the second represents the experimental systematic uncertainty.

$y_{cut}$	E-scheme	E0-scheme	P-scheme
	$D_2(y_{cut}) \pm (stat.) \pm (exp.)$	$D_2(y_{cut}) \pm (stat.) \pm (exp.)$	$D_2(y_{cut}) \pm (stat.) \pm (exp.)$
0.005	$0.669 \pm 0.060 \pm 0.080$	$28.95 \pm 0.39 \pm 1.44$	$41.80 \pm 0.47 \pm 2.43$
0.010	$2.60 \pm 0.12 \pm 0.12$	$25.25 \pm 0.37 \pm 0.50$	$31.06 \pm 0.41 \pm 0.63$
0.015	$7.07 \pm 0.20 \pm 0.27$	$19.93 \pm 0.33 \pm 0.53$	$21.24 \pm 0.34 \pm 0.28$
0.02	$10.48 \pm 0.24 \pm 0.66$	$15.85 \pm 0.29 \pm 1.04$	$14.96 \pm 0.28 \pm 0.54$
0.03	$12.28 \pm 0.18 \pm 0.39$	$11.66 \pm 0.18 \pm 0.15$	$10.82 \pm 0.17 \pm 0.37$
0.05	$10.89 \pm 0.12 \pm 0.34$	$7.01 \pm 0.10 \pm 0.19$	$6.35 \pm 0.09 \pm 0.23$
0.08	$7.22 \pm 0.08 \pm 0.22$	$3.85 \pm 0.06 \pm 0.05$	$3.16 \pm 0.05 \pm 0.09$
0.12	$3.81 \pm 0.05 \pm 0.11$	$2.02 \pm 0.04 \pm 0.07$	$1.61 \pm 0.03 \pm 0.08$
0.17	$1.97 \pm 0.03 \pm 0.05$	$1.08 \pm 0.02 \pm 0.04$	$0.791 \pm 0.021 \pm 0.037$
0.22	$0.987 \pm 0.023 \pm 0.034$	$0.537 \pm 0.017 \pm 0.026$	$0.317 \pm 0.013 \pm 0.024$
0.28	$0.467 \pm 0.015 \pm 0.017$	$0.204 \pm 0.010 \pm 0.015$	$0.069 \pm 0.006 \pm 0.005$
0.33	$0.178 \pm 0.009 \pm 0.024$	$0.068 \pm 0.006 \pm 0.021$	$0.008 \pm 0.002 \pm 0.007$

Table 6.4.  $D_2(y_{cut})$  calculated in the E-scheme, the E0-scheme, and the P-scheme (see text). The data were corrected for detector effects and for initial state photon radiation. The first error is statistical, and the second represents the experimental systematic uncertainty.

$y_{cut}$	P0-scheme	D-scheme	G-scheme
	$D_2(y_{cut}) \pm (stat.) \pm (exp.)$	$D_2(y_{cut}) \pm (stat.) \pm (exp.)$	$D_2(y_{cut}) \pm (stat.) \pm (exp.)$
0.005	$39.78 \pm 0.46 \pm 2.41$	$101.06 \pm 0.74 \pm 2.29$	$7.67 \pm 0.20 \pm 1.01$
0.010	$29.85 \pm 0.40 \pm 0.78$	$26.85 \pm 0.38 \pm 0.34$	$33.63 \pm 0.43 \pm 0.84$
0.015	$20.49 \pm 0.33 \pm 0.36$	$14.13 \pm 0.28 \pm 0.40$	$31.71 \pm 0.41 \pm 1.01$
0.02	$14.52 \pm 0.28 \pm 0.23$	$9.00 \pm 0.22 \pm 0.44$	$20.46 \pm 0.33 \pm 0.55$
0.03	$10.65 \pm 0.17 \pm 0.37$	$6.02 \pm 0.13 \pm 0.17$	$11.71 \pm 0.18 \pm 0.20$
0.05	$6.36 \pm 0.09 \pm 0.19$	$3.30 \pm 0.07 \pm 0.11$	$5.55 \pm 0.09 \pm 0.12$
0.08	$3.21 \pm 0.05 \pm 0.12$	$1.66 \pm 0.04 \pm 0.07$	$3.20 \pm 0.05 \pm 0.06$
0.12	$1.64 \pm 0.03 \pm 0.07$	$0.831 \pm 0.024 \pm 0.038$	$1.92 \pm 0.04 \pm 0.05$
0.17	$0.944 \pm 0.023 \pm 0.057$	$0.406 \pm 0.015 \pm 0.033$	$1.25 \pm 0.03 \pm 0.03$
0.22	$0.433 \pm 0.015 \pm 0.038$	$0.173 \pm 0.010 \pm 0.011$	$0.768 \pm 0.020 \pm 0.027$
0.28	$0.169 \pm 0.009 \pm 0.015$	$0.084 \pm 0.006 \pm 0.013$	$0.409 \pm 0.014 \pm 0.019$
0.33	$0.034 \pm 0.004 \pm 0.008$	$0.027 \pm 0.004 \pm 0.048$	$0.111 \pm 0.007 \pm 0.018$

Table 6.5.  $D_2(y_{cut})$  calculated in the P0-scheme, the D-scheme, and the G-scheme (see text). The data were corrected for detector effects and for initial state photon radiation. The first error is statistical, and the second represents the experimental systematic uncertainty.

$\chi$ (deg.)	$EEC(\text{rad}^{-1}) \pm(\text{stat.}) \pm(\text{exp.})$	$\chi$ (deg.)	$EEC(\text{rad}^{-1}) \pm(\text{stat.}) \pm(\text{exp.})$
0.0 - 3.6	2.265 $\pm$ 0.006 $\pm$ 0.055	90.0 - 93.6	0.0761 $\pm$ 0.0009 $\pm$ 0.0013
3.6 - 7.2	1.316 $\pm$ 0.006 $\pm$ 0.032	93.6 - 97.2	0.0764 $\pm$ 0.0009 $\pm$ 0.0025
7.2 - 10.8	0.874 $\pm$ 0.004 $\pm$ 0.020	97.2 - 100.8	0.0777 $\pm$ 0.0009 $\pm$ 0.0023
10.8 - 14.4	0.598 $\pm$ 0.003 $\pm$ 0.019	100.8 - 104.4	0.0809 $\pm$ 0.0012 $\pm$ 0.0016
14.4 - 18.0	0.425 $\pm$ 0.002 $\pm$ 0.011	104.4 - 108.0	0.0834 $\pm$ 0.0010 $\pm$ 0.0024
18.0 - 21.6	0.310 $\pm$ 0.002 $\pm$ 0.014	108.0 - 111.6	0.0874 $\pm$ 0.0010 $\pm$ 0.0022
21.6 - 25.2	0.241 $\pm$ 0.001 $\pm$ 0.005	111.6 - 115.2	0.0931 $\pm$ 0.0013 $\pm$ 0.0015
25.2 - 28.8	0.199 $\pm$ 0.001 $\pm$ 0.005	115.2 - 118.8	0.0968 $\pm$ 0.0012 $\pm$ 0.0038
28.8 - 32.4	0.168 $\pm$ 0.001 $\pm$ 0.006	118.8 - 122.4	0.1030 $\pm$ 0.0012 $\pm$ 0.0070
32.4 - 36.0	0.146 $\pm$ 0.001 $\pm$ 0.005	122.4 - 126.0	0.111 $\pm$ 0.001 $\pm$ 0.002
36.0 - 39.6	0.128 $\pm$ 0.001 $\pm$ 0.004	126.0 - 129.6	0.121 $\pm$ 0.001 $\pm$ 0.007
39.6 - 43.2	0.118 $\pm$ 0.001 $\pm$ 0.003	129.6 - 133.2	0.136 $\pm$ 0.002 $\pm$ 0.003
43.2 - 46.8	0.1099 $\pm$ 0.0008 $\pm$ 0.0026	133.2 - 136.8	0.151 $\pm$ 0.002 $\pm$ 0.004
46.8 - 50.4	0.1014 $\pm$ 0.0009 $\pm$ 0.0031	136.8 - 140.4	0.170 $\pm$ 0.002 $\pm$ 0.005
50.4 - 54.0	0.0935 $\pm$ 0.0008 $\pm$ 0.0027	140.4 - 144.0	0.193 $\pm$ 0.002 $\pm$ 0.006
54.0 - 57.6	0.0901 $\pm$ 0.0009 $\pm$ 0.0021	144.0 - 147.2	0.225 $\pm$ 0.002 $\pm$ 0.008
57.6 - 61.2	0.0867 $\pm$ 0.0008 $\pm$ 0.0023	147.2 - 151.2	0.265 $\pm$ 0.002 $\pm$ 0.007
61.2 - 64.8	0.0827 $\pm$ 0.0009 $\pm$ 0.0023	151.2 - 154.8	0.320 $\pm$ 0.003 $\pm$ 0.008
64.8 - 68.4	0.0802 $\pm$ 0.0010 $\pm$ 0.0018	154.8 - 158.4	0.390 $\pm$ 0.003 $\pm$ 0.013
68.4 - 72.0	0.0764 $\pm$ 0.0009 $\pm$ 0.0031	158.4 - 162.0	0.491 $\pm$ 0.003 $\pm$ 0.017
72.0 - 75.6	0.0770 $\pm$ 0.0010 $\pm$ 0.0010	162.0 - 165.6	0.636 $\pm$ 0.004 $\pm$ 0.012
75.6 - 79.2	0.0752 $\pm$ 0.0008 $\pm$ 0.0031	165.6 - 169.2	0.847 $\pm$ 0.006 $\pm$ 0.007
79.2 - 82.8	0.0736 $\pm$ 0.0008 $\pm$ 0.0013	169.2 - 172.8	1.098 $\pm$ 0.005 $\pm$ 0.009
82.8 - 86.4	0.0751 $\pm$ 0.0010 $\pm$ 0.0015	172.8 - 176.4	1.276 $\pm$ 0.007 $\pm$ 0.044
86.4 - 90.0	0.0744 $\pm$ 0.0010 $\pm$ 0.0014	176.4 - 180.0	0.764 $\pm$ 0.007 $\pm$ 0.050

Table 6.6. The  $EEC$  (see text). The data were corrected for detector effects and for initial state photon radiation. The first error is statistical, and the second represents the experimental systematic uncertainty.

$\chi$ (deg.)	$AEEC(\text{rad}^{-1}) \pm(\text{stat.}) \pm(\text{exp.})$	$\chi$ (deg.)	$JCEF(\text{rad}^{-1}) \pm(\text{stat.}) \pm(\text{exp.})$
0.0 - 3.6		90.0 - 93.6	0.0274 $\pm$ 0.0016 $\pm$ 0.0010
3.6 - 7.2		93.6 - 97.2	0.0403 $\pm$ 0.0020 $\pm$ 0.0012
7.2 - 10.8	0.224 $\pm$ 0.010 $\pm$ 0.002	97.2 - 100.8	0.0442 $\pm$ 0.0026 $\pm$ 0.0010
10.8 - 14.4	0.249 $\pm$ 0.009 $\pm$ 0.005	100.8 - 104.4	0.0523 $\pm$ 0.0029 $\pm$ 0.0023
14.4 - 18.0	0.211 $\pm$ 0.006 $\pm$ 0.005	104.4 - 108.0	0.0566 $\pm$ 0.0029 $\pm$ 0.0024
18.0 - 21.6	0.181 $\pm$ 0.004 $\pm$ 0.005	108.0 - 111.6	0.0613 $\pm$ 0.0034 $\pm$ 0.0026
21.6 - 25.2	0.148 $\pm$ 0.004 $\pm$ 0.006	111.6 - 115.2	0.0725 $\pm$ 0.0039 $\pm$ 0.0017
25.2 - 28.8	0.121 $\pm$ 0.003 $\pm$ 0.004	115.2 - 118.8	0.0832 $\pm$ 0.0055 $\pm$ 0.0046
28.8 - 32.4	0.0972 $\pm$ 0.0024 $\pm$ 0.0029	118.8 - 122.4	0.0858 $\pm$ 0.0051 $\pm$ 0.0016
32.4 - 36.0	0.0785 $\pm$ 0.0022 $\pm$ 0.0062	122.4 - 126.0	0.0944 $\pm$ 0.0043 $\pm$ 0.0024
36.0 - 39.6	0.0645 $\pm$ 0.0017 $\pm$ 0.0024	126.0 - 129.6	0.1051 $\pm$ 0.0061 $\pm$ 0.0055
39.6 - 43.2	0.0513 $\pm$ 0.0020 $\pm$ 0.0026	129.6 - 133.2	0.114 $\pm$ 0.005 $\pm$ 0.002
43.2 - 46.8	0.0413 $\pm$ 0.0015 $\pm$ 0.0027	133.2 - 136.8	0.131 $\pm$ 0.005 $\pm$ 0.005
46.8 - 50.4	0.0346 $\pm$ 0.0016 $\pm$ 0.0021	136.8 - 140.4	0.148 $\pm$ 0.005 $\pm$ 0.006
50.4 - 54.0	0.0275 $\pm$ 0.0013 $\pm$ 0.0060	140.4 - 144.0	0.169 $\pm$ 0.007 $\pm$ 0.004
54.0 - 57.6	0.0213 $\pm$ 0.0010 $\pm$ 0.0024	144.0 - 147.2	0.188 $\pm$ 0.007 $\pm$ 0.005
57.6 - 61.2	0.0163 $\pm$ 0.0008 $\pm$ 0.0073	147.2 - 151.2	0.228 $\pm$ 0.008 $\pm$ 0.009
61.2 - 64.8	0.0141 $\pm$ 0.0007 $\pm$ 0.0026	151.2 - 154.8	0.275 $\pm$ 0.009 $\pm$ 0.010
64.8 - 68.4	0.0129 $\pm$ 0.0010 $\pm$ 0.0008	154.8 - 158.4	0.329 $\pm$ 0.011 $\pm$ 0.013
68.4 - 72.0	0.0110 $\pm$ 0.0007 $\pm$ 0.0025	158.4 - 162.0	0.414 $\pm$ 0.011 $\pm$ 0.019
72.0 - 75.6	0.0064 $\pm$ 0.0005 $\pm$ 0.0017	162.0 - 165.6	0.551 $\pm$ 0.012 $\pm$ 0.013
75.6 - 79.2	0.0058 $\pm$ 0.0006 $\pm$ 0.0029	165.6 - 169.2	0.751 $\pm$ 0.021 $\pm$ 0.021
79.2 - 82.8	0.0041 $\pm$ 0.0004 $\pm$ 0.0020	169.2 - 172.8	1.095 $\pm$ 0.024 $\pm$ 0.019
82.8 - 86.4	0.0012 $\pm$ 0.0002 $\pm$ 0.0038	172.8 - 176.4	1.639 $\pm$ 0.032 $\pm$ 0.034
86.4 - 90.0	0.0017 $\pm$ 0.0008 $\pm$ 0.0016	176.4 - 180.0	1.530 $\pm$ 0.039 $\pm$ 0.049

Table 6.7. The  $AEEC$  and  $JCEF$  (see text). The data were corrected for detector effects and for initial state photon radiation. The first error is statistical, and the second represents the experimental systematic uncertainty.



## 6.2 Measurement of $\alpha_s(M_Z^2)$ from $\mathcal{O}(\alpha_s^2)$ Calculation

The strong coupling  $\alpha_s(M_Z^2)$  was first measured by comparing the  $\mathcal{O}(\alpha_s^2)$  QCD calculations for each observable  $y$  with the corrected data at the parton level. Each calculation was fitted to the measured distribution  $1/\sigma_t \cdot d\sigma/dy$  by minimizing  $\chi^2$  with respect to variation of  $\Lambda_{\overline{MS}}$ . In each  $y$  bin  $\chi^2$  was defined using the sum in quadrature of the statistical ( $\sigma_i^{stat.}$ ) and experimental systematic errors ( $\sigma_i^{sys.}$ ) as follows:

$$\chi^2 \equiv \sum_i \left[ \frac{(D_{parton}^{data}(y)_i - D_{parton}^{QCDtheor.}(y)_i)^2}{(\sigma_i^{stat.})^2 + (\sigma_i^{sys.})^2} \right], \quad (6.5)$$

where  $D_{parton}^{data}(y)$  is the SLD data corrected to the parton level as described in section 6.1 and  $D_{parton}^{QCDtheor.}(y)$  indicates the perturbative QCD predictions. Fits were performed at selected values of the scale  $f$  and were restricted to the range in  $y$  for which the  $\mathcal{O}(\alpha_s^2)$  calculation provides a good description of the corrected data.

The fit ranges in  $y$  were chosen to ensure that the parton level data and the QCD calculations could be compared meaningfully. The range for each observable was determined according to the following requirements: (1) the hadronization correction factors  $C_H(y)$  satisfied  $0.6 < C_H(y) < 1.4$ ; (2) the systematic uncertainties on the detector and hadronization correction factors,  $\Delta C_D(y)$  and  $\Delta C_H(y)$  respectively, satisfied  $|\Delta C_D(y), \Delta C_H(y)| < 0.3$ ; (3) three massless partons can contribute to the distribution at  $\mathcal{O}(\alpha_s)$  in perturbative QCD; (4) the  $\chi^2$  per degree of freedom,  $\chi_{dof}^2$ , for a fit at  $f = 1$  is 5.0 or less. Requirements (1) and (2) ensure that the corrected data are well measured and that the hadronization corrections are modeled reliably. Requirement (3) ensures that the kinematic regions dominated by 4-parton production at  $\mathcal{O}(\alpha_s^2)$  are excluded, as the calculation is effectively leading order, and hence unreliable, in these regions. Requirement (4) is an empirical constraint that ensures

observable	fit range	$f$ -range	$\alpha_s(M_Z^2)$	uncertainties			
				stat.	exp. sys.	had.	scale
$\tau$	0.06 – 0.32	$2 \times 10^{-4} - 4$	0.1245	$\pm 0.0008$	$\pm 0.0017$	$\pm 0.0026$	$\pm 0.0201$
$\rho$	0.04 – 0.32	$1.5 \times 10^{-3} - 4$	0.1273	$\pm 0.0008$	$\pm 0.0020$	$\pm 0.0005$	$\pm 0.0096$
$B_T$	0.12 – 0.32	$5.7 \times 10^{-3} - 4$	0.1272	$\pm 0.0008$	$\pm 0.0020$	$\pm 0.0033$	$\pm 0.0220$
$B_W$	0.06 – 0.26	$2 \times 10^{-3} - 4$	0.1196	$\pm 0.0008$	$\pm 0.0026$	$\pm 0.0024$	$\pm 0.0072$
$O$	0.08 – 0.32	$2 \times 10^{-1} - 4$	0.1343	$\pm 0.0013$	$\pm 0.0015$	$\pm 0.0087$	$\pm 0.0082$
$C$	0.24 – 0.76	$4 \times 10^{-4} - 4$	0.1233	$\pm 0.0009$	$\pm 0.0019$	$\pm 0.0032$	$\pm 0.0186$
$D_2(E)$	0.08 – 0.28	$5 \times 10^{-5} - 4$	0.1273	$\pm 0.0006$	$\pm 0.0016$	$\pm 0.0022$	$\pm 0.0217$
$D_2(E0)$	0.05 – 0.28	$1.2 \times 10^{-2} - 4$	0.1175	$\pm 0.0007$	$\pm 0.0027$	$\pm 0.0010$	$\pm 0.0083$
$D_2(P)$	0.05 – 0.22	$5.5 \times 10^{-3} - 4$	0.1207	$\pm 0.0008$	$\pm 0.0033$	$\pm 0.0025$	$\pm 0.0053$
$D_2(P0)$	0.05 – 0.28	$1.2 \times 10^{-2} - 4$	0.1190	$\pm 0.0009$	$\pm 0.0031$	$\pm 0.0020$	$\pm 0.0057$
$D_2(D)$	0.03 – 0.22	$1.7 \times 10^{-3} - 4$	0.1245	$\pm 0.0011$	$\pm 0.0032$	$\pm 0.0007$	$\pm 0.0077$
$D_2(G)$	0.12 – 0.28	$4 \times 10^{-3} - 4$	0.1191	$\pm 0.0008$	$\pm 0.0014$	$\pm 0.0029$	$\pm 0.0043$
$EEC$	$36.0^\circ - 154.8^\circ$	$3.5 \times 10^{-3} - 4$	0.1222	$\pm 0.0008$	$\pm 0.0030$	$\pm 0.0031$	$\pm 0.0121$
$AEEC$	$18.0^\circ - 68.4^\circ$	$9 \times 10^{-2} - 4$	0.1121	$\pm 0.0012$	$\pm 0.0032$	$\pm 0.0017$	$\pm 0.0031$
$JCEF$	$100.8^\circ - 158.4^\circ$	$5 \times 10^{-3} - 4$	0.1185	$\pm 0.0007$	$\pm 0.0027$	$\pm 0.0008$	$\pm 0.0045$

Table 6.8. Observables used in  $\mathcal{O}(\alpha_s^2)$  QCD fits. For each the fit range, the range of the renormalization scale factor considered, central  $\alpha_s(M_Z^2)$  value, statistical and experimental systematic errors, and hadronization and scale uncertainties are shown.

that the QCD calculation fits the data reasonably well; this is most relevant to exclude the so-called ‘two-jet region’ where multiple emissions of soft or collinear gluons are important and are not included in the  $\mathcal{O}(\alpha_s^2)$  calculations, a matter discussed further in the next section. Since the 4-jet rate  $R_4$  has been calculated only at leading order, for  $D_2$  the lower bound on  $y_{cut}$  was chosen to ensure that  $R_4$  was smaller than 1%. These fit ranges are listed in Table 6.8 and are shown in Figs. 6.4-6.7. For illustration, fits to the distributions are shown in Figs. 6.4(a)-6.7(a) for the case  $f = 1$ . The data are well described by

observable	$\alpha_s(M_Z^2)$	exp. error	theoretical uncertainty
$\tau$	0.1245	$\pm 0.0019$	$\pm 0.0203$
$\rho$	0.1273	$\pm 0.0022$	$\pm 0.0096$
$B_T$	0.1272	$\pm 0.0022$	$\pm 0.0222$
$B_W$	0.1196	$\pm 0.0027$	$\pm 0.0076$
$O$	0.1343	$\pm 0.0020$	$\pm 0.0120$
$C$	0.1233	$\pm 0.0021$	$\pm 0.0189$
$D_2(E)$	0.1273	$\pm 0.0017$	$\pm 0.0218$
$D_2(E0)$	0.1175	$\pm 0.0028$	$\pm 0.0084$
$D_2(P)$	0.1207	$\pm 0.0034$	$\pm 0.0059$
$D_2(P0)$	0.1190	$\pm 0.0032$	$\pm 0.0060$
$D_2(D)$	0.1245	$\pm 0.0034$	$\pm 0.0077$
$D_2(G)$	0.1191	$\pm 0.0016$	$\pm 0.0052$
$EEC$	0.1222	$\pm 0.0031$	$\pm 0.0125$
$AEEC$	0.1121	$\pm 0.0034$	$\pm 0.0035$
$JCEF$	0.1185	$\pm 0.0028$	$\pm 0.0046$

Table 6.9. The  $\alpha_s(M_Z^2)$  values derived from  $\mathcal{O}(\alpha_s^2)$  QCD fits.

$\mathcal{O}(\alpha_s^2)$  QCD within the fit ranges. Fits were also performed in the same ranges for different choices of the renormalization scale  $f$  such that  $10^{-4} \leq f \leq 10^2$ . In each case the fitted value of  $\Lambda_{\overline{MS}}$  was translated to  $\alpha_s(M_Z^2)$  using Eq. (2.8) discussed in chapter 2. The value of  $\alpha_s(M_Z^2)$  and the corresponding  $\chi_{dof}^2$  for the fit are shown as a function of the choice of  $f$  in Figs. 6.8 and 6.9 for all observables. Several features are common to the results from each observable:  $\alpha_s(M_Z^2)$  depends strongly on  $f$ ; the fit quality is good over a wide range of  $f$ , typically  $f \gtrsim 10^{-3}$ , and there is no strong preference for a particular scale for most of the observables; at low  $f$  the fit quality deteriorates rapidly, and neither  $\alpha_s(M_Z^2)$  nor its error can be interpreted meaningfully. For the oblateness the good fit region is  $f \gtrsim 10^{-1}$ , which is much higher than for the other observables. For  $D_2$  calculated in the E-scheme the lowest  $\chi_{dof}^2$  is found in the

region around  $f \sim 10^{-4}$ , which is much lower than for the other observables.

Figures 6.8 and 6.9 form a complete representation of the results of the fits of  $\mathcal{O}(\alpha_s^2)$  QCD to the SLD data. It is useful, however, to quote a single value of  $\alpha_s(M_Z^2)$ , together with its associated uncertainties, determined from each observable. For this purpose the following procedure was adopted.

For each observable an  $f$ -range was defined such that  $\chi_{dof}^2 < 5.0$  and  $f \leq 4.0$ . The former requirement excludes the low  $f$  regions where the fit quality is poor, which has been shown<sup>61</sup> to be due to poor convergence of the  $\mathcal{O}(\alpha_s^2)$  calculations. The latter requirement corresponds to a reasonable physical limit  $\mu \leq 2\sqrt{s}$ . This range is arbitrary, but does ensure that the smallest  $\alpha_s(M_Z^2)$  point (see Figs. 6.8 (a) and 6.9 (a)) is considered for all variables except  $B_T$ . The extrema of  $\alpha_s(M_Z^2)$  values in this  $f$ -range were taken to define a symmetric *renormalization scale uncertainty* about their average, which we defined as the central value. The  $f$ -range, central  $\alpha_s(M_Z^2)$  value, and scale uncertainty are listed in Table 6.8 for each observable.

For most observables the statistical error on  $\alpha_s(M_Z^2)$  was defined by the change in  $\alpha_s(M_Z^2)$  corresponding to an increase in  $\chi^2$  of 1.0 above the lowest value within the  $f$ -range defined above (see Figs. 6.8(b) and 6.9(b)). However, for the  $EEC$ ,  $AEEC$ , and  $JCEF$ , where there are strong bin-to-bin correlations, the statistical error on  $\alpha_s(M_Z^2)$  was estimated by applying the same fitting procedure to ten sets of Monte Carlo events, each comprising the same number of events as the data sample, and taking the *rms* deviation over the ten samples. The statistical error is less than 1% of  $\alpha_s(M_Z^2)$  for each observable, and is listed in Table 6.8.

For each observable the experimental systematic error on  $\alpha_s(M_Z^2)$  was estimated by changing the detector correction factor  $C_D$  within the systematic limits shown in Figs. 6.4(c)-6.7(c), and by repeating the correction and fitting procedures to obtain  $\Lambda_{\overline{MS}}$  and hence  $\alpha_s(M_Z^2)$  values. The systematic error, calculated from the resulting spread in  $\alpha_s(M_Z^2)$  values, was found to be 1-3%

of  $\alpha_s(M_Z^2)$  for each observable and is listed in Table 6.8.

For each observable the hadronization uncertainty on  $\alpha_s(M_Z^2)$  was estimated by changing the hadronization correction factor  $C_H$  within the systematic limits shown in Figs. 6.4(b)-6.7(b), and by repeating the correction and fitting procedures to obtain  $\Lambda_{\overline{MS}}$  and hence  $\alpha_s(M_Z^2)$  values. The hadronization uncertainty, calculated from the resulting spread in  $\alpha_s(M_Z^2)$  values, was found to be 0.4-6% of  $\alpha_s(M_Z^2)$  for each observable and is listed in Table 6.8.

The central values of  $\alpha_s(M_Z^2)$  and the errors are summarized in Table 6.9. For each observable the total experimental error is the sum in quadrature of the statistical and experimental systematic errors, and the total theoretical uncertainty is the sum in quadrature of the hadronization and scale uncertainties. In all cases the theoretical uncertainty, which derives mainly from the scale ambiguity, dominates. This uncertainty, which arises from uncalculated higher order terms in perturbation theory, varies from about 3% of  $\alpha_s(M_Z^2)$  for the *AEEC* to about 17% of  $\alpha_s(M_Z^2)$  for *B<sub>T</sub>*. The  $\alpha_s(M_Z^2)$  values from the fifteen observables are consistent within these theoretical uncertainties. Since the same data were used to measure all observables, and the observables are all highly correlated, combining these results by means of an unweighted average to obtain, then yields

$$\alpha_s(M_Z^2) = 0.1225 \pm 0.0026(\text{exp.}) \pm 0.0109(\text{theor.}),$$

where the experimental error is the sum in quadrature of the average statistical ( $\pm 0.0009$ ) and average experimental systematic ( $\pm 0.0024$ ) errors, corresponding to the assumption that all are completely correlated. The theoretical error is the sum in quadrature of the average hadronization ( $\pm 0.0024$ ) and average scale ( $\pm 0.0106$ ) uncertainties.

As a cross-check weighted averages were performed in order to combine the results from different measures. Weighting by experimental errors yields an average  $\alpha_s(M_Z^2)$  value different from the above by  $+0.0009$ ; weighting by

the total errors yields an  $\alpha_s(M_Z^2)$  value different by  $-0.0013$ . These differences are of the same order as the statistical error on a single  $\alpha_s(M_Z^2)$  measurement and are hence negligible.

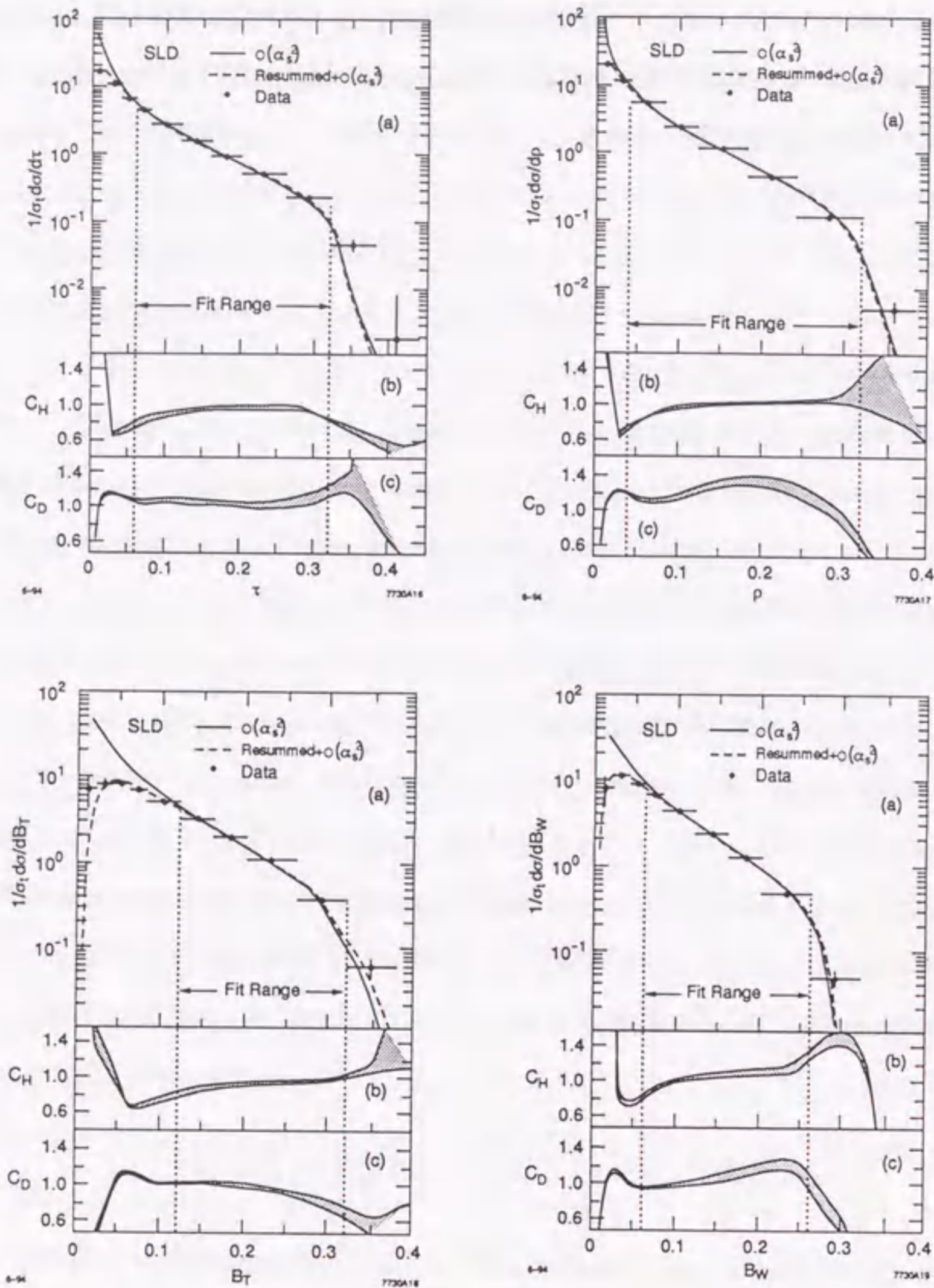


Fig. 6.4. The measured  $\tau$ ,  $\rho$ ,  $B_T$ , and  $B_W$  corrected to the parton level. The error bars include the statistical and experimental systematic errors added in quadrature. The curves show the predictions of the  $\mathcal{O}(\alpha_s^2)$  calculations (solid line) and the resummed+ $\mathcal{O}(\alpha_s^2)$  calculations with  $\ln R$ -matching (dashed line). The renormalization scale factor was fixed to 1. Sizes of the (b) hadronization correction and (c) detector correction factors; the width of the bands indicate the systematic uncertainties.

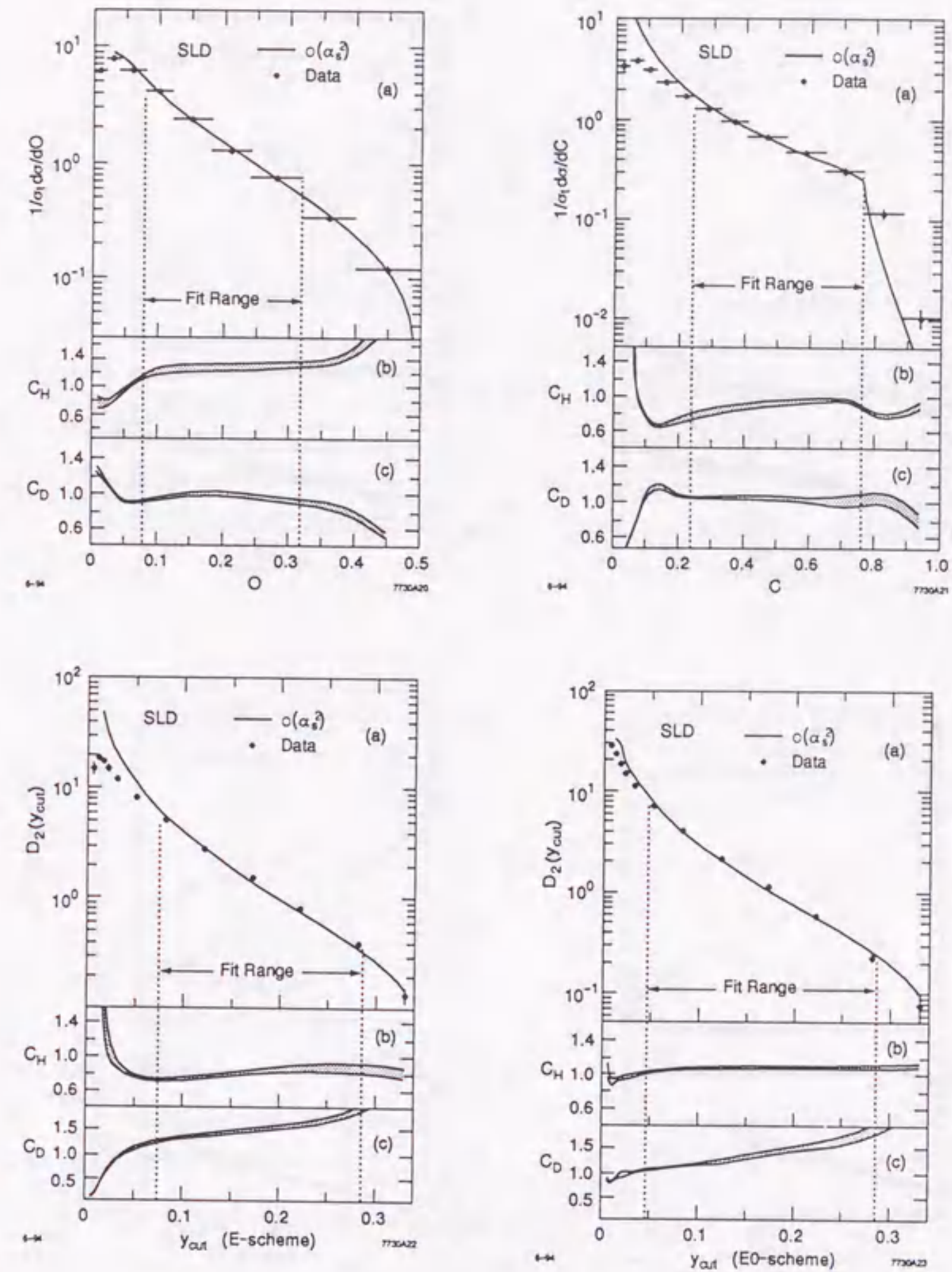


Fig. 6.5. The measured  $O$ ,  $C$ ,  $D_2(E)$ , and  $D_2(E0)$  corrected to the parton level. The error bars include the statistical and experimental systematic errors added in quadrature. The curves show the predictions of the  $\mathcal{O}(\alpha_s^2)$  calculations (solid line) and the resummed+ $\mathcal{O}(\alpha_s^2)$  calculations with  $\ln R$ -matching (dashed line). The renormalization scale factor was fixed to 1. Sizes of the (b) hadronization correction and (c) detector correction factors; the width of the bands indicate the systematic uncertainties.

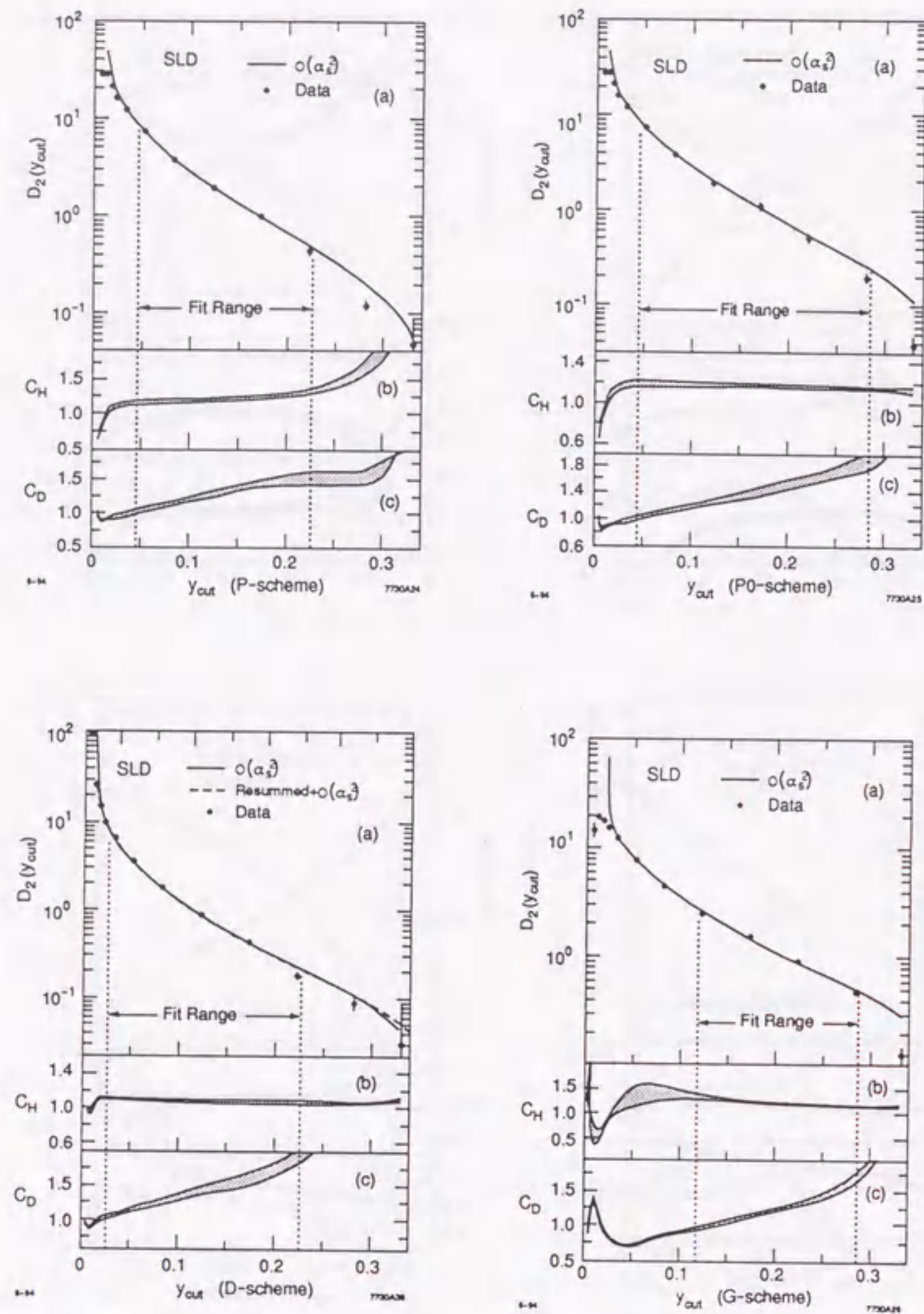


Fig. 6.6. The measured  $D_2(P)$ ,  $D_2(P0)$ ,  $D_2(D)$ , and  $D_2(G)$  corrected to the parton level. The error bars include the statistical and experimental systematic errors added in quadrature. The curves show the predictions of the  $\mathcal{O}(\alpha_s^2)$  calculations (solid line) and the resummed+ $\mathcal{O}(\alpha_s^3)$  calculations with  $\ln R$ -matching (dashed line). The renormalization scale factor was fixed to 1. Sizes of the (b) hadronization correction and (c) detector correction factors; the width of the bands indicate the systematic uncertainties.

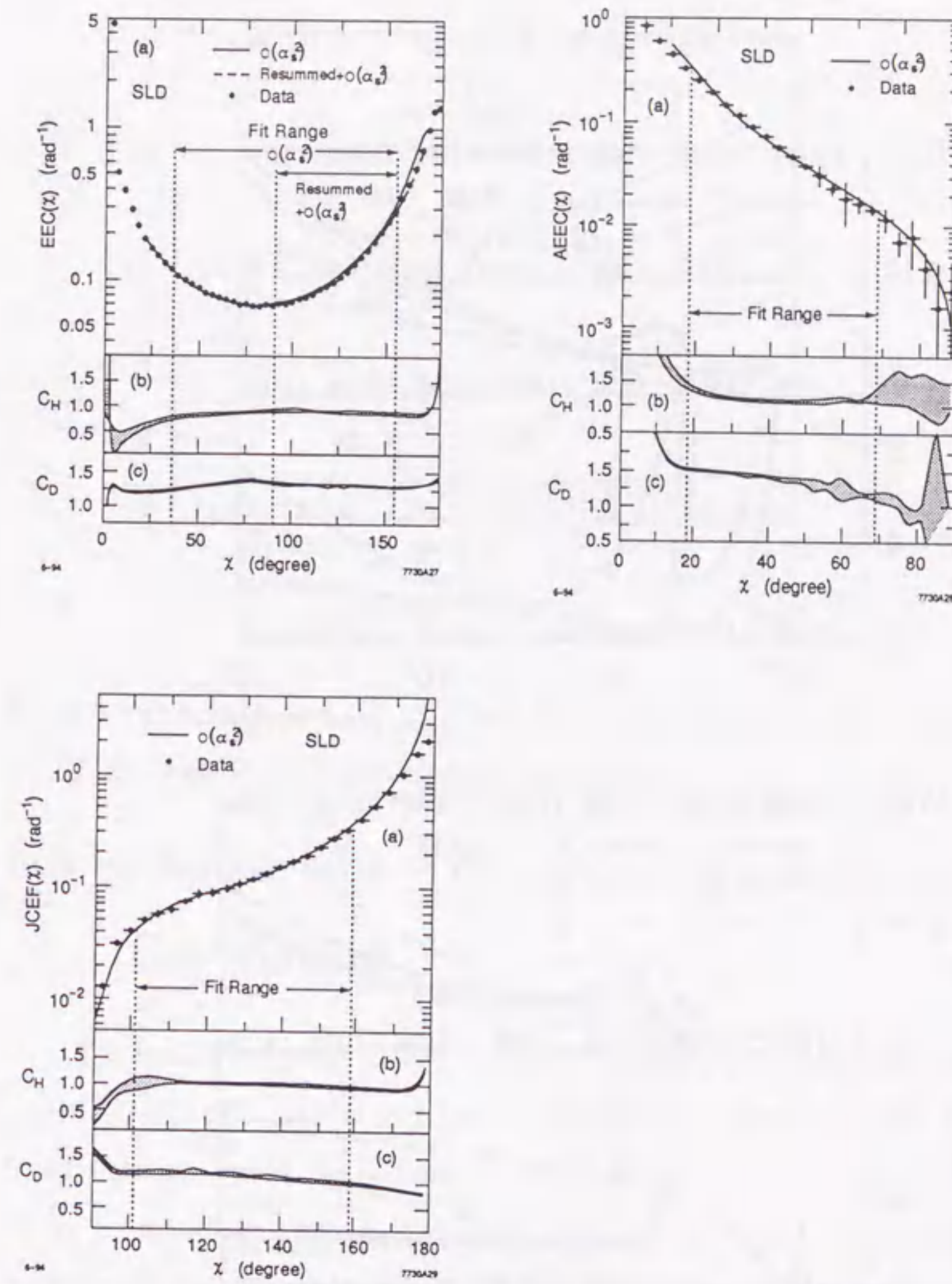


Fig. 6.7. The measured  $EEC$ ,  $AEEC$ , and  $JCEF$  corrected to the parton level. The error bars include the statistical and experimental systematic errors added in quadrature. The curves show the predictions of the  $\mathcal{O}(\alpha_s^2)$  calculations (solid line) and the resummed+ $\mathcal{O}(\alpha_s^3)$  calculations with  $\ln R$ -matching (dashed line). The renormalization scale factor was fixed to 1. Sizes of the (b) hadronization correction and (c) detector correction factors; the width of the bands indicate the systematic uncertainties.

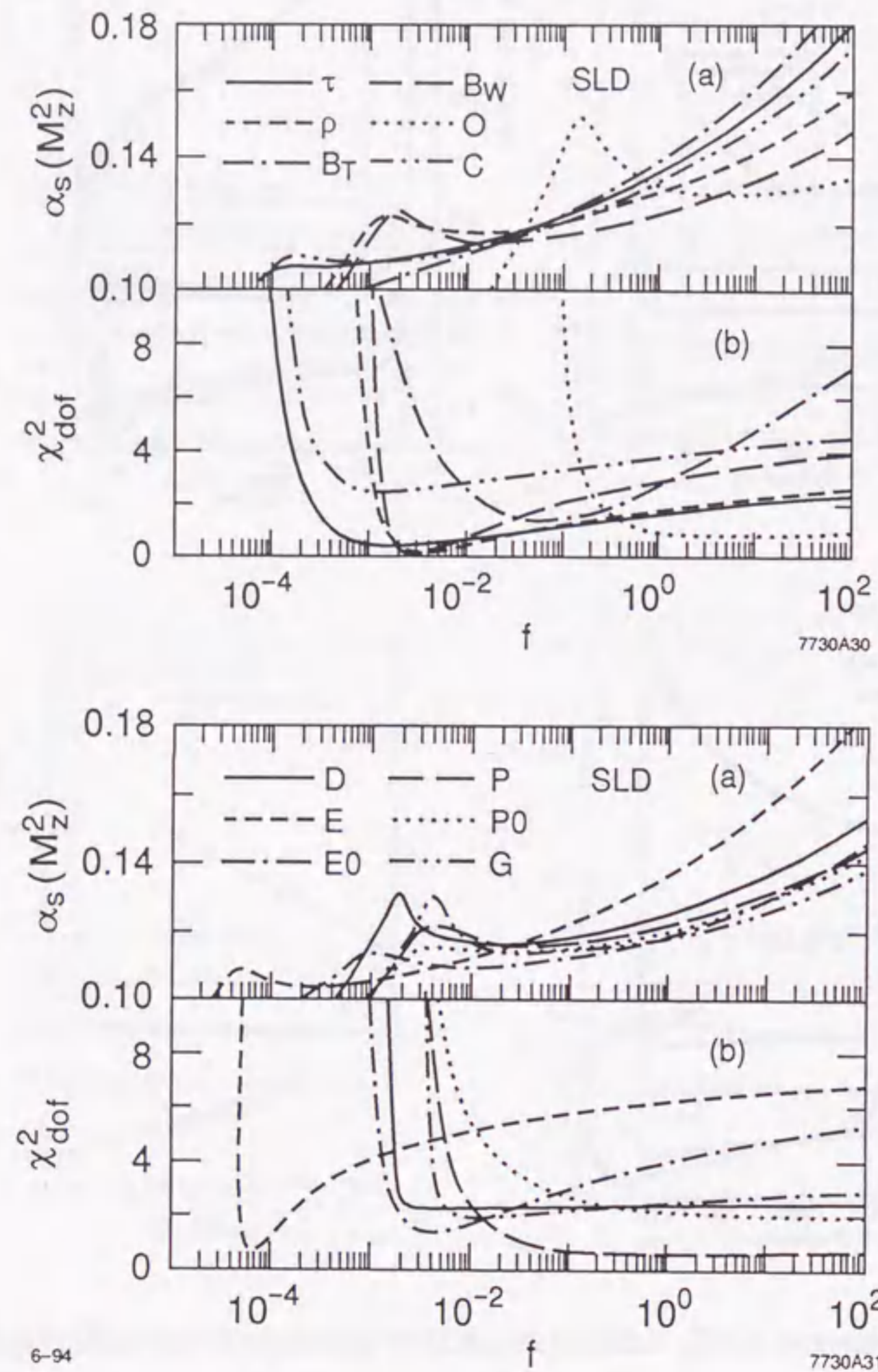


Fig. 6.8. (a)  $\alpha_s(M_Z^2)$  and (b)  $\chi^2_{\text{dof}}$  from the  $\mathcal{O}(\alpha_s^2)$  fits to the event shapes (top) and jet rates (bottom) as a function of renormalization scale factor  $f$ .

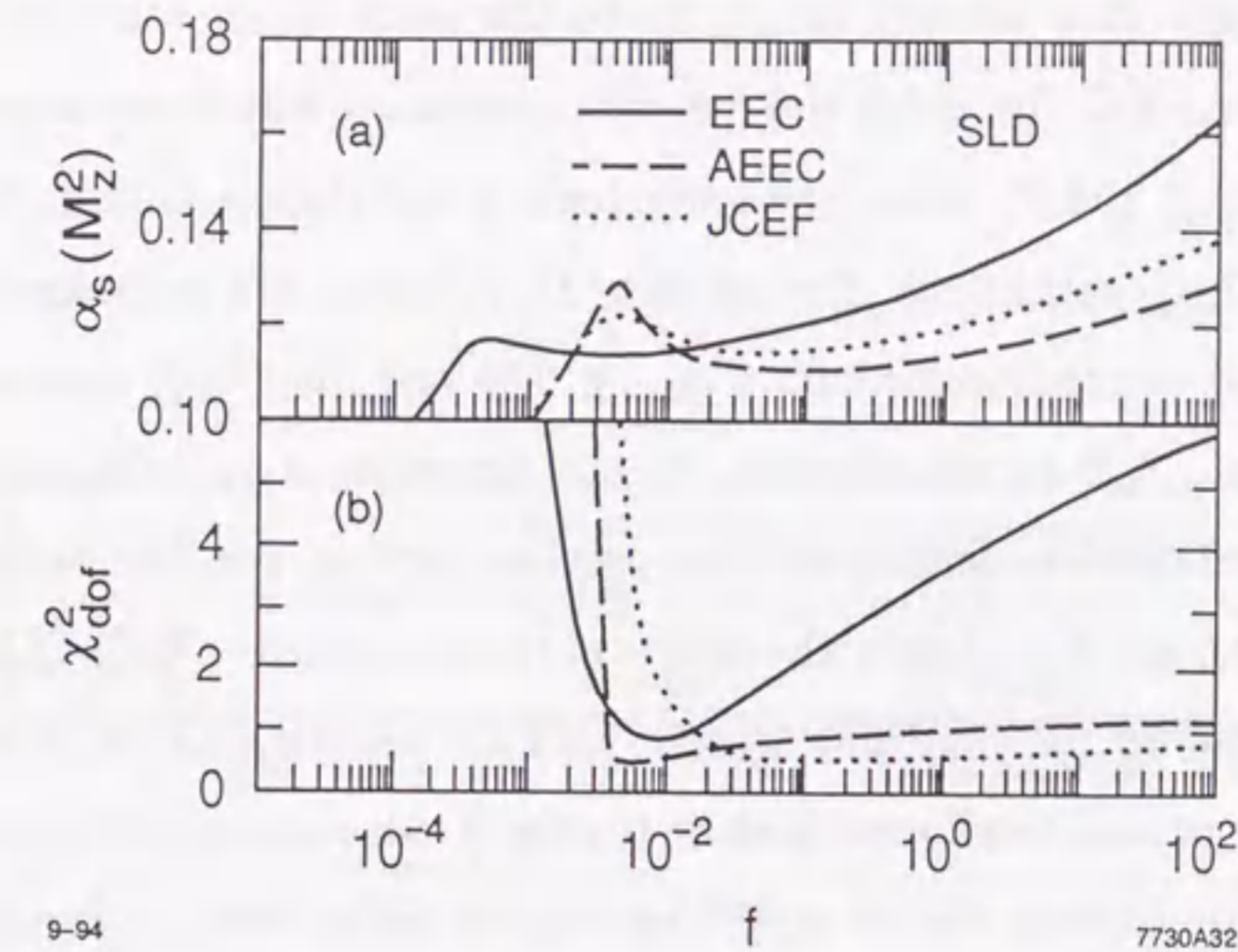


Fig. 6.9. (a)  $\alpha_s(M_Z^2)$  and (b)  $\chi^2_{\text{dof}}$  from the  $\mathcal{O}(\alpha_s^2)$  fits to the *EEC*, *AEEC*, and *JCEF* as a function of renormalization scale factor  $f$ .

### 6.3 Measurement of $\alpha_s(M_Z^2)$ from Resummed+ $\mathcal{O}(\alpha_s^2)$ Calculation

The strong coupling  $\alpha_s(M_Z^2)$  was next measured by comparing the resummed+ $\mathcal{O}(\alpha_s^2)$  calculations with the corrected data at the parton level for those observables for which the resummed+ $\mathcal{O}(\alpha_s^2)$  calculations exist, *i.e.* thrust ( $\tau$ ), heavy jet mass ( $\rho$ ), total ( $B_T$ ) and wide ( $B_W$ ) jet broadening measures, differential 2-jet rate ( $D_2$ ) calculated in the D-scheme, and energy-energy correlations (*EEC*). We considered all four matching schemes discussed in Section 4, namely, *lnR*-, *modified lnR*-, *R*-, and *modified R*-matching. However, *modified R*-matching is not applicable to  $D_2$  because the subleading term  $G_{21}^*$  is not calculated in this case. For the *EEC lnR*-matching and *modified lnR*-matching schemes cannot be applied reliably<sup>62</sup> and were not used.

\*The value of  $G_{21}$  cannot be estimated until a complete calculation of  $G_{22}$  is available.<sup>62</sup>

The fit ranges were initially chosen to be the same as for the  $\mathcal{O}(\alpha_s^2)$  fits except for the *EEC*, for which the fits were performed within the angular range  $90^\circ \leq \chi \leq 154.8^\circ$ , where the lower limit is the kinematic limit for the resummed+ $\mathcal{O}(\alpha_s^2)$  calculation. For the fit to  $D_2$  (D-scheme) a procedure<sup>63</sup> using the matched calculation for  $0.03 \leq y_{cut} < 0.05$  and the  $\mathcal{O}(\alpha_s^2)$  calculation for  $0.05 \leq y_{cut} \leq 0.33$  was adopted. Fits to determine  $\Lambda_{\overline{MS}}$ , and hence  $\alpha_s(M_Z^2)$ , were performed as described in the previous section. For illustration Figs. 6.4(a), 6.6(a), and 6.7(a) show the results of the resummed+ $\mathcal{O}(\alpha_s^2)$  QCD fits using the *modified lnR-matching* scheme with the renormalization scale factor  $f = 1$ . The data are well described by the QCD calculations within the fit ranges, and also beyond the fit ranges into the so-called ‘two-jet region’ or ‘Sudakov region’ where the resummed contributions are large.<sup>8,11</sup> This is discussed further at the end of this section. Figures 6.10 and 6.11 show (a)  $\alpha_s(M_Z^2)$  and (b) the corresponding  $\chi_{dof}^2$ , derived from fits at different values of  $f$ , for the four matching schemes.

Several features should be noted from Figs. 6.10 and 6.11. For each matching scheme and each observable the dependence of  $\alpha_s(M_Z^2)$  on  $f$  (Figs. 6.10(a) and 6.11(a)) is weaker than that from the  $\mathcal{O}(\alpha_s^2)$  fits (Figs. 6.8(a) and 6.9(a)); the range of  $f$  for which the fit quality is good (Figs. 6.10(b) and 6.11(b)) is in all cases smaller than the corresponding range from the  $\mathcal{O}(\alpha_s^2)$  fits (Figs. 6.8(b) and 6.9(b)), and some observables, most notably  $B_T$  and  $B_W$ , do display preferences for particular scales, typically in the range  $10^{-2} < f < 10$ . However, using the *R-matching* scheme it was found that the fit qualities for  $B_T$  and  $B_W$  to be very poor for all scales. For a given observable, at any given  $f$  the values of  $\alpha_s(M_Z^2)$  and  $\chi_{dof}^2$  are typically similar for both of the *lnR-matching* schemes; however, the results from the two *R-matching* schemes are typically systematically different both between the two schemes and with respect to the two *lnR-matching* schemes.

Since there is *a priori* no strong reason to reject individual matching

obs.	fit range	lnR matching	mod. lnR matching	R matching	mod. R matching
		$\alpha_s(M_Z^2) \pm \Delta\alpha_s$ f-range	$\alpha_s(M_Z^2) \pm \Delta\alpha_s$ f-range	$\alpha_s(M_Z^2) \pm \Delta\alpha_s$ f-range	$\alpha_s(M_Z^2) \pm \Delta\alpha_s$ f-range
$\tau$	0.06 – 0.32	$0.1196 \pm 0.0089$ $2.7 \times 10^{-3} - 4$	$0.1203 \pm 0.0089$ $2.7 \times 10^{-3} - 4$	$0.1226 \pm 0.0110$ $1.9 \times 10^{-3} - 4$	$0.1187 \pm 0.0091$ $2.3 \times 10^{-3} - 4$
$\rho$	0.04 – 0.32	$0.1151 \pm 0.0039$ $1.1 \times 10^{-2} - 4$	$0.1162 \pm 0.0047$ $1.1 \times 10^{-2} - 4$	$0.1178 \pm 0.0061$ $4.9 \times 10^{-3} - 4$	$0.1146 \pm 0.0044$ $1.0 \times 10^{-2} - 4$
$B_T$	0.12 – 0.32	$0.1175 \pm 0.0030$ $6.7 \times 10^{-2} - 4$	$0.1211 \pm 0.0015$ $3.0 \times 10^{-1} - 4$	–	$0.1177 \pm 0.0017$ $3.6 \times 10^{-2} - 4$
$B_W$	0.06 – 0.26	$0.1083 \pm 0.0016$ $8.2 \times 10^{-2} - 4$	$0.1095 \pm 0.0003$ $1.9 \times 10^{-1} - 4$	–	$0.1107 \pm 0.0034$ $4.9 \times 10^{-2} - 4$
$D_2(D)$	0.03 – 0.22	$0.1312 \pm 0.0060$ $1.5 \times 10^{-1} - 4$	$0.1313 \pm 0.0059$ $1.6 \times 10^{-1} - 4$	$0.1251 \pm 0.0053$ $7.0 \times 10^{-2} - 4$	N/A
<i>EEC</i>	$90.0^\circ - 154.8^\circ$	N/A	N/A	$0.1239 \pm 0.0049$ $6.1 \times 10^{-2} - 4$	$0.1336 \pm 0.0028$ $2.7 \times 10^{-1} - 4$

Table 6.10. Observables used in resummed+ $\mathcal{O}(\alpha_s^2)$  fits. For each the fit range, the range of the renormalization scale factor considered, the central  $\alpha_s(M_Z^2)$  value, and scale uncertainty ( $\Delta\alpha_s$ ) are given. Results are shown separately for each of the four matching schemes considered. Acceptable fits to the data could not be obtained for  $B_T$  and  $B_W$  with the *R-matching* scheme.

schemes from consideration, it is necessary to consider an additional theoretical uncertainty deriving from the matching ambiguity; this will be discussed below.

In order to quote a single  $\alpha_s(M_Z^2)$  value, and corresponding errors, for each observable the same procedure was applied as for the  $\mathcal{O}(\alpha_s^2)$  fits to the results from each matching scheme. Table 6.10 summarizes the  $f$ -ranges, central values of  $\alpha_s(M_Z^2)$ , and scale uncertainties. The experimental and hadronization systematic uncertainties were estimated by the methods described in the previous section and found to be similar to those from the  $\mathcal{O}(\alpha_s^2)$  analysis. For each observable the average  $\alpha_s(M_Z^2)$  value over all four matching schemes was then taken. The maximum deviation of  $\alpha_s(M_Z^2)$  from the central value was defined as the matching uncertainty, and was added in quadrature with the hadronization and scale uncertainties to obtain a total theoretical uncertainty for each observable. The scale and matching uncertainties *both* derive from uncalculated higher order perturbative contributions and are therefore correlated, although to an unknown degree. The inclusion of both contributions in the total theoretical uncertainty therefore represents a conservative, though not unreasonable, estimate of the effects of the higher order contributions. The central  $\alpha_s(M_Z^2)$  value, total experimental error, defined as the sum in quadrature of the statistical and experimental systematic errors, and the total theoretical uncertainty are listed in Table 6.10.

Comparing the results in Tables 6.9 and 6.11 it is apparent that the values of  $\alpha_s(M_Z^2)$  from the resummed+ $\mathcal{O}(\alpha_s^2)$  fits are lower than those from the  $\mathcal{O}(\alpha_s^2)$  fits by about 3% ( $\tau$ ), 6% ( $\rho$ ), and 7% ( $B_T$  and  $B_W$ ), but higher by about 4% ( $D_2(D)$ ) and 5% ( $EEC$ ). In addition, for all observables except  $D_2(D)$ , the theoretical uncertainty is considerably smaller for the resummed+ $\mathcal{O}(\alpha_s^2)$  case than for the  $\mathcal{O}(\alpha_s^2)$  case, despite the extra matching uncertainty contribution to the former. For  $D_2(D)$  the theoretical uncertainty is essentially the same for both  $\mathcal{O}(\alpha_s^2)$  and resummed+ $\mathcal{O}(\alpha_s^2)$  cases, which may relate to the fact that the resummation of next-to-leading logarithms of  $y_{cut}$  to all orders of  $\alpha_s$  is not

observable	$\alpha_s(M_Z^2)$	exp. error	theoretical uncertainty
$\tau$	0.1180	$\pm 0.0018$	$\pm 0.0115$
$\rho$	0.1163	$\pm 0.0020$	$\pm 0.0064$
$B_T$	0.1160	$\pm 0.0020$	$\pm 0.0048$
$B_W$	0.1074	$\pm 0.0025$	$\pm 0.0042$
$D_2(D)$	0.1297	$\pm 0.0035$	$\pm 0.0073$
$EEC$	0.1279	$\pm 0.0032$	$\pm 0.0069$

Table 6.11. The  $\alpha_s(M_Z^2)$  values derived from resummed+ $\mathcal{O}(\alpha_s^2)$  QCD fits.

complete<sup>†</sup>.<sup>10</sup> In all cases, however, the theoretical uncertainty is larger than the experimental error.

Combining the resummed+ $\mathcal{O}(\alpha_s^2)$  results from all six observables using an unweighted average we obtain  $\alpha_s(M_Z^2) = 0.1192 \pm 0.0025(\text{exp.}) \pm 0.0070(\text{theor.})$ , where the total experimental error is the sum in quadrature of the average statistical ( $\pm 0.0007$ ) and average experimental systematic ( $\pm 0.0024$ ) errors, and the total theoretical error is the sum in quadrature of the average hadronization ( $\pm 0.0016$ ) and average scale and matching ( $\pm 0.0065$ ) uncertainties. As a cross-check weighted averages were performed in order to combine the results from different measures. Weighting by experimental errors yields an average  $\alpha_s(M_Z^2)$  value different from the above by  $-0.0011$ ; weighting by the total errors yields an  $\alpha_s(M_Z^2)$  value different by  $-0.0015$ . These differences are of the same order as the statistical error on a single  $\alpha_s(M_Z^2)$  measurement and are hence negligible.

It is interesting to compare the resummed+ $\mathcal{O}(\alpha_s^2)$  result with the  $\mathcal{O}(\alpha_s^2)$  result. The final value quoted in the previous section is the average of the  $\mathcal{O}(\alpha_s^2)$  results over all 15 observables, whereas the value quoted above is the average of the resummed+ $\mathcal{O}(\alpha_s^2)$  results over a subset of 6 observables. For the purposes

<sup>†</sup>A complete analytic expression has recently been obtained.<sup>64</sup>



obs.	fit range	lnR matching	mod. lnR matching	R matching	mod. R matching
		$\alpha_s(M_Z^2) \pm \Delta\alpha_s$ f-range	$\alpha_s(M_Z^2) \pm \Delta\alpha_s$ f-range	$\alpha_s(M_Z^2) \pm \Delta\alpha_s$ f-range	$\alpha_s(M_Z^2) \pm \Delta\alpha_s$ f-range
$\tau$	0.02 – 0.32	$0.1170 \pm 0.0086$ $7.0 \times 10^{-2} - 4$	$0.1184 \pm 0.0075$ $1.4 \times 10^{-1} - 4$	–	$0.1191 \pm 0.0045$ $6.3 \times 10^{-1} - 4$
$\rho$	0.02 – 0.32	$0.1153 \pm 0.0071$ $2.6 \times 10^{-2} - 4$	$0.1146 \pm 0.0072$ $3.4 \times 10^{-2} - 4$	$0.1140 \pm 0.0054$ $2.0 \times 10^{-1} - 4$	$0.1124 \pm 0.0071$ $4.0 \times 10^{-2} - 4$
$B_T$	0.04 – 0.32	$0.1177 \pm 0.0040$ $2.0 \times 10^{-1} - 4$	$0.1202 \pm 0.0021$ $6.7 \times 10^{-2} - 4$	–	$0.1175 \pm 0.0023$ $1.1 \times 10^{-1} - 4$
$B_W$	0.04 – 0.26	$0.1078 \pm 0.0024$ $1.4 \times 10^{-1} - 4$	$0.1089 \pm 0.0014$ $2.8 \times 10^{-1} - 4$	–	$0.1106 \pm 0.0032$ $5.4 \times 10^{-2} - 4$
$D_2(D)$	0.01 – 0.22	$0.1269 \pm 0.0026$ $1.3 \times 10^{-1} - 4$	$0.1268 \pm 0.0025$ $1.3 \times 10^{-1} - 4$	–	N/A
$EEC$	90.0° – 162.0°	N/A	N/A	$0.1233 \pm 0.0043$ $6.9 \times 10^{-2} - 4$	$0.1337 \pm 0.0027$ $5.0 \times 10^{-1} - 4$

Table 6.12. Observables used in resummed+ $\mathcal{O}(\alpha_s^2)$  fits with the fit ranges extended into the two-jet region. For each the fit range, the range of the renormalization scale factor considered, the central  $\alpha_s(M_Z^2)$  value, and scale uncertainty ( $\Delta\alpha_s$ ) are given. Results are shown separately for each of the four matching schemes considered. Acceptable fits to the data could not be obtained for  $\tau$ ,  $B_T$ ,  $B_W$ , and  $D_2(D)$  with the *R-matching* scheme.

of comparison the  $\mathcal{O}(\alpha_s^2)$  results were averaged for  $\tau$ ,  $\rho$ ,  $B_T$ ,  $B_W$ ,  $D_2(D)$ , and  $EEC$  to obtain  $\alpha_s(M_Z^2) = 0.1242 \pm 0.0026(\text{exp.}) \pm 0.0132(\text{theor.})$ . For the *same set* of six observables, therefore, it could be found that the central  $\alpha_s(M_Z^2)$  values derived from  $\mathcal{O}(\alpha_s^2)$  and resummed+ $\mathcal{O}(\alpha_s^2)$  fits in the *same range* of each observable are in agreement to within the (correlated) experimental errors, and that the theoretical uncertainty is significantly smaller when the resummed calculations are employed.

From Figs. 6.4(a), 6.6(a), and 6.7(a), it is clear that the resummed+ $\mathcal{O}(\alpha_s^2)$

calculations are more successful than the  $\mathcal{O}(\alpha_s^2)$  calculations in describing the two-jet (Sudakov) region. This implies that multiple emissions of soft gluons, which are taken into account in the resummed terms, contribute significantly to this region. Therefore, for each observable we extended the fit range into the two-jet region and extracted  $\alpha_s(M_Z^2)$  as a function of the renormalization scale factor  $f$ . Requirements (1)-(3) (section 6.2) were applied. In addition, for  $D_2(D)$  we required the 5-jet production rate  $R_5$  to be less than 1%; for the  $EEC$  the upper limit of the fit range was extended to  $\chi = 162^\circ$  by applying the empirical criterion  $\chi_{\text{dof}}^2 < 5$ . The fit ranges are listed in Table 6.12.

The same procedure as above was applied to define a range of renormalization scale factor  $f$  over which to calculate a central  $\alpha_s(M_Z^2)$  value and scale uncertainty for each observable; the  $f$ -range, central  $\alpha_s(M_Z^2)$  value, and scale uncertainty are listed in Table 6.12 separately for fits using each of the four matching schemes. Good fits with  $\chi_{\text{dof}}^2 < 5$  could not be obtained using the *R-matching* scheme for  $\tau$ ,  $B_T$ ,  $B_W$ , and  $D_2(D)$  for any extension of the fit range beyond that used for the  $\mathcal{O}(\alpha_s^2)$  fits. By comparing Tables 6.10 and 6.12 it can be seen that the maximum change in  $\alpha_s(M_Z^2)$  when the fit range is extended into the two-jet region is  $-0.0026$  for  $\tau$  (*lnR-matching*),  $-0.0038$  for  $\rho$  (*R-matching*),  $-0.0009$  for  $B_T$  (*modified lnR-matching*),  $-0.0006$  for  $B_W$  (*modified lnR-matching*),  $-0.0045$  for  $D_2(D)$  (*modified lnR-matching*), and  $-0.0006$  for the  $EEC$  (*R-matching*). These shifts are smaller than, or comparable with, the experimental errors, and are much smaller than the theoretical uncertainties.

For each observable the average  $\alpha_s(M_Z^2)$  value over all four matching schemes, and the matching uncertainty, were calculated as before. The central  $\alpha_s(M_Z^2)$  value, the total experimental error, and the total theoretical uncertainty, defined as before, are listed in Table 6.13. Averaging over the six

observable	$\alpha_s(M_Z^2)$	exp. error	theoretical uncertainty
$\tau$	0.1159	$\pm 0.0017$	$\pm 0.0090$
$\rho$	0.1144	$\pm 0.0019$	$\pm 0.0074$
$B_T$	0.1157	$\pm 0.0020$	$\pm 0.0053$
$B_W$	0.1070	$\pm 0.0025$	$\pm 0.0041$
$D_2(D)$	0.1274	$\pm 0.0034$	$\pm 0.0027$
$EEC$	0.1285	$\pm 0.0032$	$\pm 0.0068$

Table 6.13. The  $\alpha_s(M_Z^2)$  values derived from resummed+ $\mathcal{O}(\alpha_s^2)$  QCD fits with the fit ranges extended into the two-jet region.

observables, as above, then yields

$$\alpha_s(M_Z^2) = 0.1181 \pm 0.0024(\text{exp.}) \pm 0.0057(\text{theor.}),$$

which is in good agreement with the above average of results from the restricted fit ranges.

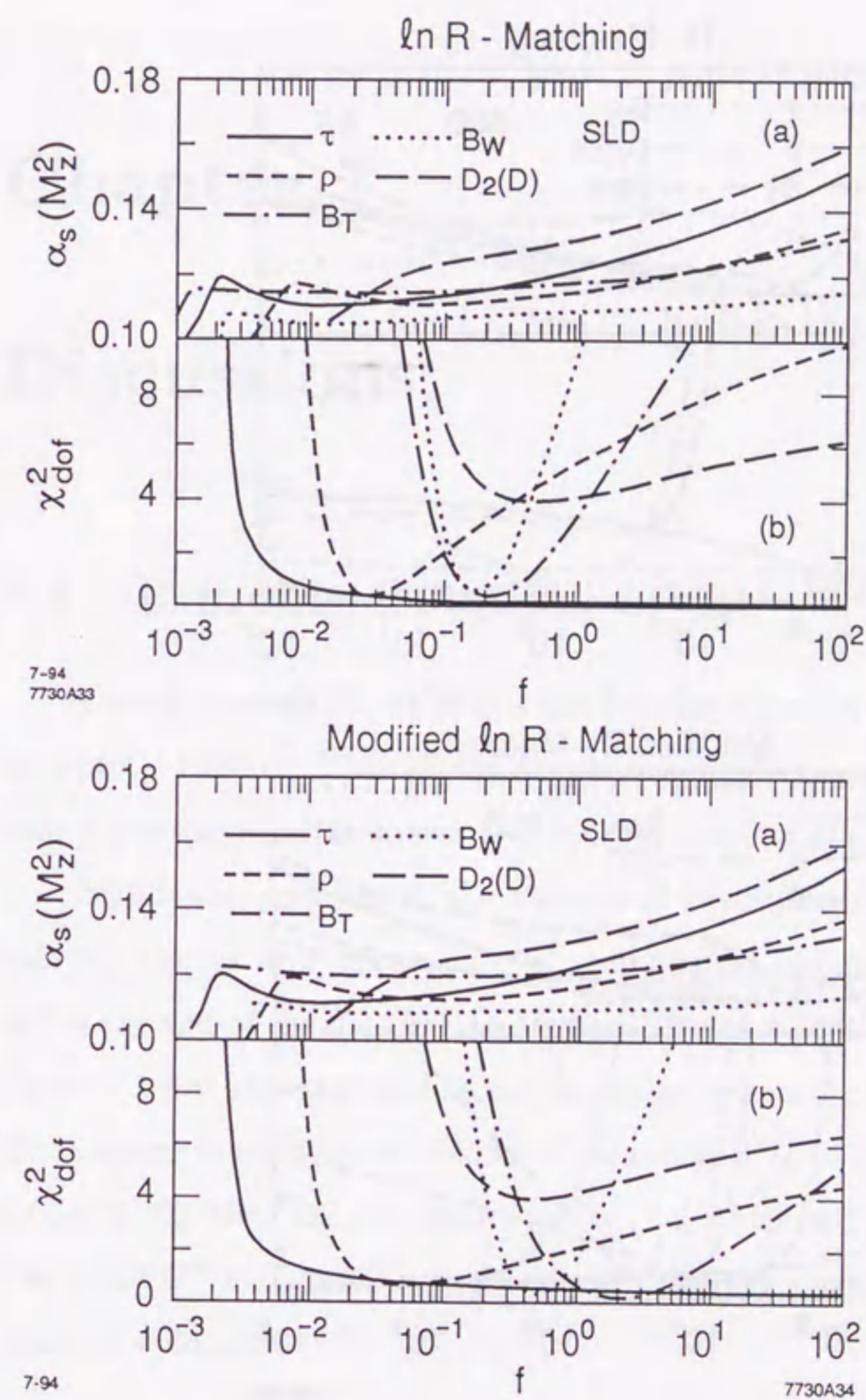


Fig. 6.10. (a)  $\alpha_s(M_Z^2)$  and (b)  $\chi^2_{\text{dof}}$  from the resummed+ $\mathcal{O}(\alpha_s^2)$  fits with  $\ln R$ - (top) and modified  $\ln R$ -matching (bottom) as a function of renormalization scale factor  $f$ .

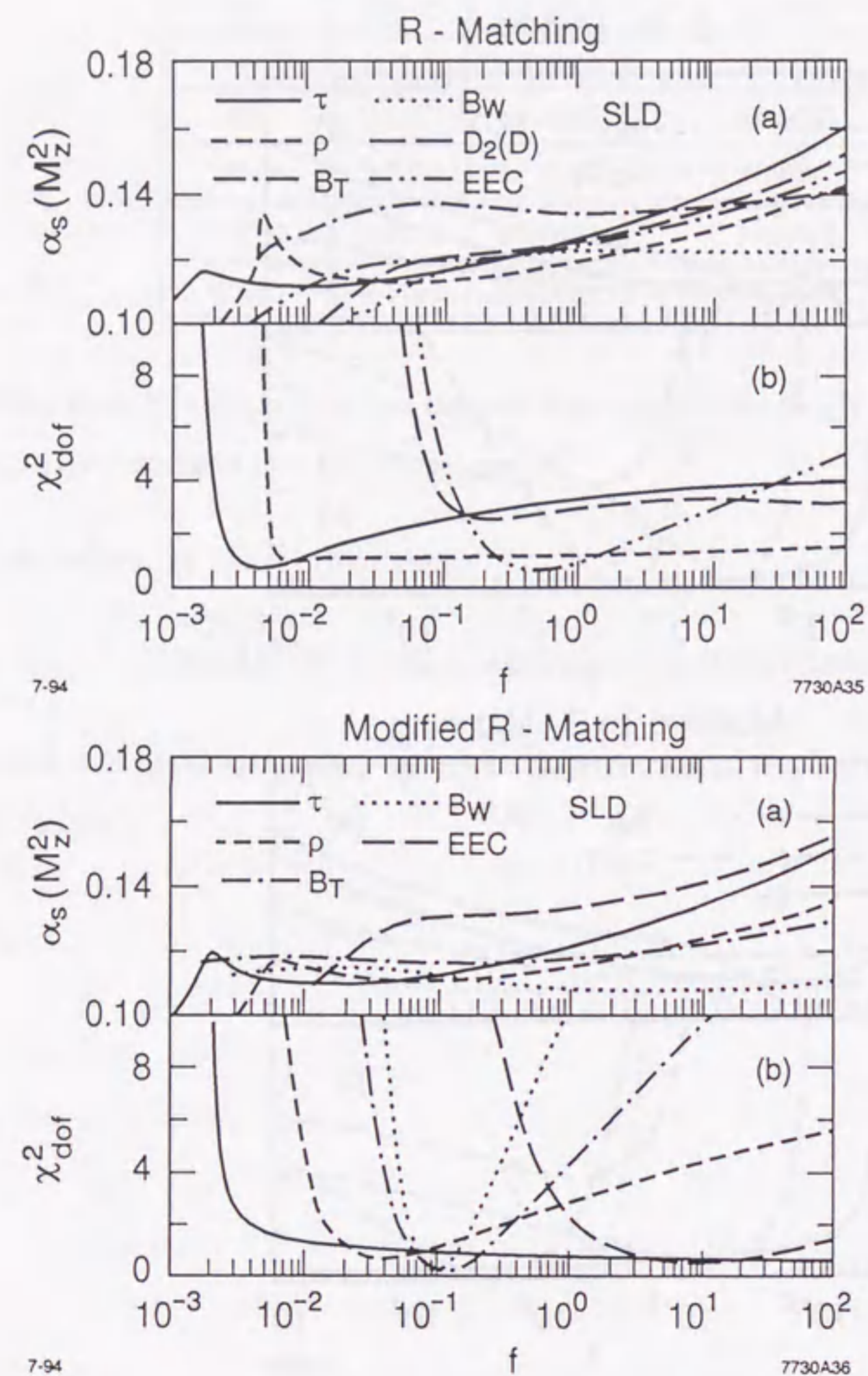


Fig. 6.11. (a)  $\alpha_s(M_Z^2)$  and (b)  $\chi^2_{\text{dof}}$  from the resummed  $+\mathcal{O}(\alpha_s^2)$  fits with *R*- (top) and *modified R*-matching (bottom) as a function of renormalization scale factor  $f$ .

## Chapter 7

### Discussions

#### 7.1 Running Coupling of $\alpha_s$

The nature of QCD, which is a non-Abelian theory, is characterized by an asymptotic freedom. This implies the strong coupling  $\alpha_s$  decreases as energy scale increases, which is known as a *running coupling of  $\alpha_s$* .

Significant progress in the theoretical predictions for the reaction of hadronic decays or  $\tau$  decays in  $e^+e^-$  annihilation has been made since the end of the end of the data taking at the PEP and PETRA in the late 1980s. Figure 7.1 just shows several recent results as well as the SLD results in this thesis among many progress results. The running of  $\alpha_s$  in terms of  $\Lambda_{\overline{MS}} = 100, 200, \text{ and } 300 \text{ MeV}$  are also shown in Fig. 7.1, which are predicted by QCD. The ALEPH<sup>65</sup> and CLEO collaborations<sup>66</sup> reported measurement of  $\alpha_s$  using hadronic  $\tau$  decays:

$$\alpha_s(M_\tau^2) = 0.330 \pm 0.046 \quad (\text{ALEPH}) \quad (7.1)$$

and

$$\alpha_s(M_\tau^2) = 0.309 \pm 0.024 \quad (\text{CLEO}). \quad (7.2)$$

The analysis comprised not only the total  $\tau$  hadronic width but also spectral

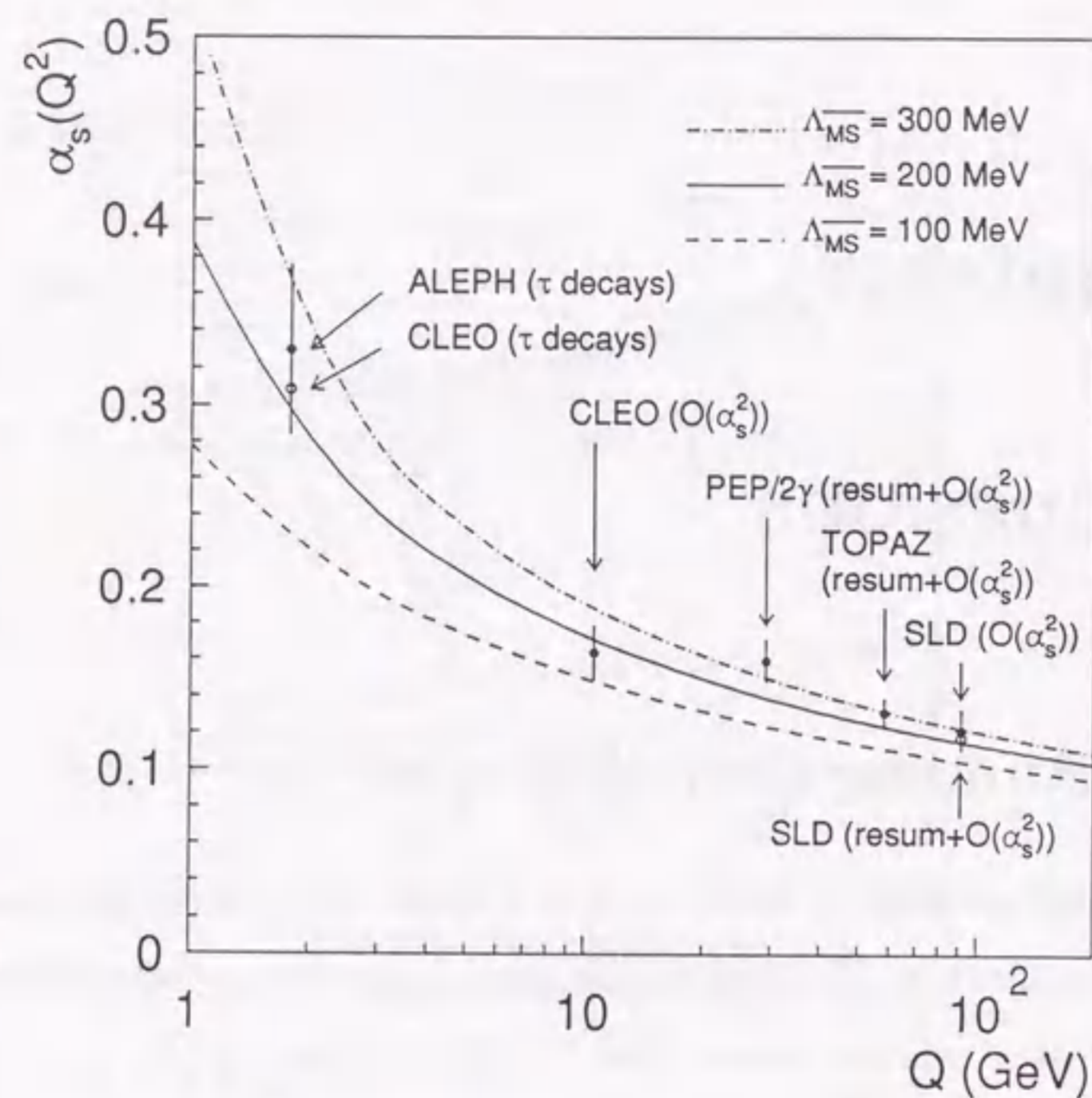


Fig. 7.1. The energy scale dependence of  $\alpha_s$ . Several recent results from different experiments are shown here.

moments of the invariant mass distribution of the hadron, which have been calculated to  $\mathcal{O}(\alpha_s^3)$ .

The CLEO collaboration also reported preliminary results<sup>67</sup> on  $e^+e^-$  jet rates in the four-flavor continuum at center-of-mass energy  $\sqrt{s} = 10.53$  GeV. Their analysis comprise the differential 2-jet rate calculated in the Durham scheme, which is similar to those at higher energies. The  $\alpha_s$  value at  $\sqrt{s} = 10.53$  GeV is obtained

$$\alpha_s(10.53^2 \text{GeV}^2) = 0.164 \pm 0.004(\text{exp.}) \pm 0.014(\text{theor.}) \quad (\text{CLEO}).(7.3)$$

The theoretical uncertainty is dominated by the renormalization scale depen-

dence of the  $\mathcal{O}(\alpha_s^2)$  prediction.

Proceeding to higher energies,  $\alpha_s$  has been measured using the resummed+ $\mathcal{O}(\alpha_s^2)$  prediction by the TPC/2 $\gamma$  and TOPAZ collaborations at 29 and 58 GeV respectively. The result of TPC/2 $\gamma$  using the differential 2-jet rate calculated in the Durham scheme is<sup>68</sup>

$$\alpha_s(29^2 \text{GeV}^2) = 0.160 \pm 0.012 \quad (\text{TPC}/2\gamma),$$

and that of TOPAZ using the thrust, heavy jet mass, and differential 2-jet rate (Durham scheme) is<sup>69</sup>

$$\alpha_s(58^2 \text{GeV}^2) = 0.132 \pm 0.008 \quad (\text{TOPAZ}).$$

The errors are also dominated by the renormalization scale uncertainty.

Figure 7.1 shows the experimental evidence for the variation of  $\alpha_s(Q^2)$  with  $Q$ .

	Experiment	Theory	$\alpha_s(M_Z^2)$
ALEPH <sup>24</sup>	shapes and jet rates	Resummed+ $\mathcal{O}(\alpha_s^2)$	$0.125 \pm 0.005$
DELPHI <sup>5</sup>	shapes, jet rates, and correlations	$\mathcal{O}(\alpha_s^2)$	$0.113 \pm 0.007$
DELPHI <sup>23</sup>	shapes, jet rates, and correlations	Resummed+ $\mathcal{O}(\alpha_s^2)$	$0.123 \pm 0.006$
L3 <sup>70</sup>	shapes, jet rates, and correlations	Resummed+ $\mathcal{O}(\alpha_s^2)$	$0.125 \pm 0.009$
OPAL <sup>6</sup>	shapes, jet rates, and correlations	$\mathcal{O}(\alpha_s^2)$	$0.122^{+0.006}_{-0.005}$
OPAL <sup>62</sup>	shapes, jet rates, and correlations	Resummed+ $\mathcal{O}(\alpha_s^2)$	$0.120 \pm 0.006$
OPAL <sup>71</sup>	cone jet algorithm*	$\mathcal{O}(\alpha_s^2)$	$0.119 \pm 0.008$
OPAL <sup>71</sup>	cone jet algorithm†	$\mathcal{O}(\alpha_s^2)$	$0.116 \pm 0.008$
SLD	shapes, jet rates, and correlations	$\mathcal{O}(\alpha_s^2)$	$0.123 \pm 0.011$
SLD	shapes, jet rates, and correlations	Resummed+ $\mathcal{O}(\alpha_s^2)$	$0.118 \pm 0.006$

Table 7.1. Summary of some of the  $\alpha_s$  measurement at the  $Z^0$  resonance.

At  $Z^0$  energy the study of the strong coupling  $\alpha_s$  was performed by not only SLD but also the four experimental groups at LEP. In order to compare

\*The analysis utilized the dependence of jet rates on the minimum jet energy.

†The analysis utilized the dependence of the angular size of the cone.

the results in this analysis with those from LEP, the values of  $\alpha_s(M_Z^2)$  are summarized in Table 7.1. The results from SLD are consistent with the LEP experiments in  $e^+e^-$  annihilation at the  $Z^0$  resonance.

## 7.2 Optimization of Renormalization Scale

One of the serious difficulties making impossible precise determination of the strong coupling  $\alpha_s$  is the scale uncertainty of the perturbative QCD predictions. A measurable observable described in chapter 5 is written in the form

$$R(y, f) = \mathcal{A}(y)\tilde{\alpha}_s + \left[ \mathcal{B}(y) + \mathcal{A}(y)\frac{\beta_0}{2} \ln f \right] \tilde{\alpha}_s^2 + \dots, \quad (7.4)$$

where  $f \equiv \mu^2/Q^2$ ,  $\beta_0 = 11 - 2n_f/3$ , and  $\tilde{\alpha}_s \equiv \alpha_s(\mu^2)/2\pi$  is the renormalized coupling defined in a specific renormalization scheme such as  $\overline{\text{MS}}$ . Since  $R(y, f)$  is a physical quantity, it must be independent of the choice of the renormalization scale  $\mu$  as well as renormalization scheme. However, the predictions depend on  $\mu$  because of the truncated perturbative QCD predictions to a given finite order  $\alpha_s^n$ . In fact only up to  $\mathcal{O}(\alpha_s^2)$  ( $\mathcal{O}(\alpha_s^3)$  for  $\tau$  decays or total hadronic decay width) and the LL and NLL terms to all orders in  $\alpha_s$  can be controlled now.

The renormalization scale dependence of the truncated QCD predictions is often used as a guide to assess the accuracy of the perturbative predictions, because this dependence reflects the presence of the uncalculated terms. However, the renormalization scale dependence of  $R(y, f)$  only reflects one aspect of the total series, which has been recently pointed out by Maxwell *et al.*<sup>72</sup>

Various methods to set the renormalization scale in the perturbative QCD predictions up to  $\mathcal{O}(\alpha_s^2)$  have been proposed in the literature:

- *Fastest Apparent Convergence (FAC)*.<sup>73</sup> This corresponds to a choice of

renormalization scale  $\mu$  such that the next-to-leading order coefficient:

$$\mathcal{B}(y) + \mathcal{A}(y)\frac{\beta_0}{2} \ln f = 0. \quad (7.5)$$

Thus, the renormalization scale factor is set to

$$f \equiv \frac{\mu^2}{Q^2} = \exp \left[ -\frac{2}{\beta_0} \left( \frac{\mathcal{B}(y)}{\mathcal{A}(y)} \right) \right]. \quad (7.6)$$

- *Principle of Minimum Sensitivity (PMS)*.<sup>74</sup> Since the exact (all orders) result is independent of the renormalization scale, the idea is that one should choose the second order approximation  $R^{\mathcal{O}(\alpha_s^2)}(y, f)$  to mimic the property of the exact result and to be as insensitive as possible to the choice of the renormalization scale  $\mu$ . This suggests that

$$\frac{dR^{\mathcal{O}(\alpha_s^2)}(y, f)}{d\mu} = 0 \quad (7.7)$$

and the PMS scheme chooses the renormalization scale factor:

$$f \equiv \frac{\mu^2}{Q^2} = \exp \left[ -\frac{2}{\beta_0} \left( \frac{\mathcal{B}(y)}{\mathcal{A}(y)} + \frac{\beta_1}{2(\beta_0 + \beta_1\tilde{\alpha}_s)} \right) \right]. \quad (7.8)$$

- *Brodsky-Lepage-Mackenzie (BLM)*.<sup>4</sup> In the BLM scale-fixing method, the scale is chosen such that the coefficients  $\mathcal{A}(y)$  and  $\mathcal{B}(y)$  are independent of the number of quark flavors  $n_f$  renormalizing the gluon propagators. This prescription ensures that, as in quantum electrodynamics, vacuum polarization contributions due to fermion pairs are all incorporated into coupling rather than the coefficients. In the case of non-Abelian theory, the BLM method resums the corresponding gluon as well as quark vacuum polarization contributions because the coupling  $\alpha_s$  is controlled by  $\beta$  function.
- *Fitting  $\mu$  and  $\Lambda_{\overline{\text{MS}}}$  to the data*.<sup>6</sup> This method is a simultaneous best fit for  $\mu$  and  $\Lambda_{\overline{\text{MS}}}$  for each observable over a range of the kinematical variables.

Figure 7.2 shows the optimized scale for each observables over a range of the kinematical variables using FAC and PMS. It should be emphasized that FAC and PMS in NLO are very similar since the difference between them is the term of  $\sim \exp(-\beta_1/\beta_0^2)$ . It is also true that NNLO (Next-to-Next-to-Leading Order) FAC and PMS remain close to each other.<sup>75</sup> For the PMS approach, however, the coupling and  $\beta$  function are unphysical quantities, and it is not clear even if their all orders are defined.

Figure 7.3 shows the  $\alpha_s$  values obtained from (a) FAC and PMS, and (b) fitting at fixed scale  $f = 1$  and fitting of  $f$  and  $\Lambda_{\overline{MS}}$  simultaneously. The results from SLD (this thesis) are also indicated in the figure. For  $B_T$  fitting procedure using FAC and PMS could not be done due to poor convergence at FAC and PMS scale. For  $D_2$  calculated in P0-scheme and  $AEEC$  by fitting of  $f$  and  $\Lambda_{\overline{MS}}$  could not be done because a clear minimum point of  $\chi^2$  could not be found between the  $f$  range considered. From Fig. 7.3 the results of SLD covers the results from above four scale fixing methods, namely FAC, PMS, fixed scale  $f = 1$ , and fitting of  $f$  and  $\Lambda_{\overline{MS}}$ , except for  $AEEC$ . It should be noted that the evaluation of the uncertainties on  $\alpha_s$  in the SLD results is the most conservative.

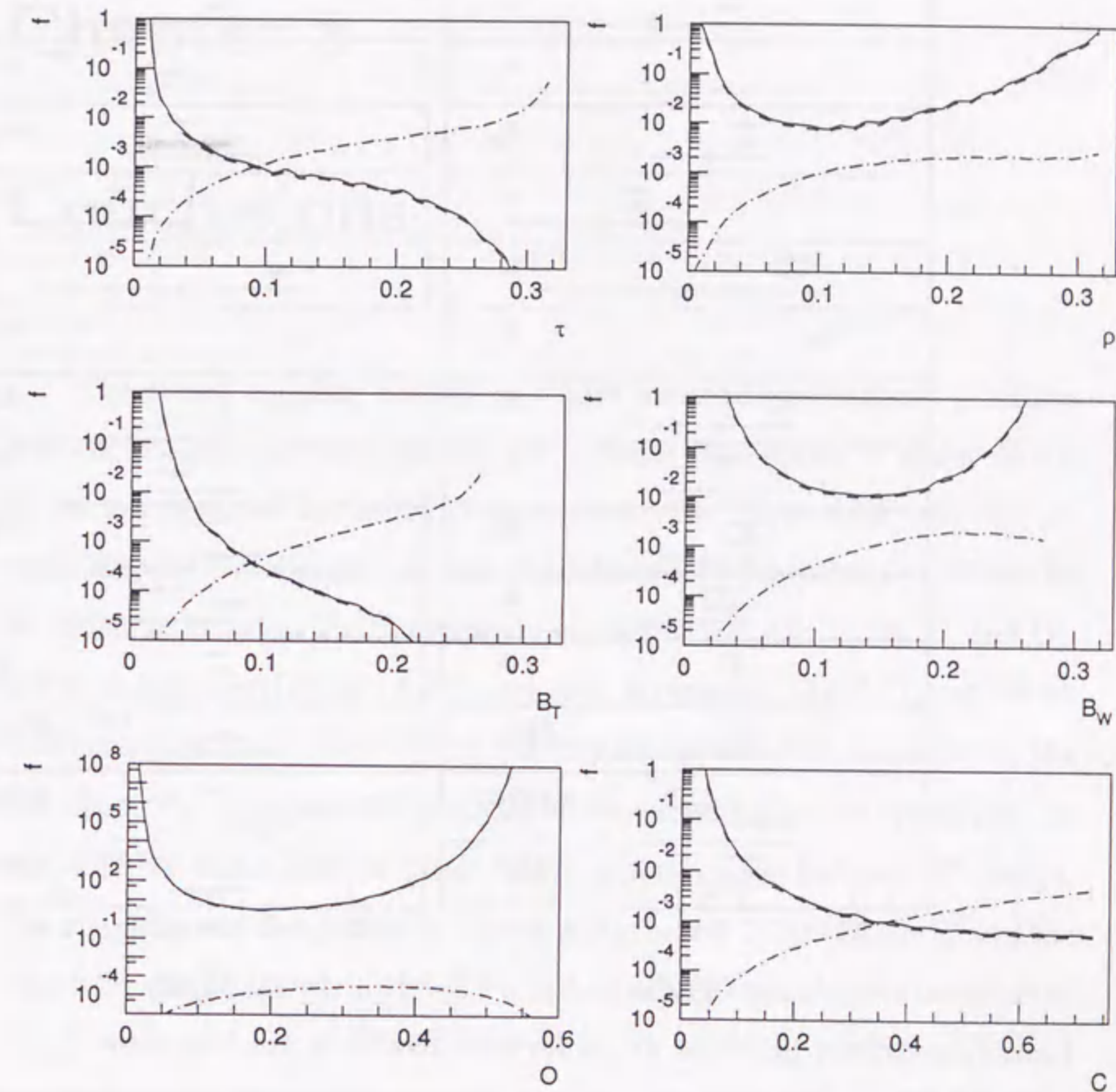


Fig. 7.2. Optimized scale  $f$  as a function of variable for event shapes. Solid line shows the scale from FAC, and dashed line shows PMS, and dot-dashed line shows BLM method.

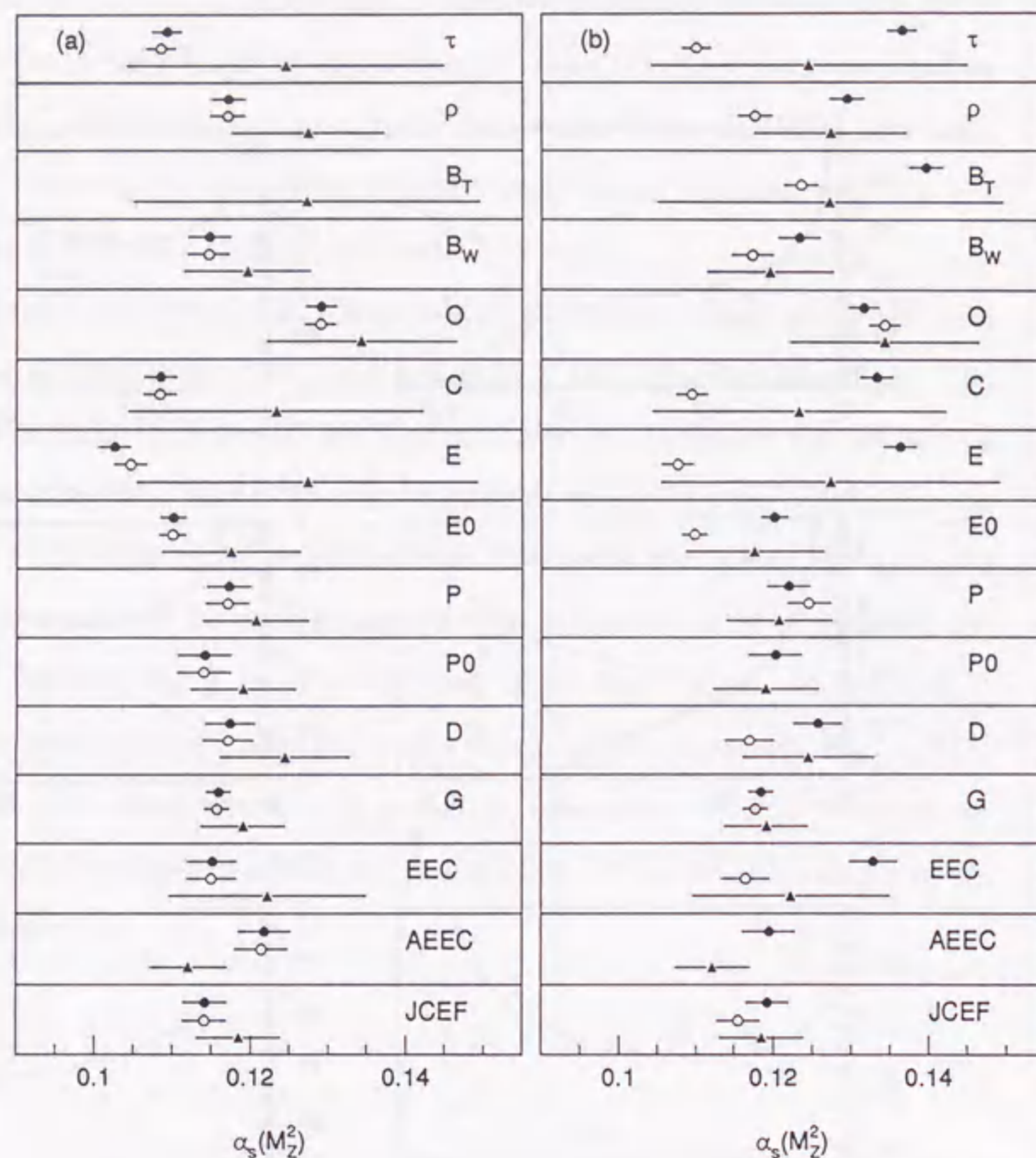


Fig. 7.3. The results of  $\alpha_s$  using various scale optimizing methods. (a) Solid circle shows the results of FAC, open circle those of PMS, and triangle indicates the results of SLD (this thesis). The error bars for FAC and PMS are only experimental errors, and those for the SLD results are total errors including both experimental and theoretical uncertainties. (b) Solid circle shows the results at the fixed scale  $f = 1$ , and open circle those of fitting of scale  $f$  and  $\Lambda_{\overline{MS}}$  simultaneously whose errors are experimental errors only. The results of SLD are also indicated.

## Chapter 8

### Conclusions

The strong coupling  $\alpha_s(M_Z^2)$  has been measured by analyses of fifteen different observables that describe the hadronic final states of about 60,000  $Z^0$  decays recorded by the SLD experiment. The observables comprise six event shapes ( $\tau$ ,  $\rho$ ,  $B_T$ ,  $B_W$ ,  $O$ , and  $C$ ), differential 2-jet rates ( $D_2$ ) defined by six different jet resolution/recombination schemes (E, E0, P, P0, D, and G), energy-energy correlations (EEC) and their asymmetry (AEEC), and the jet cone energy fraction (JCEF). The quantity JCEF has been measured for the first time. The measured distributions of these observables are reproduced by the JETSET and HERWIG Monte Carlo simulations of hadronic  $Z^0$  decays. The coupling was determined by fitting perturbative QCD calculations to the data corrected to the parton level. Perturbative QCD calculations complete to  $\mathcal{O}(\alpha_s^2)$  were used for all fifteen observables. In addition, recently-performed resummed calculations were matched to the  $\mathcal{O}(\alpha_s^2)$  calculations using four matching schemes and applied to the six observables for which the resummed calculations are available.

It can be found that the  $\mathcal{O}(\alpha_s^2)$  calculations are able to describe the data in the hard 3-jet region of all 15 observables for a wide range of the QCD renormalization scale factor  $f$ . The fitted  $\alpha_s(M_Z^2)$  value depends strongly both on the choice of  $f$ , which limits the precision of the  $\alpha_s(M_Z^2)$  measurement from

each observable, and on the choice of observable. The *AEEC* shows the smallest renormalization scale uncertainty of about 3%, which is just larger than the experimental error. The  $\alpha_s(M_Z^2)$  values from the various observables are consistent with each other only within the scale uncertainties. The large scale uncertainties and systematically different  $\alpha_s(M_Z^2)$  values determined from different observables imply that the uncalculated  $\mathcal{O}(\alpha_s^3)$  perturbative QCD contributions are significant and cannot be ignored if  $\alpha_s(M_Z^2)$  is to be determined with a precision of better than 10%.

The resummed+ $\mathcal{O}(\alpha_s^2)$  calculations yield a reduced renormalization scale dependence of  $\alpha_s(M_Z^2)$ , and fit a wider kinematic region, including the two-jet or Sudakov region, and give similar fitted values of  $\alpha_s(M_Z^2)$  to the  $\mathcal{O}(\alpha_s^2)$  case. However, the different matching schemes give different  $\alpha_s(M_Z^2)$  values, which reflects a residual uncertainty in the inclusion of terms in the resummed+ $\mathcal{O}(\alpha_s^2)$  calculations. For all observables except  $D_2(D)$  the theoretical uncertainty is smaller than in the  $\mathcal{O}(\alpha_s^2)$  case, but still dominates the uncertainty in the measurement of  $\alpha_s(M_Z^2)$ .

Figure 8.1 summarizes the measured  $\alpha_s(M_Z^2)$  values from all fifteen observables using  $\mathcal{O}(\alpha_s^2)$  calculations, and from the six observables using resummed+ $\mathcal{O}(\alpha_s^2)$  calculations in the extended kinematic region. Since the same data were used to measure all observables, and the observables are highly correlated, the results were combined by taking unweighted averages of the  $\alpha_s(M_Z^2)$  values and experimental and theoretical errors, obtaining

$$\begin{aligned}\alpha_s(M_Z^2) &= 0.1225 \pm 0.0026(\text{exp.}) \pm 0.0109(\text{theor.}) && \mathcal{O}(\alpha_s^2) \\ \alpha_s(M_Z^2) &= 0.1181 \pm 0.0024(\text{exp.}) \pm 0.0057(\text{theor.}) && \text{resummed} + \mathcal{O}(\alpha_s^2),\end{aligned}$$

where in both cases the theoretical uncertainty is dominated by the lack of knowledge of higher order terms in the QCD calculations. Here the estimation of the theoretical uncertainty is larger than that quoted by some of the LEP experiments because more observables and wider variations of the renormal-

ization scale have been considered, and unweighted averages have been taken. These average values are shown in Fig. 8.1; they are consistent with measurements from other  $e^+e^-$  experiments at the  $Z^0$  resonance<sup>55,23,24,62,70</sup> and from lower energy  $e^+e^-$  and deep inelastic scattering experiments.<sup>76</sup>

One expects *a priori* the  $\alpha_s(M_Z^2)$  value determined from a resummed+ $\mathcal{O}(\alpha_s^2)$  fit to be more reliable than that from an  $\mathcal{O}(\alpha_s^2)$  fit. However, the former is only available for six of the fifteen observables. In order to quote a final result, therefore, we took the unweighted average of the  $\alpha_s(M_Z^2)$  values and uncertainties over the combined set of six resummed+ $\mathcal{O}(\alpha_s^2)$  results and nine  $\mathcal{O}(\alpha_s^2)$  results for which there is no corresponding resummed+ $\mathcal{O}(\alpha_s^2)$  result. This yields a final average of

$$\alpha_s(M_Z^2) = 0.1200 \pm 0.0025(\text{exp.}) \pm 0.0078(\text{theor.}),$$

also shown in Fig. 8.1, corresponding to  $\Lambda_{\overline{MS}} = 253_{-96}^{+130}$  MeV.



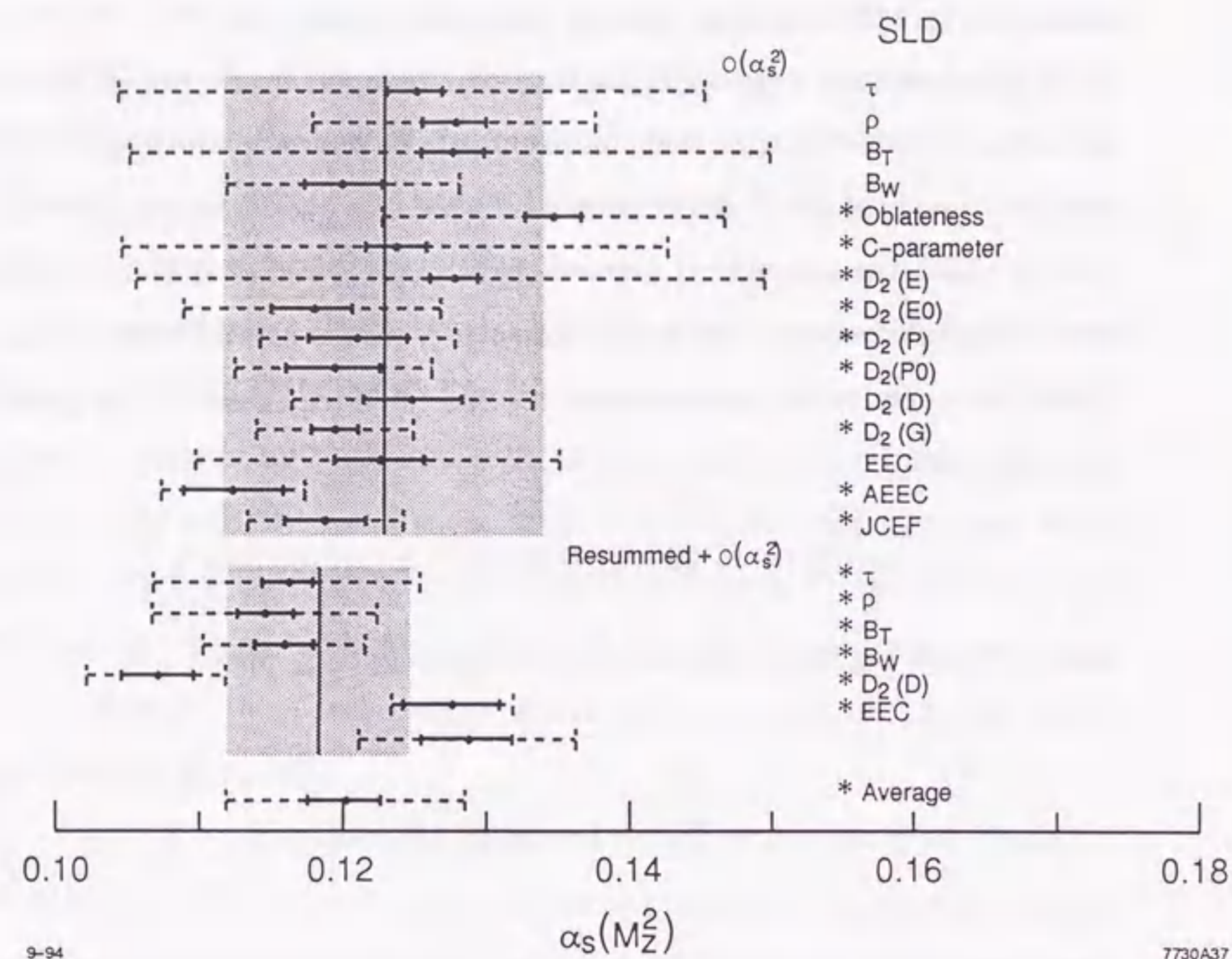


Fig. 8.1. Compilation of final values of  $\alpha_s(M_Z^2)$ . For each observable the solid bar denotes the experimental error, while the dashed bar shows the total uncertainty comprising the experimental error and theoretical uncertainty in quadrature. Shown separately for the  $\mathcal{O}(\alpha_s^2)$  results and resummed+ $\mathcal{O}(\alpha_s^2)$  results are a vertical line and a shaded region representing the average  $\alpha_s(M_Z^2)$  value and uncertainty, respectively, in each case. Also shown is the final average of six resummed+ $\mathcal{O}(\alpha_s^2)$  and nine  $\mathcal{O}(\alpha_s^2)$  results indicated by stars.

## References

1. SLD Collab., K. Abe *et al.*, Phys. Rev. Lett. **73** (1994) 25.  
LEP Collaborations and LEP Electroweak Working Group, CERN-PPE-93-157 (1993).
2. H. Fritzsch, M. Gell-Mann and H. Leutwyler, Phys. Lett. **B47** (1973) 365.  
D. J. Gross and F. Wilczek, Phys. Rev. Lett. **30** (1973) 1343.  
H. D. Politzer, Phys. Rev. Lett. **30** (1973) 1346.
3. W.A. Bardeen *et al.*, Phys. Rev. **D18** (1978) 3998.
4. S.J. Brodsky and H.J. Lu, SLAC-PUB-6481 (1994); to appear in Phys. Rev. **D**.
5. DELPHI Collab., P. Abreu *et al.*, Z Phys. **C54** (1992) 55.
6. OPAL Collab., P.D. Acton *et al.*, Z Phys. **C55** (1992) 1.
7. Z. Kunszt, P. Nason, G. Marchesini and B.R. Webber, Proceedings of the Workshop on Z Physics at LEP I, eds. G. Altarelli, R. Kleiss and C. Verzegnassi, CERN Report 89-08 (1989).
8. S. Catani, G. Turnock, B.R. Webber and L. Trentadue, Phys. Lett. **B263** (1991) 491.
9. S. Catani, G. Turnock and B.R. Webber, Phys. Lett. **B272** (1991) 368.
10. S. Catani, Yu.L. Dokshitzer, M. Olsson, G. Turnock and B.R. Webber, Phys. Lett. **B269** (1991) 432.
11. S. Catani, G. Turnock and B.R. Webber, CERN-TH-6570/92 (1992).
12. G. Turnock, Cavendish-HEP-92/3 (1992).
13. S. Catani, L. Trentadue, G. Turnock and B.R. Webber, Nucl. Phys. **B407** (1993) 3.
14. Gauge-invariant regularization is discussed by W. Pauli and F. Villars, Rev. Mod. Phys. **21** (1949) 434.  
Dimensional regularization is discussed by G. 't Hooft and M. Veltman, Nucl. Phys. **B44** (1972) 189.  
See also E. R. Speer in "Renormalization Theory", Erice Summer School

- 1975, edited by G. Velo and A.S. Wightman, D. Reidel publishing company, Dordrecht, Holland, and Boston, Mass., 1976.
15. N.N. Bogoliubov and O.S. Parasiuk, *Acta Math.*, **97** (1957) 227, appear also in the textbook of the first author and D.V. Shirkov, "Introduction to the Theory of Quantized Fields", Interscience, New York, 1959.
  16. Early work on the renormalization group was done by E.C.G. Stueckelberg and A. Peterman, *Helv. Phys. Acta*, **26** (1953) 499, and M. Gell-Mann and F.E. Low, *Phys. Rev.* **95** (1954) 1300.
  17. R.K. Ellis, D.A. Ross and A.E. Terrano, *Nucl. Phys.* **B178** (1981) 421.
  18. S. Brandt *et al.*, *Phys. Lett.* **12** (1964) 57.  
E. Farhi, *Phys. Rev. Lett.* **39** (1977) 1587.
  19. L. Clavelli, *Phys. Lett.* **B85** (1979) 111.
  20. S. Catani, G. Turnock and B. R. Webber, *Phys. Lett.* **B295** (1992) 269.
  21. S. Bethke *et al.*, *Nucl. Phys.* **B370** (1992) 310.
  22. C.L. Basham *et al.*, *Phys. Rev. Lett.* **41** (1978) 1585;  
*Phys. Rev.* **D17** (1978) 2298;  
*Phys. Rev.* **D19** (1979) 2018.
  23. DELPHI Collab., P. Abreu *et al.*, *Z. Phys.* **C59** (1993) 21.
  24. ALEPH Collab., D. Decamp *et al.*, *Phys. Lett.* **B284** (1992) 163.
  25. B.R. Webber, CERN-TH-6706-92 (1992);  
Proceedings of the Workshop "QCD-20 years later", Aachen, June 9-13, 1992.
  26. D. Schultz *et al.*, SLAC-PUB-6060 (1993).
  27. J.E. Clendenin *et al.*, SLAC-PUB-6080 (1993).
  28. T.H. Fieguth and J.J. Murray, SLAC-PUB-3174 (1983); published in *Fermilab Accel.* (1983) 401.
  29. T. Limberg *et al.*, SLAC-PUB-6210 (1993).
  30. F.J. Decker *et al.*, SLD Note 238 (unpublished) (1994).
  31. SLD Design Report, SLAC Report 273 (1984).

32. C. J. S. Damerell *et al.*, *Nucl. Inst. Meth.* **A288** (1990) 288. M.G. Strauss *et al.*, SLAC-PUB-5970 (1992).
33. M. Cavalli-Sforza *et al.*, SLAC-PUB-5123 (1990).
34. D. Axen *et al.*, *Nucl. Inst. Meth.* **A328** (1993) 472.
35. A. C. Benvenuti *et al.*, *Nucl. Inst. Meth.* **A290** (1990) 353.
36. S.C. Berridge *et al.*, SLAC-PUB-5694 (1991).
37. T. Sjöstrand and M. Bengtsson, *Comp. Phys. Comm.* **43** (1987) 367.
38. G. Marchesini *et al.*, *Comp. Phys. Comm.* **67** (1992) 465.
39. F.A. Brends and R. Kleiss, *Nucl. Phys.* **B178** (1981) 141. F.A. Brends, R. Kleiss and S. Jadach, *Nucl. Phys.* **B202** (1982) 63.
40. R. Odorico, *Nucl. Phys.* **B172** (1980) 157.
41. T. Sjöstrand *et al.*, Proceedings of the Workshop on Z Physics at LEP I, eds. G. Altarelli, R. Kleiss and C. Verzegnassi, CERN Report 89-08 (1989).
42. T. Sjöstrand, CERN-TH-6488-92 (1992).
43. G. Altarelli and G. Parisi, *Nucl. Phys.* **B126** (1977) 298.
44. V.N. Gribov and I.N. Lipatov, *Sov. J. Nucl. Phys.* **15** (1972) 438.
45. Yu.L. Dokshitzer, D.I. D'yakonov and S.I. Troyan, Proceedings of the 13th Winter School of LNPI, Leningrad (1978), SLAC-TRANS-183 (1978).
46. G.P. Korchemskii, *Phys. Lett.* **B220** (1989) 629.
47. X. Artru and G. Mennessier, *Nucl. Phys.* **B70** (1974) 93.
48. B. Andersson, G. Gustafson, G. Ingelman and T. Sjöstrand, *Phys. Rep.* **97** (1983) 31.
49. D. Amati and G. Veneziano, *Phys. Lett.* **B181** (1981) 90.
50. R. Brun *et al.*, CERN-DD-78-2 (1978).
51. G. Grindhammer *et al.*, *Nucl. Inst. Meth.* **A290** (1990) 469.
52. MARK-J Collab., D. P. Barber *et al.*, *Phys. Rev. Lett.* **43** (1979) 830;  
*Phys. Lett.* **B89** (1979) 139.
53. G. Parisi, *Phys. Lett.* **B 74** (1978) 65.  
J. F. Donoghue, F. E. Low and S. Y. Pi, *Phys. Rev.* **D20** (1979) 2759.
54. CDF Collab., F. Abe *et al.*, *Phys. Rev.* **D44** (1991) 601.

55. Mark II Collab., S. Komamiya *et al.*, Phys. Rev. Lett. **64** (1990) 987.
56. JADE Collab., W. Bartel *et al.*, Z. Phys. **C33** (1986) 23.
57. Y. Ohnishi and H. Masuda, SLAC-PUB-6560 (1994); submitted to Phys. Rev. D.
58. P. N. Burrows, Z. Phys. **C41** (1988) 375,  
OPAL Collab., M. Z. Akrawy *et al.*, Z. Phys. **C47** (1990) 505.
59. CLEO Collab., R. Giles *et al.*, Phys. Rev. **D30** (1984) 2279.  
ARGUS Collab., H. Albrecht *et al.*, Z. Phys. **C54** (1992) 13,  
Z. Phys. **C58** (1993) 191.
60. V. Blobel, Proceedings of 8th CERN School of Computing, Aiguablava, Spain, September 9-22, 1984, CERN 85-09 (1985).
61. P.N. Burrows and H. Masuda, Z. Phys. **C63** (1994) 235.
62. OPAL Collab., P. D. Acton *et al.*, Z. Phys. **C59** (1993) 1.
63. SLD Collab., K. Abe *et al.*, Phys. Rev. Lett. **71** (1993) 2528.
64. C.N. Lovett-Turner, DTP-94-24 (1994).
65. ALEPH Collab., D. Buskulic *et al.*, Phys. Lett. **B307** (1993) 209.
66. CLEO Collab., J.P. Alexander *et al.*, CLEO CONF 94-26 (1994).
67. CLEO Collab., R. Balest *et al.*, CLEO CONF 94-28 (1994).
68. PEP/ $2\gamma$  Collab., D.A. Bauer *et al.*, SLAC-PUB-6518 (1994).
69. TOPAZ Collab., Y. Ohnishi *et al.*, Phys. Lett. **B313** (1993) 475.
70. L3 Collab., O. Adriani *et al.*, Phys. Lett. **B284** (1992) 471.
71. OPAL Collab., R. Akers *et al.*, Z Phys. **C63** (1994) 197.
72. D.T. Barclay, C.J. Maxwell, and M.T. Reader, UICHEP-TH/93-14 (1993).
73. G. Grunberg, Phys. Lett. **B95** (1980) 70; Phys. Lett. **B110** (1982) 501;  
Phys. Rev. **D29** (1984) 2315.
74. P.M. Stevenson, Phys. Lett. **B100** (1981) 61; Phys. Rev. **D23** (1981) 2916;  
Nucl. Phys. **B203** (1982) 472; Nucl. Phys. **B231** (1984) 65.
75. C.J. Maxwell and J.A. Nicholls, Phys. Lett. **B213** (1988) 217.  
J. Chýla, A Kataev, and S. Larin, Phys. Lett. **B267** (1991) 269.
76. S. Bethke, in Proceedings of the XXVI<sup>th</sup> ICHEP, Dallas, (1992) 81.

副論文